Component Terminal Dynamics in Weakly and Strongly Interacting Blends

A DISSERTATION
SUBMITTED TO THE FACULTY OF THE GRADUATE SCHOOL
OF THE UNIVERSITY OF MINNESOTA
BY

Sehban N. Ozair

IN PARTIAL FULFILMENT OF THE REQUIREMENTS
FOR THE DEGREE OF
DOCTOR OF PHILOSOPHY

Timothy P. Lodge, Advisor

December 2009

© Sehban N. Ozair, 2009

Acknowledgements

The past five years have shaped my life in more ways than I could have ever imagined. I enrolled in graduate school, got married, had a daughter, and am now at the finish line of my doctorate studies. First and foremost, I thank God for providing me with the opportunity to pursue a Ph.D. and for blessing me with the capability and resources to accomplish this feat. Without God's help and blessings, I would have achieved nothing. I thank my parents for their support and prayers, and for instilling in me the love for knowledge and for encouraging me to pursue a graduate degree. As for my ever patient and loving wife, Nashiah, who is the rock of our family, I thank her for her numerous sacrifices for myself and for our family, for her patience, and for the care and affection she has showered on me. My daughter, Sakinah, is the peace and tranquility of my heart and fills my life with joy and happiness. I am a content and happy man because of her and Nashiah. My siblings have also been instrumental in making it possible for me to pursue and complete my Ph.D. and for that I will forever be grateful to them.

When I first visited University of Minnesota, my brief meeting with my advisor, Tim, made me realize I wanted to come to Minnesota and work in his group. He is a great advisor, a terrific scientist, a wonderful person, and a great intellectual thinker. I have learned a great deal about scientific research from him and truly appreciate his mentorship. I thank him for giving me an opportunity to work under his guidance.

Among my peers, I'd like to acknowledge four people specifically: Dr. Jeff Haley, Dr. Ilan Zeroni, Ashish Gaikwad, and Dr. Atsushi Noro. Dr. Haley was instrumental in teaching me the FRS technique. Dr. Zeroni taught me anionic polymerization, and we had

many insightful discussions about polymer dynamics, parenting, and world financial markets. Ashish taught me how to use the DSC apparatus, and provided me with great insights in the area of polymer dynamics. Dr. Noro taught me RAFT polymerization and provided me with critical knowledge related to my research – the technique for hydrolyzing P*t*BOS to obtain PVPh.

My research experience would not be complete without Sayeed Abbas, Peter Simone, Brad Jones, and Rajiv Taribagil. All these colleagues deserve my appreciation for many insightful discussions I've had with them regarding polymer science as well as a wide variety of other topics including, but not limited to, neutron scattering data analysis, the intricacies of MS Word, politics and current affairs, the good and not so good aspects of various sports including hockey and soccer, the annual Chemistry Department softball league, global warming, and Walmart labor practices.

My life in graduate school was made a lot easier by Mary Nissen, Lynn Johnsrud, Teresa Bredahl, and Julie Prince. Mary always went out of her way to make sure my payroll appointment was done correctly and on time. Julie Prince was always there to answer questions regarding departmental policies, industrial recruiting, etc. Similarly Teresa was a great resource for finding any and all information about the CEMS department. Lynn was always very helpful for trip reimbursement issues as well as providing information to us CEMS students about happenings in the Chemistry department.

Anyone who has come and gone in my life over the past five years and I have had a chance to interact with, he/she has made a difference for me. I thank them all.

Abstract

Miscible blend dynamics have been long been a subject of interest and are not as well understood as dynamics of homopolymer melts. Their anomalous behavior, such as time–temperature superposition failure, broadening of calorimetric glass transition, etc., makes these systems very intriguing and challenges our understanding of miscible blend dynamics.

In this work we investigated temperature and composition dependence of two different, dynamically heterogeneous blend systems using rheology and forced Rayleigh scattering (FRS). The first blend investigated was a weakly interacting one comprising poly(ethylene oxide) (PEO) and poly(methyl methacrylate) (PMMA). Monomeric friction factors of PEO and PMMA were reported for a wide range of temperature and composition. PEO terminal dynamics were found to have strong composition dependence unlike that of PEO segmental dynamics previously reported. Also, PEO maintained its rapid relaxation mechanisms even in stiffer surroundings. The PEO hydroxyl end groups were found to have no significant impact on component chain dynamics. The FRS and rheology results agreed remarkably well for this system. The Lodge–McLeish model failed to describe the experimental results.

In order to understand the role of hydrogen bonding on chain dynamics, a strongly interacting system of PEO/poly(vinyl phenol) (PVPh) was investigated using rheology. The blends consisted of a high molecular polymer tracer dispersed in low molecular weight matrix to extract relevant dynamic information from tracer contribution to material properties. Monomeric friction factors were reported for a wide temperature and

composition range. Time–temperature superposition failure was observed in PEO tracer blends at high PVPh concentration. The shape of tracer relaxation spectra for PVPh tracer blends had a strong composition dependence while those for PEO tracer blends were independent of composition. The tracer contribution to blend viscosity had a strong temperature dependence at high PVPh composition. Across the composition range, single and narrow glass transitions were observed for these blends.

PVPh chain conformations were investigated using SANS and contradictory conclusions were reached. Therefore, no conclusive remarks can be made regarding PVPh chain conformations in dilute solution.

Table of Contents

Acknowledgements i

Abstract iii

Table of Contents v

List of Figures viii

List of Tables xiii

Chapter 1. Introduction 1
1.1 Introduction 1
1.2 References 6

Chapter 2. Background 7
2.1 Introduction 7
2.2 Viscoelasticity Models for Polymer Melts 7
2.2.1 Rouse Model 8
2.2.2 Reptation Model 12
2.2.3 Constraint Release 17
2.2.4 Contour Length Fluctuations 17
2.3 Importance of Monomeric Friction Factor 19
2.3.1 Temperature Dependence of Monomeric Friction Factor 19
2.3.2 Monomeric Friction Factor in Miscible Blends 23
2.4 Dynamic Phenomena in Miscible Blends 24
2.4.1 Complex Composition and Temperature Dependence of Friction Factors 25
2.4.2 Broadening of the Calorimetric Glass Transition 27
2.4.3 Breakdown of Time–Temperature Superposition 31
2.4.4 Composition dependence of η 33
2.5 Theoretical Models for Blend Dynamics 35
2.5.1 Concentration Fluctuations 35
2.5.2 Chain Connectivity and Self–Concentration 38
2.6 Overview of PEO/PMMA Blend Dynamics 41
2.7 Strongly Interacting Blends 45
2.7.1 Thermodynamics of mixing 45
2.7.2 Miscibility and Dynamics in Interacting Blends 48
2.7.3 Dynamics in PEO/PVPh Blends 50
2.8 References 51

Chapter 3. Experimental Methods 56
3.1 Introduction 56
3.2 Forced Rayleigh Scattering 56

3.2.1 Overview 56
3.2.2 Forced Rayleigh Scattering Background 60
3.2.3 Forced Rayleigh Scattering Experimental Technique 61
3.2.4 Forced Rayleigh Scattering Instrumentation 74
3.2.5 Forced Rayleigh Scattering Sample Preparation 75
3.3 Chemical Synthesis for FRS experiments 78
3.3.1 Dye Synthesis 78
3.3.2 Polymer Labeling 86
3.4 Poly(4–vinyl phenol) Synthesis and Characterization 89
3.4.1 Synthesis 89
3.4.2 NMR Analysis 93
3.4.3 Determination of dn/dc 93
3.4.4 MALDI–TOF Mass Spectrometry 97
3.5 Rheological Measurements 99
3.5.1 Rheometry 102
3.6 Differential Scanning Calorimetry 103
3.7 Small Angle Neutron Scattering 104
3.9 References 108

Chapter 4. Component Terminal Dynamics in PEO/PMMA Blends 109
4.1 Introduction 109
4.2 Results 111
4.2.1 Materials 111
4.2.2 Forced Rayleigh Scattering (FRS) 112
4.2.3 Rheology 125
4.3 Discussion 127
4.3.1 Composition and Temperature Dependence of Monomeric Friction Factors 127
4.3.2 Comparison of FRS and Rheology Results 130
4.3.3 Analysis of Assumptions for Diffusion Measurements 131
4.3.4 Analysis of Assumptions for Rheology Measurements 133
4.3.5 Effects of PEO Hydroxyl Groups 135
4.3.6 Lodge–McLeish Model Predictions 136
4.4 Summary 141
4.5 References 141

Chapter 5. Component Terminal Dynamics in Strongly Interacting Blends 143
5.1 Introduction 143
5.2 Results 146
5.2.1 Materials 146
5.2.2 Component Dynamics from Rheology 147
5.2.3 Tracer Rheology 148
5.2.4 Rheological Data Representation for Extraction of Dynamic Information 148
5.2.5 Determination of ζ from Rheology 154
5.2.6 Extraction of ζ from η and η'' 154
5.2.7 Extraction of ζ in the absence of η'' peaks 157
5.2.8 DSC Thermograms 164

5.2.9 Quantification of Hydrogen Bonds 168

5.3 Discussion 174
5.3.1 Coleman–Graf–Painter Association Model Predictions 174
5.3.2 Time–Temperature Superposition Breakdown 175
5.3.3 Composition and Temperature Dependence of ζ 180
5.3.4 Composition and Temperature Dependence of Matrix Viscosities 181
5.3.5 PEO–845 tracer contribution to blend viscosity 182
5.3.6 PVPh–290 tracer contribution to blend viscosity 185
5.3.7 Comparison of PVPh and PEO tracer blend viscosities 186
5.3.8 Shape of PEO and PVPh Tracer Blend Relaxation Spectra 189
5.3.9 Calorimetric Glass Transition 197
5.4 Summary and Conclusions 200
5.5 References 201

Chapter 6. Determination of PVPh Chain Conformations and Dimensions Using Small Angle Neutron Scattering 203
6.1 Introduction 203
6.2 Experimental 205
6.2.1 Materials 205
6.2.2 SANS Experiments 207
6.3 Results and Discussion 207
6.4 Summary 224
6.5 References 225

Chapter 7. Summary and Outlook 226
7.1 Introduction 226
7.2 Outlook 230
7.3 References 231

Bibliography 233

Appendix A 240

List of Figures

Figure 2.1. The bead and spring model used to develop the Rouse theory of polymer dynamics.....10

Figure 2.2. Schematic representation of the reptation process. As time progresses, the reptating chain diffuses out of the initial "tube" and eventually completely escapes it.....15

Figure 2.3. DSC scans of different compositions of the PI/PVE blend. The middle composition range shows significant glass transition broadening relative to that in homopolymers.....29

Figure 2.4. (a) DSC curves for different compositions of PEO/PMMA blends. (b) Corresponding derivative curves of the DSC traces in (a).....30

Figure 2.5. Breakdown of time–temperature superposition in a miscible blend of PEO/PMMA. 32

Figure 2.6. Illustration of chain connectivity and resulting self concentration effects. The volume enclosed by the circle contains a higher concentration of filled polymer segments than rest of the blend. 40

Figure 3.1 Relative intensity distribution near the crossover of two similarly polarized, Gaussian laser beams. 62

Figure 3.2. Top view of interference pattern of laser beams of wavelength λ, intersecting each other at an angle θ. The wave vectors for each beam are denoted by k_1 and k_2, and d is the distance between intensity maxima and minima.....63

Figure 3.3. Ring closing reaction during photoisomerization of ONS–COOH. Both steps are irreversible and the intermediate product is the dye isomer formed during FRS experiment. The second step is an oxidation step and occurs only in the presence of oxygen at elevated temperature. 66

Figure 3.4. (a)Types of possible FRS signals as a result of complimentary gratings contributing to diffracted signal. (b) The grid shows the necessary conditions for each type of decay profile in terms of time constants, τ, and grating amplitudes, A of each grating type. (Adapted from Ref. 19).....73

Figure 3.5. A schematic of FRS setup in the writing mode 76

Figure 3.6. A schematic representation of FRS setup in the reading mode 77

Figure 3.7. ^{1}H NMR spectrum of *o*–nitro–*p*–tolunitrile in chloroform.....80

Figure 3.8. ^{1}H NMR spectrum of ONS–CN in acetone 82

Figure 3.9. ^{1}H NMR spectrum of ONS–COOH in acetone 84

Figure 3.10. Synthesis of ONS–COOH 85

Figure 3.11. Condensation reaction of PEO with ONS–COOH 87

Figure 3.12. SEC spectrum of labeled PEO after purification. Small amount of attached dye can still be seen in the spectrum. 88

Figure 3.13. ^{1}H NMR spectrum of P*t*BOS in deuterated acetone 94

Figure 3.14. ^{1}H NMR of PVPh in deuterated DMSO 95

Figure 3.15. Determination of dn/dc for P*t*BOS and PVPh. (▲) PVPh, (▼) P*t*BOS 96

Figure 3.16. MALDI – TOF mass spectrum for PVPh–5. 98

Figure 4.1. FRS intensity profiles for PEO/PMMA 50/50 blend at 55 °C for different grating spacing. Dots are experimental data while solid line is the best fit to equation 4.1. 116

Figure 4.2. FRS intensity profiles for PEO/PMMA 20/80 blend at 40 °C for different grating spacing. Dots are experimental data while solid line is the best fit to equation 4.1. 117

Figure 4.3. FRS intensity profiles for PEO/PMMA 10/90 blend at 70 °C for different grating spacing. Dots are experimental data while solid line is the best fit to equation 4.1. 118

Figure 4.4. FRS intensity profiles for PEO/PMMA 01/99 blend at 70 °C for different grating spacing. All of the PEO in this blend is PEO–1*. Dots are experimental data while solid line is the best fit to equation 4.1. 119

Figure 4.5. Plots of (a) $<\tau_1>$ vs. d^2 and (b) $1/<\tau_1>$ vs. $1/d^2$ for PEO/PMMA 10/90 at 100 °C. 121

Figure 4.6. Monomeric friction factors of PEO in PEO/PMMA blends. Blend composition is indicated by wt.% PMMA in the blend. Solid and dashed lines are WLF fits to PEO and PMMA homopolymer friction factors respectively. FRS data is represented by (▲). Literature FRS data (Δ) is also shown for comparison purposes and is shifted horizontally by 17.5 K to account for T_g differences. All other symbols are rheology data. Different symbols are used to designate different methods of extraction of ζ that are not discussed here. Reproduced from reference 8. 128

Figure 4.7. Monomeric friction factors of PMMA in PEO/PMMA blends. Blend composition is indicated by wt.% PMMA in the blend. Solid and dashed lines are WLF fits to PEO and PMMA homopolymer friction factors respectively. All the data is obtained from rheology experiments. PEO homopolymer data are added for comparison purposes. Reproduced from reference 8. 129

Figure 4.8. Comparison of monomeric friction factors for 20/80 blends of PEO/PMMA and PEO-DME/PMMA. 137

Figure 4.9. Lodge–McLeish predictions (solid lines) for (a) PEO and (b) PMMA with $\phi_{self,\ PEO} = \phi_{self,\ PMMA} = 0$. Thick dashed lines are homopolymer WLF fits and percentages indicate PMMA content in the blends. (▲) FRS data, and (♦) rheology data. 140

Figure 5.1. Plot of η', η'' vs. reduced frequency for PVPh–290 tracer in (a) 20% PVPh, and (b) 35% PVPh blends. Reference temperature for the master curves is 80 °C. (×) η' for tracer blend, (+) η'' for tracer blend, and solid line is for matrix η'. 150

Figure 5.2. Plot of η', η'' vs. reduced frequency for PEO–845 tracer in (a) 20% PVPh, and (b) 35% PVPh blends. Reference temperature for the master curves is 80 °C. (×) η' for tracer blend, (+) η'' for tracer blend, and solid line is for matrix η'. 152

Figure 5.3. Monomeric friction factors of PVPh as a function of temperature for various PEO/PVPh blend compositions. (■) 10% PVPh, (●) 20% PVPh, (▲) 35% PVPh, (♦) 50% PVPh, (▼) 65% PVPh. Solid line represents homopolymer PEO–1, and dashed line represents homopolymer PVPh–5. 158

Figure 5.4. Monomeric friction factors of PEO as a function of temperature for various PEO/PVPh blend compositions. (■) 10% PVPh, (●) 20% PVPh, (▲) 35% PVPh, (♦) 50% PVPh, (▼) 65% PVPh. Solid line represents homopolymer PEO–1, and dashed line represents homopolymer PVPh–5. 159

Figure 5.5. Ratios of PVPh and PEO friction factors as a function of temperature for various PEO/PVPh blend compositions. (■) 10% PVPh, (●) 20% PVPh, (▲) 35% PVPh, (♦) 50% PVPh, (▼) 65% PVPh. 160

Figure 5.6. Matrix viscosities as a function of temperature for PEO–1/PVPh–5 blends. (■) 10% PVPh, (●) 20% PVPh, (▲) 35% PVPh, (♦) 50% PVPh, (▼) 65% PVPh. Solid line represents homopolymer PEO–1, and dashed line represents homopolymer PVPh–5. 163

Figure 5.7. DSC scans for various compositions of PEO–1/PVPh–5 blends. The percent compositions listed for each scan in the figure are those of PVPh in the blend. 165

Figure 5.8. Differential DSC scans for various compositions of PEO–1/PVPh–5 blends. The percent compositions listed for each scan in the figure are those of PVPh in the blend. 166

Figure 5.9. Fraction of hydrogen bonded (a) OH groups, and (b) EO groups as a function of PVPh composition at (●) 40 °C, (▼) 140 °C.....172

Figure 5.10. In 1g of PEO–1/PVPh–5 blend, number of (a) total hydrogen bonded OH groups, (b) hydrogen bonded EO groups, and (c) intra–associated OH groups as a function of PVPh composition at (●) 40 °C, (▼) 140 °C.....173

Figure 5.11. Plot of η', η'' vs. reduced frequency for PEO–900 tracer in PEO–1/PMMA–1.5 blends for (a) 80% PMMA, and (b) 90% PMMA compositions. (×) η' for tracer blend, (+) η'' for tracer blend. 176

Figure 5.12. Ratio of (a) PEO–845 tracer blend viscosity to matrix viscosity, (b) PVPh–290 tracer blend viscosity to matrix viscosity as a function of temperature for PEO–1/PVPh–5 blends. (■) 10% PVPh, (●) 20% PVPh, (▲) 35% PVPh, (♦) 50% PVPh, (▼) 65% PVPh.....183

Figure 5.13. Ratio of PVPh tracer blend viscosity to that of PEO tracer blend viscosity as a function of temperature for various PEO–1/PVPh–5 blend compositions. (■) 10% PVPh, (●) 20% PVPh, (▲) 35% PVPh, (♦) 50% PVPh, (▼) 65% PVPh. 188

Figure 5.14. Ratio of η'' to η''_{max} as a function of normalized frequency for (a) PEO–845 tracer, (b) PVPh–290 tracer in PEO/PVPh blends. (●) 20% PVPh, (♦) 35% PVPh, (▼) 50% PVPh, (▲) 65% PVPh. Solid line is the Rouse prediction and the dotted line is the Zimm prediction.....191

Figure 5.15. Ratio of η'' to η''_{max} as a function of normalized frequency for (a) PEO–900 tracer, and (b) PMMA–100 tracer in PEO–1/PMMA–1.5 blends. (▲) 50% PMMA, (▼) 80% PMMA, (■) 90% PMMA, (●) 100% PMMA. Solid line is the Rouse prediction and the dotted line is the Zimm prediction. 195

Figure 5.16. Composition dependence of PEO–1/PVPh–5 blend T_gs (a) before accounting for PEO crystallinity in blend, (b) after accounting for PEO crystallinity in blend. Dotted line represents linear composition dependence. 199

Figure 6.1. Coherent scattering profiles of PVPh in DMSO. Symbols are experimental data points while the solid lines are the best fits to Debye function as determined by linear regression.....208

Figure 6.2. Coherent scattering profiles of PVPh in THF. Symbols are experimental data points while the solid lines are the best fits to Debye function as determined by linear regression.....209

Figure 6.3. Coherent intensity profiles of different molecular weights of PVPh in THF. 211

Figure 6.4. Concentration dependence of R_g values for PVPh in DMSO obtained by fitting the Debye function. Solid symbols are infinite dilution values of R_g. 214

Figure 6.5. Concentration dependence of R_g values for PVPh in THF obtained by fitting the Debye function. Solid symbols are infinite dilution values of R_g. 215

Figure 6.6. (a) Kratky plot for 4.3 wt.% solution of PVPh–10 in DMSO, and (b) modified Kratky plot for the same polymer solution. The linear dependence of $q^2I(q)$ on q in (a) indicates presence rigid rod configuration of polymer chains. The horizontal plateau at high q in (b) confirms presence of rigid rods. 218

Figure 6.7. Molecular weight dependence of R_g in (a) DMSO, and (b) THF. The scaling exponent of 0.66 in (b) was obtained by fitting power law only to the first three data points. 220

Figure A.1. Kratky plots for PVPh–5 in DMSO. 241

Figure A.2. Kratky plots for PVPh–10 in DMSO. 242

Figure A.3. Kratky plots for PVPh–35 in DMSO. 243

Figure A.4. Kratky plots for PVPh–290 in DMSO. 244

Figure A.5. Kratky plots for PVPh–5 in THF. 245

Figure A.6. Kratky plots for PVPh–10 in THF. 246

Figure A.7. Kratky plots for PVPh–35 in THF. 247

Figure A.8. Kratky plots for PVPh–290 in THF. 248

List of Tables

Table 2.1. Bond Energies of Different Intermolecular Forces 47

Table 3.1. Neutron scattering lengths of elements commonly found in polymers 106

Table 4.1. Properties of Polymers Used in This Work 112

Table 4.2. PEO/PMMA blend compositions and corresponding temperature ranges over which diffusion measurements were carried out. 113

Table 4.3. FRS Parameters and Diffusion Coefficients for PEO/PMMA Blends 122

Table 5.1. Properties of Polymers Used in this Work.....146

Table 5.2. Thermal Properties of PEO/PVPh Blends Used in This Study.....167

Table 5.3. Parameters used for quantification of hydrogen bonds in PEO/PVPh blends .170

Table 6.1. PVPh molecular weights and solution concentrations used for each solvent ..206

Table 6.2. Comparison of infinite dilution R_g values from Debye and Guinier analysis..213

Table 6.3. Comparison of experimental and theoretical R_g values 222

Table 6.4. R_g values for a stretched helix of atactic PS.....223

Chapter 1. Introduction

1.1 Introduction

Miscible polymer blends are technologically important because they provide a low cost alternative route to new materials with tunable properties. The ability to fine tune properties of a material makes polymer mixtures such as miscible blends and block co-polymers commercially viable. It is important to develop a fundamental understanding of the dynamic and viscoelastic properties of polymer melts and miscible blends because of the need to properly optimize processing conditions and material properties. Extensive studies have been done on homopolymer melts and solutions and their dynamic and viscoelastic behavior is well established. However, such behavior in miscible blends is much more complex and not as well understood.

A polymer chain is made up of N monomers or repeat units. A few of these repeat units make up a polymer segment. Each segment has a characteristic length known as statistical segment length, b, which is usually on the order of 5–7 Å. The mean square end-to-end distance of a polymer chain can be determined if b is known. When polymer chains move, they experience a frictional drag due to the presence of surrounding chains. This drag is known as the monomeric friction factor, ζ. It is important to realize that ζ is a measure of the frictional force experienced by entire chain but expressed on a per monomer basis. The dynamic and viscoelastic properties of unentangled polymers can be predicted if N, ζ, and b are known. However, if entanglements are present, additional

information such as knowledge of the spacing between entanglements, is also required to predict the dynamic and viscoelastic properties.

When polymer chains undergo conformational transitions of backbone bonds, such small length scale movement is characterized as *segmental dynamics*. On the other hand, motion on a length scale of entire polymer chain is characterized as *terminal dynamics*. Well established theories such as Rouse[1] and reptation[2] can describe the dynamic and rheological behavior in homopolymers but such behavior in miscible blends has a more complex temperature and composition dependence. The investigations into terminal dynamics[3–7] and segmental dynamics[8,9] have revealed phenomena that are not observed in homopolymer melts.

The complexities in miscible blends arise from the fact that ζ of each component exhibits a distinct composition and temperature dependent behavior. This gives rise to different temperature and composition dependences of segmental and terminal dynamics of both components. The segmental and terminal dynamics of homopolymers have the same temperature dependence far away from the glass transition temperature, T_g, but exhibit different temperature dependences near T_g. This trend is also observed in some miscible blends such as poly(isoprene)/poly(vinylethylene) (PI/PVE),[10] but in some other blends such as poly(ethyleneoxide)/poly(methylmethacrylate) (PEO/PMMA), the temperature dependence of segmental and terminal dynamics are vastly different even at temperatures significantly above T_g of the slow moving component.[11] Such a complex behavior makes universal prediction of dynamic properties difficult based on the behavior of one blend system.

Miscible blends also exhibit some other phenomena that are not observed in single component systems. These include failure of the time–temperature superposition principle,[4,12–14] and broadening of the glass transition.[15–18] These observations in blends are a result of each component's unique ζ and their different temperature and composition dependences.

PEO/PMMA blends have drawn considerable attention in recent years because of anomalous PEO dynamics in these blends. The mobilities of PEO and PMMA are very different and these blends exhibit *dynamic heterogeneity*, i.e., there exists significant discrepancy in the dynamic behavior of components in the blend. PEO segmental dynamics have been reported to be hardly influenced by the more glassy, slow moving, PMMA over the entire blend composition.[19] There is also increasing evidence of decoupling of segmental and terminal dynamics in PEO/PMMA blends.[11,19] Component terminal dynamics in PEO/PMMA blends have been previously investigated but these studies have investigated dynamics over limited range of temperature and composition.[4,20] Therefore, we undertook an investigation of component terminal dynamics in PEO/PMMA blends over as wide a temperature and composition range as possible to contribute to the understanding of anomalous PEO/PMMA dynamics.

PEO/PMMA blends are one of many weakly interacting blends that have garnered the attention of the scientific community to understand component dynamics. However, there has been relatively little research done to understand component dynamics, either at segmental or terminal level, in blends with strong specific interactions such as hydrogen bonding. Today, it is well established that hydrogen bonding enhances miscibility in otherwise immiscible systems.[21–24] Intermolecular hydrogen bonding can potentially lead

to simplification of blend dynamics by coupling component dynamics. Because of the relative scarcity of dynamics studies on strongly interacting systems, we undertook investigation of component chain dynamics in a strongly interacting blend of PEO/poly(4–vinyl phenol) (PEO/PVPh) to understand the role of hydrogen bonding in blend dynamics. This blend was chosen because PEO and PVPh are completely miscible over the entire composition range,[25–27] form stronger intermolecular hydrogen bonds as opposed to intramolecular hydrogen bonds, and have a large difference in homopolymer T_gs making the blends *dynamically asymmetric*. The choice of PEO as the blend partner for PVPh is also motivated by the study of PEO/PMMA blend dynamics that will be discussed in this dissertation which reveals relaxation mechanisms of PEO that are not completely understood. The study of PEO/PVPh blend dynamics is a major part of this work and produces the bulk of the results and analysis.

In addition to studying dynamics in PEO/PVPh blends, we undertook a study of chain conformations of PVPh in dilute solutions. This study was motivated by the fact that no reliable information on PVPh chain dimensions is present in the literature. We performed small angle neutron scattering experiments to investigate PVPh chain conformations.

The experimental methods of choice for studying component dynamics have been forced Rayleigh scattering (FRS) and rheology. The blends prepared for FRS measurements contained optical tracers labeled with photochromic dyes and were of the same molecular weight as the matrix component. Blends for rheology experiments contained large molecular weight tracers dispersed in a low molecular weight matrix.

The blends studied in this work contained low molecular weight PEO (M_n = 1 kg/mol). PEO and PMMA form a miscible blend over a wide temperature range.[28] The miscibility, however, does not extend to all blend compositions. PEO crystallizes around 50–60 °C in a blend containing more than 20-30% PEO by weight.[20,29] Hence, to minimize interference from crystallization in the experimental temperature range, the PEO molecular weight was kept low. Similarly, in PEO/PVPh blends PEO crystallization was observed for temperatures less than 40 °C for blends with greater than 65 wt.% PEO.

This dissertation breaks down the work done on understanding dynamics in miscible blends into several chapters. Chapter 2 will provide background information on polymer dynamics theories, dynamic phenomena in miscible blends, and a review of hydrogen bonding in blends. Chapter 3 describes in detail the experimental methods used in this work, and the synthesis and characterization of polymers and photochromic dyes. Chapter 4 lays out in detail the results and analysis of diffusion and rheological studies on PEO/PMMA blends. A discussion of effects of hydroxyl end groups on component dynamics as well as influence of dye molecules on chain diffusion is also presented. Chapter 5 details the results and analysis of component dynamics in PEO/PVPh blends. A detailed analysis is presented on temperature and composition dependence of component chain dynamics as well as viscoelastic properties. A theoretical model in the literature is described that predicts the amount of hydrogen bonding present in these blends. All discussion takes place on the basis of predictions of this theoretical model. Chapter 6 describes the results and analysis of a study of PVPh chain conformations in dilute solutions. Finally, Chapter 7 summarizes the work presented in this dissertation and offers an outlook for further exploration in this area of study.

1.2 References

[1] Rouse, P. E. *J.Chem. Phys.* **1953**, *21*, 1272.
[2] de Gennes, P. G. *J. Chem. Phys.* **1971**, *55*, 572.
[3] Green, P. F.; Adolf, D. B.; Gilliom, L. R. *Macromolecules* **1991**, *24*, 3377.
[4] Colby, R. H. *Polymer* **1989**, *30*, 1275.
[5] Composto, R. J.; Kramer, E. J.; White, D. M. *Polymer* **1990**, *31*, 2320.
[6] Kim, E.; Kramer, E. J.; Wu, W. C.; Garrett, P. D. *Polmer* **1994**, *35*, 5706.
[7] Kim, E.; Kramer, E. J.; Osby, J. O. *Macromolecules* **1995**, *28*, 1979.
[8] Chung, G. C.; Kornfield, J. A.; Smith, S. D. *Macromolecules* **1994**, *27*, 5729.
[9] Chin, Y. H.; Inglefield, P. T.; Jones, A. A. *Macromolecules* **1993**, *26*, 5372.
[10] Haley, J. C.; Lodge, T. P.; He, Y.; Ediger, M. D.; Von Meerwall, E. D.; Mijovic, J. *Macromolecules* **2003**, *36*, 6142.
[11] Haley, J. C.; Lodge, T. P. *J. Chem. Phys.* **2005**, *122*, 324914.
[12] Minnick, M. G.; Schrag, J. L. *Macromolecules* **1980**, *13*, 1690.
[13] Arendt, B. H.; Krishnamoorti, R,; Kornfield, J. A.; Smith, S. D. *Macromolecules* **1997**, *30*, 1127.
[14] Pathak, J. A.; Colby, R. H.; Floudas, G.; Jerome, R. *Macromolecules* **1999**, *32*, 2553.
[15] Roovers, J.; Toporowski, P. M. *Macromolecules* **1992**, *25*, 3454.
[16] Trask, C. A.; Roland, C. M. *Macromolecules* **1989**, *22*, 256.
[17] Roovers, J.; Toporowski, P. M. *Macromolecules* **1992**, *25*, 1096.
[18] Chung, G. C.; Kornfield, J. A.; Smith, S. D. *Macromolecules* **1994**, *27*, 5729.
[19] Lutz, T. R.; He, Y.; Ediger, M. D.; Cao, H.; Lin, G.; Jones, A. A. *Macromolecules* **2003**, *36*, 1724.
[20] Zawada, J. A.; Ylitalo, C. M.; Fuller, G. G.; Colby, R. H.; Long, T. E. *Macromolecules* **1992**, *25*, 2896.
[21] Coleman, M. M.; Lee, J. Y.; Serman, C. J.; Wang, Z.; Painter, P. C. *Polymer* **1989**, *30*, 1298.
[22] Kuo, S. W.; Chang, F. C. *Macromolecules* **2001**, *34*, 5224.
[23] Kuo, S. W.; Chang, F. C. *Macromolecules* **2001**, *34*, 4089.
[24] Serman, C. J.; Xu, Y.; Painter, P. C.; Coleman, M. M. *Polymer* **1991**, *32*, 516.
[25] Qin, C.; Cheng, C.; Pires, A. T. N.; Belfiore, L. A. *Polym. Mater. Sci. Eng.* **1989**, *61*, 945.
[26] Moskala, E. J.; Varnell, D. F.; Coleman, M. M. *Polymer* **1985**, *25*, 228.
[27] Zhang, X.; Takegoshi, K.; Hikichi, K. *Macromolecules* **1992**, *25*, 2336.
[28] Ito, H.; Russell, T. P.; Wignall, G. D. *Macromolecules* **1987**, *20*, 2213.
[29] Dionisio, M.; Fernandes, A. C.; Mano, J. F.; Correia, N. T.; Sousa, R. C. *Macromolecules* **2000**, *33*, 1002.

Chapter 2. Background

2.1 Introduction

In this chapter, the background information of miscible blend dynamics is reviewed. First, the molecular models for homopolymer dynamics and viscoelasticity such as Rouse and reptation are discussed. Then, the phenomenology of miscible blends is described in detail, followed by a review of theoretical models for blend dynamics. Finally, a review of the miscible blend literature is presented.

2.2 Viscoelasticity Models for Polymer Melts

Linear homopolymers are the simplest class of polymeric materials. The viscoelastic and dynamic behavior of homopolymer melts has been extensively studied and well understood. Over the past half century or so, several theories and models have been developed that provide a universal description of the viscoelastic and dynamic behavior of monodisperse, homopolymer melts.

As the molecular weight of polymers is increased, there comes a critical molecular weight above which topological constraints by neighboring chains become significant and the polymer chains entangle with each other. The viscoelastic behavior of un–entangled and entangled polymers differ significantly; hence, different molecular theories are needed to describe various physical phenomena in each type of system.

In this section, we first discuss the Rouse model that has been applied to low molecular weight, unentangled melts. The reptation model, developed for entangled

systems will then be discussed, followed by a discussion of contour length fluctuations and constraint release to better describe chain relaxation mechanisms in entangled melts.

2.2.1 Rouse Model

The Rouse model[1,2] is probably the simplest polymer dynamics model. It was originally developed for dynamics of flexible coils in dilute solutions but has found widespread application in predicting dynamics of flexible chains in low molecular weight, un-entangled melts. This model represents the polymer chain as a series of beads connected to each other by Hookean springs. A key assumption of the model is that the beads interact only through the spring forces and therefore any hydrodynamic interactions between the chains are ignored. This bead–spring model has n+1 beads and n springs as shown in Figure 2.1

A force balance described by equation 2.1 represents the motion of each bead.[1,2]

$$\zeta_{bead}\frac{d\bar{R}_n}{dt} = -K\left(2\bar{R}_n - \bar{R}_{n+1} - \bar{R}_{n-1}\right) + \bar{f}_n \tag{2.1}$$

where ζ_{bead} is the friction coefficient of the bead when it moves through the surrounding medium, $\bar{R}_n$ is the position of bead n, $\bar{f}_n$ is the Brownian force acting on the bead n, and K is the spring constant:

$$K = \frac{3k_BT}{b^2} \tag{2.2}$$

where k_B is the Boltzmann constant, T is the absolute temperature and b is the root mean square spring length. The force balances on beads at the chain ends (1 and n+1) are:

$$\zeta_{bead} \frac{d\bar{R}_1}{dt} = -K\left(\bar{R}_1 - \bar{R}_2\right) + f_1 \tag{2.3}$$

$$\zeta_{bead} \frac{d\bar{R}_{n+1}}{dt} = -K\left(\bar{R}_{n+1} - \bar{R}_n\right) + f_{n+1} \tag{2.4}$$

Solving eqs. 2.1 – 2.4 gives predictions for several dynamic and viscoelastic parameters. The solutions have been outlined elsewhere.[1,2] The key predictions of the Rouse model are the macroscopic properties of polymers such as zero shear viscosity, η, the center of mass self diffusion coefficient, D, and the time dependent shear modulus, $G(t)$.

The Rouse model makes universal predictions for the viscoelastic and dynamic properties of polymers regardless of their identity because the structural details are contained in the segment length, b, and ζ_{bead}. The prediction for the relationship between longest relaxation time, τ_1, and molecular weight, M, is given by eq. 2.5[2]:

$$\tau_1 = \frac{\zeta b^2}{3\pi^2 k_B T}\left(\frac{M}{M_o}\right)^2 \tag{2.5}$$

where ζ is the monomeric friction factor, M_o is the molecular weight of a repeat unit and remaining symbols have been previously described. It should be noted that ζ is not a

direct measure of segmental dynamics, but characterizes the terminal dynamics on a per monomer basis. As can be seen from eq. 2.5, the longest relaxation time scales with M^2 i.e. $\tau_1 \sim M^2$.

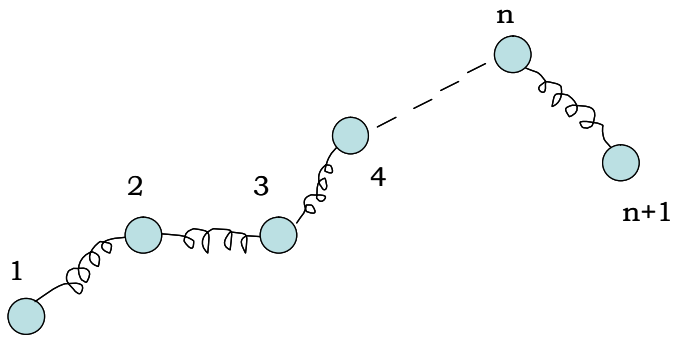

Figure 2.1. The bead and spring model used to develop the Rouse theory of polymer dynamics

The correlation between ζ and D is described by eq. 2.6, while that between ζ and steady shear viscosity, η, is given by eq. 2.7:[2,3]

$$D = \frac{k_B T}{\zeta N} \tag{2.6}$$

$$\eta = \frac{\rho N_A b^2}{36 M_o} N\zeta \tag{2.7}$$

where N is the degree of polymerization, N_A is Avogadro's number, and ρ is the bulk density of the polymer melt. The scaling predictions of the Rouse model in these two cases is $D \sim M^{-1}$ and $\eta \sim M$.

The Rouse model prediction for $G(t)$ is:

$$G(t) = \frac{\rho RT}{M} \sum_{p=1}^{n} \exp\left(- \frac{tp^2}{\tau_1} \right) \tag{2.8}$$

where R is the ideal gas constant and p is an integer between 1 and n introduced to label the set of characteristic time constants, τ_p. The pth relaxation time, τ_p, is the average time taken by a segment of the bead–spring chain containing n/p springs to relax completely from a non–equilibrium position. This bead-spring chain has n such relaxation times, ranging from τ_1, the relaxation time of the end-to-end vector of the whole chain, to τ_n, the relaxation time for a single bead spring unit. After some analysis that will not be described here, a very useful relationship between τ_p and τ_1 emerges:

$$\tau_p = \frac{\tau_1}{p^2} \tag{2.9}$$

Using equations 2.8 and 2.9 along with the Generalized Maxwell Model, the Rouse Model predictions for dynamic shear moduli can be obtained:

$$G' = \frac{\rho RT}{M} \sum_{p=1}^{N} \frac{(\omega\tau_p)^2}{1+(\omega\tau_p)^2} \tag{2.10}$$

$$G'' = \frac{\rho RT}{M} \sum_{p=1}^{N} \frac{\omega\tau_p}{1+(\omega\tau_p)^2} \tag{2.11}$$

These results give the same predictions as the Maxwell model at low frequencies ($\omega\tau_1 << 1$), $G' \sim \omega^2$, and $G'' \sim \omega$. In the limit of high frequencies ($\omega\tau_1 >> 1$), $G' \sim \omega^0$, and $G'' \sim \omega^{-1}$.

2.2.2 Reptation Model

As this dissertation focuses almost completely on dynamics of Rouse chains, the reptation theory and entanglement pheonomena will not be discussed in great detail. Readers are directed to other sources[2,4,5] if they are interested in a more through analysis.

The reptation model was originally developed by de Gennes[6] for flexible chains in entangled polymer melts. This theory was further modified by Doi and Edwards[2,7–10] for

linear and non–linear rheological behavior of polymers. This molecular model relates the macroscopic viscoelastic properties of entangled polymeric systems to the time required for a single chain to escape from an imaginary "tube" of topological constraints.

A chain can be imagined to be trapped in a tube-like region defined by the surrounding chains. The conformations of the trapped chain that protrude outside of the tube violate the topological constraints. The obstacles that trap the moving polymer chain have an average spacing, *a*. This average spacing measures the mesh size of the entanglement network. The chain is treated as a Rouse chain within the tube with a diffusion coefficient described by eq. 2.6. The obstacles surrounding the chain are assumed to be thin lines, so that they do not have any effect on static properties but have a serious impact on dynamic properties of the trapped chain by imposing topological constraints.[2]

Since only large scale fluctuations of the chain are of interest, the small–scale fluctuations are ignored and time evolution of a primitive path are discussed. The model proposes that the chain escapes the confining tube by wriggling along its primitive path in the tube. As the chain moves along the tube via random walk, it starts to escape the confines of the tube. This movement causes the memory of previous chain locations to be erased. The time it takes for the middle segments of the chain to escape the confines of the initial set of obstacles is the longest relaxation time.[11] Within the tube, Rouse dynamics are assumed and it is the confinement of the chain to the tube that alters the diffusion and relaxation times. The description of this process is schematically depicted in Figure 2.2.

One of the main assumptions in the reptation model is that the primitive chain can move back and forth only along itself with the Rouse diffusion coefficient. Movement of the chain perpendicular to the tube is not possible. Since the chain and contour length of the primitive path must have the same end–to–end distance, the contour length can be expressed in terms of chain dimensions and mesh size of the entanglement network:

$$L = \frac{Nb^2}{a} \tag{2.12}$$

where a is the average spacing between entanglements, also referred to as the tube diameter. The relationship of a to entanglement molecular weight, M_e is given by:

$$a^2 = \frac{4}{5}\frac{M_e}{M}Nb^2 \tag{2.13}$$

where M_e is determined by the plateau modulus, G_N^o using the relationship:

$$M_e = \frac{\rho RT}{G_N^o} \tag{2.14}$$

The reptation model prediction for the longest relaxation time is more complex than that of the Rouse model, and is given by:

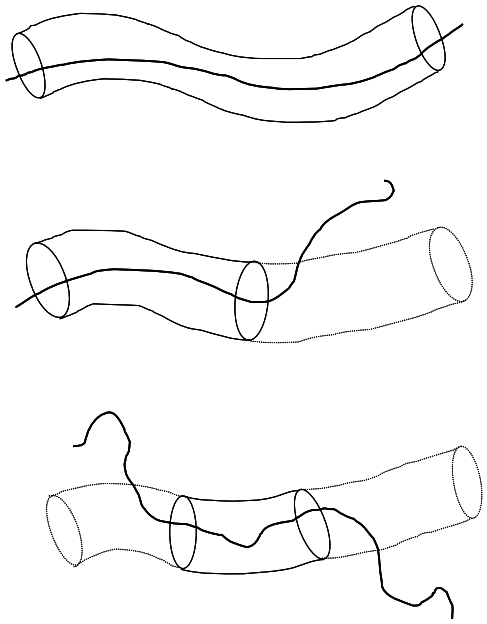

Figure 2.2. Schematic representation of the reptation process. As time progresses, the reptating chain diffuses out of the initial "tube" and eventually completely escapes it.

$$\tau_1 = \frac{15}{24\pi^2}\frac{\zeta b^2}{k_B T}\left(\frac{M}{M_e}\right)\left(\frac{M}{M_o}\right)^2 \tag{2.15}$$

The other key predictions of this model are:

$$D = \frac{Nb^2}{3\pi^2\tau_1} = \frac{4M_e k_B T}{15M_o}\frac{1}{N^2\zeta} \tag{2.16}$$

$$\eta = \frac{\pi^2}{12}G_N^o\tau_1 = \frac{5\rho N_A M_o b^2}{48M_e^2}N^3\zeta \tag{2.17}$$

The scaling laws for D and η with molecular weight are highlighted by the above relationships. It is shown that $D \sim M^{-2}$ and $\eta \sim M^{3}$. However, these scaling laws are slightly different from the experimentally determined ones,[12] which are $D \sim M^{-2.3}$ and $\eta \sim M^{3.4}$.

The reptation model predictions for dynamic moduli are:

$$G' = G_N^o\frac{8}{\pi^2}\sum_{odd\ p}\frac{1}{p^2}\frac{(\omega\tau_p)^2}{1+(\omega\tau_p)^2} \tag{2.18}$$

$$G'' = G_N^o\frac{8}{\pi^2}\sum_{odd\ p}\frac{1}{p^2}\frac{\omega\tau_p}{1+(\omega\tau_p)^2} \tag{2.19}$$

2.2.3 Constraint Release

Reptation does not tell the complete story of chain relaxation. The discrepancies between theoretical predictions and experimental results of viscosity and diffusion coefficient suggest that additional factors are involved in chain relaxation. "Constraint release" effects and "contour length fluctuations" are the additional relaxation processes that can explain discrepancies between experimental and predicted results.

The reptation model[7–10] assumes motions of polymer chains in a field of fixed obstacles. This assumption holds true only in special circumstances such as polymer diffusion in a cross–linked network. In fact this was the original reptation model proposed by de Gennes.[6] For polymer melts this assumption does not hold, and it is particularly poor for polydisperse melts.

In a polymer melt network, in addition to the reptating chain, the entangled chains are also moving and therefore the topological constraints placed on the chain of interest are fluctuating. At certain times, some entanglements disappear while new ones appear. Therefore, it can be imagined that the tube develops openings or "leaks", and the reptating chain can escape through such openings rather than escaping through either end of the tube. This process is known as constraint release and it causes effective reorganization of the tube.[13,14] Constraint release accelerates the chain relaxation, which therefore affects its dynamic properties.

2.2.4 Contour Length Fluctuations

In the development of the reptation model it was assumed that the polymer chain reptates through a "tube" that has a *fixed primitive contour length*. However, in reality,

the contour length fluctuates around an average value. The contour length fluctuations result in a decrease in the effective tube length. For very long chains, this reduction in tube length can be ignored, but for most systems it is a significant decrease. A correction for contour length fluctuations can reproduce the experimental molecular weight dependence of η and D.[11] These fluctuations also result in a more rapid stress relaxation at the chain ends, thus reducing the predicted values of τ_1. The quantitative prediction of τ_1 using contour length fluctuation theory is given by:[15]

$$\tau_1 = \tau_e \left(\frac{M}{M_e} \right)^3 (1 - s_d)^2 \tag{2.20}$$

where τ_e is the timescale at which a polymer segment first encounters the tube wall, s_d is the fraction of the chain that relaxes via contour length fluctuations, and is determined by solving equation 2.21:[15]

$$s_d = \left[0.037 \frac{M_e}{M} (1 - s_d)^2 \right]^{1/4} \tag{2.19}$$

By applying the mechanism of stress relaxation in star polymers (arm retraction) and modeling the linear chain as a two–armed star, Milner and McLeish[15] have successfully taken into account contour length fluctuations to predict the experimental molecular weight dependence of viscosity ($\eta \sim M^{3.4}$). Contour length fluctuations can also account

for the experimentally observed molecular weight dependence of the self diffusion coefficient ($D \sim M^{-2.3}$).[16]

2.3 Importance of Monomeric Friction Factor

The monomeric friction factor, ζ, used in the Rouse and reptation models is a frictional drag coefficient of a polymer chain on a per monomer basis. The friction factor describes the dynamics of polymers on a molecular level. A polymer chain is divided into segments and each of those segments experience a frictional force due to their surroundings. ζ of a particular polymer depends on several factors such as chemical structure, polar nature of the molecule, temperature, composition of a mixture, etc. The dependence of ζ on temperature is remarkably strong; it can vary over several orders of magnitude over just tens of degrees of temperature variation. Similarly, ζ can exhibit a strong composition dependence as well. The temperature and composition dependence of ζ will be discussed in further detail in subsequent sections and chapters. The friction factor can be extracted from the tracer diffusion coefficient and zero shear viscosity using the relationships described in the Rouse and reptation models in Sections 2.2.1 and 2.2.2, respectively.

2.3.1 Temperature Dependence of Monomeric Friction Factor

The temperature dependence of ζ is of primary importance for the work described in this dissertation. This temperature dependence has been studied in detail and is well understood for single component homopolymer melts.[3] The temperature dependence of

all dynamic properties for a polymer melt should be the same. The ratio of ζ of a polymer at a temperature, T, to that at some reference temperature, T_{ref}, is equal to the time-temperature superposition horizontal shift factor, a_T:

$$a_T = \frac{\zeta(T)}{\zeta(T_{ref})} = \frac{\eta(T)}{\eta(T_{ref})} \tag{2.22}$$

The temperature dependence of ζ is often discussed in terms of the free volume theory.[3] This approach relates the friction factor to the amount of free volume that is available within the material. To understand this relationship, we will start with the Doolittle equation:[17]

$$\ln \eta = \ln A + B\left(\frac{1}{f} - 1\right) \tag{2.23}$$

where A and B are empirical constants and f is the fractional free volume equal to $v_f/(v_o+v_f)$. Here v_f is the free volume while v_o is the volume occupied by the molecules. If eq. 2.23 is used for ζ instead of η and rearranged to determine a_T, the following result is obtained:

$$\log a_T = \frac{B}{2.303}\left(\frac{1}{f} - \frac{1}{f_{ref}}\right) \tag{2.24}$$

where f_{ref} is the fractional free volume at reference temperature, T_{ref}. If the fractional free volume is assumed to be linearly dependent on temperature, then:

$$f = f_o + \alpha(T - T_o) \tag{2.25}$$

where α is the thermal expansion coefficient of free volume. Combining equations 2.24 and 2.25 and after some manipulations, the following relationship is obtained:

$$\log a_T = -\left(\frac{B}{2.303 f_{ref}}\right)\left(\frac{T - T_{ref}}{\left(f_{ref}/\alpha\right) + T - T_{ref}}\right) \tag{2.26}$$

Eq. 2.26 is of the same form as the Williams-Landel-Ferry (WLF) equation[18]:

$$\log a_T = -\frac{C_1\left(T - T_{ref}\right)}{C_2 + T - T_{ref}} \tag{2.27}$$

Comparing eq. 2.26 and 2.27, it is determined that $C_1 = B/2.303 f_{ref}$ and $C_2 = f_{ref}/\alpha$. Substitution of eq. 2.22 into eq. 2.27 gives the temperature dependence of the monomeric friction factor:

$$\log \frac{\zeta}{\zeta_{ref}} = -\frac{C_1\left(T - T_{ref}\right)}{C_2 + T - T_{ref}} \tag{2.28}$$

To eliminate the discrepancies caused by different choices of reference temperature, another form of WLF equation is commonly used:

$$\log \frac{\zeta}{\zeta_g} = -\frac{C_1^g \left(T - T_g\right)}{C_2^g + T - T_g} \tag{2.29}$$

where the reference temperature is the glass transition temperature, T_g, and the constants C_1^g and C_2^g are evaluated at T_g.

The WLF equation is not universal for all polymers, i.e., the absolute values of C_1^g and C_2^g are not the same for all polymers, although they do tend to be similar. The WLF equation is usually applicable over the range of T_g to T_g + 100 °C after which an Arrhenius dependence is observed in $\zeta(T)$. The development of a universal friction factor is also not possible because of differences in monomer chemical structure and specific interactions such as hydrogen bonding, dipole interactions, etc. The effect of hydrogen bonding on friction factor will be discussed in more detail in Chapter 5.

At this point in our discussion of the friction factor, it is important to realize that ζ is inferred from the *center of mass motion* of monomers and provides us with no direct information regarding reorientation of backbone bonds. Hence, ζ describes the *terminal dynamics* or *chain dynamics*, i.e., end–to–end chain vector reorientation on a per monomer basis. The backbone bond reorientations are characterized as *segmental dynamics* and are described by a characteristic time constant, τ_{seg}. Often, a direct correlation between ζ and τ_{seg} is assumed. This assumption is often valid for temperatures significantly higher than T_g, but as T_g is approached, this direct relationship breaks down

because of different temperature dependences of segmental and terminal dynamics.[19] This is true for both homopolymers as well as miscible blends.[19–22]

2.3.2 Monomeric Friction Factor in Miscible Blends

In homopolymer melts, a single monomeric friction factor, ζ is used to describe the melt dynamics. However, in a binary, miscible blend of polymers A and B, two distinct friction factors, ζ_A and ζ_B, will be needed to describe terminal dynamics of each component in the blend. Each of these friction factors may exhibit different temperature and composition dependences. In a homopolymer melt, each segment dissipates energy through contacts with segments of identical chemical structure. In the blends, this is clearly not the case and the friction experienced by each component varies with blend composition and there is no mean friction factor of the blend. A detailed discussion on unique temperature and composition dependence of friction factors of blend components will be presented in Section 2.4.1.

In addition to the change in mean friction experienced by each blend component, the local environment experienced by blend components changes upon blending. This results in variation of effective component glass transition temperatures, $T_{g,eff}$ in the blend. Several models have been proposed to describe the friction factor of component *i*, ζ_i, in the blend, but most have not been successful in simultaneously predicting ζ_i and $T_{g,eff}$. For a blend of polymers A and B, Brochard–Wyart[23] suggested the simplest blending rule:

$$\zeta_{A,blend} = \phi_A \zeta_{AA} + \phi_B \zeta_{AB} \tag{2.30}$$

where $\zeta_{A,blend}$ is the friction factor of component A in the blend, ζ_{AA} and ζ_{AB} are the friction factor values for contacts between A and A monomer, and A and B monomers respectively, and ϕ_A and ϕ_B are volume fractions. To use equation 2.30, prior knowledge of an expression describing ζ_{AB} is required.

A more detailed blending model was proposed by Wu[24]:

$$\log(\zeta) = \phi_A \log(\zeta_{AA}) + \phi_B \log(\zeta_{BB}) + 2\phi_A\phi_B \log\left(\frac{\zeta_{AB}}{\sqrt{\zeta_{AA}\zeta_{BB}}}\right) \tag{2.31}$$

where ζ_{AA} and ζ_{BB} are the friction coefficients for A-A and B-B contacts respectively and ζ_{AB} is the friction coefficient for A-B contacts. Equation 2.31 is claimed to be valid for Rouse chains in the blend. Hence, equation 2.31 makes it possible to evaluate friction factors in the blend using homopolymer properties, even though this method provides only an average value for ζ_{blend}.

2.4 Dynamic Phenomena in Miscible Blends

The dynamics of miscible blends and other polymer mixtures such as copolymers provide important information that gives us insight into the transport properties of polymers, their rheological behavior and their material processing properties. The viscoelastic and transport properties of homopolymer melts have been thoroughly studied and the segmental and chain dynamics are well understood. In miscible blends, however, each component exhibits its own segmental and terminal dynamics, which results in a

complex macroscopic response that is not as well understood. We now examine some of the most common experimental observations in miscible polymer blend dynamics and offer qualitative interpretations.

2.4.1 Complex Composition and Temperature Dependence of Friction Factors

Tracer diffusion and rheological measurements have been used to study terminal dynamics of each component in binary miscible blends. Similarly, NMR, dielectric relaxation spectroscopy and several other techniques have been used to study the segmental dynamics of miscible blend components. Blends of poly(styrene) and poly(phenylene oxide) (PS/PPO) have been studied by Composto and coworkers[25] to determine the composition and temperature dependence of monomeric friction factor, ζ. Each blend component was found to have a unique ζ that was different from the homopolymer ζ, and each of those component ζs had its own composition and temperature dependence. Similar studies have been performed on miscible blends of PS and poly(vinylmethylether) (PS/PVME),[26] PS and tetramethyl bisphenol A polycarbonate (PS/TMPC)[27], and polymethylmethacrylate and styrene-acrylonitrile random copolymers (PMMA/PSAN)[28] and the findings are similar to those of Composto *et al.*, emphasizing the system–specific composition dependence of ζ. The mixing model proposed by Brochard–Wyart[23] (eq. 2.30) was found to be inadequate in describing the composition dependence of friction factors in a blend. These results are significant because they illustrate that a single value of ζ is not capable of describing the terminal dynamics in a miscible blend. In addition to that, the component ζs do not share the same temperature and composition dependence, which gives rise to complex rheological and transport

properties as will be seen in subsequent sections and chapters. It has been observed that ζ for the higher T_g component is a stronger function of temperature and composition than that for the lower T_g component.

The investigation of component dynamics in PMMA/PSAN by Kim *et al.*[28] highlights the unpredictable nature of ζ in mixtures. It was found that ζ_{PSAN} and ζ_{PMMA} increased significantly with the addition of either component. This implies that dynamics of the slower component are retarded even more with the addition of the faster component.

The strange and unpredictable composition dependence of segmental dynamics has also been observed in miscible blends. The local polymer segmental reorientations occur during a characteristic time frame designated as τ_{seg}. Experiments by Chung, *et al.*[29] and Le Menestrel, *et al.*[30] on PI/PVE and PS/PVME blends, respectively, demonstrate that each blend component has a distribution of segmental relaxation times. In similar studies, the mean relaxation times for each blend component were found to be different with distinct temperature and composition dependences.[31–36] Just as in the case of terminal dynamics, τ_{seg} of the higher T_g component has been observed to have stronger temperature and composition dependences.

In homopolymers the temperature dependence of terminal and segmental dynamics is the same at temperatures at least 30 ºC above T_g, but as the T_g is approached, segmental dynamics exhibit a stronger temperature dependence than do the terminal dynamics.[19] In miscible blends, however, this trend is sometimes similar while on other occasions it is not, depending on the identity of the blend components. The segmental and terminal dynamics of polyisoprene and polyvinylethylene (PI/PVE) have the same

temperature dependence over a wide range of temperatures.[36] In polybutadiene and PVE (PB/PVE) blends, the terminal dynamics exhibit a slightly stronger temperature and composition dependence than segmental dynamics.[34] In PEO/PMMA blends, the terminal dynamics of PEO are several orders of magnitude different from the segmental dynamics over a wide temperature range. In addition to that, the terminal dynamics have a strong composition dependence whereas the segmental dynamics are hardly influenced by presence of PMMA. Also, in PEO/PMMA blends terminal dynamics vary much more strongly with temperature than do the segmental dynamics.[37]

2.4.2 Broadening of the Calorimetric Glass Transition

The differential scanning calorimetry (DSC) scans of homopolymers show glass transitions that span a temperature range usually no more than 10 ºC. However, in miscible polymer blends, the glass transition process broadens significantly.[38–40] The broadening of the glass transition is caused by each component exhibiting its own distinct T_g, which is different from the one exhibited by the same components in their homopolymer melts. This suggests that when a broad T_g is present, the segments are exposed to distinct local environments, which leads to a wide distribution of T_gs, hence broadening the glass transition.

Figure 2.3 shows DSC scans of several compositions of PI/PVE blends ranging from weight fractions of 100% PI to 100% PVE.[35] Several important observations can be made in this figure. Maximum broadening of calorimetric glass transitions takes place when both components occupy roughly the same fraction of the blend; however, this is not always the case. In this case, the peak broadens by as much as 40 degrees. Also, the

DSC curves are asymmetric for blend compositions other than 50/50. For blends rich in PI (low T_g component), the glass transition is much narrower than for blends rich in PVE (high T_g component).

Recent advances in calorimetry techniques, such as the use of modulated DSC[41,42] have increased temperature resolution, making it easier to resolve individual component T_gs in blends rather than obtaining one broad peak. It is rare to resolve two component T_gs by standard DSC methods because the widths of individual transitions overlap each other. However, if there is a large enough difference in individual T_gs of the two components, it is possible to resolve those using standard DSC methods as shown by Lodge, *et al.*[43] and Gaikwad, *et al.*[44] They demonstrated two glass transitions in low molecular weight, miscible blends of PEO/PMMA, PEO/poly(vinyl acetate) (PEO/PVAc), and PEO/poly(lactide) (PEO/PLA) respectively. The component T_g differences in these blends ranged from 96–198 °C.

Standard DSC traces and the corresponding derivative curves for different compositions of a PEO/PMMA blend[43] are shown in Figure 2.4. The component T_gs are clearly visible in blends ranging in composition from 25% to 75% PEO. Thus, a generally used practice of assigning a single T_g as one of the criteria for polymer blend miscibility is shown to be inaccurate because PEO/PMMA is a miscible blend and it exhibits two distinct T_gs in intermediate composition range. Similar results obtained from PEO/PVAc and PEO/PLA blends also emphasize this point.

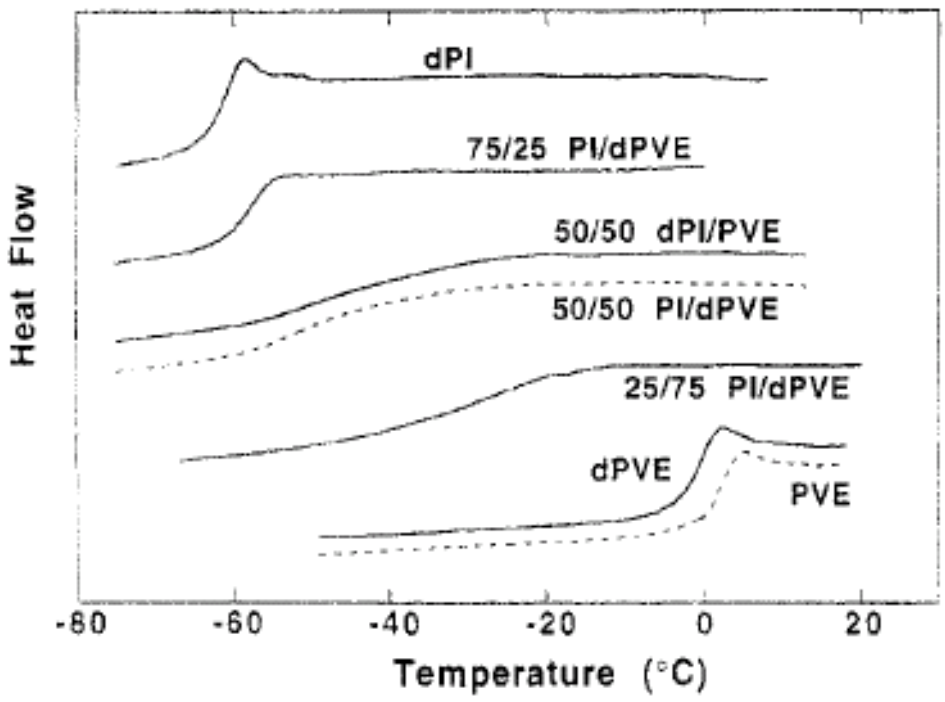

Figure 2.3. DSC scans of different compositions of the PI/PVE blend.[35] The middle composition range shows significant glass transition broadening relative to that in homopolymers. Reproduced with permission from reference 35.

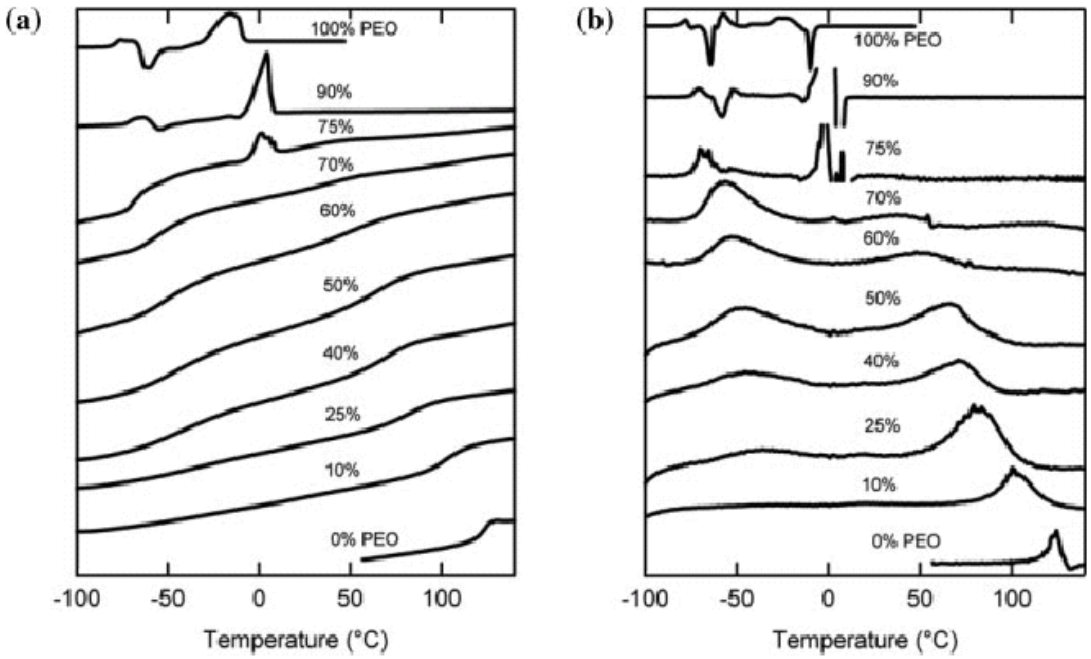

Figure 2.4. (a) DSC curves for different compositions of PEO/PMMA blends. (b) Corresponding derivative curves of the DSC traces in (a). Reproduced with permission from reference 43.

2.4.3 Breakdown of Time–Temperature Superposition

One consequence of two separate relaxation times of miscible blends components is that the time-temperature superposition (tTS) principle, which is very successful in homopolymers, breaks down in most miscible polymer blends. In homopolymers, the tTS principle assumes that all relaxation modes in a polymer have the same temperature dependence. However, this assumption breaks down in miscible blends because of distinct temperature dependence of component segmental dynamics.

The failure of tTS has been observed in blends of PEO/PMMA,[37,45,46] PI/PVE,[47,48] and PS/PVME.[21] The components in each of these binary blends have significantly different T_gs. Colby suggested that tTS failure might be due to each blend component experiencing its own unique and composition dependent effective T_g.[45] Figure 2.5 shows the tTS breakdown in PEO/PMMA blends as reported by Colby.

A study on PMMA/PSAN blends showed that application of tTS was successful.[49] The T_gs of the two components in this blend are not much different, which suggests that tTS failure will be undetectable, or at least difficult to detect, if the component T_gs are similar. These observations give credence to Colby's argument of unique and composition dependent effective T_gs. If the difference in component T_gs is large, then their segmental relaxation times are probably going to be different along with the temperature dependence, which will give rise to tTS failure. However, if the component T_gs are similar, the temperature dependence of relaxation times will be similar, and the tTS will be followed. Pathak and coworkers suggested that tTS might still fail in systems such as PMMA/PSAN at temperatures approaching T_g because of the strong temperature dependence of relaxation times near T_g.[49]

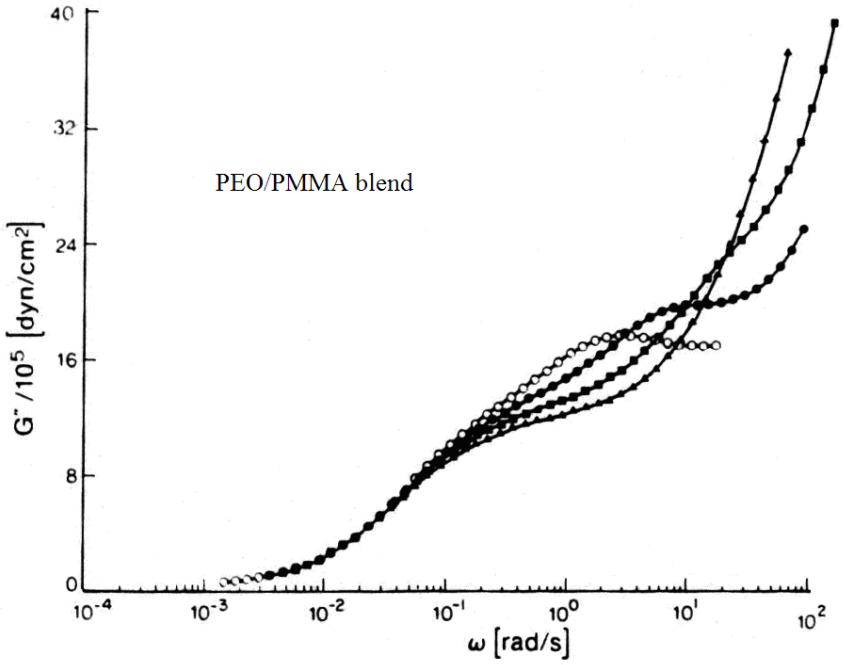

Figure 2.5. Breakdown of time–temperature superposition in a miscible blend of PEO/PMMA.[45] Reproduced with permission from reference 45.

2.4.4 Composition dependence of η

In this work, we performed rheology experiments to determine steady shear viscosity from steady shear measurements. Since we were interested in understanding component chain dynamics, the blends used for these experiments contained a small amount of larger molecular weight tracers. To properly understand the effects on η of mixing the high molecular weight tracer with low molecular weight polymer matrix and to also understand the effects on mixing just two low molecular weight polymers, an overview of various mixing theories is presented here.

The classic Arrhenius mixing rule[50] for η is:

$$\log(\eta_{blend}) = x_A \log(\eta_A) + x_B \log(\eta_B) \tag{2.32}$$

where x_A and x_B are the mole fractions of components A and B, respectively. The Arrhenius mixing rule has not been very successful in predicting blend viscosities,[51,52] because the composition dependence of η is quite complex. Some modifications to the Arrhenius mixing rule have been proposed, one of them being replacing the mole fractions with volume fractions,[52] but such modifications still fall short of making Arrhenius model a truly universal one.

The complex composition dependence of η has emerged as a result of large number of studies performed on several miscible blends. For miscible polyolefin blends,[53] PMMA/polystyrene acrylonitrile (PMMA/PSAN)[54] blends, and for blends of polybutadiene,[38] a linear dependence of $\log(\eta)$ on composition, ϕ, (just like Arrhenius

prediction) has been reported. *Concave up* dependence of $\log(\eta)$ on ϕ has been reported for blends of PMMA and poly(vinylidene fluoride) (PMMA/PVDF)[24,55], poly(styrene) and tetramethyl polycarbonate (PS/TMPC)[56], and PSAN and poly(ε-caprolactone) (PSAN/PCL).[57] Blends of PMMA/PSAN[58,55] have been reported to exhibit a *concave down* dependence of $\log(\eta)$ on ϕ. Thus, PMMA/PSAN blends show linear as well as concave down composition dependence of $\log(\eta)$. Some blends of PEO/PMMA[24] and PMMA/PVDF[59] have also been reported to exhibit a minimum in viscosity at intermediate compositions. The non–linearity (on a $\log\eta$ vs. composition scale) in the composition dependence of viscosity most probably arises because of contacts of two different chemical species (in the case of binary blends) or contacts of different molecular weight chains (in case of bimodal blends of same species). Such contacts are absent in hompolymers, and hence give rise to dynamical process that cannot be modeled by a linear Arrhenius–type relationship.

In our work, we have blended small amounts (1 wt.%) of large molecular weight polymer tracers with low molecular weight matrix. In this case, a linear relationship of the form $\eta_{blend} = \phi_{tracer}\eta_{tracer} + \phi_{matrix}\eta_{matrix}$ is also inadequate in describing the influence of polymer tracer on blend viscosity. The non-linearity in composition dependence of blend viscosity is taken into account by the following relationship[60]:

$$\eta_{blend} = \left(\phi_{tracer} + A\phi_{tracer}^2\right)\eta_{tracer} + \phi_{matrix}\eta_{matrix} \tag{2.33}$$

where A is a fitting parameter.

2.5 Theoretical Models for Blend Dynamics

In miscible polymer blends, observations such as time-temperature superposition failure, broadening of the calorimetric glass transition, and composition dependent monomeric friction factors, arise from different contributions of each component to the macroscopic behavior of the blend. Not only that, but each component exhibits characteristics that are unique to itself and/or to its surroundings. The molecular origins of distinct segmental and terminal dynamics are not completely understood. Several theories and models have been proposed to explain the temperature and composition dependence of monomeric friction factors, segmental relaxation times, and other characteristic phenomena observed in miscible blends. These models are extensions of well-established molecular models that describe rheological and transport phenomena in homopolymers. A more in–depth analysis of some of the theoretical models is presented in this section.

2.5.1 Concentration Fluctuations

The models proposed for miscible blends use differences in local environment to explain why each component experiences different segmental relaxation times. Differences in local environment lead to differences in T_g experienced locally, resulting in local mobility differences. Since significant emphasis is placed on local phenomena rather than occurrences in the whole system, it is important to define a local region. The local environment is a region surrounding a polymer segment that influences the segment's motion. It is assumed that each blend component resides in a unique and composition dependent local environment. This in turn affects the glass transition

temperature experienced locally by the chain segments because of local concentration differences. Weakly interacting blends ($\chi \approx 0$) are usually characterized by significant concentration fluctuations in the single phase regime. In blends with strong inter-molecular interactions, concentration fluctuations may be suppressed.

Fischer and coworkers, in their attempts to describe the broadening of segmental relaxation curves in blends proposed a concentration fluctuation model.[61] They used the well–known Landau expression[62] which uses a Gaussian function to describe the probability, $P(\phi)$, of local concentration experienced by a chain segment:

$$P(\phi_i) \propto \exp\left[-\frac{(\phi_i - <\phi>^2)}{2(\Delta\phi)^2}\right] \tag{2.34}$$

where $<\phi>$ is the mean composition of the macroscopic blend and $(\Delta\phi)^2$ is the variance of local concentration fluctuation. This variance is inversely proportional to the volume of the fluctuation. The fluctuation in composition results in regions with different local T_g values, which in turn leads to a distribution of segmental motions.

Kumar, Colby, and coworkers apply similar ideas and propose that volume of the fluctuation is a function of the local composition.[63,64] The variance in composition fluctuation is related to blend thermodynamics by:[63,65]

$$(\Delta\phi)^2 = \frac{b^3 S(0)}{V} \tag{2.35}$$

where V is the volume over which fluctuations are sampled and $S(0)$ is the structure factor at a scattering angle of 0. This is described by the random phase approximation theory (RPA):[66,67]

$$\frac{1}{S(0)} = \frac{1}{\phi_1 N_1} + \frac{1}{\phi_2 N_2} - 2\chi \tag{2.36}$$

where N_1 and N_2 are the degree of polymerization of components 1 and 2 respectively and χ is the thermodynamic interaction parameter. Equation 2.36 gives a convenient measure of concentration fluctuations. The larger the value of $S(0)$, greater the concentration fluctuations will be in the system of interest. As can be seen from eq. 2.36, χ greatly affects $(\Delta\phi)^2$. Favorable thermodynamic interactions between components lead to negative values of χ, which results in a decrease in value of $S(0)$ and hence, a decrease in concentration fluctuations. Similarly, as N becomes smaller, $S(0)$ decreases, thus suppressing concentration fluctuations. A reduction in concentration fluctuations decreases the composition dependence of ζ.

Kumar, Colby and coworkers have suggested that V (in eq. 2.35) varies with temperature and have proposed several methods for its calculation.[64,63] Experimental evidence indicates that V might be weakly dependent on temperature in some blend components, whereas in other cases it appears independent of temperature.[68]

The concentration fluctuation approach does not uniquely predict an effective glass transition temperature for each component in miscible blends because this theory is inadequate. Kumar, Colby and coworkers have proposed some changes to the model.[63]

These changes include modification of $P(\phi_1)$[65] to reflect the chain connectivity effects that are discussed in detail in the following section.

2.5.2 Chain Connectivity and Self–Concentration

In the self-concentration theory, a polymer segment experiences an immediate environment that is richer in composition of itself due to chain connectivity. If we consider a polymer segment, because of chain connectivity there will be at least two immediate neighboring units that are of the same type. Hence, the volume in immediate vicinity of the segment under consideration will have a higher concentration of these segments. This increase in local concentration due to chain connectivity is known as self–concentration.[29,35] Figure 2.6 illustrates this concept in the form of a cartoon. The higher concentration of polymer chains of the same type surrounding a particular polymer segment leads to a difference in glass transition temperatures experienced by each component. A unique local environment for each component in a polymer blend is a natural consequence of chain connectivity.

Lodge and McLeish proposed a self-concentration model to calculate the effects of chain connectivity on local composition. The Lodge–McLeish model[69] assumes that segmental relaxation process of a given polymer segment in a blend is affected by the local composition in a surrounding region that has a length scale on the order of one Kuhn segment length, l_k. Due to self concentration effects, the local effective concentrations of each component, ϕ_{eff}, in a binary blend is given by:[69]

$$\phi_{eff} = \phi_{self} + (1 - \phi_{self})\phi \tag{2.37}$$

where ϕ_{self} is the self-concentration of the polymer under consideration and ϕ is the average blend composition. The self-concentration of any blend component is described by the relationship:

$$\phi_{self} = \frac{C_\infty M_o}{k\rho N_A V} \tag{2.38}$$

where C_∞ is the characteristic ratio, M_o is molecular weight of a repeat unit, k is the number of backbone bonds per monomer, ρ is the bulk density of polymer blend, N_A is Avogadro's number and V is the self concentration volume ($V \sim l_k^3$).

This model associates the average local concentration, ϕ_{eff}, for each component with a local glass transition temperature, which in other words is the effective glass transition temperature, $T_{g,eff}$, for each component. The $T_{g,eff}$ for each component is evaluated using the Fox equation[70] but using ϕ_{eff} instead of ϕ in the equation.

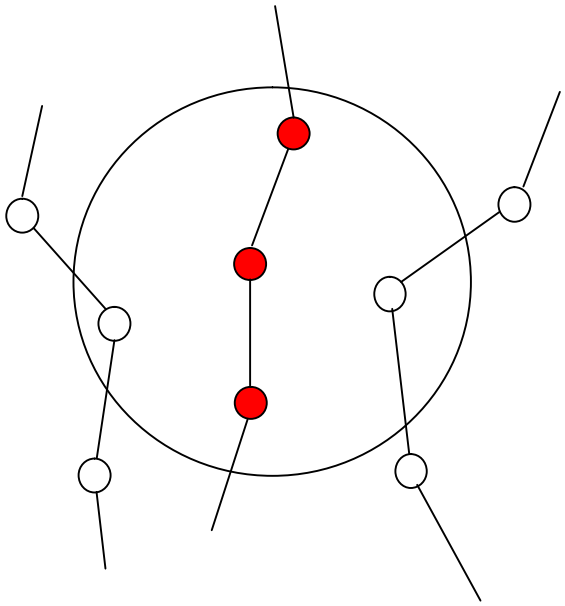

Figure 2.6. Illustration of chain connectivity and resulting self concentration effects. The volume enclosed by the circle contains a higher concentration of filled polymer segments than rest of the blend.

The temperature and composition dependence of the segmental relaxation time and the monomeric friction factor is then modeled by the WLF equation:[18]

$$\log\left(\frac{\tau_{seg,i}(T,\phi)}{\tau_{g,i}(\phi)}\right) = -\frac{C_1\left(T - T^i_{g,eff}(\phi)\right)}{C_2 + \left(T - T^i_{g,eff}(\phi)\right)} \tag{2.39}$$

$$\log\left(\frac{\zeta_i(T,\phi)}{\zeta_{g,i}(\phi)}\right) = -\frac{C_1\left(T - T^i_{g,eff}(\phi)\right)}{C_2 + \left(T - T^i_{g,eff}(\phi)\right)} \tag{2.40}$$

where i represents component A or B, and the constants C_1 and C_2 are assumed to be independent of temperature and composition. Hence, they can be extracted from measurements on homopolymers.

The Lodge–McLeish model has been shown to be relatively successful in predicting dynamic[32,34,71,72] or calorimetric results.[32,73–76] However, the relative accuracy of predictions depends largely on use of ϕ_{eff} as a fitting parameter rather than estimating its value using equation 2.36.

2.6 Overview of PEO/PMMA Blend Dynamics

One of the two blends we have extensively studied in this work is the PEO/PMMA blend. This system has been of interest to researchers over the past couple of decades because (1) it is a weakly interacting blend that is miscible. Usually, blends with weak intermolecular interactions are not readily miscible because of negligible

entropy of mixing as a result of high molecular weigh chains. (2) PEO and PMMA have a large difference in their homopolymer T_gs (~180 °C) making their blends *dynamically asymmetric*. This dynamic asymmetry leads to several interesting characteristics such as tTS failure, unique composition and temperature dependence of segmental and terminal dynamics, etc.

PEO/PMMA miscibility has been investigated by several researchers[77–80] and the blends have been found to be completely miscible across the composition range up to a lower critical solution temperature (LCST) of 225 °C. The dynamic heterogeneity in PEO/PMMA blends as a result of large difference in homopolymer T_gs causes a significant difference in component friction factors and their temperature and composition dependences. The difference in dynamic behavior of each component has made this system suitable for segmental and terminal dynamics studies. Despite plenty of literature on PEO/PMMA segmental dynamics,[81–89] terminal dynamics has not been as well studied for this system. The data on PEO/PMMA chain dynamics is limited to relatively small temperature and composition ranges. In addition, most of these studies do not resolve component dynamics in the blends. To better understand relaxation mechanisms in PEO/PMMA blends and to extend that understanding to other miscible blends, it is important to investigate chain dynamics over a large composition and temperature range.

It may be useful at this point to list the different techniques used for investigating terminal relaxation mechanisms in PEO/PMMA blends. Component terminal dynamics result have been reported using rheology,[37,45] forced Rayleigh scattering (FRS),[37] and infrared dichroism and birefringence.[90] Other techniques used for investigation of chain

dynamics are laser light scattering spectroscopy,[91] photon correlation spectroscopy,[92] and X–ray photon correlation spectroscopy.[93]

PEO/PMMA has drawn considerable attention over the past decade or so because of highly anomalous behavior of PEO in these blends. One study of PEO/PMMA blends reported that the segmental dynamics of PEO as measured by NMR[33] over the entire blend composition range were hardly influenced by the considerably more glassy, and slow moving PMMA. The experimental results of this study demonstrated that PEO chains present in trace amounts in the blend are slowed by less than an order of magnitude over a temperature range of 180–200 °C when compared with pure PEO homopolymer. This result was even valid at temperatures reaching well below T_g of the PMMA matrix, where segmental relaxation times of PMMA are almost 12 orders of magnitude greater than that of the more flexible, and rapidly moving PEO. This provocative result indicates that PEO barely "feels" the presence of a much more rigid, PMMA matrix. This observation makes the dynamics of PEO/PMMA unlike that of any other blend system studied thus far. It has been proposed that rapid relaxation of PEO regardless of its rigid surroundings is due to the fact that its ether oxygen has no side groups.[33] Terminal dynamics study by Zawada *et al.*[90] suggests that PMMA influences PEO terminal dynamics more strongly than segmental dynamics.

Further evidence of unusual PEO/PMMA dynamics is the study of diffusion of small molecule probes in a PMMA matrix. The diffusion coefficient of diethyl ether, roughly a dimer of PEO,[94] was found to be more than six orders of magnitude greater than straight chain hydrocarbons, such as *n*–butane and *n*–heptane[95] of similar size at roughly the same temperatures. The only difference between these straight chain

hydrocarbons and dimethyl ether is replacement of a middle carbon atom along with its adjoining hydrogen atoms with an ether oxygen.

Terminal and segmental dynamics in hompolymers usually have similar temperature dependences at temperatures far above the glass transition temperature, T_g. Near T_g, the segmental dynamics usually vary more strongly with temperature than do the terminal dynamics.[19] Therefore it is appealing to assume that at temperatures far above T_g, there exists a simple relationship that correlates the bond vector reorientations (segmental dynamics) to terminal dynamics. Such a direct correlation was tested for PEO hompolymer and it predicted experimental results very well.[37] However, when this relationship (correlating monomeric friction factor, ζ, and segmental relaxation time, τ_{seg}) was tested for a small amount of PEO (0.3 wt.%) dissolved in a PMMA matrix, this expected direct relationship was unable to even qualitatively predict the experimental results.[37] The inferred friction factor from segmental dynamics was two to six orders of magnitude smaller than the experimental friction factor obtained from FRS and rheology. Not only was the magnitude of friction factor inferred from segmental dynamics measurements grossly underpredicted, the temperature dependence of the friction factor was also not predicted.[37] The direct relationship between segmental and terminal dynamics has been successfully applied in other blend systems such as poly(isoprene)/poly(vinyl ether) (PI/PVE),[36] and at least qualitatively applied in blends such as poly(butadiene)/PVE (PB/PVE).[34] In no other system has the failure of this relationship been as stark as in PEO/PMMA.

Another example of anomalous behavior in PEO/PMMA blends is the failure of Lodge–McLeish model (LMM). In most blends, LMM has been relatively successful in

predicting dynamic and/or calorimetric results at least qualitatively, if not quantitatively. LMM describes segmental dynamics of PEO in PEO/PMMA blends[33] but only when one of its key parameters, self concentration, ϕ_{self}, is used as a fitting parameter rather than being calculated via a relationship described in the model. However, when applied to terminal dynamics data, it not only fails to predict friction factor values for PEO/PMMA but also their temperature dependence.[60]

2.7 Strongly Interacting Blends

So far, the discussion of blend dynamics has been limited to weakly interacting blends. The intermolecular interactions in polymers can be dipole–dipole, hydrogen bonding, charge transfer complexes, or ionic interactions. A significant portion of the work presented in this dissertation involved blends with strong intermolecular interactions. Therefore, in this section, we will review some thermodynamics concepts that will help explain the role of intermolecular interactions in miscibility of polymers. A review of blend dynamics and miscibility in interacting blends will then be presented followed by a discussion of dynamics in poly(ethylene oxide)/poly(vinyl phenol) (PEO/PVPh) blends that were used in this work.

2.7.1 Thermodynamics of mixing

For a blend to be miscible, two requirements must be fulfilled: (a) $\Delta G_{mix} < 0$ and (b) $(\partial^2 \Delta G_{mix}/\partial x_i^2)_{T,p} > 0$. ΔG_{mix} is the free energy change upon mixing and x_i is the mole

fraction of component *i*. For polymers, the free energy change upon mixing can be expressed in terms of entropy of mixing and enthalpy of mixing:

$$\frac{\Delta G_{mix}}{RT} = \frac{\phi_1 \ln(\phi_1)}{N_1} + \frac{\phi_2 \ln(\phi_2)}{N_2} + \chi\phi_1\phi_2 \qquad (2.41)$$

where N_1 and N_2 are the degrees of polymerization of polymers 1 and 2 respectively, ϕ_1 and ϕ_2 are volume fractions, R is the ideal gas constant, T is the absolute temperature and χ is the Flory–Huggins interaction parameter. For miscible blends, usually $\chi < \sim 0.002$.[108] The first two terms on the right hand side of eq. 2.41 represent the ideal entropy of mixing, while the last term represents the enthalpy of mixing. As can be seen from the first two terms of equation 2.39, when two large molecular weight polymers are mixed, the gain in entropy is quite small and the bulk of the contribution to free energy of mixing is from the enthalpy term. ΔG_{mix} can only be negative if the enthalpy of mixing is negative or almost zero. Any positive values of χ will result in a positive ΔG_{mix}, making the blend immiscible.

In literature, there is not a strict definition of what the criteria for strong attractive interactions and weak attractive interactions are. For example, some reports consider miscible polymer blends with $\chi = -0.01$ to be weakly interacting while those with $\chi = -0.05$ to be strongly interacting. These seem to be arbitrary criteria and it may be better to consider relative strengths of different intermolecular forces to determine whether a miscible polymer has weak or strong interactions. Intermolecular forces have

been discussed extensively in literature.[96,97] Table 2.1 summarizes different types of interactions present in polymer blends and the typical energies of those interactions.

Table 2.1. Bond Energies of Different Intermolecular Forces[136]

Type of interactions	Bond Energy (kJ/mol)
Ionic	850 – 1700
Hydrogen bonding	50 – 170
Dipole – Dipole	2 – 8
van der Waals	~1

As can be seen from Table 2.1, the bond energies of hydrogen bonding and dipole–dipole interactions are significantly greater than those of van der Waals forces. Thus miscible polymer blends with hydrogen bonding will be considered strongly interacting while those with only van der Waals forces will be considered weekly interacting blends.

In blends with hydrogen bonding, even though strong intermolecular interactions can produce favorable enthalpy of mixing, such interactions tend to further minimize the entropy of the system due to limitations of chain mobility and rotational freedom because polymer chains are forced to assume configurations that are non random. This introduces a certain level of complexity in determining the free energy of mixing. Coleman and

Painter have proposed adding a term to the Flory Huggins expression for free energy of mixing to account for free energy of hydrogen bond formation:[98–101]

$$\frac{\Delta G_{mix}}{RT} = \frac{\phi_1 \ln(\phi_1)}{N_1} + \frac{\phi_2 \ln(\phi_2)}{N_2} + \chi\phi_1\phi_2 + \frac{\Delta G_H}{RT} \tag{2.42}$$

ΔG_H may be determined from enthalpies of hydrogen bond formation and equilibrium constants. Since the entropy of mixing is very small, the free energy of mixing and hence the miscibility of an interacting polymer blend is determined by the competition between enthalpy of mixing and that of hydrogen bond formation.

2.7.2 Miscibility and Dynamics in Interacting Blends

A large class of polymers form miscible blends with appropriate blend partners via formation of inter–associated hydrogen bonds. Hence, hydrogen bonding interactions are well known to enhance miscibility in otherwise immiscible systems.[102–105] For an excellent review on hydrogen bonded polymer blends, readers are directed to works of Painter and Coleman.[98,106]

Infrared spectroscopy and NMR spectroscopy are the most commonly used techniques used to investigate hydrogen bonds in polymeric systems. Other methods used for studying hydrogen bonds in polymers are Raman spectroscopy, gas–phase microwave rotational spectroscopy, deuteron nuclear quadrupole coupling, neutron diffraction, and X–ray diffraction.[107] The strength and extent of hydrogen bonding in polymer blends or in copolymers depend on respective affinities between the proton donors and

acceptors.[108–110] The most common proton–donating polymers are poly(4–vinyl phenol) (PVPh), poly(vinyl alcohol) (PVAL), and poly(acrylic acid) (PAA), while the most common proton accepting polymers are polyesters, polyacrylates, polyamines, and polyethers. Factors other than bond energies and equilibrium constant between hydrogen bonding components, that affect the strength of hydrogen bonding are acidity of the proton donor, basicity of the proton acceptor, bulkiness of the side group, tacticity, and rigidity of the polymer chains.

Over the past couple of decades, a number of researchers have investigated miscibility of polymer blends with specific interactions, such as hydrogen bonds. Some of the blend systems investigated are those of PVPh which forms miscible blends with poly(vinyl methyl ether) (PVME),[111–113] poly(ε–caprolactone) (PCL),[114] poly(vinyl acetate) (PVAc),[114,115] polyacrylates,[116–120] poly(4–vinylpyridine) (P4VP),[121122] poly(2-vinylpyridene) (P2VP),[123] and poly(ethylene oxide) (PEO)[124–126] to cite a few. Despite the plethora of literature present on miscibility of strongly interacting blends, surprisingly very little attention has been paid in investigating dynamics, either at segmental or terminal level, in blends with strong interactions such as hydrogen bonding. Most of the studies of miscible blend dynamics have focused on athermal or weakly interacting blends.

Runt and coworkers have been the primary investigators of segmental dynamics in strongly interacting blends. They have used dielectric spectroscopy to study segmental dynamics in blends of PVPh/PVAc,[115] PEO/poly(styrene–*co*–vinylphenol) (PEO/PSVPh),[127,128] (PVPh/PMMA),[129] PVPh/poly(ethyl methacrylate) PVPh/PEMA,[123] PVPh/PVME,[113] PVPh/poly(ethylene–*co*–vinyl acetate) (PVPh/PEVAc),[130] and

PVPh/poly(vinyl ethyl ether) (PVPh/PVEE).[131] In general, theses segmental dynamics studies have found strong intermolecular coupling as a result of hydrogen bonding. Very few studies thus far have looked at chain dynamics or viscoelastic behavior in strongly interacting blends.[132–134]

2.7.3 Dynamics in PEO/PVPh Blends

PEO/PVPh is an excellent system for studying the role of hydrogen bonds on component dynamics because of the large difference in hompolymer T_gs. PVPh T_g is 170 °C while that of PEO is –60 °C. Therefore, this blend is *dynamically asymmetric*. Hence, this was our choice for investigation of component dynamics in an interacting blend system.

Intermolecular hydrogen bonding can potentially lead to simplification of blend dynamics by coupling component dynamics, as indicated by applicability of time–temperature superposition principle in PEO/PVPh blends.[135,136] Jack, *et al.* investigated molecular motion in PEO/PVPh blends using solid–state ^{13}C $T_{1\rho}$ measurements.[137] Another study by Zhang and co workers investigated molecular motion in a blend of PEO/PVPh using high resolution solid–state ^{13}C NMR spectroscopy[126] and both these studies concluded that molecular motions of the two polymers in the miscible amorphous phase affect each other strongly. To our knowledge, no comprehensive investigation of the temperature and composition dependence of component chain dynamics in PEO/PVPh blends has yet been undertaken.

2.8 References

[1] Rouse, P. E. *J. Chem. Phys.* **1953**, *21*, 1272.
[2] Doi, M.; Edwards, S. F. *The Theory of Polymer Dynamics*; Oxford University Press: Oxford **1986**.
[3] Ferry, J. D. *Viscoelastic Properties of Polymers*, Third edition; John Wiley & Sons: New York, **1980**.
[4] Lodge, T. P.; Rotstein, N. A.; Prager, S. *Advances in Chemical Physics* **1990**, *LXXIX*, 1.
[5] de Gennes, P.G.; Leger, L. *Annu. Rev. Phys. Chem.* **1982**, *33*, 49.
[6] de Gennes, P. G. *J. Chem. Phys.* **1971**, *55*, 572.
[7] Doi, M.; Edwards, S. F. *J. Chem. Soc. Farad. Trans.2: Mol. Chem. Phys.* **1979**, *75*, 38.
[8] Doi, M.; Edwards, S. F. *J. Chem. Soc. Farad. Trans.2: Mol. Chem. Phys.* **1978**, *74*, 1789.
[9] Doi, M.; Edwards, S. F. *J. Chem. Soc. Farad. Trans.2: Mol. Chem. Phys.* **1978**, *74*, 1802.
[10] Doi, M.; Edwards, S. F. *J. Chem. Soc. Farad. Trans.2: Mol. Chem. Phys.***1978**, *74*, 1818.
[11] Hiemenz, P. C.; Lodge, T. P. *Polymer Chemistry*, Second Ed.; CRC Press: Boca Raton, **2007**.
[12] Lodge, T. P. *Phys. Rev. Lett.* **1999**, *83*, 3218.
[13] de Gennes, P. G. *J. Phys.* **1975**, *36*, 1199.
[14] de Gennes, P. G. *Macromolecules* **1976**, *9*, 587.
[15] Milner, S. T.; McLeish, T. C. B. *Phys. Rev. Lett.* **1998**, *81*, 725.
[16] Frischknecht, A. L.; Milner, S. T. *Macromolecules* **2000**, *33*, 5273.
[17] Doolittle, A. K.; Doolittle, D. B. *J. App. Phys.* **1957**, *28*, 901.
[18] Williams, M. L.; Landel, R. F.; Ferry, J. D. *J. Am. Chem. Soc.* **1955**, *77*, 3701.
[19] Roland, C. M.; Ngai, K. L.; Santangelo, P. G.; Qiu, X. H.; Ediger, M. D.; Plazek, D. J. *Macromolecules* **2001**, *34*, 6159.
[20] Adachi, K.; Hirano, H. *Macromolecules* **1998**, *31*, 3958.
[21] Pathak, J. A.; Colby, R. H.; Floudas, G.; Jerome, R. *Macromolecules* **1999**, *32*, 2553.
[22] He, Y.; Lutz, T. R.; Ediger, M. D.; Ayyagari, C.; Bedrov, D.; Smith, G. D. *Macromolecules* **2004**, *37*, 5032.
[23] Brochard-Wyart, F. *C. R. Acad. Sci. Par.* **1987**, *305*, 657.
[24] Wu, S. *J. Polym. Sci., Part B: Polym. Phys.* **1987**, *25*, 2511.
[25] Composto, R. J.; Kramer, E. J.; White, D. M. *Polymer* **1990**, *31*, 2320.
[26] Green, P. F.; Adolf, D. B.; Gilliom, L. R. *Macromolecules* **1991**, *24*, 3377.
[27] Kim, E.; Kramer, E. J.; Osby, J. O. *Macromolecules* **1995**, *28*, 1979.
[28] Kim, E.; Kramer, E. J.; Wu, W. C.; Garrett, P. D. *Polymer* **1994**, *35*, 5706.
[29] Chung, G. C.; Kornfield, J. A.; Smith, S. D. *Macromolecules* **1994**, *27*, 964.
[30] Le Menestrel, C.; Kenwright, A. M.; Sergot, P.; Lauprêtre, F.; Monnerie, L. *Macromolecules* **1992**, *25*, 3020.
[31] Min, B.; Qiu, X.; Ediger, M. D.; Pitsikalis, M.; Hadjichristidis, N. *Macromolecules* **2001**, *34*, 4466.
[32] Lutz, T. R.; He, Y.; Ediger, M. D.; Pitsikalis, M.; Hadjichristidis, N. *Macromolecules* **2004**, *37*, 6440.

[33] Lutz, T. R.; He, Y.; Ediger, M. D.; Cao, H.; Lin, G.; Jones, A. A. *Macromolecules* **2003**, *36*, 1724.
[34] He, Y.; Lutz, T. R.; Ediger, M. D. *Macromolecules* **2004**, *37*, 9889.
[35] Chung, G. C.; Kornfield, J. A.; Smith, S. D. *Macromolecules* **1994**, *27*, 5729.
[36] Haley, J. C.; Lodge, T. P.; He, Y.; Ediger, M. D.; Von Meerwall. E. D.; Mijovic, J. *Macromolecules* **2003**, *36*, 6142.
[37] Haley, J. C.; Lodge, T. P. *J. Chem. Phys.* **2005**, *122*, 234914.
[38] Roovers, J.; Toporowski, P. M. *Macromolecules* **1992**, *25*, 1096.
[39] Trask, C. A.; Roland, C. M. *Macromolecules* **1989**, *22*, 256.
[40] Roovers, J.; Toporowski, P. M. *Macromolecules* **1992**, *25*, 3454.
[41] Sakaguchi, T.; Taniguchi, N.; Urakawa, O.; Zadachi, K. *Macromolecules* **2005**, *38*, 422.
[42] Silva, G. G.; Machado, J. C.; Song, M.; Hourston, D. J. *J. App. Polym. Sci.* **2000**, *77*, 2034.
[43] Lodge, T. P.; Wood, E. R.; Haley, J. C. *J. Polym. Sci., Part B: Polym. Phys.* **2005**, *44*, 756.
[44] Gaikwad, A. N.; Wood, E. R.; Ngai, T.; Lodge, T. P. *Macromolecules* **2008**, *41*, 2502.
[45] Colby, R. H. *Polymer* **1989**, *30*, 1275.
[46] Minnick, M. G.; Schrag, J. L. *Macromolecules* **1980**, *13*, 1960.
[47] Zawada, J. A.; Fuller, G. G.; Colby, R. H.; Fetters, L. J.; Roovers, J. *Macromolecules* **1994**, *27*, 6861.
[48] Arendt, B. H.; Krishnamoorti, R.; Kornfield, J. A.; Smith, S. D. *Macromolecules* **1997**, *30*, 1127.
[49] Pathak, J. A.; Colby, R. H.; Kamath, S. Y.; Kumar, S. K.; Stadler, R. *Macromolecules* **1998**, *31*, 8988.
[50] Arrhenius, S. Z. *Physik. Chem.* **1887**, *1*, 285.
[51] Gisser, D. J.; Ediger, M. D. *J. Phys. Chem.* **1993**, *97*, 10818.
[52] Kendall, J.; Monroe, K. P. *J. Am. Chem. Soc.* **1917**, *39*, 1787.
[53] Liu, C.; Wang, J.; He, J. *Polymer* **2002***, 43*, 3811.
[54] Wu, S. *Polymer* **1987**, *28*, 1144.
[55] Yang, H. H.; Han, C. D.; Kim, J. K. *Polymer* **1994**, *35*, 1503.
[56] Wisnewsky, C.; Marin, G.; Monge, P. *Eur. Polym. J.* **1984**, *20*, 691.
[57] Han, C. D.; Yang, H. H. *J. Appl. Polym. Sci.* **1987**, *33*, 1199.
[58] Aoki, Y.; Tanaka, T. *Macromolecules*, **1999**, *32*, 8560.
[59] Chuang, H. K.; Han, C. D. *J. App. Polym. Sci.* **1984**, *29*, 2205.
[60] Zeroni, I.; Ozair, S.; Lodge, T. P. *Macromolecules* **2008***, 41*, 5033.
[61] Zetsche, A.; Fischer, E. W. *Act. Polym.* **1994**, *45*, 168.
[62] Landau, L. D.; Lifshitz, E. M. *Statistical Physics (Part 1)* **1980**, Pergamon Press, New York, NY, 3rd ed.
[63] Kumar, S. K.; Colby, R. H.; Anastasiadis, S. H.; Fytas, G. *J. Chem. Phys.* **1996**, *105*, 3777.
[64] Kamath, S.; Colby, R. H.; Kumar, S. K.; Karatasos, K.; Floudas, G.; Fytas, G.; Roovers, J. E. L. *J. Chem. Phys.* **1999**, *111*, 6121.
[65] Salaniwal, S.; Kant, R.; Colby, R. H.; Kumar, S. K. *Macromolecules* **2002**, *35*, 9211.

[66] de Gennes, P. G. *Scaling Concepts in Polymer Physics* **1979**, Cornell University Press, Ithaca, NY.
[67] Doi, M. *Introduction to Polymer Physics* **1996**, Clarendon Press, Oxford.
[68] Kant, R.; Kumar, S. K.; Colby, R. H. *Macromolecules* **2003**, *36*, 10087.
[69] Lodge, T. P.; McLeish, T. C. B. *Macromolecules* **2000**, *33*, 5278.
[70] Fox, T. G. *Bull. Am. Phys. Soc.* **1956**, *1*, 123
[71] He, Y.; Lutz, T. R.; Ediger, M. D. *J. Chem. Phys.* **2003**, *119*, 9956.
[72] He, Y.; Lutz, T. R.; Ediger, M. D.; Lodge, T. P. *Macromolecules* **2003**, *36*, 9170.
[73] Miwa, Y.; Tanabe, T.; Yamamoto, K.; Sugino, Y.; Sakaguchi, M.; Sakai, M.; Shimada, S. *Macromolecules* **2004**, *37*, 8612.
[74] Hirose, Y.; Urakawa, O.; Adachi, K. *Macromolecules* **2003**, *36*, 3699.
[75] Leroy, E.; Alegria, A.; Colmenero, J. *Macromolecules* **2002**, *35*, 5587.
[76] Miwa, Y.; Usami, K.; Yamamoto, K.; Sakaguchi, M.; Sakai, M.; Shimada, S. *Macromolecules* **2005**, *38*, 2355.
[77] Fernandes, A. C.; Barlow, J. W.; Paul, D. R. *J. App. Polym. Sci.* **1986**, *32,* 5481.
[78] Min, K. E.; Chiou, J. S.; Barlow, J. W.; Paul, D. R. *Polymer* **1987**, *28*, 1721.
[79] Ito, H.; Russell, T. P.; Wignall, G. D. *Macromolecules* **1987**, *20*, 2213.
[80] Hokinson, I.; Kiff, F. T.; Richards, R. W.; King, S. M.; Farren, T. *Polymer* **1995**, *36*, 3523.
[81] Ngai, K. L.; Roland, C. M. *Macromolecules* **2004**, *37*, 2817.
[82] Jin, X.; Zhang, S.; Runt, J. *Macromolecules* **2004**, *37*, 2817.
[83] Dionisio, M.; Fernandes, A. C.; Mano, J. F.; Correia, N. T.; Sousa, R. C. *Macromolecules* **2000**, *33*, 1002.
[84] Sakai, V. G.; Maranas, J. K.; Peral, I.; Copley, J. R. D. *Macromolecules* **2008**, *41*, 3701.
[85] Sakai, V. G.; Chen, C.; Maranas, J. K.; Chowdhuri, Z. *Macromolecules* **2004**, *37*, 9975.
[86] Lartigue, C.; Guillermo, A.; Cohen-Addad, J. P. *J. Polym. Sci., Part B:Polym. Phys.* **1997**, *35*, 1095.
[87] Waestlund, C.; Maurer, F. H. J. *Macromolecules* **1997**, *30*, 5870.
[88] Schantz, S. *Macromolecules* **1997**, *30*, 1419.
[89] Brosseau, C.; Guillermo, A.; Cohen-Addad, J. P. *Macromolecules* **1992**, *25*, 4535.
[90] Zawada, J. A.; Ylitalo, C. M.; Fuller, G. G.; Colby, R.H.; Long, T. E. *Macromolecules* **1992**, *25*, 2896.
[91] Wang, C. H.; Zhang, X. Q.; Fytas, G.; Kanetakis, J. *J. Chem. Phys.* **1989**, *91*, 3160.
[92] Xia, J. L.; Wang, C. H. *J. Chem. Phys.* **1991**, *94*, 3229.
[93] Lumma, D.; Borthwick, M. A.; Falus, P.; Lurio, L. B.; Mochrie, S. G. J. *Phys. Rev. Lett.* **2001**, *86*, 2042.
[94] Cao, H.; Lin, G.; Jones, A. A. *J. Polym. Sci., Part B: Polym. Phys.* **2004**, *42*, 1053.
[95] Berens, A. R.; Hopfenberg, H. B. *J. Membr. Sci.* **1982**, *10*, 283.
[96] Huyskens, P. L.; Luck, W. A. P.; Zeegers-Huyskens, T. *Intermolecular Forces*; Springer-Verlag: New York, **1991**.
[97] Israelachvili, J. N. *Intermolecular and Surface Forces*, 2nd ed.; Academic Press: New York, **1991**.
[98] Coleman, M. M.; Painter, P. C. *Prog. Polym. Sci.* **1995**, *20*, 1.

[99] Painter, P. C.; Park, Y.; Coleman, M. M. *Macromolecules* **1988**, *21*, 66.
[100] Painter, P. C.; Park, Y.; Coleman, M. M. *Macromolecules* **1989**, *22*, 570.
[101] Painter, P. C.; Park, Y.; Coleman, M. M. *Macromolecules* **1989**, *22*, 580.
[102] Serman, C. J.; Xu, Y.; Painter, P. C.; Coleman, M. M. *Polymer* **1991**, *32*, 516.
[103] Coleman, M. M.; Lee, J. Y.; Serman, C. J.; Wang, Z.; Painter, P. C. *Polymer* **1989**, *30*, 1298.
[104] Kuo, S. W.; Chang, F. C. *Macromolecules* **2001**, *34*, 4089.
[105] Kuo, S. W.; Chang, F. C. *Macromolecules* **2001**, *34*, 5224.
[106] Coleman, M. M.; Graf, J.; Painter, P. C. *Specific Interactions and the Miscibility of Polymer Blends*, 1991, Technomic Publishing Co.: Lancaster, PA.
[107] Jeffery, G. A. *An Introduction to Hydrogen Bonding* **1997**, Oxford University Press, New York.
[108] He, Y.; Zhu, B.; Inoue, Y. *Prog. Polym. Sci.* **2004**, *29*, 1021.
[109] Kuo, S. W.; Huang, C. F.; Chang, F. C. *J. Poym. Sci., Part B: Polym. Phys.* **2001**, *39*, 1348.
[110] Kuo, S. W.; Lin, C. L.; Chang, F. C. *Polymer* **2002**, *43*, 3943.
[111] Pedrosa, P.; Pomposo, J. A.; Calahorra, E.; Cortazar, M. *Macromolecules* **1994**, *27*, 102.
[112] Lezcano, E. G.; De Arellano, D. R.; Prolongo, M. G.; Coll, C. S. *Polymer* **1998**, *39*, 1583.
[113] Zhang, S. H.; Jin, X.; Painter, P. C.; Runt, J. *Polymer* **2004**, *45*, 3933.
[114] Moskala, E. J.; Howe, S. E.; Painter, P.C.; Coleman, M. M. *Macromolecules* **1984**, *17*, 1671.
[115] Zhang, S.; Painter, P. C.; Runt, J. *Macromolecules* **2002**, *35*, 8478.
[116] Landry, C. J. T., Teegarden, D. M. *Macromolecules* **1991**, *24*, 4310.
[117] Zhu, K. J.; Chen, S. F.; Ho, T.; Pearce, E. M.; Kwei, T. K. *Macromolecules* **1990**, *23*, 150.
[118] Coleman, M. M.; Lichkus, M. A.; Painter, P. C. *Macromolecules* **1989**, *22*, 586.
[119] Serman, C. J.; Painter, P. C.; Coleman, M. M. *Polymer* **1991**, *32*, 1049.
[120] Xu, Y., Painter, P. C.; Coleman, M. M. *Macromolecules* **1992**, *25*, 7076.
[121] Wang, J.; Cheung, M. K.; Mi, Y. *Polymer* **2001**, *42*, 3087.
[122] Vivas de Meftahi, M.; Fréchet, J. M. J. *Polymer* **1988**, *19*, 477
[123] Zhang, S.; Painter, P. C.; Runt, J. *Macromolecules* **2004**, *37*, 2636.
[124] Moskala, E. J.; Varnell, D. F.; Coleman, M. M. *Polymer* **1985**, *25*, 228.
[125] Qin, C.; Cheng, C.; Pires, A. T. N.; Belfiore, L. A. *Polym. Mater. Sci. Eng.*, **1989**, *61*, 945.
[126] Zhang, X.; Takegoshi, K.; Hikichi, K. *Macromolecules* **1992**, *25*, 2336.
[127] Jin, X.; Zhang, S.; Runt, J. *Macromolecules* **2004**, *37*, 4808.
[128] Jin, X.; Zhang, S.; Runt, J. *Macromolecules* **2003**, *36*, 8033.
[129] Zhang, S.; Runt, J. *J. Polym. Sci., Part B. Polym. Phys.* **2004**, *42*, 3405.
[130] Zhang, S. H.; Casalini, R.; Runt, J.; Roland, C. M. *Macromolecules* **2003**, *36*, 9917.
[131] Zhang, S.; Painter, P. C.; Runt, J. *Macromolecules* **2002**, *35*, 9403.
[132] Akiba, I.; Akiyama, S. *Polym. Networks Blends* **1997**, *7*, 147.
[133] Cai, H.; Ait-Kadi, A.; Brisson, J. *Polymer* **2003**, *44*, 1481.
[134] Yang, Z.; Han, C. D. *Macromolecules* **2008**, *41*, 2104.

[135] Cai, H.; Ait-Kadi, A.; Brisson, J. *Polymer* **2003**, *44*, 1481.
[136] Yang, Z.; Han, C. D. *Macromolecules* **2008**, *41*, 2104
[137] Jack, K. S.; Whittaker, A. K. *Macromolecules* **1997**, *30*, 3560.

Chapter 3. Experimental Methods

3.1 Introduction

This chapter outlines in detail the experimental techniques and equipment used in the work that will be discussed in subsequent chapters. Rheology and forced Rayleigh scattering (FRS) have been the primary experimental techniques used in this work. In addition, the experimental procedures of polymer and other chemical synthesis and their characterization techniques will also be discussed in this chapter.

3.2 Forced Rayleigh Scattering

This section gives a general overview of forced Rayleigh scattering and briefly outlines the basic principles behind this technique. The experimental procedure and a description of the experimental setup follows.

3.2.1 Overview

To measure chain diffusion in polymers, several aspects have to be taken into consideration when choosing a technique. A suitable technique should be able to probe chain diffusion coefficients varying over several orders of magnitude. This allows for investigating chain diffusion processes for different temperatures, and different molecular weights of the polymer matrix as well as the diffusing chain. The technique should also offer flexibility to select a specified direction along which to measure diffusion

coefficients. However, such a requirement is not necessary for isotropic systems. Another preferred characteristic would be the ability to measure tracer diffusion of a single component in arbitrarily complex systems[1].

Over the past few decades, several diffusion measurement techniques have been developed. These include fluorescence recovery after pattern photobleaching (FRAPP),[2] forced Rayleigh scattering (FRS),[1,3] elastic recoil detection (ERD),[4] and forward recoil spectrometry (FRES).[4] However of all these techniques, only FRS meets all the aforementioned criteria. The most striking advantage of FRS over all other experimental techniques is its ability to measure diffusion coefficients, D, in the range of 10^{-5} cm^2/s to 10^{-17} cm^2/s. The upper limit is typical of small molecule fluids with viscosities near 1 cP, whereas the latter is reported for small–molecule glasses, highly entangled polymer melts, and microstructured block copolymers.[1]

FRS is a transient holographic grating technique used primarily for measuring the tracer diffusion coefficients of a photochromic species in polymer melts and solutions. The basis for FRS is a periodic spatial inhomogeneity in refractive index or extinction coefficient created in the sample. The experiment involves measuring the characteristic time needed for the diffusion process to erase this inhomogeneity. The photochromic dye could be used as a small molecule probe dispersed in a material, or attached to macromolecules to study mobility of polymer chains. Following is a brief summary of how the FRS technique works. A detailed description of FRS apparatus and its functionality will be presented later.

Two mutually coherent laser beams intersect each other within the sample creating an interference pattern. In regions of constructive interference, the photochromic

species (dye) will undergo photo–induced isomerization, while in regions of destructive interference, it will not. The difference in refractive indices or extinction coefficients of the dye isomers results in formation of an optical grating. A third, low intensity beam is then directed onto the grating such that diffraction occurs. The diffracted intensity decreases with time as the grating is erased by inter–diffusion of isomers. The characteristic time needed for this decay is measured and is used to determine the diffusivity of the photochromic species using well–established relationships.

Having briefly discussed the details of FRS technique, at this point it will be useful to summarize the merits of FRS and the advantages this experimental technique offers over several other methods of measuring polymer diffusion/mobility.[5]

1. As mentioned earlier, FRS offers a very large range of diffusion coefficients (10^{-5} to 10^{-17} cm^2/s) to measure tracer diffusivities. This enables diffusion measurements in almost any material and media.
2. The distance at which diffusion takes place is well defined and microscopic. This is different from other techniques which measure diffusion over a macroscopic distance. This difference proves to be very important because of the amount of time that can be saved in measuring slow diffusing species. To understand the effect of diffusion over a microscopic vs. macroscopic scale, let us compare the time it takes for a species to diffuse over a 1 μm distance and a 1 cm distance. Diffusion over 1 μm is 10^8 times faster than diffusion over a 1 cm distance.
3. The experiment "sees" i.e. optically detects only the motion of dye molecules, whether they are freely dispersed in the sample or covalently bonded to other

molecules. Hence, the detection of motion of one species in a complex mixture is not only possible, but straightforward.

4. Diffusion can be measured in samples at equilibrium or evolving in time since no macroscopic concentration gradient is necessary for diffusion measurement.[1]
5. Sample size required for FRS experiments is quite small (on the order of a few hundred mg).
6. The experiment is free of surface effects because the optical grating is created inside the sample and diffusion process does not involve transport across an interface as with sorption/permeation techniques.
7. The experiment is uniaxial because only the diffusion perpendicular to grating planes is detected.
8. Data analysis is simple and results in determination of diffusion coefficient without use of any theoretical models.

It needs to be emphasized that this experimental technique is not perfect and has its limitations. Some of the disadvantages of FRS are listed below:

1. The sample has to be completely transparent, microscopically homogeneous, and dust–free to prevent false diffraction readings.
2. The dye molecule has to have functional groups for covalent attachment to polymer chains in order to make diffusion measurements. Because of the need covalent attachment, choices of dye molecules are limited.
3. Polymer labeling, i.e., covalently attaching the dye to polymer chains can be complicated, and it cannot be guaranteed that an attached dye molecule will behave identically to a freely suspended one.

4. If the polymer chains are not significantly larger than the attached dye molecules, the dye can affect chain mobility and result in inaccurate diffusion measurements.
5. FRS measurement is done in a sample area so small that the sample has to be homogeneous for the measurement to be representative of the bulk material.

3.2.2 Forced Rayleigh Scattering Background

FRS is considered part of a broader set of techniques known as holographic grating techniques. The FRS technique was first developed to study thermal diffusion by Pohl and Eichler who published their first papers in 1973.[6,7] To study thermal diffusion, FRS makes use of periodic variation of temperature rather than of dye concentration. Pohl investigated heat conduction in a NaF crystal and Eichler performed measurements on organic liquids.

Although FRS has been used for other investigations of thermal diffusivities, it is the technique's tracer diffusion measurement capabilities that are now used extensively. The adaption of FRS to measure mass diffusivities was first done by Hervet *et al*.[8] to measure dye diffusion in a well–aligned liquid crystal. Diffusivities both parallel and perpendicular to the orientation axis were measured by changing the orientation of the sample with respect to the crossing beams. Other interesting mass diffusion applications of FRS include the measurement of electrophoretic mobility in aqueous systems,[9,10] and the determination of self–diffusion coefficient of water droplets in a three component microemulsion.[11] Currently the primary use of FRS is in measuring small molecule diffusion and polymer diffusion in polymer solutions and melts.

Application of FRS to study diffusion in polymeric systems is made possible because the technique requires that the probe be photochromic or at least contains a photochromic species, usually a dye. In a medium containing dye molecules, FRS detects the motion of dye molecules only; so if they are attached to a polymer chain, their motion is because of movement of polymer chains. FRS results for diffusion in polymer systems first appeared in 1979 when Hervet and co–workers[12] reported a study of poly(styrene) self-diffusion in benzene as a test of scaling-law predictions for the semi–dilute concentration regime. FRS continues to be a powerful technique with applications in liquid crystal diffusion, surfactant solutions and block copolymers.

3.2.3 Forced Rayleigh Scattering Experimental Technique

The FRS experiment can be divided into three distinct, sequential steps: creation, recording, and reading of the grating. These steps are outlined in detail below:

Creation of the grating

Two intense, mutually coherent laser beams of wavelength λ intersect each other in the sample at an angle θ creating an interference pattern. The treatment of these intersecting beams assumes that the beams are collimated, i.e., they can be represented by planar rather than spherical wavefronts. It is also assumed that the electric field amplitude across the beam is constant. In reality, the beams are slightly diverging and have an approximately Gaussian intensity profiles through their cross sections. The case of diverging, unfocused beams has been tested[13,14] and it has been found that the wavefronts can be treated as planar as long as the beams intersect at the beam waist. The resulting interference pattern with relative intensity distribution is shown in Figure 3.1. The top

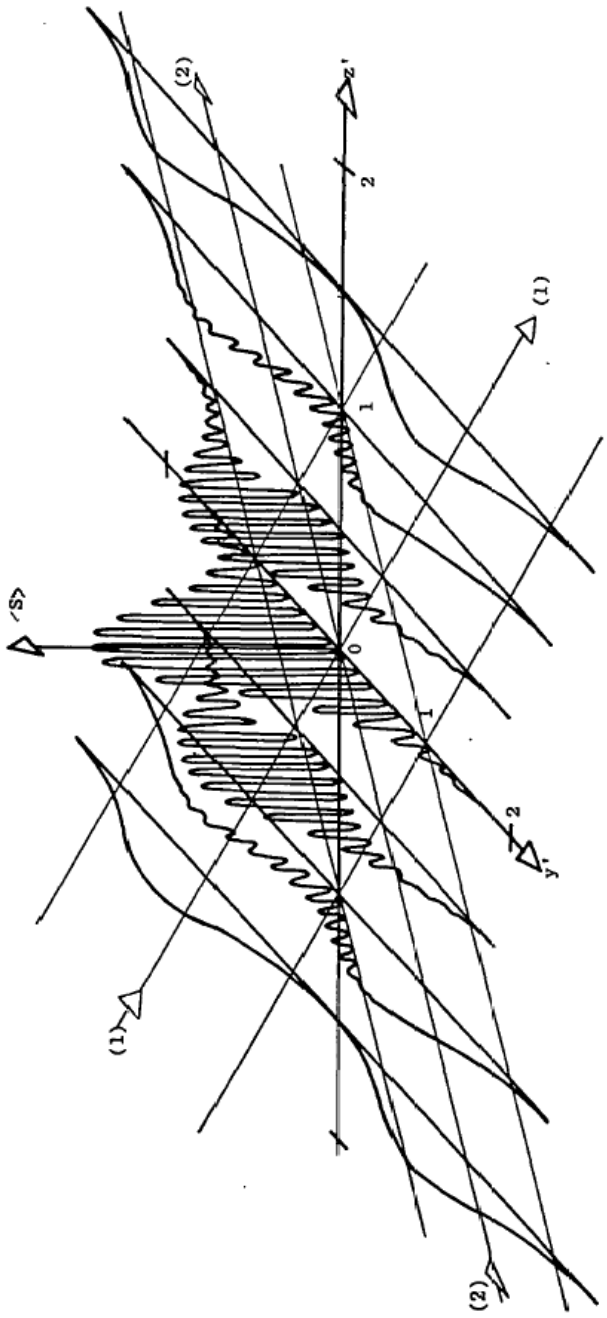

Figure 3.1. Relative intensity distribution near the crossover of two similarly polarized, Gaussian laser beams. Reproduced from reference 15.

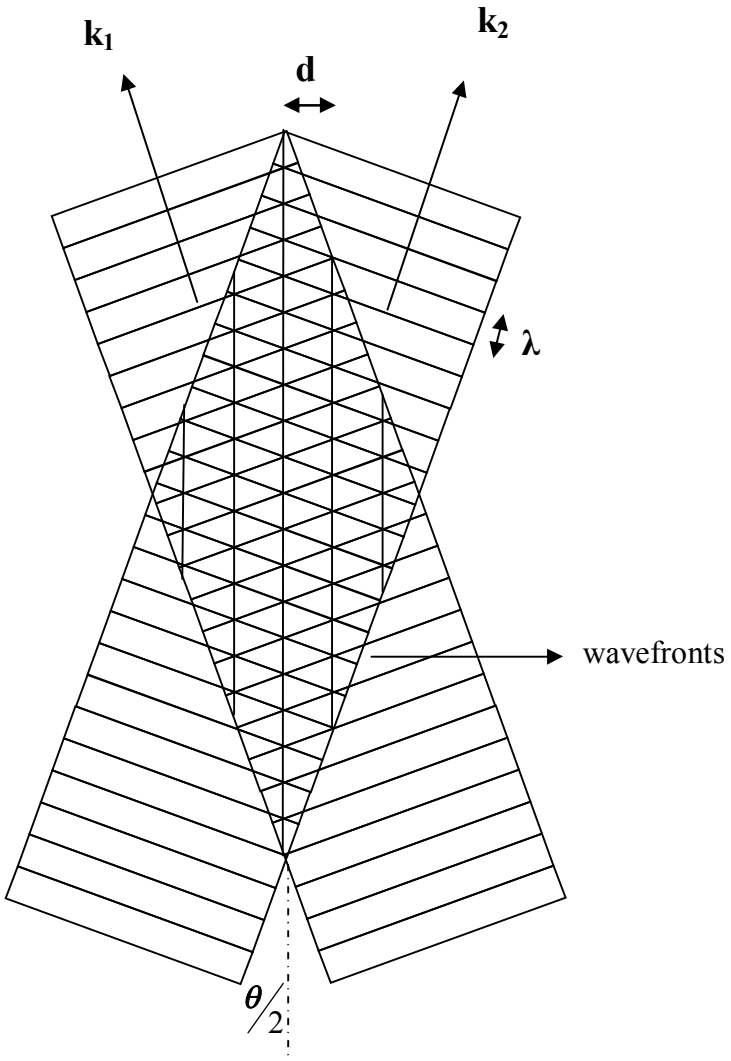

Figure 3.2. Top view of interference pattern of laser beams of wavelength λ, intersecting each other at an angle θ. The wave vectors for each beam are denoted by $\boldsymbol{k}_1$ and $\boldsymbol{k}_2$, and d is the distance between intensity maxima and minima.

view of this interference pattern is shown in Figure 3.2. The two beams are designated as beam 1 and 2, with respective wave vectors: $\boldsymbol{k_1}$ and $\boldsymbol{k_2}$. The beams intersect each other at an angle θ, creating the interference pattern. The grating is characterized by the difference in wave vectors, $\boldsymbol{q}$[16]:

$$\boldsymbol{q} = \pm (\boldsymbol{k_1} - \boldsymbol{k_2}) \tag{3.1}$$

The grating spacing, d, is determined by the path length difference between the waves and the wavelength of the laser beam:[6]

$$d = \frac{2\pi}{|\boldsymbol{q}|} = \frac{\lambda}{2\sin\left(\theta/2\right)} \tag{3.2}$$

where $|\boldsymbol{q}|$ is the magnitude of vector**,** $\boldsymbol{q}$. The grating spacing, which is also the characteristic diffusion distance, can be controlled by varying the intersection angle, θ. Typical values of d range from 0.6 μm to 40 μm, which explains how FRS is able to measure diffusivities ranging over 11 orders of magnitude. This control over grating spacing also shortens the time taken for one measurement by shortening the distance.

Recording the grating

In the recording phase, the grating that is created in the first phase is mapped on to the sample as a result of photochemistry that takes place in the sample. When laser beams intersect, constructive and destructive interference takes place. In constructive interference regions, the light intensity is high enough to make the photochromic species attached to the polymer chain undergo a photoisomerization reaction. In the destructive

interference regions, the intensity is not sufficient for dye isomerization and the dye remains in its original state. This is how a cosinusoidal variation in laser intensity is recorded by the sample.

The photochromic species used in this work is the dye 4'–(*N*,*N*-dimethylamino)–2–nitrostilbene–4–carboxylic acid (ONS–COOH), which undergoes a ring–closing photoisomerization reaction[17] upon exposure to high intensity laser beam, as shown in Figure 3.3.

The dye isomer can react further if exposed to oxygen at elevated temperature. This oxidation step is prevented from occurring by sealing the sample under argon between two glass disks separated by a 1 mm thick aluminum spacer. Also, the writing laser beams are left on only long enough for dye to isomerize. Such short exposure time minimizes heating effects.

As a result of dye photochemistry, the sample contains a cosinusoidal spatial modulation in concentration of the dye. This modulation acts as an optical grating due to the difference in absorptivity and/or refractive index between the two isomers. There are two types of gratings formed in an FRS experiment. If the grating results because of a difference in absorptivities, it is referred to as an "amplitude grating" whereas if the grating is formed because of a difference in refractive indices, it is referred to as a "phase grating". In amplitude gratings, the same wavelength is used for writing (creation of grating) and reading while in a phase grating, different wavelengths are required for the two steps. The two isomers of ONS–COOH exhibit a significant difference in their

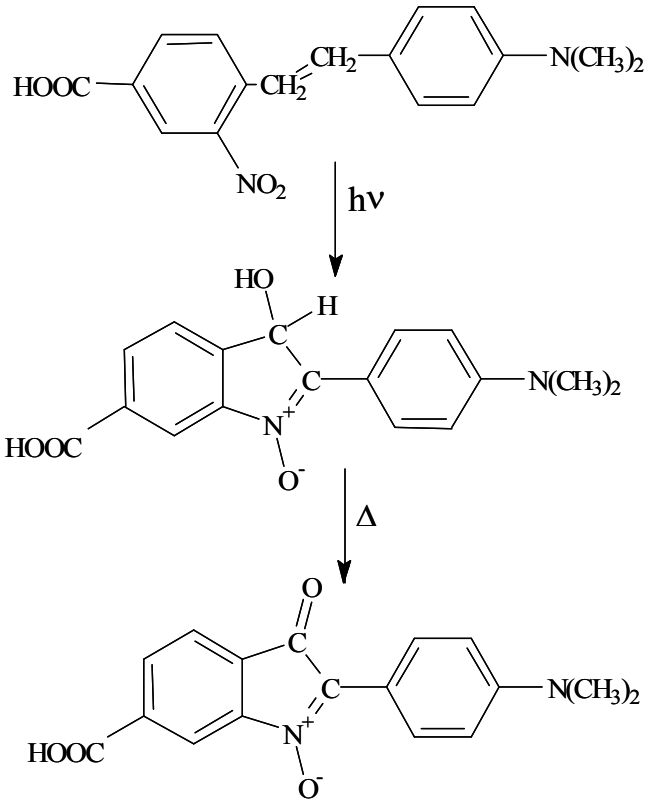

Figure 3.3. Ring closing reaction during photoisomerization of ONS–COOH. Both steps are irreversible and the intermediate product is the dye isomer formed during the FRS experiment. The second step is an oxidation step and occurs only in the presence of oxygen at elevated temperature.

absorptivities and thus in this work the amplitude gratings were used to probe tracer diffusion in polymer blends.

Reading the grating

The grating is "read", i.e., probed by a third beam of much lower intensity to prevent further isomerization of the dye. Due to the cosinusoidal optical grating, diffraction only occurs at the first–order Bragg angles that satisfy eq. 3.2. and is monitored by a photomultiplier tube. As mentioned earlier, FRS experiments measure uniaxial diffusion in an anisotropic system – only in the direction normal to grating. As the dye isomers inter–diffuse normal to the grating, the diffracted intensity decreases with diminishing contrast of the grating. However, the grating contrast could also diminish if reversible dye isomerization is thermally accessed on time scales similar to that of diffusion. To ensure that grating erasure occurs only due to diffusion, selection of the appropriate dye becomes extremely important. ONS–COOH undergoes an irreversible ring closure when exposed to light, thus making it a suitable dye for experiments discussed in this dissertation. There are other dyes, e.g., azobenzene that reisomerize to their original states after a period of time. Such dyes would not be suitable for our system.

In this work, the dye molecules were attached to the polymer chains and motion of the dye was observed, which was made possible by motion of polymer chains. The polymer center of mass motion causes relaxation of dye concentration profile resulting in erasure of the optical gratings. To understand the dynamics of grating erasure, an analysis of diffusion equations is presented here. First, the case of no dye reconversion (such as in the case of ONS–COOH which isomerizes irreversibly) is analyzed.

The diffusion of dye isomers is a mutual diffusion process. However, in the case of FRS, the mutual diffusion coefficients determined are identical to tracer diffusion coefficients in our system. The governing equations for this diffusion process are those described by Fick's second law:

$$\frac{\delta c_1(x,t)}{\delta t} = D_1 \frac{\delta^2 c_1(x,t)}{\delta x^2} \tag{3.3}$$

$$\frac{\delta c_2(x,t)}{\delta t} = D_2 \frac{\delta^2 c_2(x,t)}{\delta x^2} \tag{3.4}$$

where D_1 and D_2 are diffusion coefficients of isomers 1 (original form of dye) and 2 (photoisomerized form) respectively. The initial conditions for eqs. 3.3 and 3.4 are given by:

$$c_1(x,0) = c_{tot} - c_0\left(1 + \cos\left(\boldsymbol{q}x - \phi\right)\right) \tag{3.5}$$

$$c_2(x,0) = c_0\left(1 + \cos\left(\boldsymbol{q}x - \phi\right)\right) \tag{3.6}$$

where $\boldsymbol{q}$ is described by eq. 3.2. and c_0 is the concentration at time $t = 0$ and c_{tot} is the total concentration which equals the sum of c_1 and c_2. Using separation of variables, the solution to eqs. 3.3 and 3.4 is determined to be:

$$c_1(x,t) = c_{tot} - c_0\left(1 + \exp\left(-\boldsymbol{q}^2 D_1 t\right)\cos\left(\boldsymbol{q}x - \phi\right)\right) \tag{3.7}$$

$$c_1(x,t) = c_0\left(1 + \exp\left(-\boldsymbol{q}^2 D_1 t\right)\cos\left(\boldsymbol{q}x - \phi\right)\right) \tag{3.8}$$

If D_1 and D_2 are the same, the time–dependent sum of c_1 and c_2 is constant throughout the sample. However if both isomers have different diffusivities, then the total dye concentration can exhibit spatial maxima and minima at intermediate diffusion times. Eventually, the isomer concentration values will converge to their average values at all points in the sample. From eqs. 3.7 and 3.8, it can be seen that concentration profiles retain the original cosinusoidal form of position dependence, but the time dependence exhibits an exponential decay. This is an indication of the exponential decay of the amplitude while the wavelength of the grating remains unchanged. The rate at which the amplitude diminishes exponentially is given by q^2D.

The diffracted intensity is measured by the photomultiplier tube at the first order diffraction spot. In addition to the diffracted beam, the measured intensity also includes intensity from scattered light. The scattered light can be coherent with the diffracted beam or incoherent with it. The measured light intensity can be expressed as:

$$I_{\text{measured}} = (E_{\text{diff}} + E_{\text{coh}}) * (E_{\text{diff}} + E_{\text{coh}}) + E^2_{\text{incoh}} \tag{3.9}$$

where E is the electric field amplitude. The detailed solution of eq. 3.9 can be found elsewhere.[18] If both isomers have the same diffusivities, i.e., $D_1 = D_2$, the measured intensity at the first–order diffraction spot can be expressed in terms of coherent and incoherent scattered intensities as well as electric field amplitudes:

$$I(t) = \left(A\exp\left(-\,t/\tau\right) + B_{coh}\right)^2 + B_{incoh}^2 \tag{3.10}$$

where A is the amplitude of initial diffracted electric field, B_{coh} is the contribution of coherent scattered light to measured intensity, while B_{incoh} is the same for incoherent scattered light, τ is the time constant for grating decay and can be expressed as:

$$\tau = \left(q^2 D\right)^{-1} = \frac{d^2}{4\pi^2 D} \tag{3.11}$$

If both isomers have different diffusion coefficients, i.e. $D_1 \neq D_2$, then the measured intensity is expressed as:

$$I(t) = \left(A_1\exp\left(-\,t/\tau_1\right) - A_2\exp\left(-\,t/\tau_2\right) + B_{coh}\right)^2 + B_{incoh}^2 \tag{3.12}$$

where A_i and τ_i are the amplitude and time constants for the two grating decays. In the case of a pure phase or pure amplitude grating, the concentration profiles formed are 180° out of phase with one another, making A_1 and A_2 have opposite signs. Equation 3.12 can result in three different relaxation profiles as shown in Figure 3.4: A monotonic decay (I), a decay–growth–decay (II), and a rise followed by a decay (III).[19] The grid in Figure 3.4 shows the range amplitude and time constant ratios of the gratings (A_1/A_2, τ_1/τ_2) that produce each type of FRS signal profile.

An important comment has to be made at this point regarding double exponential decays. In the aforementioned discussion, we have assumed that diffusivities of both isomers are different which results in two gratings being formed and the signal exhibits a double exponential decay. However, same result can be obtained even if both isomers diffuse at the same rate; polymer chains exhibit two different modes of relaxation, e.g., in an anisotropic medium such as cylindrical block copolymer melts.[20] The optical grating can relax by diffusing along the cylinder and across it. These two modes can have different rates of diffusion and would give rise to a decay function that can be modeled by eq. 3.12. The decay in this case is that of a single grating but through two decay mechanisms, so the amplitudes would be in phase with one another and would have the same sign. The relative magnitudes of A_1 and A_2 would indicate the relative amounts of chains diffusing in each direction.

Having discussed in detailed the case of irreversible dye isomerization, let us now briefly address the case in which thermal reisomerization occurs on a time scale similar to that of diffusion. In this case, the aforementioned analysis is not applicable. The governing diffusion equations for this process are:

$$\frac{\delta c_1(x,t)}{\delta t} = D_1 \frac{\delta^2 c_1(x,t)}{\delta x^2} + \kappa c_2(x,t) \tag{3.13}$$

$$\frac{\delta c_2(x,t)}{\delta t} = D_2 \frac{\delta^2 c_2(x,t)}{\delta x^2} - \kappa c_2(x,t) \tag{3.14}$$

where κ is the reisomerization rate constant. The initial conditions are the same as those given in eqs. 3.5 and 3.6. The solutions to these diffusion equations are much more complicated and will not be discussed here. A detailed analysis can be found elsewhere.[18] The measured intensity expression at the first–order diffraction spot for this case can be written as:

$$I(t) = \left(A_1 \exp\left(- \, t / \tau_1 \right) - A_2 \exp\left(- \, t / (\tau_2 + \kappa) \right) + B_{coh} \right)^2 + B_{incoh}^2 \qquad (3.15)$$

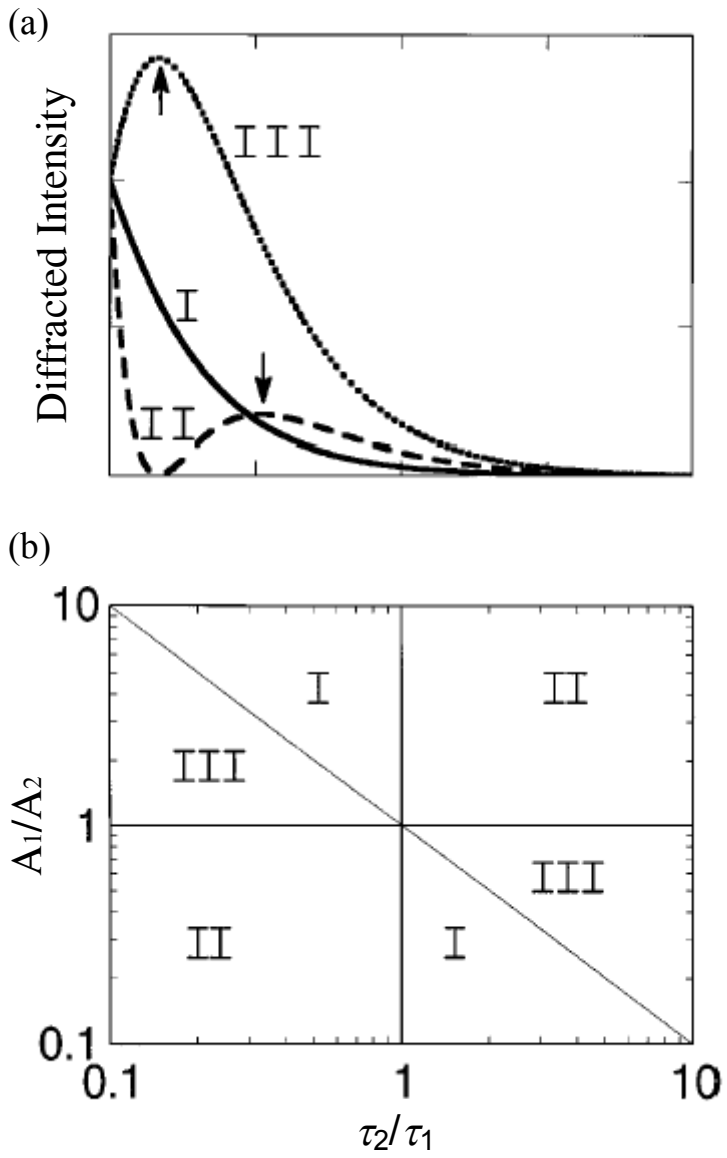

Figure 3.4. (a) Types of possible FRS signals as a result of complimentary gratings contributing to diffracted signal. (b) The grid shows the necessary conditions for each type of decay profile in terms of time constants, τ, and grating amplitudes, A of each grating type. (Adapted from Ref. 19)

3.2.4 Forced Rayleigh Scattering Instrumentation

Schematic diagrams of FRS in the writing and reading modes are shown in Figure 3.5 and Figure 3.6 respectively. The light used to create and probe the optical grating in the sample originates from an argon laser (Lexel, model 95), tuned to a wavelength of 488 nm. The light beam is directed by a series of mirrors labeled M1, M2, M3 and M4. The angle of these mirrors can be adjusted, as well as the angle and position of two smaller mirrors labeled mm1 and mm2.

A neutral density filter, used as an attenuator to reduce the beam intensity by a factor of 10^4, is mounted on a pneumatic cylinder (Clippard Minimatic, Model 75D-1). During the writing phase, the attenuator is withdrawn from the beam path, and is placed back in the path during the reading phase. The beam passes through some or all of the shutters 1–3, depending on the stage of the experiment, before being reflected by one of the mirrors. The three shutters (A. W. Vincent Associates, Model 23X) can be opened or closed, again depending on the stage of the experiment, to let the beam pass or not. A beam splitter (Melles Griot) is used to split the beam into two equal intensity components for the writing stage of the experiment. To detect the scattered light intensity, a photomultiplier tube (PMT) (Hamamatsu Corporation, Model R928) is used. A flight tube is placed between shutter 3 and the PMT to reduce the amount of stray light reaching the PMT. The PMT produces a current, which is then converted to a voltage, digitized, and recorded by a computer.

The FRS sample is held in a Teflon insulated copper sample holder that can be heated. This unit is mounted on a translation stage (Newport Corp., 435–2) so it can be moved horizontally. This facilitates beam alignment and access to different sample

locations for the beams to intersect in. Similarly, the copper sample holder can be moved vertically by tightening or loosening a screw in order to facilitate different sample locations. The temperature of the sample is controlled with a Fenwal 144 temperature controller. A resistance temperature detector (RTD) is used to measure the temperature of the copper sample holder near the sample.

3.2.5 Forced Rayleigh Scattering Sample Preparation

The labeled (tracer) and unlabeled (matrix) polymers were co–dissolved (1% by weight tracer) in methylene chloride. To protect the polymers from oxidation during heating, 0.1 wt.% 2,6-di–*tert*–butyl-4-methyl phenol (BHT) was added to the polymer solution. The solution was then filtered using a glass syringe and a 0.45 μm filter and most of the solvent was removed by evaporation under nitrogen purge. The sample was completely dried in a vacuum oven at 150 ^{o}C until no further weight change was observed.

The FRS samples were prepared in a glove box (under an argon atmosphere) by sealing the polymer blend with silicone adhesive between two glass disks (1”x1/16” thick), separated by a 1.0 mm thick aluminum spacer. The sealant was dried overnight to ensure a proper seal in order to prevent any leakage of the blend during the experiment.

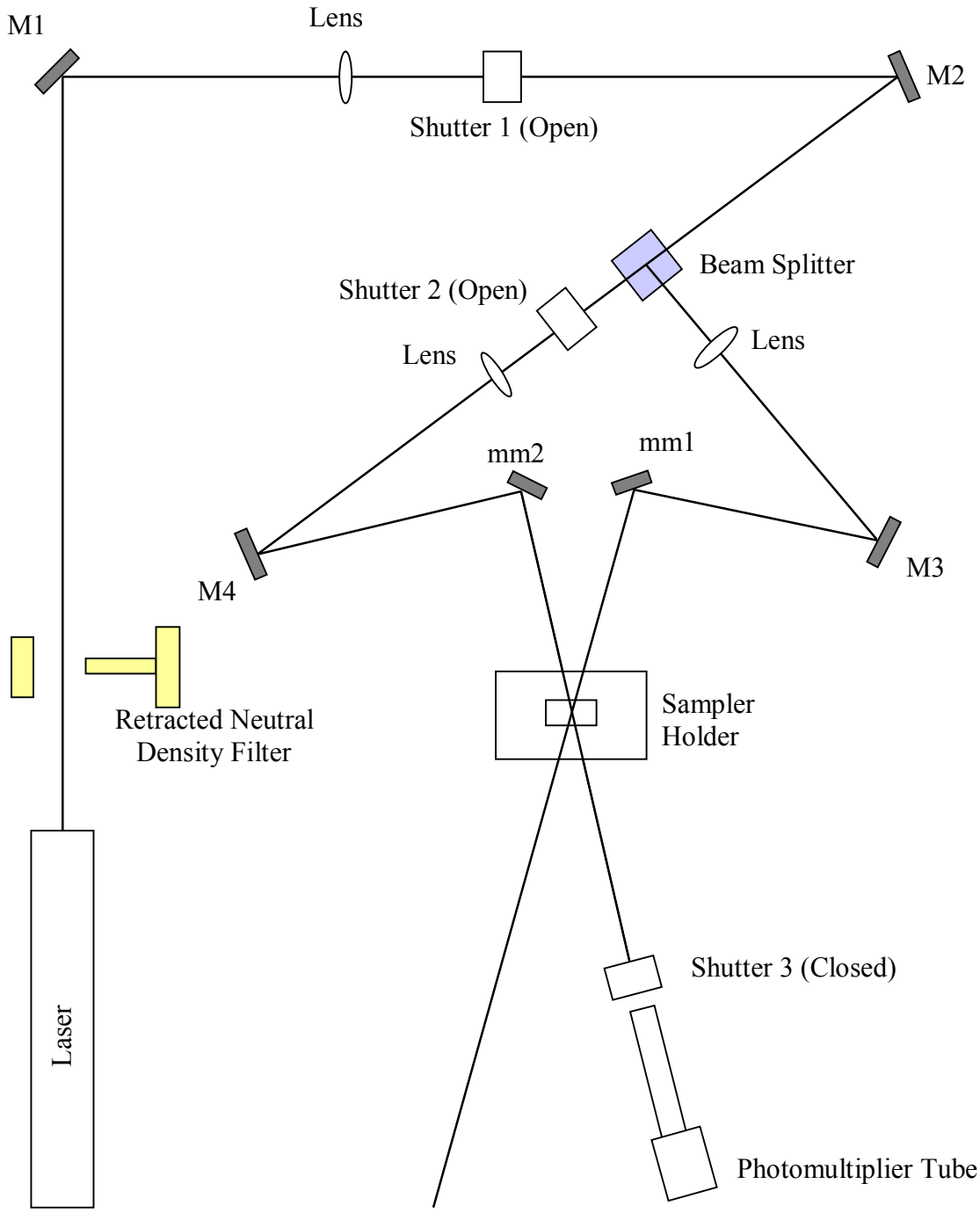

Figure 3.5. A schematic of FRS setup in the writing mode

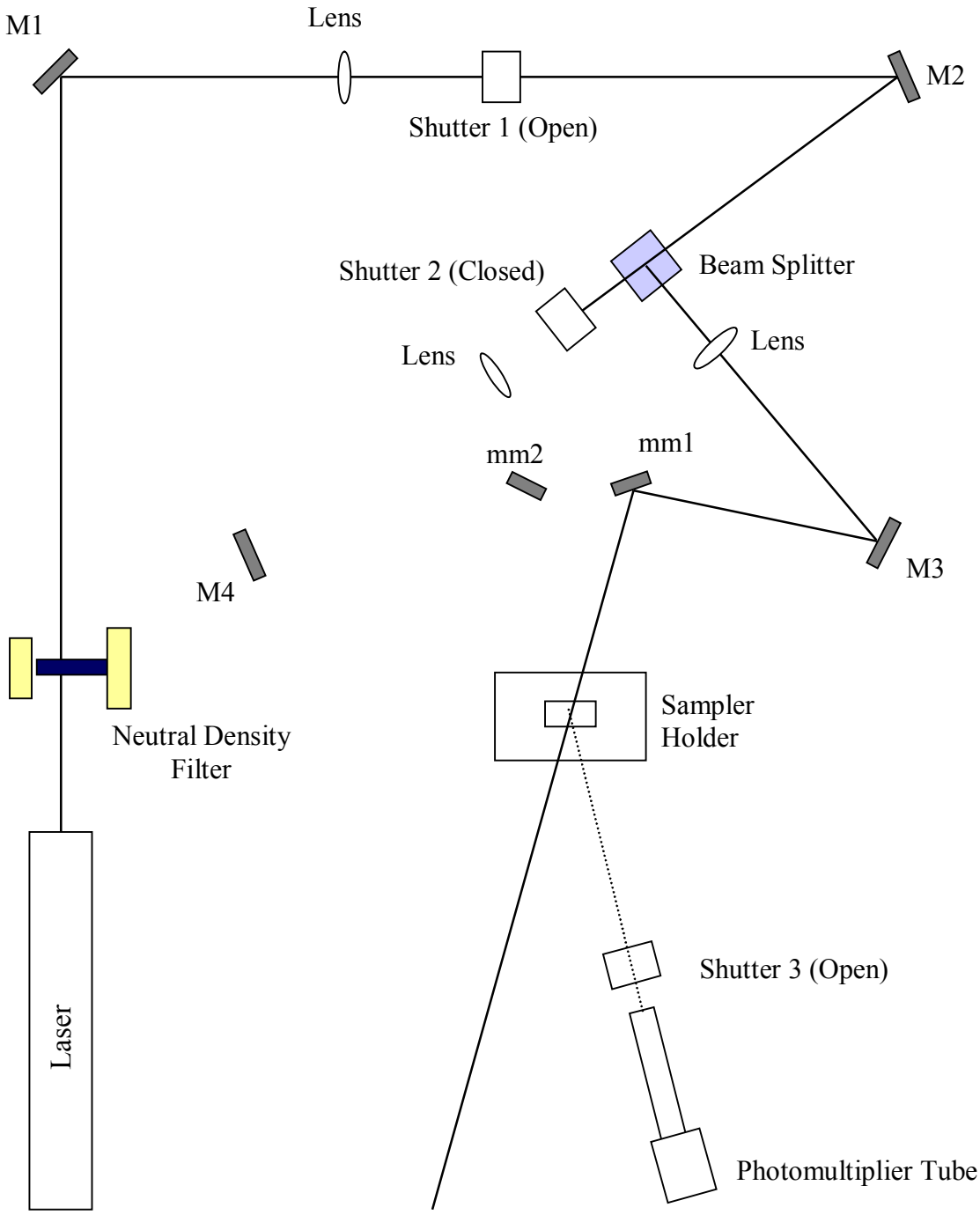

Figure 3.6. A schematic representation of FRS setup in the reading mode

3.3 Chemical Synthesis for FRS experiments

This section describes in detail synthesis of the dye ONS–COOH and its attachment to PEO chains.

3.3.1 Dye Synthesis

FRS experiments utilize photoisomerization reaction of a dye attached to polymer chains to monitor chain diffusion. Hence, the dye plays a critical role in these experiments. The choice of a dye is dependent upon several factors such as ease of being attached to polymer chains, kind of photochemical reactions the dye undergoes, dye mobility, dye molecular size relative to that of polymer chains, thermal stability of the dye, laser wavelength and intensity required to isomerizes the dye, etc. There are two types of photochemical reactions that the dyes undergo: *cis-trans* or irreversible (ring opening – closing reactions.

The dye used in this work is 4'–(*N*,*N*–dimethylamino)–2–nitrostilbene–4–carboxylic acid (ONS–COOH), which undergoes a ring closing photoisomerization reaction[17] in the presence of light as shown in Figure 3.3. ONS–COOH has properties that are well suited for use as a dye in our experiments. It has a carboxylic group that can be easily attached to poly(ethylene oxide) (PEO) with hydroxyl end groups. Also, ONS–COOH reacts irreversibly which makes diffusion analysis simpler by eliminating the need to worry about dye reisomerization at time scales similar to that of diffusion. Since our FRS experiment used an Ar+ ion laser with a wavelength of 488 nm, ONS–COOH is well suited because the unexcited form of ONS–COOH has an absorption peak at 450

nm, and the photoisomer has a peak at 350 nm. In addition, the extinction coefficient is sufficiently different between the two photoisomers that an amplitude grating is formed.

The dye was synthesized using the method described by Cavicchi.[21] The dye synthesis comprises three main steps, the first of which is nitration of *p*–tolunitrile to produce *o*-nitro-*p*-tolunitrile. This is achieved by mixing in a 1:3 volume ratio (35 mL: 110 mL) 65% nitric acid and 98% sulfuric acid in a beaker. The mixture is cooled in an ice bath to 10 °C. 25.1 g of *p*–tolunitrile (purchased from Aldrich) is warmed in a water bath until it liquefies and then added dropwise to the acid solution. Adding *p*–tolunitrile to the acid solution very slowly while stirring the solution vigorously is critical in order to keep the temperature below 20 °C. Above 30 °C, hydrolysis of the nitrile functional group is possible. Once all *p*–tolunitirle has been added, the solution is stirred for a further 45 minutes. The resulting product is precipitated by pouring the solution over ice. The precipitate is filtered, dried overnight under atmospheric conditions and recrystallized in absolute ethanol. For recrystallization, *o*-nitro–*p*–tolunitrile is dissolved in ethanol at 55 °C and then gradually cooled to room temperature. The crystals were filtered and dried overnight in a vacuum oven. Approximately 20.4 g of *o*–nitro–*p*–tolunitrile was recovered after purification. Figure 3.7 shows ^{1}H NMR spectrum of *o*–nitro–*p*–tolunitrile in deuterated chloroform with TMS as the reference.

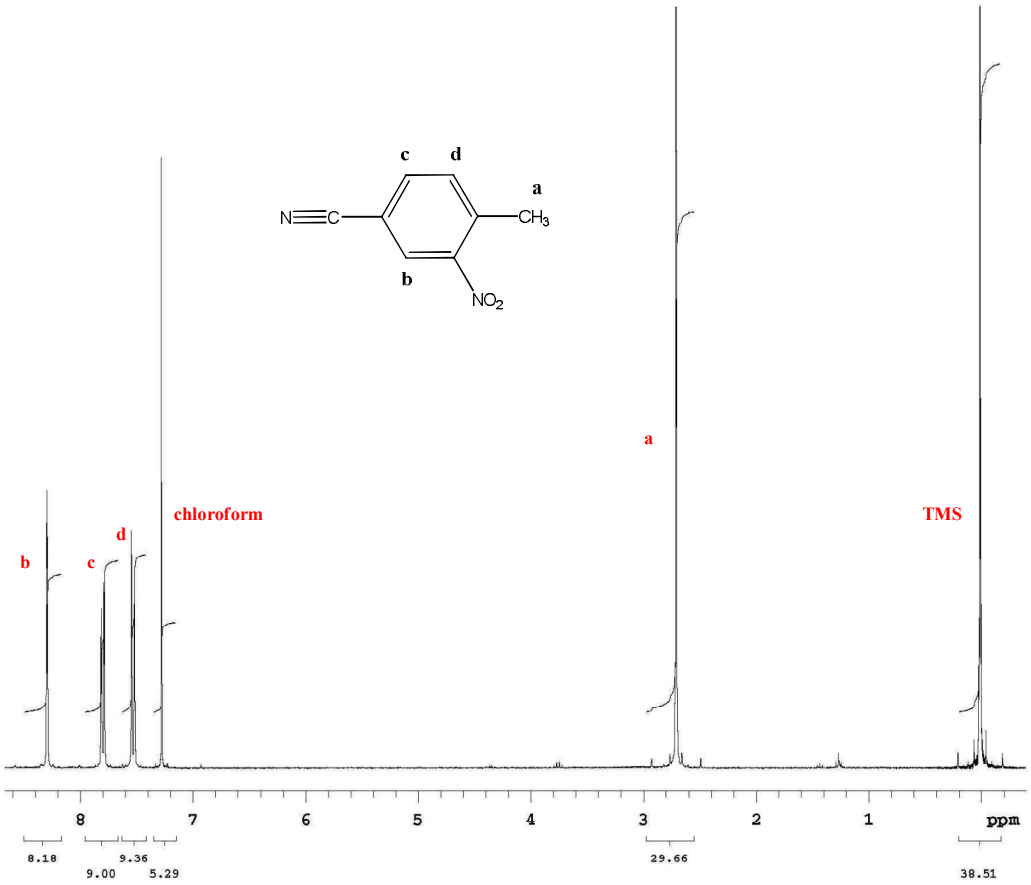

Figure 3.7. ^{1}H NMR spectrum of *o*–nitro–*p*–tolunitrile in chloroform

In the second step, *o*–nitro–*p*–tolunitrile is converted to 4'–(*N*,*N*–dimethylamino) –2–nitrostilbene–4–nitrile (ONS–CN). 5.34 g of *o*–nitro–*p*–tolunitrile and 4.91 g of *p*–dimethylaminobenzaldehyde were added to a 50 mL round bottomed flask that was open to atmosphere. These amounts correspond to an equimolar mixture of *o*–nitro–*p*–tolunitrile and *p*–dimethylaminobenzaldehyde. The solution was heated to 120 °C, which resulted in the solution turning orange in color. 0.3 mL (~35 drops) of piperidine was added to the hot solution to function as a catalyst. This turned the solution deep red in color. The reaction was continued for 3 hours, after which the product was cooled to room temperature and recrystallized using acetic acid. Approximately 20 mL of acetic acid was used. To completely dissolve the impure product, the ONS–CN/acetic acid solution was heated to 100 °C. The yield of ONS–CN after purification was 7.1 g. Figure 3.8 shows the ^{1}H NMR spectrum of ONS–CN in deuterated acetone.

The third step entails conversion of ONS–CN to ONS–COOH. 1.94 g of ONS–CN were added to a 100 mL round bottomed flask along with 2 times molar excess of potassium hydroxide (0.79 g). The reactants were dissolved in 30–40 mL of isopropanol/water mixture (1:1 v/v). The solution was heated at 100 °C under reflux overnight. The resulting dye was precipitated with a 6% hydrochloric acid solution. The bright yellow precipitate was repeatedly washed with water causing it to change to a deep red, almost blood red color. This is the final product, ONS–COOH.

To check for impurities in ONS–COOH, thin layer chromatography (TLC) was performed using a chloroform/methanol mixture (4:1 v/v). In two separate vials, small amounts of ONS–CN and ONS–COOH were dissolved in acetone. In a glass jar, a small quantity of the chloroform/methanol mixture was added. On the TLC plate, a thin

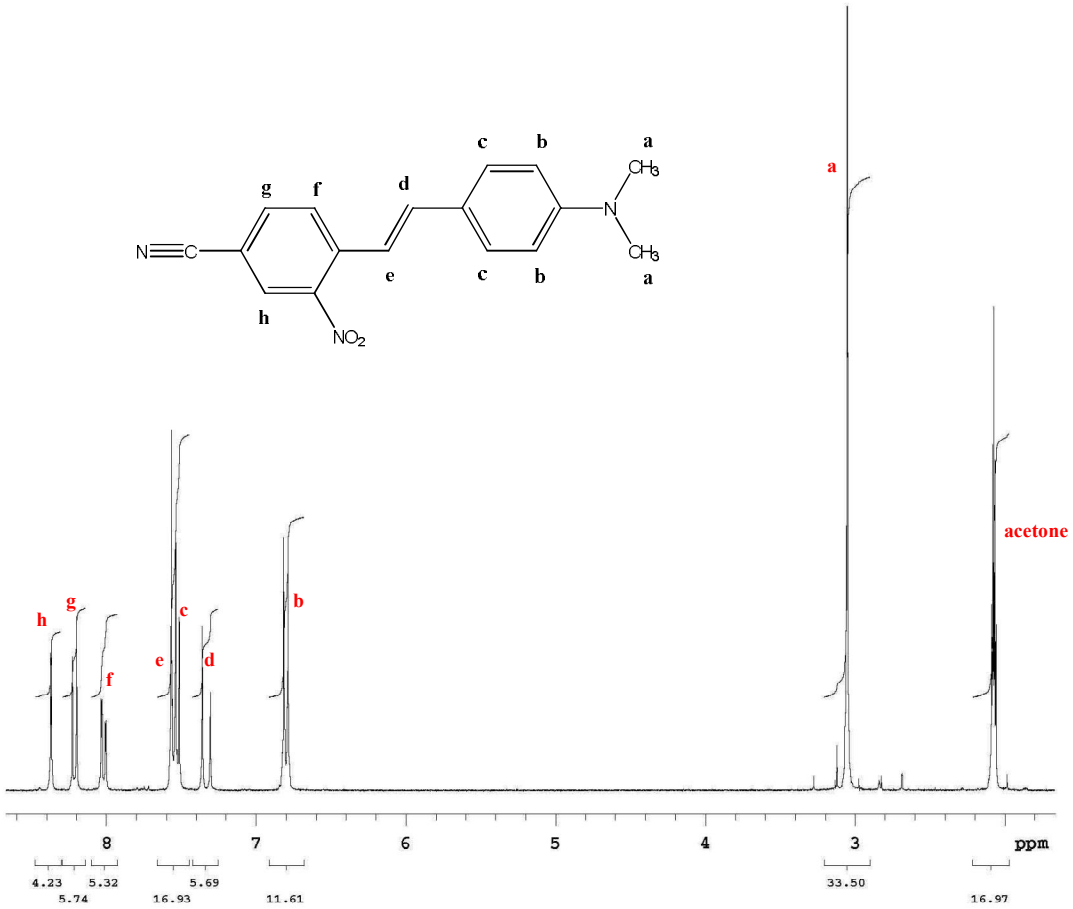

Figure 3.8. ^{1}H NMR spectrum of ONS–CN in acetone

line was drawn with pencil to designate the starting point. Using a capillary tube, a drop each of ONS–CN and ONS–COOH were placed side by side at the starting line. The solvent on the TLS plate was dried and the plate was placed vertically in the jar. Care was taken to ensure that the starting line was above the liquid level in the jar. The glass jar was sealed with a lid and the movement of the dyes was monitored with time. The ONS–CN spot stayed intact throughout its journey up the TLC plate indicating it was completely pure (which should be the case since ONS–CN was thoroughly purified). However, the ONS–COOH separated into two spots – one corresponding to pure ONS–COOH while the other to impurities present in the dye.

To purify this dye, equimolar amounts of ONS–COOH and cesium carbonate were dissolved in a water/ethanol mixture (1:1 v/v). For 120 mg of dye, 90 mL each of water and ethanol were used. The reaction mixture was stirred overnight after which the solvent was evaporated under a nitrogen purge, leaving behind the cesium salt of the dye ($ONS–COO^{-}Cs^{+}$) and impurities. The product was dissolved in distilled water because the salt is readily soluble in water whereas the impurities are not. The solution was filtered and the filtrate was recovered. The salt was reconverted to ONS–COOH by adding a 6% hydrochloric acid solution to the dye, followed by repeated washing with deionized water and centrifugation until the pH became neutral. TLC was performed on the purified ONS–COOH and only one spot was observed confirming the removal of all impurities. The ^{1}H NMR spectrum of purified ONS–COOH in deuterated acetone is shown in Figure 3.9. The ONS-COOH synthesis is summarized in Figure 3.10.

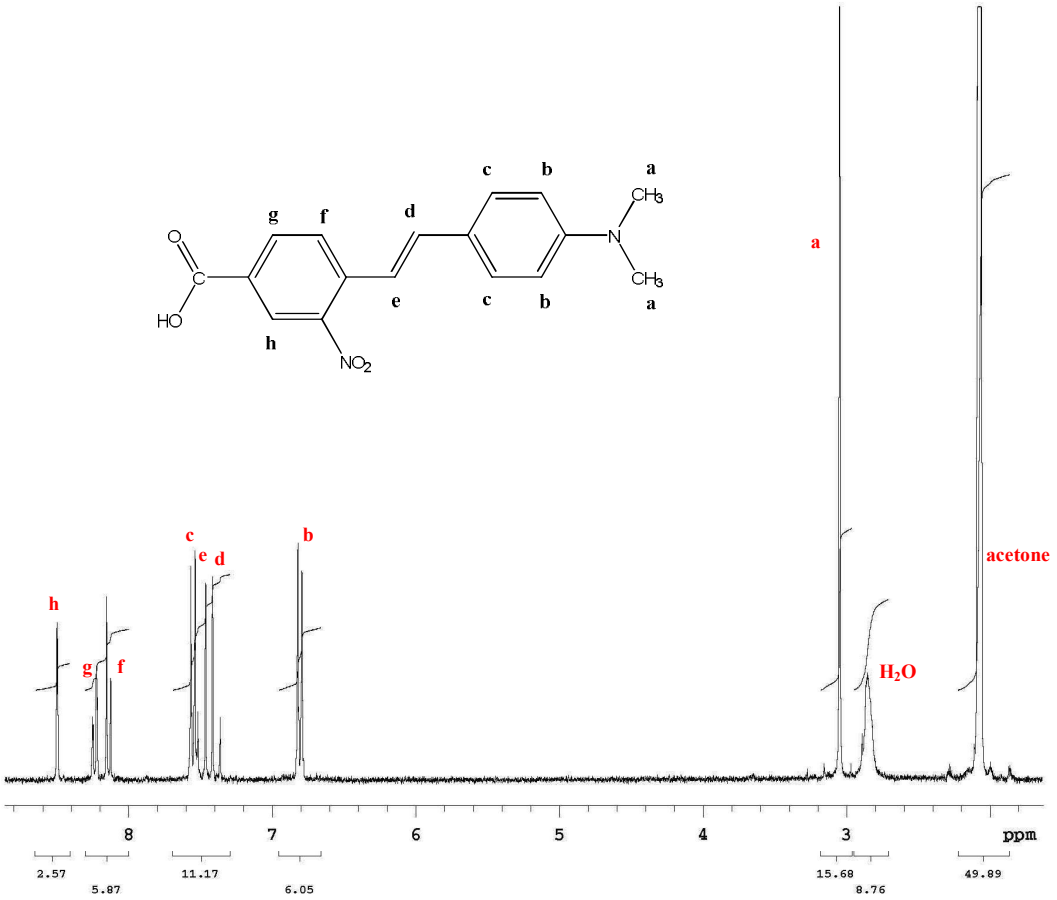

Figure 3.9. ^{1}H NMR spectrum of ONS–COOH in acetone

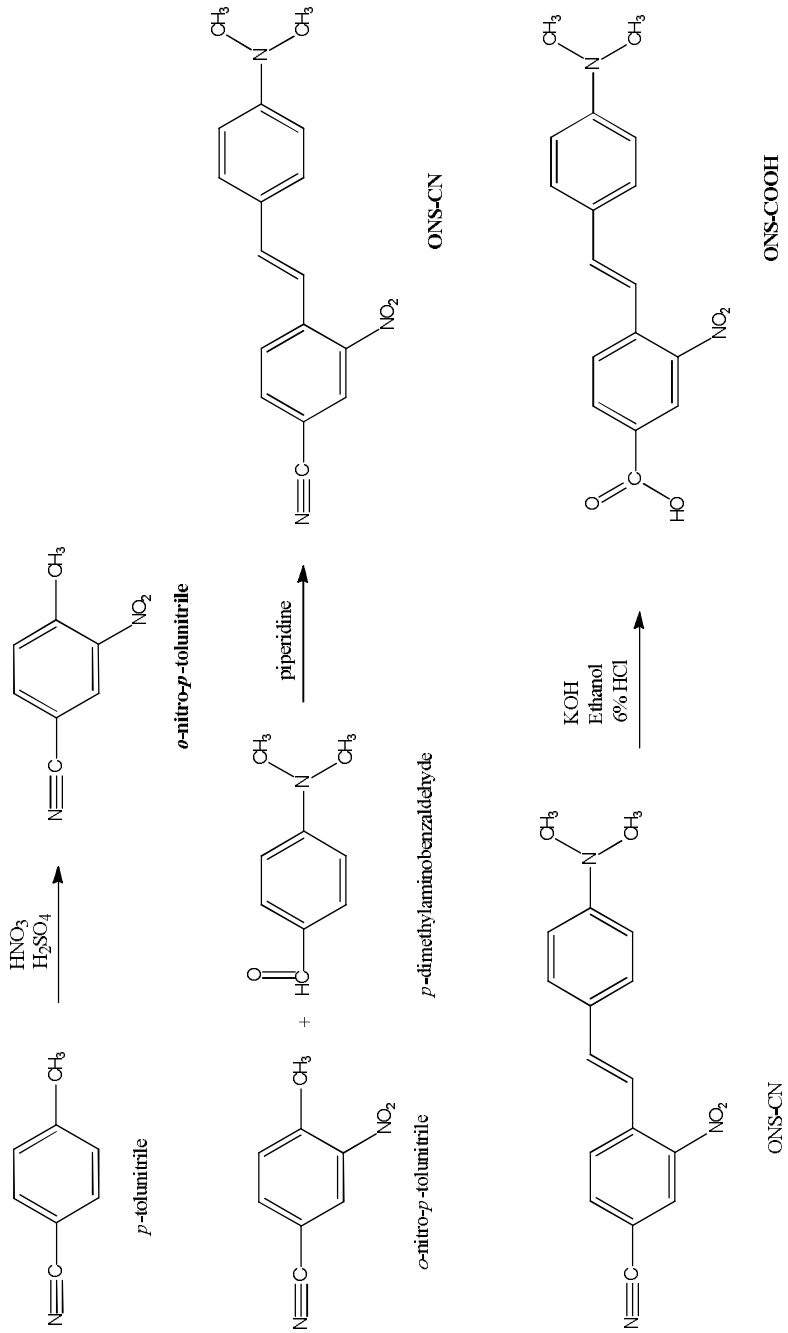

Figure 3.10. Synthesis of ONS–COOH

3.3.2 Polymer Labeling

To measure diffusion processes using FRS, the polymer that will be used a tracer will have to be "labeled", i.e., a dye will have to be attached to it. In this work, FRS was used to measure PEO diffusion in blends of PEO and PMMA. The PEO used was hydroxyl terminated. Since ONS-COOH has a carboxyl functional group, it can be easily attached to PEO chains via esterification. The PEO labeling reaction is illustrated in Figure 3.11. A 1,000 g/mol PEO (PEO–1) was obtained from Aldrich and used in the PEO/PMMA blends.

The solvent, methylene chloride was dried using an activated alumina column. Approximately 115 mg of PEO–1 was dissolved in 40 mL of dry methylene chloride with a five–fold molar excess of ONS–COOH, and a ten–fold molar excess of dicyclohexylcarbodimide (DCC), and dimethylaminopyridine (DMAP) in a round bottomed flask. The solution was refluxed at 50 °C under a nitrogen purge for 48–72 hours. The reaction mixture was dried, dissolved in water, and vacuum filtered to remove the unreacted mixture.

The filtrate was dried, redissolved in methylene chloride, and passed through a silica gel column to remove unreacted ONS–COOH. The extent of separation was monitored using a size exclusion chromatography (SEC) column equipped with refractive index (RI) and ultra violet (UV) detectors. Details of the SEC setup will be presented later in this chapter. ONS–COOH shows strong absorbance at 350 nm.[17] The final SEC spectrum is shown in Figure 3.12. Small trace of unattached ONS-COOH can be seen in this spectrum. However, this amount is not significant enough to warrant further purification.

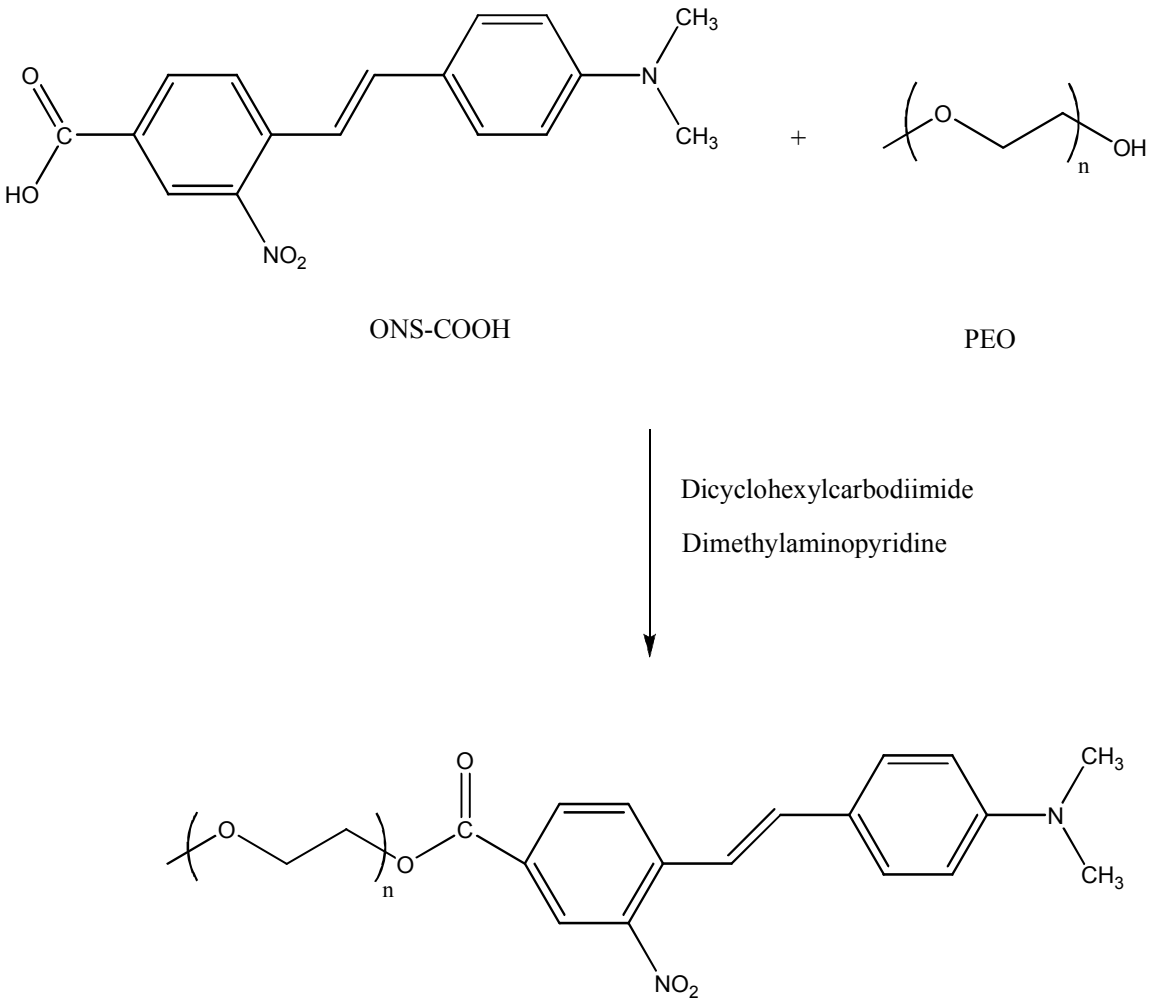

Figure 3.11. Condensation reaction of PEO with ONS–COOH

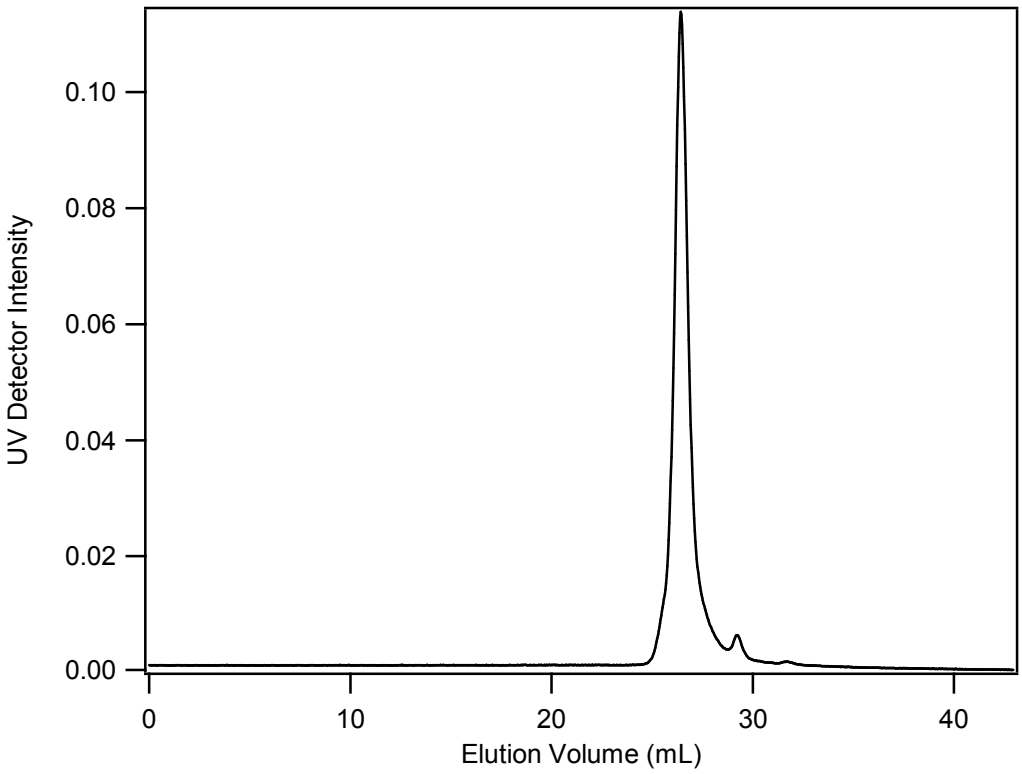

Figure 3.12. SEC spectrum of labeled PEO after purification. Small amount of unattached dye can still be seen in the spectrum at an elution volume of approximately 29 mL.

3.4 Poly(4–vinyl phenol) Synthesis and Characterization

For investigation of component dynamics in strongly interacting blends, the blend system used in this work was PEO/poly (4–vinyl phenol) (PEO/PVPh). The PEO/PVPh blends comprised a high molecular weight polymer tracer blended with low molecular weight matrix components. The PVPh samples used in this work were 5 kg/mol (PVPh–5) and 290 kg/mol (PVPh–290).

3.4.1 Synthesis

The high molecular weight PVPh (PVPh–290), and the low molecular weight PVPh (PVPh–5) were synthesized via anionic polymerization.[22,23] *Sec*–butyllithium and 4–*tert*–butoxystyrene (*t*–BOS) were purchased from Aldrich. Tetrahydrofuran (THF) was dried by passing through alumina and silica columns. In a two–port, round bottomed flask, *t*–BOS was added along with calcium hydride and a magnetic stir bar. A freeze–pump–thaw cycle was carried out three times to completely degas the *t*–BOS monomer after which it was stirred over calcium hydride for 48 hours. The monomer was then distilled to a tared, degased, and flamed burette. After monomer transfer was complete, the burette was weighed again to determine the amount of monomer transferred. The burette containing *t*–BOS was kept in a dry ice/isopropyl alcohol bath until the main anionic reactor was ready for reaction.

A large reactor with six ports was set up for reaction with three of the ports used for a thermocouple well, a septum, and a manifold for connection to Argon and vacuum manifolds. A large magnetic stir bar was placed in the reactor and remaining ports were

sealed. The reactor was then degassed and flamed. It was then baked over a heating mantle at 275 °C overnight.

Two round bottomed solvent flasks were degased, flamed, and then sealed by closing the valve at the neck. Dried THF was transferred to these evacuated flasks under vacuum. Once enough THF was filled in each flask, the flasks were pressurized with argon to prevent any air leaking in.

The solvent flasks and the monomer burette were attached to the reactor under argon flow. The reactor was then evacuated followed by pressurizing with argon up to 6 psi pressure. This cycle was repeated ten times to ensure removal of any moisture. The monomer burette was attached to the center port to ensure that monomer drips in center of the reactor for proper mixing.

Under positive argon pressure, THF was added to the reactor, cooled to –70 °C using an isopropyl alcohol/dry ice bath, and stirred vigorously. The initiator, *sec*–butyllithium was taken out from its bottle stored inside a glove box using a glass, air–tight syringe and injected into the stirring THF through the septum followed by drop–wise addition of *t*–BOS. Care was taken to keep the reaction temperature constant at –70 °C during monomer addition to the reactor. As soon as the first drops of *t*–BOS dissolved in THF, the solution turned bright orange. As the reaction progressed, the color faded to some extent. During PVPh–290 synthesis, the color faded almost completely indicating formation of large molecular weight polymer chains. Once all the monomer had dripped into the reactor, the solution was stirred for a further 30 minutes before being terminated by degassed methanol. The poly(*tert*–butoxystyrene) (P*t*BOS) was precipitated in water and dried under vacuum at 70 °C for several days.

To convert to PVPh, P*t*BOS was hydrolyzed by adding to a solution of dioxane (10 times by weight) and excess 37 wt.% hydrochloric acid. The solution was stirred for 48–72 hours at 40 °C in a sealed, round bottomed flask. The resulting polymer solution was concentrated and PVPh was precipitated in a methanol/water mixture (3:7 v/v)[24] and dried under vacuum at 70 °C until constant weight was achieved.

The low molecular weight PVPh (PVPh–5) was characterized by proton NMR spectroscopy and its molecular weight determined by matrix assisted laser desorption ionization – time of flight mass spectrometry (MALDI–TOF), which is a very accurate and reliable technique for determining molecular weights and polydispersities for relatively low molecular weight polymers (M_n < 20,000). The details of MALDI–TOF will be presented later. Usually size exclusion chromatography (SEC) is performed on polymers to determine their molecular weights as it is a very convenient and easily accessible method. In the case of PVPh, it was found that the polymer would stick to SEC columns, resulting in an inaccurate determination of molecular weight and polydispersity. This is why for PVPh–5, we made use of MALDI–TOF to determine the molecular weight and polydispersity.

For the high molecular weight PVPh (PVPh–290), we could not use MALDI–TOF because the polymer molecular weight was much higher than what this experimental technique is capable of measuring. SEC was also unsuitable because of PVPh sticking to SEC columns. So to circumvent these issues, we used SEC to determine molecular weight of P*t*BOS, which is the precursor to PVPh. Unlike PVPh, P*t*BOS does not stick to SEC columns. ^{1}H NMR analysis showed complete conversion of P*t*BOS to

PVPh. So we used the monomer molecular weight ratio of these two polymers to determine molecular weight of PVPh–290 as shown in equation 3.16.

$$M_{PVPh} = \frac{M_{VPh}}{M_{tBOS}} \times M_{PtBOS} \tag{3.16}$$

The molecular weight of 4–vinyl phenol (VPh) is 120 g/mol while that of 4–*tert*–butoxystyrene (*t*BOS) is 176 g/mol.

The polydispersity of high molecular weight PVPh was determined to be 1.59 which was higher than our requirements. Since we intended to use this high molecular weight PVPh as a tracer in the blends, we only needed ~1g of the polymer for all experiments whereas we had synthesized ~45 g of the polymer. So fractionation was performed to reduce polydispersity and the fractionated polymer was PVPh–290 which was used as tracer in the blends for rheology experiments.

It is pertinent to mention an important point regarding synthesis of high molecular weight PVPh. Since the desired molecular weight was higher than 100,000 g/mol, a very high monomer to initiator ratio was required. If a miniscule amount of initiator is used, chances of failure are much higher as some initiator is bound to be lost to impurities in the solvent. Adding large amounts of initiator will require significantly large amounts of the monomer which would be impractical because of financial and reactor space constraints. Another consideration to be taken into account is the amount of solvent present in the flask. If the solvent is not enough, the solution could become viscous as polymerization progresses, making stirring of the solution more difficult. Irregular stirring because of high solution viscosity could result in high polydispersity.

3.4.2 NMR Analysis

The NMR results show complete conversion of P*t*BOS to PVPh. NMR sample of PtBOS was prepared in deuterated acetone while that for PVPh was prepared in deuterated dimethyl sulfoxide (DMSO). All NMR spectra were obtained using a 300 MHz ^{1}H NMR instrument. Figure 3.13, and Figure 3.14 show ^{1}H NMR spectra of P*t*BOS and PVPh, respectively.

3.4.3 Determination of *d*n/*d*c

To determine absolute molecular weight of P*t*BOS and PVPh, their *d*n/*d*c values were determined using a refractometer. For these measurements, the polymer samples used were 51 kg/mol P*t*BOS (P*t*BOS–51) and 30 kg/mol PVPh (PVPh–30). Several solutions of P*t*BOS–51 and PVPh–30 in THF were prepared ranging in concentration from 0.04–0.12 g/mL. Refractive indices of these solutions and of pure THF were measured and the results were plotted against solution concentration. A liner model was fitted to the experimental data and *d*n/*d*c values were determined from slope of the liner fit. Figure 3.15 shows the refractive index dependence on solution concentration for P*t*BOS and PVPh. The slope, and hence *d*n/*d*c for P*t*BOS was 0.097 ± 0.005 mL^{-1} while that for PVPh was 0.159 ± 0.028 mL^{-1}.

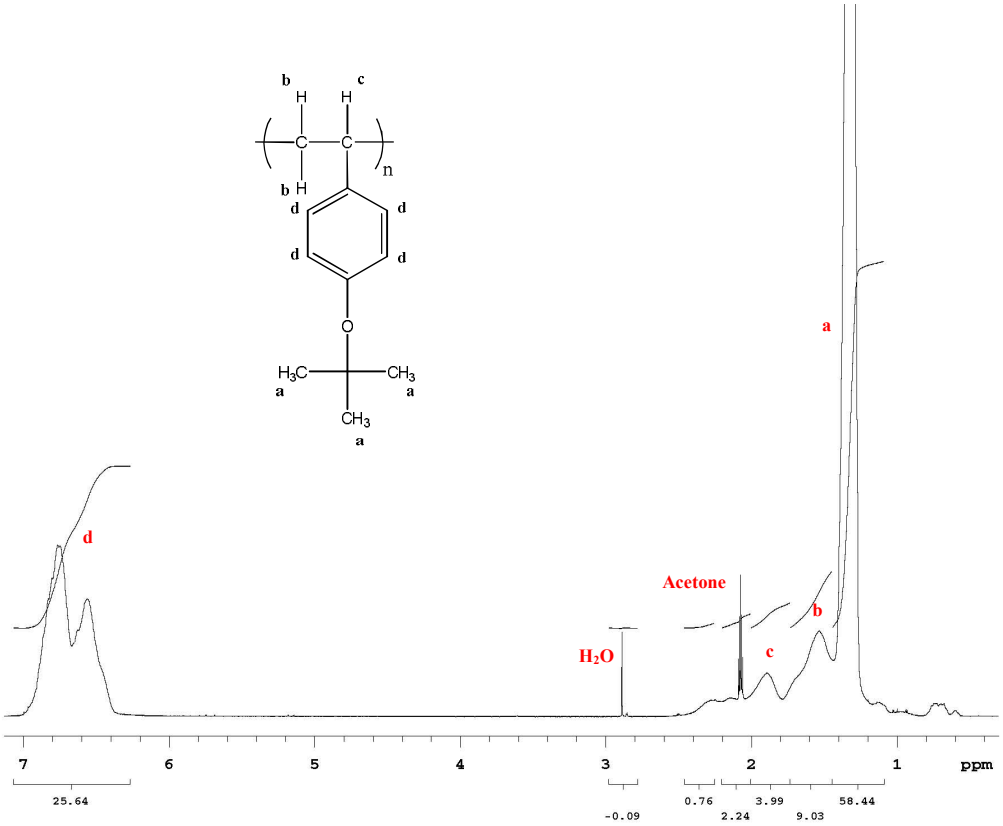

Figure 3.13. ^{1}H NMR spectrum of P*t*BOS in deuterated acetone

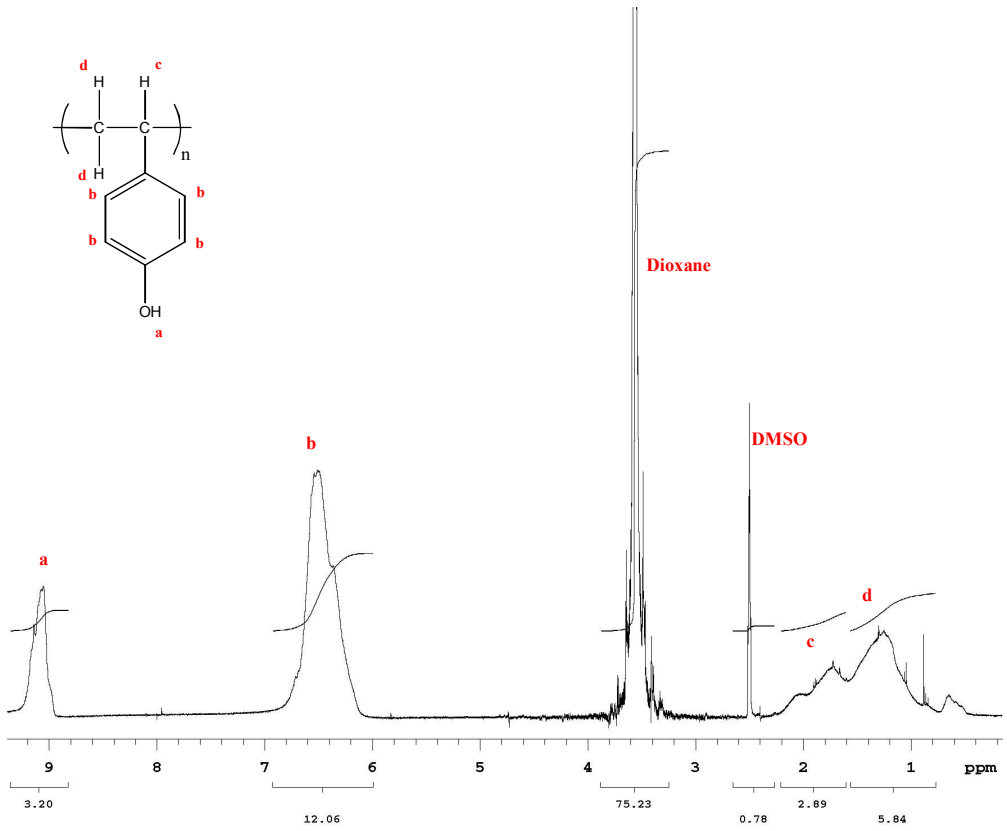

Figure 3.14. ^{1}H NMR of PVPh in deuterated DMSO

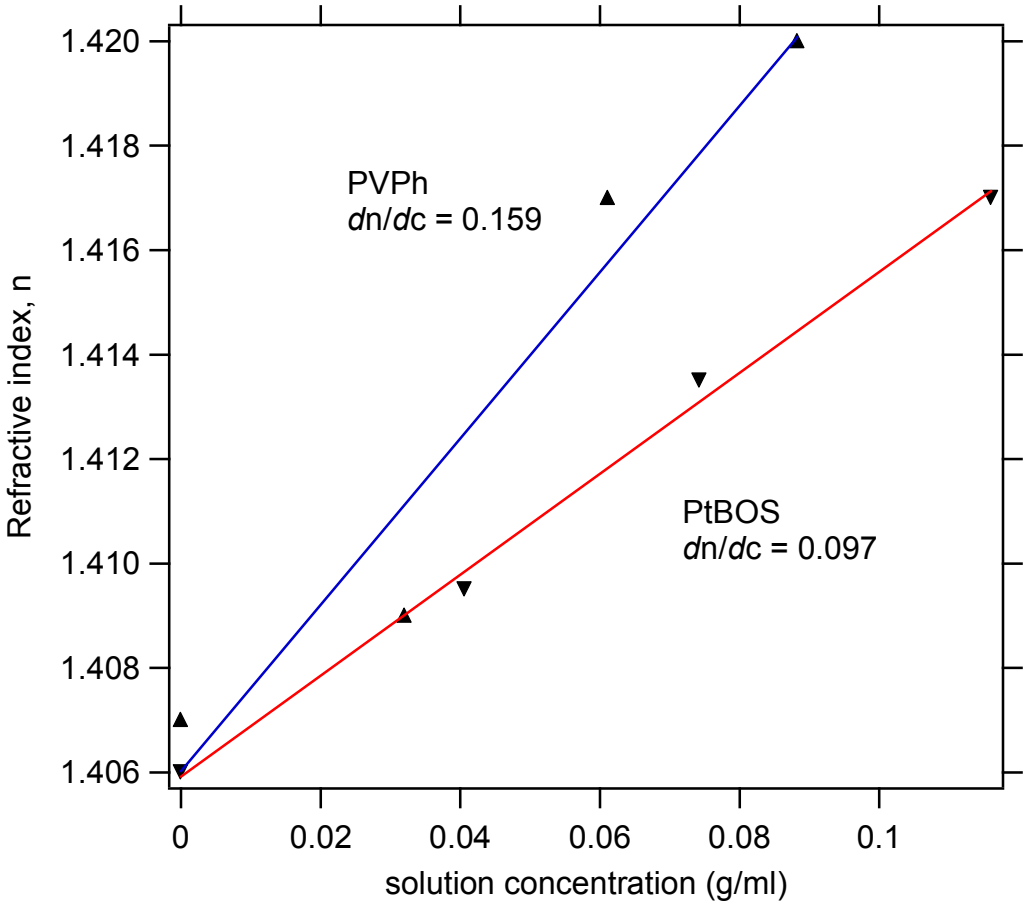

Figure 3.15. Determination of *d*n/*d*c for P*t*BOS and PVPh. (▲) PVPh, (▼) P*t*BOS.

3.4.4 MALDI–TOF Mass Spectrometry

The molecular weight of PVPh–5 was determined using MALDI–TOF. The sample was prepared by dissolving PVPh–5, dithranol (matrix), and sodium trifluoroacetate (cationizing agent) in THF. Typically 10 μL of 10 mg/mL PVPh–5 solution were mixed in a vial with 80 μL of 30 mg/mL matrix solution, and 10 μL of 10 mg/mL of the salt solution. Figure 3.16 shows the MALDI–TOF spectrum for PVPh–5.

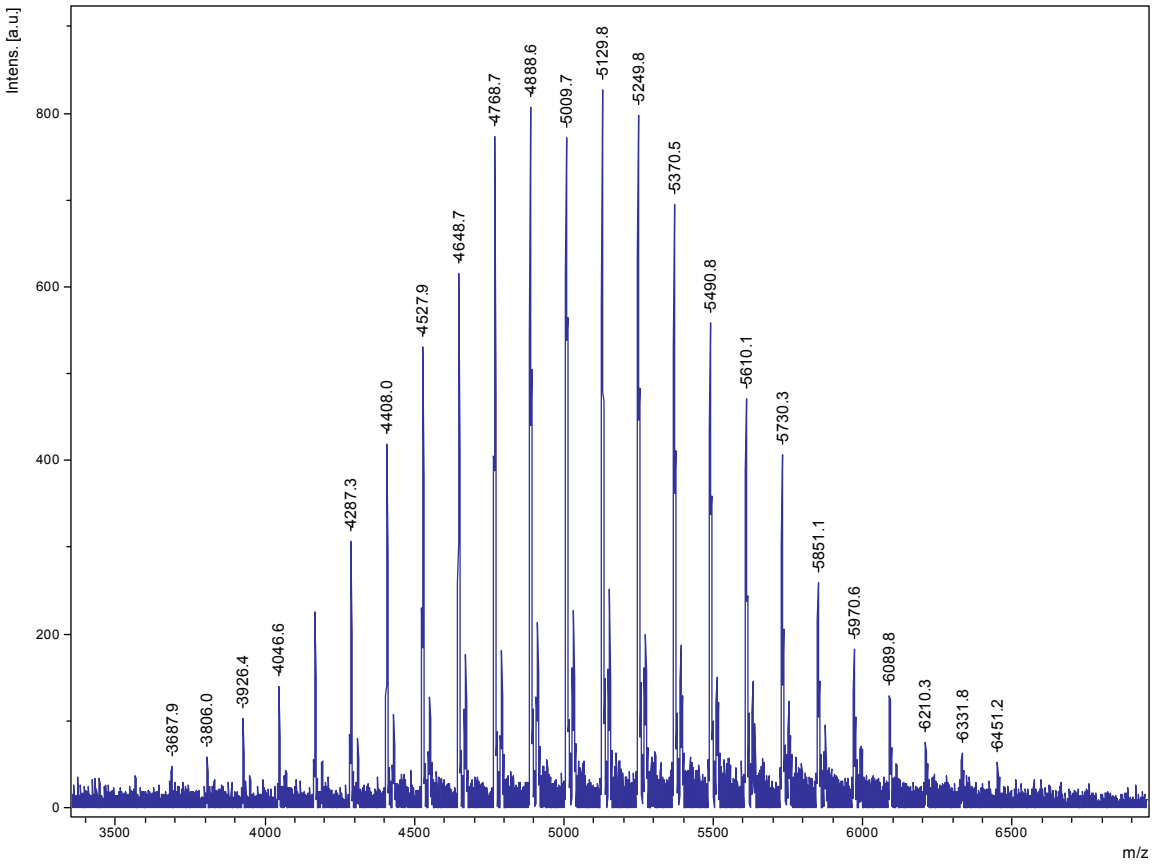

Figure 3.16. MALDI–TOF mass spectrum for PVPh–5.

3.5 Rheological Measurements

Rheology yields a wide variety of material properties such as moduli and viscosity and these properties can be functions of time, temperature, thermal or stress history. The measurements made on polymer blends were small amplitude oscillatory shear measurements as well as steady shear measurements.

In oscillatory shear measurements, the sample is subjected to an oscillatory shear strain of the form:

$$\gamma = \gamma_o \sin(\omega t) \tag{3.17}$$

where γ_o is the strain amplitude, ω is the oscillation frequency and t is the time. There are two limiting cases for linear material response: a Hookean solid and a Newtonian liquid. Most polymeric materials exhibit behavior between the ideal elastic solid and viscous liquid, and hence, they are referred as viscoelastic materials. This means that for a given strain, the observed stress is a combination of viscous and elastic responses and will be out of phase with the applied strain by a phase angle, δ.

$$\sigma = \sigma_o \sin(\omega t + \delta) \tag{3.18}$$

where σ is shear stress and σ_o is the stress magnitude. Equation 3.18 can be rewritten as:

$$\sigma = \sigma_o \cos(\delta)\sin(\omega t) + \sigma_o \sin(\delta)\cos(\omega t) \tag{3.19}$$

Assuming that stress is independent of strain, i.e., frequency is in the linear viscoelastic regime, equation 3.19 can be divided by the strain amplitude, γ_o, to obtain:

$$\frac{\sigma}{\gamma_o} = G'\sin(\omega t) + G''\cos(\omega t) \tag{3.20}$$

where *G'* and *G''* frequency dependent moduli referred to as the storage (or elastic) modulus and the loss modulus, respectively.[25] The ratio of these moduli gives the phase angle between the applied strain and observed stress:

$$\tan\delta = \frac{G''(\omega)}{G'(\omega)} \tag{3.21}$$

G' and *G''* can be grouped together into the complex modulus:

$$G^*(\omega) = G'(\omega) + iG''(\omega) \tag{3.22}$$

where G^* is the complex modulus and $i = \sqrt{-1}$. Another useful relationship that has been extensively used in this work is that between components of complex viscosity and storage and loss moduli. The complex viscosity can be written as:

$$\eta^*(\omega) = \eta'(\omega) - i\eta''(\omega) \tag{3.23}$$

where

$$\eta'(\omega) = \frac{G''(\omega)}{\omega} \tag{3.24}$$

and

$$\eta''(\omega) = \frac{G'(\omega)}{\omega} \tag{3.25}$$

Another useful relationship to extract zero shear viscosity from oscillatory shear experiments is:

$$\eta = \lim_{\omega \to 0} \eta'(\omega) \tag{3.26}$$

Equation 3.26 is valid in the terminal regime of the viscoelastic spectrum where η' is independent of ω.

For high viscosity materials (greater than 10^6 Pa.s.), equation 3.26 is not really applicable because very low frequencies are required to reach a constant η'. This requires too much time, and hence is not practical. Similarly, this method of determining zero shear viscosity for very low viscosity materials (viscosity less than 1 Pa.s.) is also not desirable because of very weak torque signal making the measurements suspect. To overcome this issue, steady shear measurements of η can be made. The steady shear measurements can determine viscosities as high as 10^8 Pa.s. and as low as 10^{-2} Pa.s.

All the aforementioned discussion about oscillatory shear measurements is based on the assumption that measurements are made in the linear viscoelastic region, i.e.,

where the dynamic moduli are functions of only frequency and temperature, and the stress response of the material is independent of the applied strain. Typically polymeric materials exhibit a linear region below a certain strain amplitude. Above this amplitude, a non-linear response develops so that dynamic moduli are also functions of strain. This is why all rheological measurements were made after checking for linear viscoelastic regime at different temperatures. This was achieved by performing a strain sweep and determining the range of strains where *G'* and *G"* remained independent of applied strain.

3.5.1 Rheometry

The rheometer used for all rheological measurements was the TA instruments Advanced Rheometric Expansion System (ARES) LS2 equipped with a 2KFRTN1 force re–balance transducer. Parallel plate geometry of 7.9, 25, or 50 mm diameter was used depending on the sample. Smaller diameter plates were used for more glassy blends and larger diameter plates for less glassy ones. The temperature was controlled using a convection oven. Each sample was annealed at 100 °C and sheared at that temperature for at least 10 minutes at 10 rad/s before conducting any measurements. This allowed for any air bubbles to move to the center of the plate where it minimally affected the torque. Every time temperature was changed, the sample loading was visually checked to ensure a flat edge. Thermal expansion of the parallel plates was assumed to be 2.4 μm/K and was taken into account to adjust for the actual gap at each temperature. All steady shear viscosity data were taken at several shear rates spanning at least two decades. The

oscillatory shear measurements were carried out by maintaining a constant strain which was predetermined to be in the linear viscoelastic regime.

To check for reproducibility of results and to ensure that annealing at 100 °C for 10 minutes was enough, the experiments were repeated at 100 °C at the end of all measurements, in which temperatures ranged from 40 °C – 140 °C at 10 °C intervals. At each temperature, the sample was equilibrated for 10 minutes. In all the results reported in this work, the 100 °C measurements were reproducible, thus ensuring the samples were equilibrated and sufficiently annealed.

3.6 Differential Scanning Calorimetry

Differential Scanning Calorimetry (DSC) is a calorimetric technique that provides rich information about thermal properties of the material under consideration. In this technique, a small amount of sample is subjected to a constant heating or cooling rate and the power required to achieve that heating and cooling rate is measured. First order transitions, such as crystallization, produce a peak on the DSC thermogram (Power input vs. Temperature). The endothermal or exothermal direction of the peak provides information about the nature of the transition. The transition peak is on the endothermal side of the thermogram for melting and on the exothermal side for crystallization.

Second order transitions, such as glass transitions are represented by a shift in the plateau values of power input. If the shift in plateaus is not clearly visible, the glass transition can be more conclusively determined by plotting the temperature derivative of the power signal against temperature (dPower/dT vs. T). Analyzing the data in this

manner produces a peak at the glass transition and the peak position represents the glass transition temperature (T_g).

For the work presented in this dissertation, DSC was used to determine T_g of PEO and PVPh homopolymers as well as PEO/PVPh blends. Also determined from DSC measurements was percent crystallinity of PEO in these blends. The T_gs were measured using the TA Instruments Q1000 instrument. All samples were prepared by sealing ~8–12 mg of sample in an aluminum hermetic pan. An empty hermetic pan was used as a reference during the experiment. The samples were heated to a temperature above T_g of either blend component or above T_g of homopolymers to erase any thermal history. Samples were then quenched to a temperature below T_g of either component (in case of blends). DSC thermograms were recorded during heating of sample at a rate of 10 °C/min followed by a cooling and a subsequent heating cycle at the same ramp rate. T_g is taken as the mid–point of the transition in the second scan.

3.7 Small Angle Neutron Scattering

A small angle neutron scattering (SANS) experiment involves a well collimated beam of neutron, directed at the sample under consideration. The sample can be a melt, aqueous solution, crystals, or powder. Most of the incident beam passes through the sample without any interactions. However, a certain part of the beam is scattered and a very small part is absorbed. The scattered neutrons are detected by a 2–dimensional detector and the scattered intensity is recorded as a function of position. For the experiments conducted in this work, the scattering was considered to be *elastic scattering* i.e., energy transfer between the neutron beam and the sample was ignored.

In SANS, the neutrons scatter due to interactions with atomic nuclei. The scattering intensity is proportional to a "contrast factor" as shown in equation 3.27:

$$I(q) = \frac{K}{v} S(q) \tag{3.27}$$

where q is the magnitude of the scattering vector described by equations 3.1 and 3.2, *I(q)* is the scattered intensity, K is the contrast factor, and $S(q)$ is the static structure factor, which is discussed in detail elsewhere.[26] Therefore, to achieve a good signal from scattering, the contrast factor has to be as large as possible. The contrast originates from a difference in coherent scattering length, b. The neutron scattering contrast factor for a system consisting of components A and B is defined as:

$$K = \left(b_A - b_B\right)^2 \tag{3.28}$$

The scattering length, b, of atoms commonly found in polymers is listed in Table 3.1. The scattering length of a molecule is determined from the sum of individual scattering lengths of its constituent atoms. The repeat unit of PEO consists of one oxygen atom, two carbon atoms, and four hydrogen atoms. Therefore the scattering length of PEO would be $[1(0.58) + 2(0.665) + 4(-0.374)] \times 10^{12} = 0.414 \times 10^{12}$ cm.

Table 3.1. Neutron scattering lengths of elements commonly found in polymers[26,27]

Element	Scattering Length ($x10^{12}$ cm)
^{1}H, Hydrogen	–0.374
^{2}H, Deuterium (D)	0.667
^{12}C, Carbon	0.665
^{14}N. Nitrogen	0.936
^{16}O, Oxygen	0.580

The scattered intensity in neutron scattering is dependent on three factors: contrast between constituent elements, amplitude of concentration fluctuations in the mixture, and spatial correlations among these concentration fluctuations. The total scattered intensity arises from two types of scattering: coherent and incoherent scattering.

The incoherent scattering originates from random concentration fluctuations and it represents the baseline in SANS experiments. Coherent scattering arises from spatial correlations among concentration fluctuations that are on the length scale of the incident wave. Upon interaction with particles in the sample, the incident radiation emits scattered waves which contain phase differences. These phase differences result in constructive and destructive interference between the waves and can be related to the underlying structure.

As mentioned in the beginning of this section, SANS is a very useful technique to investigate polymer chain configurations in a melt or dilute solution. This is not possible

via conventional light scattering methods because of the inability to access large q values. The wavelengths of neutrons are much smaller than a conventional He–Ne laser source (0.1 – 2 nm vs. 632.8 nm for He–Ne) and this is what allows access to a larger q range when compared to other radiation sources. The aim is to try to access as large a q range as possible by varying the sample to detector distance in order to obtain data in the Guinier regime (small q values). The Guinier regime is reached when product of q and radius of gyration, R_g, is less than 1, i.e., $qR_g \leq 1$. This allows for determination of R_g values without making a priori assumptions about structure of the coil since no such information is required for Guinier analysis. If one cannot access the Guinier regime, i.e. if $1 \leq qR_g \leq 10$, then a structure factor specific to the shape of the molecule such as a coil, or hard sphere or rigid rod, has to be taken into account for determination of R_g.

SANS experiments were performed at the National Institute of Standards and Technology (NIST) in the Center for Neutron Research (NCNR) in Gaithersburg, MD at the 30 m NIST/Exxon/University of Minnesota beamline (NG7). A wavelength of 6 ± 0.1 Å was used as the incident radiation. The sample to detector distance was adjusted between a range of 1 m – 13 m. The samples were dilute polymer solutions, so they were sealed in quartz banjo cells which were 1–1.5 mm thick. The samples were exposed for 10–20 minutes. All scattering experiments were performed at room temperature. Data was corrected for solvent scattering, empty cell, and detector sensitivity and placed on an absolute scale using the direct beam method. The obtained 2–dimensional pattern was then azimuthally averaged to obtain a plot of intensity, I, (in units of cm^{-1}) vs. q (in units of Å).

3.9 References

[1] Lodge, T. P.; Chapman, B. *Trends in Polymer Science (Cambridge, United Kingdom)* **1997**, *5*, 122.
[2] Smith, B. A.; Samulski, E. T.; Yu, L. P.; Winnik, M. A. *Phys. Rev. Lett.* **1984**, *52*, 45.
[3] Pohl, D. W. *IBM J. Res.Devel.* **1979**, *23*, 604.
[4] Mills, P. J.; Green, P. F.; Palmstrom, C. J.; Mayer, J. W.; Kramer, E. J. *J. Poly. Sci., Poly. Phys.* **1986**, *24*, 1.
[5] Smeltzly, M. A. *Ph.D. Thesis*, University of Minnesota, **1989**.
[6] Pohl, D. W.; Schwarz, S. E.; Irniger, V. *Phys. Rev. Lett.* **1973**, *31*, 32.
[7] Eichler, H.; Salje, G.; Stahl, H. *J. Appl. Phys.* **1973**, *44*, 5383.
[8] Hervet, H.; Urbach, W.; Rondelez, F. *J. Chem. Phys.* **1978**, *68*, 2725.
[9] Kim, H.; Chang, T. ; Yu, H. *J. Chem. Phys.* **1984**, *88*, 3946
[10] Rhee, K. W.; Shibata, J.; Barish, A.; Gabriel, D. A.; Johnson, C. S. *J. Phys. Chem.* **1984**, *88*, 3944
[11] Dozier, W. D.; Kim, M. W.; Chaikin, P. M. *J. Coll. Inter. Sci.* **1987**, *115*, 545.
[12] Hervet, H.; Leger, L.; Rondelez, F. *Phys. Rev. Lett* **1979**, *42*, 1681.
[13] Siegman, A. E. *J. Opt. Soc. Am.* **1977**, *67*, 545.
[14] Wesson, J. A. *Ph.D. Thesis*, University of Wisconsin-Madison **1983**
[15] Brayton, D. B. *Appl. Opt.* **1974**, *13*, 2346
[16] Sillescu, H.; Ehlich, D. *Application of Laser in Polymer Science and Technology*, CRC: Boca Raton, Fl, **1989**
[17] Splitter, J. S.; Calvin, M. *J. Org. Chem.* **1955**, *20*, 1086.
[18] Frick, T. S. *Ph.D. Thesis*, University of Minnesota, **1989**
[19] Spiegel, D. R.; Sprinkle, M. B.; Chang, T. *J. Chem. Phys.* **1996** *104*, 4920.
[20] Hamersky, M. W. *Ph.D. Thesis*, University of Minnesota **1997**
[21] Cavicchi, K. *Ph.D. Thesis*, University of Minnesota **2003**
[22] Lin, C.; Chen, W.; Liao, C.; Su, Y.; Huang, C.; Kuo, S.; Chang, F. *Macromolecules* **2005**, *38*, 6435
[23] Ndoni, S.; Papadakis, C. M.; Bates, F. S.; Almdal, K. *Rev. Sci. Instrum.* **1995**, *66*, 1090
[24] Li, M.; Douki, K.; Goto, K.; Li, X.; Coenjarts, C.; Smilgies, D. M.; Ober, C. K.; *Chem. Mater*. **2004**, *16*, 3800
[25] Ferry, J. D. *Viscoelastic Properties of Polymers*; 3rd ed.; Wiley: New York, **1980**.
[26] Higgins, J. S.; Benoit, H. C. *Polymers and Neutron Scattering*; Clarendon Press: Oxford, 1994.
[27] Roe, R-J. *Methods of X-Ray and Neutron Scattering in Polymer Science*; Oxford University Press: New York, Oxford, **2000.**

Chapter 4. Component Terminal Dynamics in PEO/PMMA Blends

4.1 Introduction

PEO/PMMA has drawn considerable attention in recent years because of highly anomalous PEO dynamics in these blends. One study of PEO/PMMA blends reported that segmental dynamics of PEO over the entire blend composition were hardly influenced by the more glassy, and slow moving, PMMA.[1] This result indicates that PEO barely feels the presence of a much more rigid, PMMA matrix. This remarkable observation makes the dynamics of PEO/PMMA unlike that of most other blend systems studied thus far. It has been proposed that rapid relaxation of PEO regardless of its rigid surroundings is due to the fact that its ether oxygen has no side groups.[1]

Further evidence of unusual PEO/PMMA dynamics is presented by comparing terminal and segmental dynamics data. Terminal and segmental dynamics in hompolymers usually have similar temperature dependences at temperatures far above T_g.[2,3] In the vicinity of T_g, segmental dynamics usually vary more strongly with temperature than do terminal dynamics, suggesting some decoupling of the two relaxation modes.[2] Therefore, at temperatures far above T_g, a simple relationship can be assumed that correlates data obtained from direct measurements of segmental motions to that obtained from chain dynamics measurements but scaled to a per monomer basis. Such a direct correlation was tested for PEO hompolymer and it described the experimental results very well.[4] However, this relationship failed for a PEO tracer (0.3

wt.%) dissolved in a PMMA matrix, and was unable to even predict the experimental results qualitatively.[4] The direct correlation between segmental and terminal dynamics has been successful in other blends such as PI/PVE,[5] and moderately successful in PB/PVE.[6]

Another example of anomalous behavior in PEO/PMMA blends is the failure of Lodge–McLeish model,[7] which has demonstrated reasonable success in several miscible blends, but was unable to predict either segmental or terminal dynamics data.[8,9] The failure of Lodge–McLeish model to predict terminal dynamics data will be discussed in this chapter. All these phenomena together distinguish PEO/PMMA from other blend systems.

Component terminal dynamics in PEO/PMMA blends have been previously investigated,[4,10,11] but all the studies have investigated dynamics over rather limited ranges of temperature and composition. Some other studies have investigated PEO/PMMA dynamics but without resolving component dynamics. Therefore, we undertook an investigation of component terminal dynamics in PEO/PMMA over as wide a temperature and composition range as possible. Diffusion and rheological measurements were employed to study the dynamic behavior. Major results of this work have been previously published.[8]

In this chapter, we will present and discuss results of diffusion measurements of the terminal dynamics of PEO in the blends, followed by a discussion of rheology results exploring PEO and PMMA dynamics in the blends. A discussion of effects of dye labeling on tracer diffusion will also be presented. This chapter will focus more heavily on the analysis and discussion of diffusion results and less on rheology results, because

the rheology experiments, carried out by my ex–colleague, Dr. Ilan Zeroni, have been previously reported and discussed in detail.[8,12] However, results obtained from rheology experiments constitute an integral part of the study of PEO/PMMA dynamics and will be discussed to the extent necessary in understanding the dynamic phenomena.

4.2 Results

4.2.1 Materials

For diffusion experiments, low molecular weight PEO (M_n = 1.1 kg/mol, PEO–1) was purchased from Aldrich. PEO–1 was labeled with ONS–COOH (PEO–1*) as described in Chapter 3 to be used as an optical tracer in forced Rayleigh scattering (FRS) experiments. PMMA (M_n = 1.5 kg/mol, PMMA–1.5) was synthesized via anionic polymerization by Dr. Ilan Zeroni.[12] For rheology experiments, a high molecular weight sample of PEO (M_n = 898 kg/mol, PEO–900) was purchased from Polymer Laboratories. Also used in rheology experiments was the low molecular weight PEO (PEO–1). Two different PMMA samples (PMMA–1.5 and PMMA–100), synthesized via anionic polymerization by Dr. Ilan Zeroni, were used. All polymers have polydispersity indices less than 1.1. Table 4.1 summarizes different properties of polymers used in this work.

Table 4.1. Properties of Polymers Used in This Work

Sample	M_n (kg/mol)	M_w/M_n	T_g (°C)	Use
PEO–1	1.1	1.04	–67	FRS/Rheology Matrix/Tracer
PMMA–1.5	1.54	1.05	57	FRS/Rheology Matrix
PEO–900	898	1.08	–60	Rheology Tracer
PMMA–100	101	1.09	132	Rheology Tracer

Blends for diffusion experiments were prepared by dissolving PEO–1* (1% by weight), PEO–1, and PMMA–1.5, and trace amounts of the antioxidant, 2,6-di-*tert*-butyl-4-methyl-phenol (BHT) in methylene chloride. The solution was filtered using a glass syringe and a 0.45 μm filter and the solvent was removed by evaporation. The blends were dried to a constant weight in a vacuum oven at 150 ^{o}C.

Blends for rheology experiments were prepared by co–dissolving the matrix polymers (PEO–1 and PMMA–1.5) and high molecular weight tracers (PEO–900 or PMMA–100) in benzene and then removing the solvent by evaporation. The blends were dried in a vacuum oven at 40 °C for 5 days.

4.2.2 Forced Rayleigh Scattering (FRS)

Tracer diffusion experiments were carried out using FRS on different blend compositions of PEO/PMMA. The measurements were carried out over temperature ranges that differed for each blend because of differences in tracer diffusion rates. Table

4.2 lists the blend compositions and the corresponding temperature range over which diffusion experiments were carried out. FRS experiments were carried out only on blends with 50 wt% or more PMMA because PEO tracer diffusion rates were so fast for blends rich in PEO that they could not be measured reliably. Diffusion rates for blends with PMMA tracer were not studied because of the time consuming nature of FRS experiments. PMMA dynamics in the blends were studied only via rheology as will be described later in this chapter. The nomenclature used for designating blend composition is the name of blend components followed by their respective compositions. For example, PEO/PMMA 10/90 contains 10 wt.% PEO–1 and 90 wt.% PMMA–1.5. Of the 10 wt.% PEO in the blend, 1% is labeled PEO (PEO–1*) while the remaining 9% is unlabeled PEO (PEO–1). The PEO–1* composition is constant throughout the blends.

Table 4.2. PEO/PMMA blend compositions and corresponding temperature ranges over which diffusion measurements were carried out.

PEO/PMMA Blends	Diffusion Measurement Temperature Range (°C)
01/99	90 – 170
10/90	50 – 120
20/80	40 – 90
50/50	40 – 90

Scattered intensity (I) was measured as a function of time for several different grating spacings (d) at each temperature. Diffusion measurements were mostly made at 10 °C intervals. The FRS intensity decay profiles for most samples exhibited only one relaxation mode and were fitted with equation 4.1:

$$I(t) = \left[A \exp\left\{ -\left(\frac{t}{\tau_1} \right)^{\beta} \right\} \right]^2 + I_{bl} \tag{4.1}$$

where A and β are fitting parameters, τ_1 is the experimental relaxation time, and I_{bl} is the baseline scattering intensity in the absence of a grating. The extracted β values were in the range of 0.55–1.0, indicating that the experimental decays were broader than a single exponential decay. This broadening can be attributed primarily to experimental noise near the base line and sample polydispersity.[4] To account for the decay broadening, the actual mean relaxation time, $<\tau_1>$ was determined using equation 4.2:[13]

$$<\tau_1> = \frac{\tau_1}{\beta} \Gamma\left(\frac{1}{\beta} \right) \tag{4.2}$$

where $\Gamma(x)$ is the gamma function. Once $<\tau_1>$ was determined from FRS decay curves, it was used to calculate diffusion coefficient of PEO–1* using the following relationship:

$$<\tau_1> = \frac{d^2}{4\pi^2 D} \tag{4.3}$$

FRS decays at low temperatures for the PEO/PMMA 01/99 blend possibly exhibited two modes in the scattering data. These scattering profiles were fitted with the following equation:

$$I(t) = \left[A_1 \exp\left\{ -\left(\frac{t}{\tau_1} \right)^{\beta} \right\} + A_2 \exp\left\{ -\frac{t}{\tau_2} \right\} \right]^2 + I_{bl} \qquad (4.4)$$

where A_1, A_2, τ_1, τ_2, and β are fitting parameters. Equation 4.4 fit the data better than equation 4.1. The two decay modes consisted of a faster mode (parameters A_2 and τ_2) which has previously been attributed to the dye photochemistry and/or thermal relaxation in the sample.[14,15] The mean relaxation, $<\tau_1>$ of the slower diffusive mode is determined by equation 4.3. Representative FRS intensity profiles are shown for selected temperatures for each of the four blends in Figures 4.1 – 4.4. Each figure shows the FRS intensity profiles for different grating spacings. The intensity profiles were arbitrarily shifted vertically so they could be shown on the same axes.

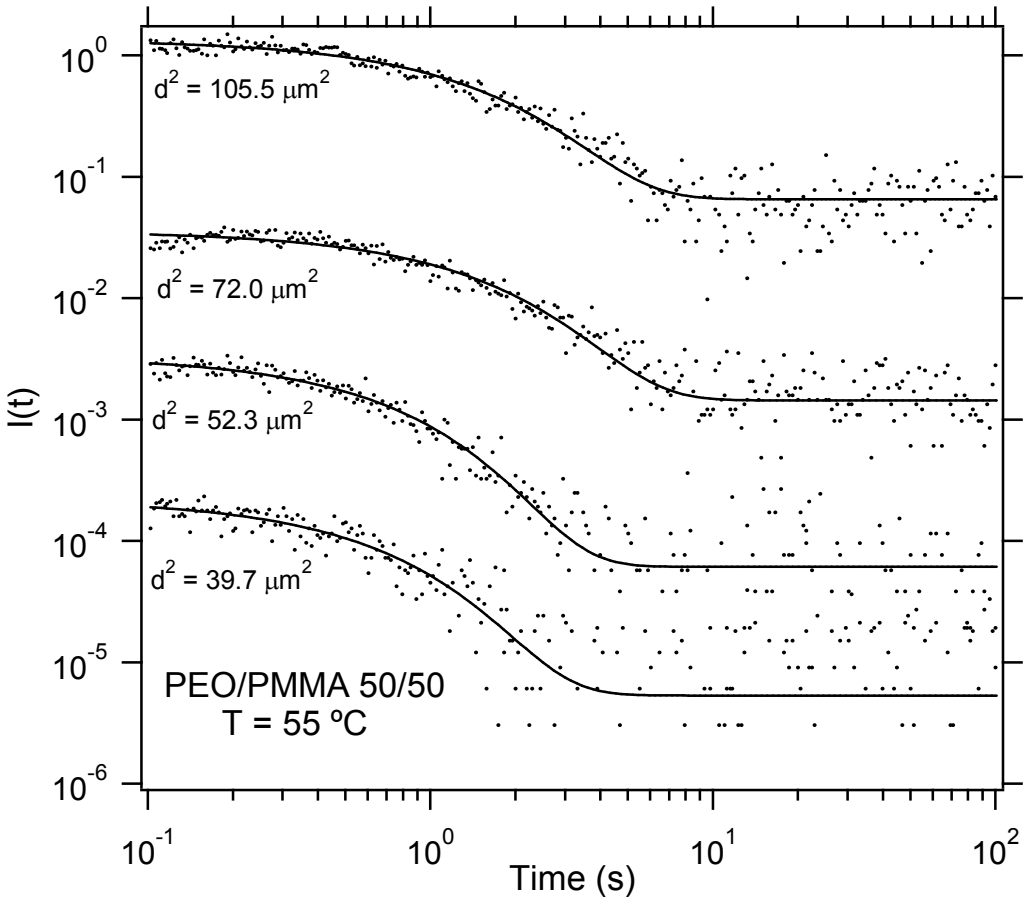

Figure 4.1. FRS intensity profiles for PEO/PMMA 50/50 blend at 55 °C for different grating spacing. Dots are experimental data while solid line is the best fit to equation 4.1. The intensity profiles have been vertically shifted using an arbitrary shift factor.

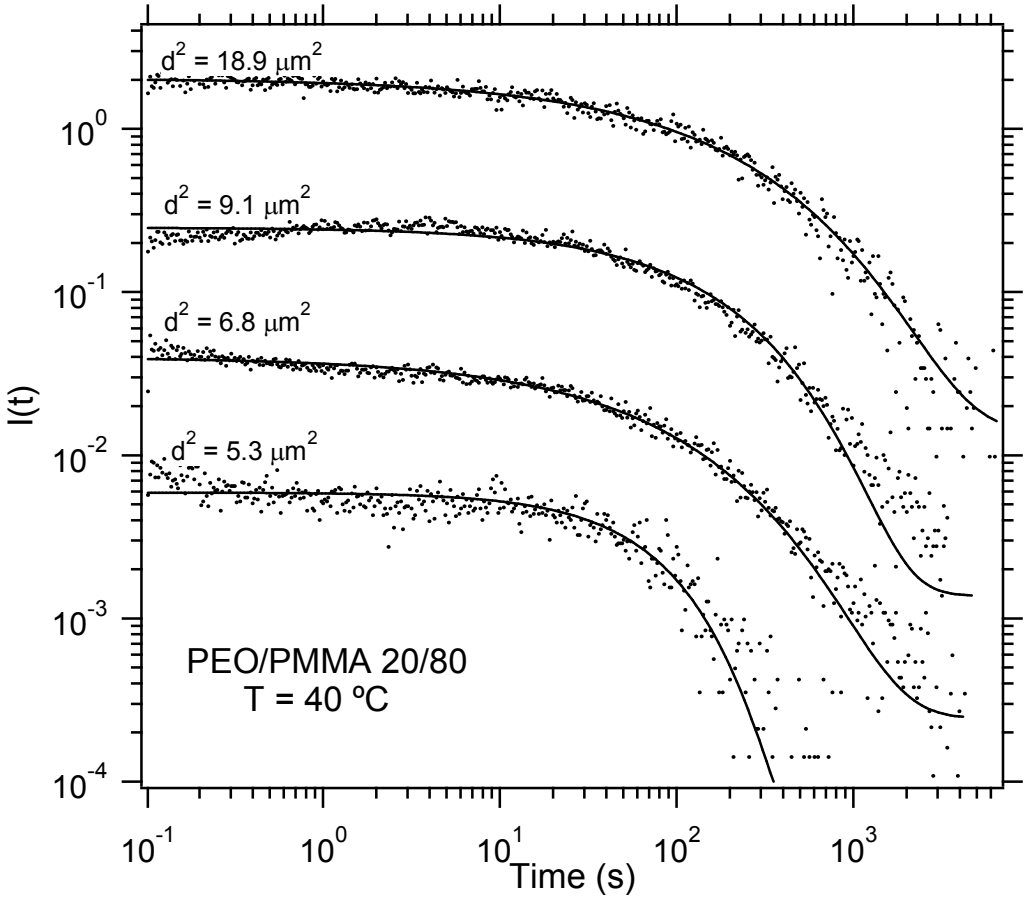

Figure 4.2. FRS intensity profiles for PEO/PMMA 20/80 blend at 40 °C for different grating spacing. Dots are experimental data while solid line is the best fit to equation 4.1. The intensity profiles have been vertically shifted using an arbitrary shift factor.

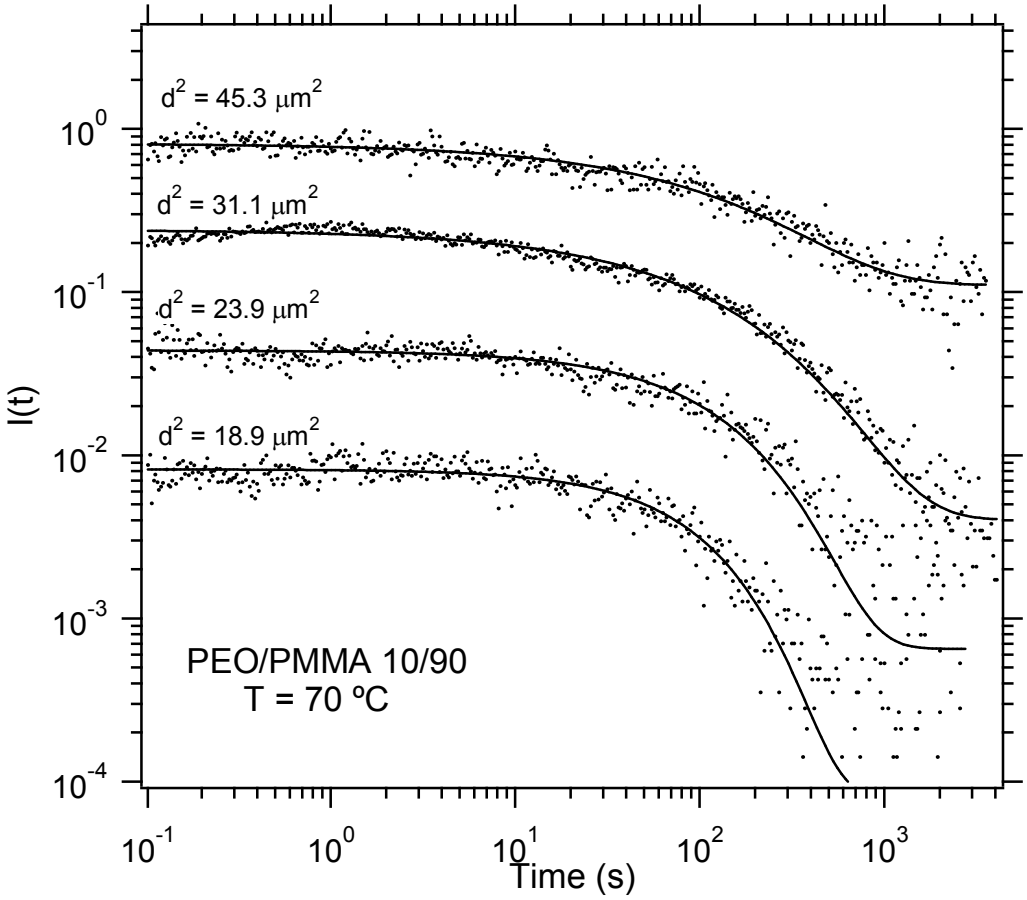

Figure 4.3. FRS intensity profiles for PEO/PMMA 10/90 blend at 70 °C for different grating spacing. Dots are experimental data while solid line is the best fit to equation 4.1. The intensity profiles have been vertically shifted using an arbitrary shift factor.

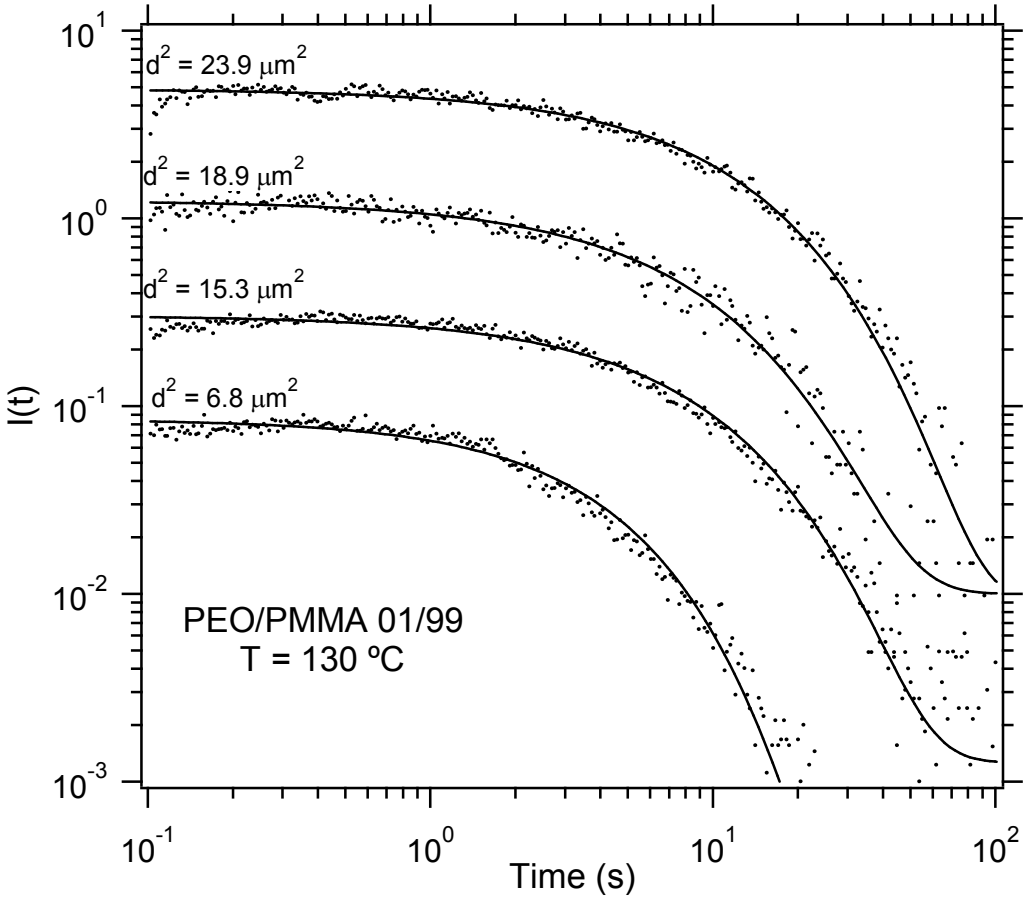

Figure 4.4. FRS intensity profiles for PEO/PMMA 01/99 blend at 70 °C for different grating spacing. All of the PEO in this blend is PEO–1*. Dots are experimental data while solid line is the best fit to equation 4.1. The intensity profiles have been vertically shifted using an arbitrary shift factor.

Figures 4.1 – 4.4 exhibit the effects of varying grating spacing. As the grating spacing, d, increases, so does the longest relaxation time as seen by shifting of curvature to longer times.

For each blend, $<\tau_1>$ was plotted as a function of d^2 for different temperatures. As expected, $<\tau_1>$ varied linearly with d^2 confirming erasure of optical grating due to diffusion only. Also plotted was $1/<\tau_1>$ vs. $1/d^2$ and the slope of the best fit line in each plot was used to determine the diffusion coefficient, D, as seen in equation 4.3. The reported diffusion coefficient is the average of the two diffusion coefficients determined from $<\tau_1>$ vs. d^2 and $1/<\tau_1>$ vs. $1/d^2$ plots. Representative plots of $<\tau_1>$ vs. d^2 and $1/<\tau_1>$ vs. $1/d^2$ are shown in Figure 4.5 for PEO/PMMA 10/90 blend at 100 °C. Table 4.3 summarizes fit parameters and diffusion coefficients for all the blends.

(a)

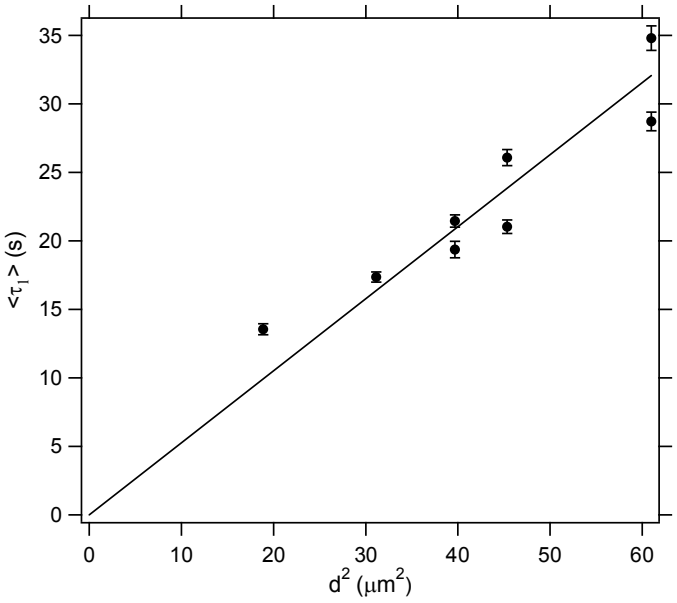

(b)

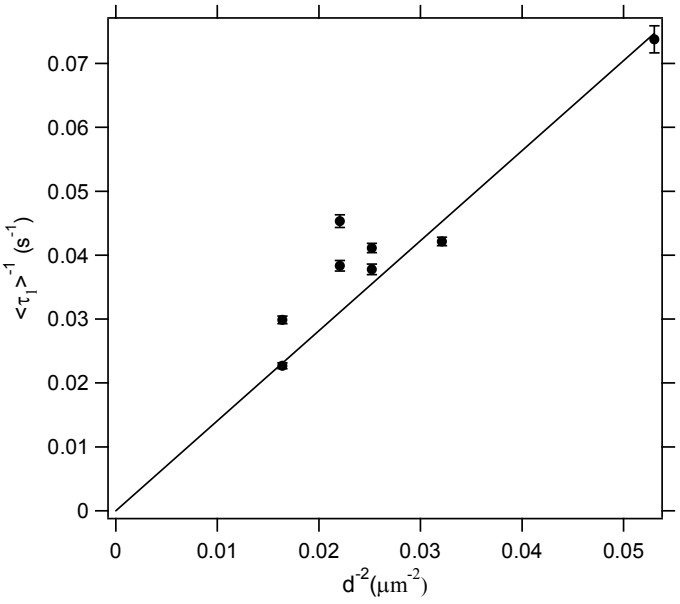

Figure 4.5. Plots of (a) $<\tau_1>$ vs. d^2 and (b) $1/<\tau_1>$ vs. $1/d^2$ for PEO/PMMA 10/90 at 100 °C.

Table 4.3. FRS Parameters and Diffusion Coefficients for PEO/PMMA Blends

Blend (PEO/PMMA)	T (°C)	D (cm^2/s)	d^2 (μm)^2	β	$<\tau_1>$ (s)
01/99	90	1.8×10^{-12}	5	1	1732
			7	1	2643
			11	1	8434
			15	1	7594
	110	4.7×10^{-11}	7	1	124
			11	0.74	179
			15	1	289
			56	1	885
	130	7.5×10^{-10}	7	1	7.6
			15	0.9	18.0
			19	0.9	17.4
			24	0.9	24.4
	150	5.0×10^{-9}	7	1	1.1
			15	1	2.7
			19	1	3.0
			24	0.9	3.5
	170	2.4×10^{-8}	15	1	0.4
			19	1	0.7
			24	1	0.8
10/90	60	1.0×10^{-11}	24	1	1625
			31	0.6	2615
			45	0.7	3899
	70	6.0×10^{-11}	19	0.98	209
			24	0.85	308
			31	0.6	534
			45	0.6	627
	80	1.5×10^{-10}	19	1	77
			24	0.8	170
			31	0.7	154
			45	0.6	270
	90	4.4×10^{-10}	19	1	32
			24	0.9	48
			31	0.65	55
			45	0.65	89
			45	0.61	79
	100	1.2×10^{-9}	19	1	14
			24	0.9	26
			31	0.65	24

Blend (PEO/PMMA)	T (°C)	D (cm^2/s)	d^2 (μm)^2	β	$<\tau_1>$ (s)
10/90 contd.			45	0.91	22
			45	1	26
			61	0.77	33
			61	0.7	44
	110	4.1×10^{-9}	19	0.6	1.9
			24	1	7.5
			31	0.7	9.1
			45	1	11.9
	120	6.3×10^{-9}	24	0.65	3.3
			31	0.8	3.3
			45	0.91	4.5
			40	0.86	4.9
			40	0.9	4.7
			61	1	8.9
			61	1	9.0
20/80	40	1.7×10^{-11}	5	1	160
			7	0.6	380
			9	0.75	485
			19	0.5	1145
	50	6.7×10^{-11}	5	0.7	49
			7	0.7	119
			9	0.9	121
			19	0.67	215
	60	2.2×10^{-10}	5	1	19
			7	1	27
			9	0.75	34
			19	0.87	64
	70	5.4×10^{-10}	5	1	6.6
			7	0.74	12.3
			9	0.75	12.5
			19	0.75	29.4
	80	1.4×10^{-9}	5	0.55	3.8
			7	1	4.5
			9	0.95	4.3
			19	0.91	9.2
	90	2.8×10^{-9}	5	0.7	1.1
			7	0.7	3.0
			9	0.95	2.5
			19	0.9	6.0

Blend (PEO/PMMA)	T (°C)	D (cm^2/s)	d^2 (μm)^2	β	$<\tau_1>$ (s)
50/50	40	7.1×10^{-9}	31	1	3.6
			44	1	6.0
			70	1	7.4
			106	0.5	10.1
	50	1.4×10^{-8}	31	1	1.9
			42	1	2.1
			61	1	3.4
			86	1	5.2
	55	2.5×10^{-8}	40	1	1.3
			52	1	1.4
			72	1	3.0
			106	1	2.8
	60	2.8×10^{-8}	15	1	0.45
			19	0.9	0.46
			31	1	1.1
			56	1	1.8
			86	0.77	2.2
	70	4.6×10^{-8}	31	1	0.5
			42	1	0.7
			56	1	1.3
			86	0.85	1.4
	80	6.6×10^{-8}	56	0.9	0.6
			66	0.85	0.9
			79	1	1.0
			106	1	1.2
			132	1	1.7
	90	1.1×10^{-7}	56	0.68	0.59
			66	0.89	0.58
			79	1	0.54
			95	0.94	0.68
			118	0.88	0.86

4.2.3 Rheology

In the past, rheological measurements have been carried out to extract component terminal dynamics in miscible blends. For such measurements, it is of interest to choose components and molecular weights so that their contribution to some rheological material function is measurable and relatively easy to extract. One such feature is a peak in η'' that indicates the longest relaxation time of one component. However, it is usually not trivial to resolve the contribution of both components to η'' or G'. One way of doing that is to prepare blends in which a high molecular weigh tracer is dispersed in a low molecular weight matrix, as previously shown for PEO tracers in PMMA.[4]

The rheology results will not be discussed in detail as they have been previously described elsewhere.[8,12] Only important, pertinent results will be presented here. Also, a detailed explanation of analysis of rheology data will be presented in Chapter 5.

The blends contained 1 wt.% high molecular weight tracer (either PEO–900 or PMMA–100) in a low molecular weight matrix of PEO–1 and PMMA–1.5. Dynamic frequency sweeps were carried out in the linear viscoelastic regime and the longest relaxation times were determined via low frequency peaks in η''. These longest relaxation times were used to extract ζ, as will be described in Section 4.2.4. Also, steady rate sweeps were performed to determine the steady shear viscosity, η, of PEO–1 and PMMA–1.5 homopolymers.

4.2.4 Extraction of ζ

The monomeric friction factor can be determined from experimental measurements of D, τ_1 and η by assuming a particular polymer dynamics model. PEO–1

and PMMA–1.5 samples used in FRS as well as rheology experiments are well below their entanglement molecular weights ($M_{e,PEO}$ = 1,500 g/mol, $M_{e,PMMA}$ = 13,000 g/mol).[16]. The PMMA–100 and PEO–900 samples used in rheology as tracers, even though well above their entanglement molecular weight, are present in such dilute concentrations in the blend that they do not entangle with themselves. Thus, the dynamics of all samples used in FRS and rheology experiments are assumed to follow the Rouse model. The Rouse model relationships have been described in Chapter 2, but for convenience are reproduced below.

Equation 4.5 is used to extract the PEO–1* ζ from the diffusion coefficient:[17,18]

$$D = \frac{k_B T}{N\zeta} \tag{4.5}$$

The ζ for PEO–900 and PMMA–100 in tracer blends was determined from τ_1 using equation 4.6:[17]

$$\tau_1 = \frac{\zeta b^2}{3\pi^2 k_B T}\left(\frac{M}{M_o}\right)^2 \tag{4.6}$$

ζ for PEO–1 and PMMA–1.5 homopolymers was determined from steady shear viscosity data using equation 4.7:

$$\eta = \frac{\rho N_A b^2}{36 M_o} N\zeta \tag{4.7}$$

The resulting monomeric friction factors for PEO are plotted as a function of temperature in Figure 4.6 while those for PMMA are plotted in Figure 4.7.

4.3 Discussion

4.3.1 Composition and Temperature Dependence of Monomeric Friction Factors

From Figures 4.6 and 4.7, it is seen that both PEO and PMMA monomeric friction factors increase monotonically upon addition of the slower component, PMMA, and upon reduction in temperature. The effect of PEO on the PMMA friction factor is significant as seen by the considerable drop in PMMA friction factor upon addition of a small amount of PEO. However, PEO is not as strongly affected by the presence of PMMA, at least for compositions less than 80% PMMA. For 90% PMMA or greater, the PEO monomeric friction factor increases significantly with composition. ζ_{PMMA} in pure PEO assumes the value of host matrix, ζ_{PEO}, i.e. the terminal dynamics of PMMA in PEO are dictated by the host matrix. On the other hand, ζ_{PEO} in pure PMMA is much smaller than that of the host matrix, i.e., the terminal dynamics of PEO are not dictated by the host matrix. This implies that PEO can relax via conformation changes that do not depend on the surrounding matrix. Across the entire composition range, the PEO friction factor varies by 5–6 orders of magnitude. This strong composition dependence is in contrast to the very weak composition dependence of PEO segmental dynamics.[1] Overall, the composition and temperature dependence of friction factors is reasonable: all friction factors *increase* with decreasing temperature at a fixed composition and with increase in high T_g, slower component at a fixed temperature.

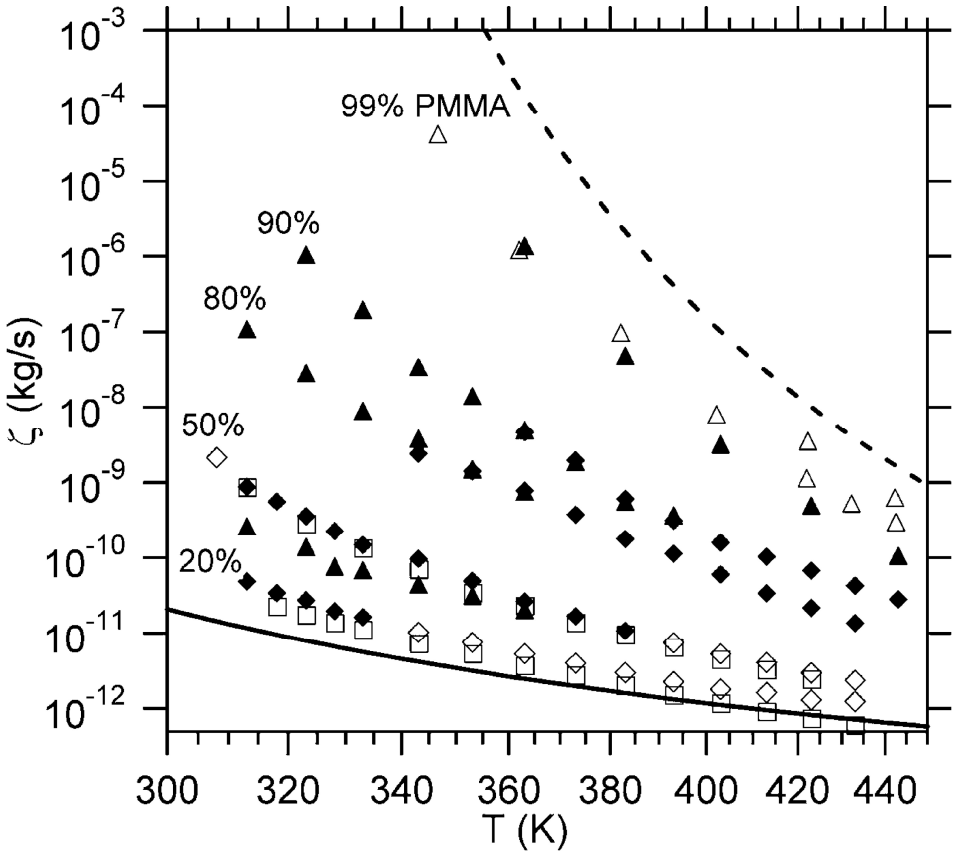

Figure 4.6. Monomeric friction factors of PEO in PEO/PMMA blends. Blend composition is indicated by wt.% PMMA in the blend. Solid and dashed lines are WLF fits to PEO and PMMA homopolymer friction factors, respectively. FRS data is represented by (▲). Literature FRS data[4] (Δ) is also shown for comparison purposes and is shifted horizontally by 17.5 K to account for T_g differences. All other symbols are rheology data. Different symbols are used to designate different methods of extraction of ζ that are not discussed here. Reproduced from reference 8.

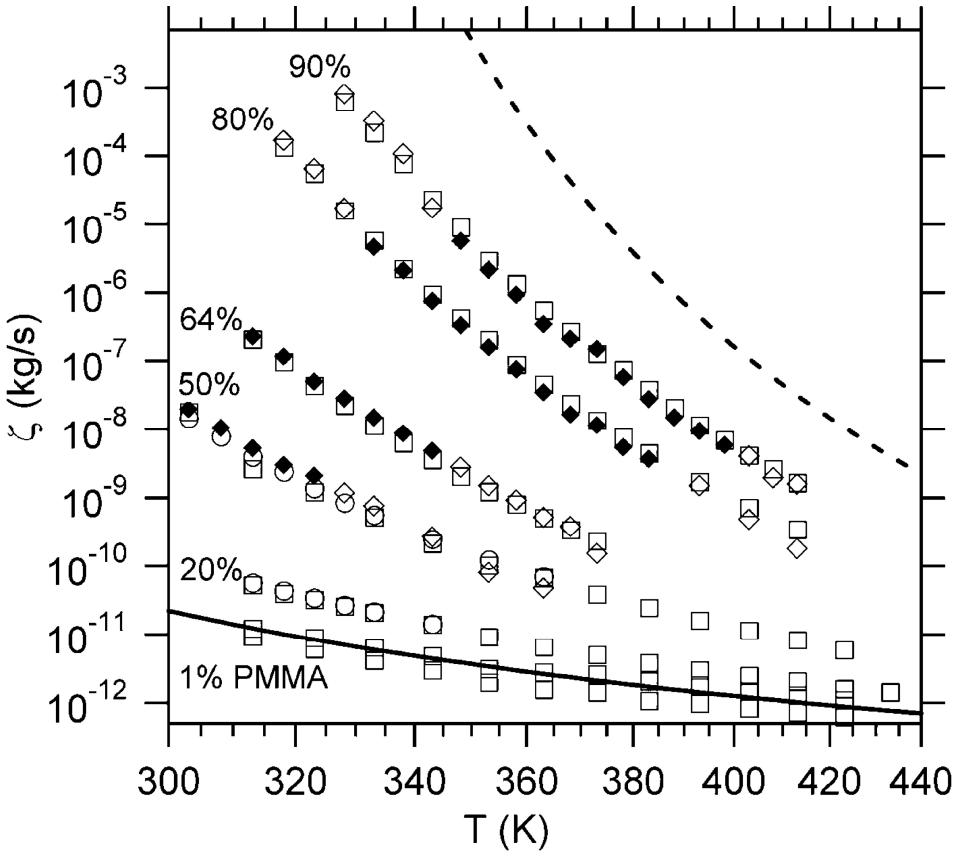

Figure 4.7. Monomeric friction factors of PMMA in PEO/PMMA blends. Blend composition is indicated by wt.% PMMA in the blend. Solid and dashed lines are WLF fits to PEO and PMMA homopolymer friction factors, respectively. All the data are obtained from rheology experiments. PEO homopolymer data are added for comparison purposes. Reproduced from reference 8.

4.3.2 Comparison of FRS and Rheology Results

Figure 4.6 shows monomeric friction factors obtained from rheology as well as FRS experiments. The 80% and 90% PMMA blends show very good agreement between data obtained from both methods. For the 50% blend, the data is not in such good agreement. FRS data results in a lower friction factor than that determined by rheology and this discrepancy increases as temperature is lowered.

To understand the reasons behind this discrepancy, FRS intensity profiles were re-examined for 50% PMMA blends and it was discovered that PEO–1* relaxes quite rapidly in this blend, and the short time scale plateau in FRS decays is much smaller than that in other blends, or even non–existent in some cases. Fitting equation 4.1 to these FRS decays could have resulted in errors. This could be the reason behind the lack of agreement in FRS and rheology data. One way to address this issue is to use larger grating spacing to allow for longer diffusion times, and hence, achieving better fits to experimental decays.

The agreement between FRS and rheology results for 80% and 90% PMMA blends is remarkable given the fact that both techniques use very different molecular tracers for probing terminal dynamics. A 1 kg/mol PEO sample is used as tracer in FRS while a 900 kg/mol PEO sample is used as tracer in rheology. Despite such a large difference in tracer molecular weights, the good agreement between FRS and rheology data, each with its own unique sets of assumptions, lends support to our measurement techniques and validates the analysis techniques used for either experimental method.

Since both experimental methods are fundamentally very different from each other, choosing one over the other requires knowledge of advantages and disadvantages

of each technique. Rheology and FRS allow for determination of ζ at temperatures or compositions that are unattainable to the same extent by both techniques. Rheology can allow for investigations at temperatures lower than room temperature which our current FRS setup cannot. This is because the rheomoeter sample holder can be cooled by liquid nitrogen. One advantage that FRS has over rheology is its ability to carry out measurements on trace amounts of one component in the blend even if its molecular weight is very low. This is why the data for 99% PMMA blend is only obtained by FRS and could not be determined by rheology. In that blend, the PEO tracer in PMMA did not significantly contribute to any rheological function since the blend dynamics are dominated by the slow PMMA. Since FRS can probe dynamics of PEO exclusively, regardless of the contribution from PMMA, it yields valuable data. However, since the matrix is almost completely PMMA, the PEO–1* dynamics are very slow and it takes hours, even days to obtain a single data point. This is true especially for very large grating spacing. Hence, the experiment has its limitations because it is time consuming.

4.3.3 Analysis of Assumptions for Diffusion Measurements

The main assumption employed during analysis of diffusion results is that all FRS decays are from PEO–1* diffusion. In any FRS experiment, there is always the possibility that the measured decay is a result of some species or phenomena not intended. The FRS decays for PEO–1* diffusion are representative of normal FRS intensity profiles. The grating spacing, and hence angle dependent, diffusive mode is present where the experimental signal decays to the baseline scattering intensity. After the scattering intensity baseline has been reached, the FRS grating has completely

relaxed, eliminating any possibility of the presence of slower moving labeled species in our samples. Theoretically, there exists the possibility of a sub–population of labeled species that diffuse on time scales shorter than the extracted grating relaxation times, but this is not the case. The time scale for the grating formation process is 100 ms. So diffusion of any species on time scales greater than that will be easily detected. However there is no evidence of it. All these observations coupled with the fact that grating relaxation time varies linearly with grating spacing over a large range, gives us confidence that the only diffusing species in our samples are the labeled polymer chains, and that erasure of optical grating occurs because of diffusion and not some other process.

A shortcoming of the FRS technique is the possible effect of the photochromic dye on diffusion of labeled polymer chains. This effect can be significant if the labeled polymer is of low molecular weight, making its size comparable to that of the dye. This is certainly the case for PEO–1. If the free dye molecule has a diffusion coefficient similar to or less than that of unlabeled PEO–1 chains, the friction of the dye molecule could potentially have a strong influence on the diffusion of labeled PEO–1 (PEO–1*) chains. The results of a study of ONS–COOH diffusion in a PMMA matrix[19] were compared to diffusion results of labeled PEO in a similar molecular weight PMMA matrix. It was found that tracer diffusion coefficient of ONS–COOH in PMMA is roughly one order of magnitude greater than that of labeled PEO (PEO–1*) over the entire temperature range investigated. Thus, it can be concluded that ONS–COOH does not have any significant impact on diffusion of labeled PEO chains.

In addition to the effects of photochromc dye on chain diffusion, other possibilities have to be considered as well. It is possible that some of PEO–1* chemically couples to PMMA–1.5 because of photochemical bleaching of the dye. If indeed coupling does happen, the slower diffusion of coupled species is surely going to affect diffusion results. However, this scenario does not take place in the case of PEO–1* diffusion because there is evidence of only one diffusive mode in FRS decays, which confirms presence of only one diffusing species. If coupling had taken place, there would be multiple diffusive modes present in the decays. Thus, absence of multiple decays is strong evidence that no coupling takes place. Also, reproducibility of experimental decays argue against any coupling reactions.

4.3.4 Analysis of Assumptions for Rheology Measurements

For extraction of ζ from rheology measurements, the terminal dynamics of PEO–900 or PMMA–100 were assumed to follow the Rouse model. This assumption is not necessarily obvious because after all the tracers used in these blends are of very high molecular weight. It could be that reptation model may have been a better choice to address entanglements in tracers, or that Zimm model may have been a good choice for interpreting rheology data because of presence of large molecular weight tracers in low molecular weight matrices making the blends analogous to polymer solutions. However, the following analysis should confirm use of Rouse model as the appropriate choice.

The large molecular weight tracers, even though well entangled in their homopolymer melts, are present in dilute concentrations in the blend. The tube diameter of a PEO melt is calculated to be approximately 40 Å using eq. 2.13. If we consider the

PEO tracer blend to be a theta solution, the tube diameter of 1% PEO–900 in the blend is calculated to be approximately 860 Å, using the scaling relationship proposed by Colby and Rubinstein.[20] The end-to-end distance of PEO–900 tracer is determined to be approximately 715 Å using the PEO statistical segment length, b_{PEO} = 5.6 Å.[21] Similarly, the tube diameter of a PMMA melt is calculated to be approximately 65 Å. Approximating the PMMA tracer blend as a theta solution, the tube diameter of 1% PMMA–100 in the blend is determined to be approximately 1,300 Å using the Colby-Rubinstein scaling relationship.[20] The end-to-end distance of PMMA–100 tracer is found to be approximately 200 Å (using b_{PMMA} = 6.5 Å).[21]

The end-to-end distances of PMMA and PEO tracers are smaller than the predicted tube diameter. For entanglements to be present in these blends, the end-to-end distances will have to be several times the tube diameter. Thus, possibility of entanglement effects can be safely ruled out.

Using the Zimm model instead of Rouse model would result in different values of friction factor. Predictions of Zimm and Rouse models are identical in terms of the form of the equation (not for molecular weight dependence though), but differ in relative values of relaxation times. The Rouse and Zimm predictions for temperature dependence of tracer diffusion coefficients are the same, thus eliminating any concerns about different conclusions as a result of using one model vs. the other. Another reason why Zimm model does not need to be considered is because there was good agreement of FRS and rheology results. In FRS, a 1 kg/mol PEO tracer was used, while in rheology, a 900 kg/mol PEO tracer was used. Since rheology results agreed well with those of FRS (for

which Rouse model is the only practical choice), we can conclude that Rouse model is an appropriate choice for analysis of rheology results.

4.3.5 Effects of PEO Hydroxyl Groups

The PEO–1 sample used as the matrix component in FRS as well as rheology is an α,ω–hydroxy–terminated polymer, raising the possibility of presence of hydrogen bonds. The hydroxyl end groups could act as hydrogen bond donors and interact with either PEO ether oxygens or PMMA carbonyl oxygens. The presence of hydrogen bonds could affect the relaxation of the tracer as well as the matrix.

In a previous study,[22] the enthalpy of mixing of low molecular weight analogs of PEO and PMMA was shown to be affected by hydroxyl end groups. In this study, tetraethylene glycol with two, one, and no hydroxyl end groups were mixed with methylisobutyrate (MIB). It was found that increasing number of hydroxyl end groups resulted in the interaction parameter becoming more positive. This effect was attributed to favorable self association among the hydroxyl end groups vs. cross–interaction with MIB. Hence, there exists the possibility of hydroxyl end groups affecting blend dynamics.

We investigated the effects of hydroxyl end groups by preparing a 20% PMMA blend with matrix PEO with no hydroxyl end groups, i.e., PEO–dimethylether (PEO–DME–1). Monomeric friction factors of PEO–DME/PMMA 20/80 blends were obtained at various temperatures and compared with those for α,ω–hydroxy–terminated PEO/PMMA previously studied, the results of which were presented in Figure 4.6. The

comparison of friction factors for PEO/PMMA and PEO–DME/PMMA 80/20 blends is presented in Figure 4.8.

It can be seen that the temperature dependence of ζ_{PEO} is exactly the same for both blends. However, the blend with PEO–DME exhibits friction factors that are consistently 20 – 30% less than that of PEO. Even though this seems like a significant difference, but it is not, considering the fact that ζ varies over two orders of magnitude just for this blend and if we take into account other blends, the variation is over 6–7 orders of magnitude. Thus, regardless of the difference in ζ values for PEO and PEO–DME, the impact of hydroxyl end groups on temperature and composition dependence is minimal and any conclusions drawn remain unchanged. The same can be said regarding the rheology results; it was found that PEO and PEO–DME monomeric friction factors obtained from rheology data almost overlapped with each other.[8] In addition, ζ values of 1% PMMA tracer in PEO DME overlap with those of the host matrix, just as ζ of 1% PMMA tracer in PEO do. Hence, it can be safely concluded that hydroxyl end groups do not significantly affect the dynamics of either component in the blend.

4.3.6 Lodge–McLeish Model Predictions

The Lodge–McLeish model (LMM)[7] is a self–concentration model proposed to determine the effect of chain connectivity on local composition. LMM provides an expression for self–concentration, ϕ_{self}, that sometimes yields values that do not lead to very good fits to experimental data. Therefore, ϕ_{self} has been more commonly used as a fitting parameter, and this approach has shown considerable success.[9]

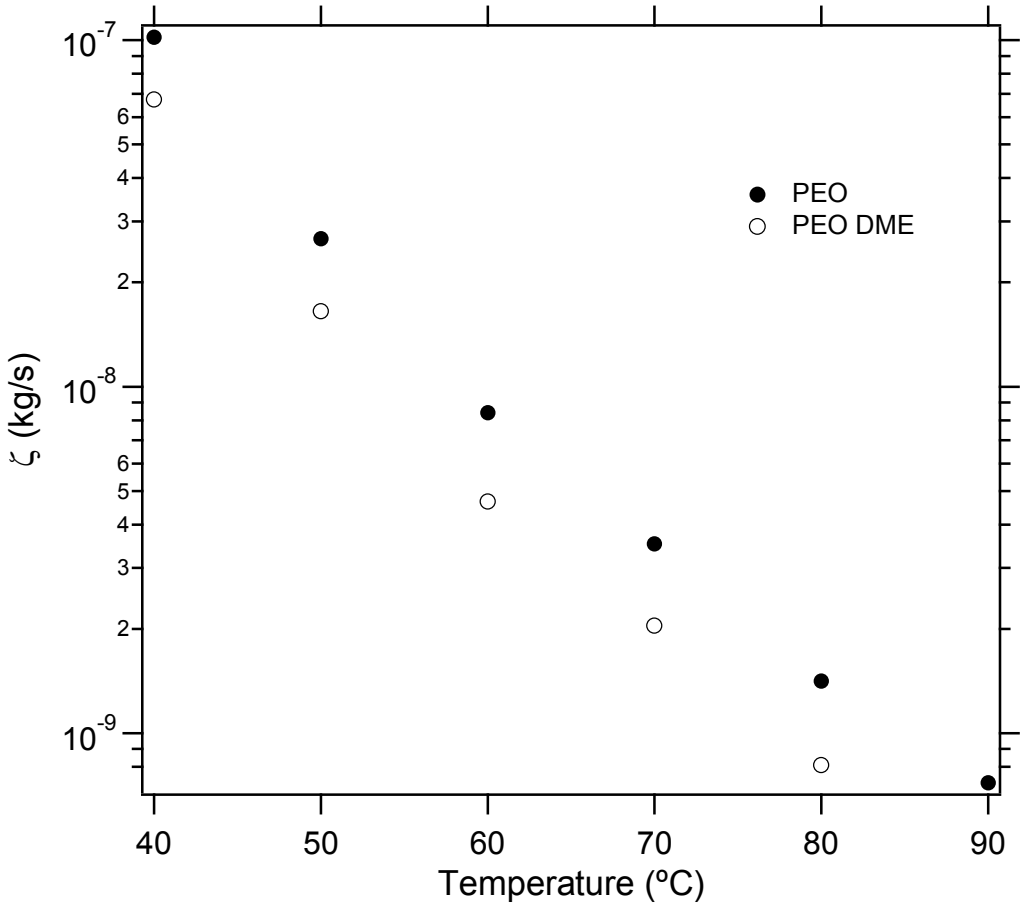

Figure 4.8. Comparison of monomeric friction factors for 20/80 blends of PEO/PMMA and PEO-DME/PMMA.

The LMM has been found to describe segmental dynamics of PEO in PEO/PMMA blends but with ϕ_{self} as a fitting parameter rather than being determined by the expression provided by LMM (equation 2.38). The ϕ_{self} value used for data fitting was larger than that anticipated from LMM expression.[9] LMM was also able to describe PEO segmental data from another study, but was only successful for PEO–rich blends and for very small values of ϕ_{self}. However, LMM hasn't shown much success in fitting terminal dynamics data in PEO/PMMA blends. The results of PEO/PMMA terminal dynamics study by Zawada *et al.* were fitted to LMM by He and co–workers[9] and the model was unable to describe the experimental results. Based on this finding, we would expect LMM to be unable to describe terminal dynamics data for our PEO/PMMA blends.

To implement this model, PEO and PMMA homopolymer viscosity data were fitted with the WLF equation (eq. 2.40). The obtained WLF constants, C_1^g and C_2^g for PEO–1 are 8.2 and 52.5 respectively, while those for PMMA–1.5 are 9.4 and 48.7 respectively. The reference temperatures were homopolymer T_gs ($T_{g,PEO-1}$ = –63 °C, $T_{g,PMMA-1.5}$ = 57 °C). The effective glass transition temperature, $T_{g,eff}$ of each component is then calculated using the Fox equation:[23]

$$\frac{1}{T_{g,eff,a}} = \frac{\phi_{eff,a}}{T_{g,a}} + \frac{1-\phi_{eff,a}}{T_{g,b}} \tag{4.8}$$

where $T_{g,a}$ and $T_{g,b}$ are glass transition temperatures of components *a* and *b*, respectively. From $T_{g,eff}$, the component ζ is calculated with WLF equation[18] that is reproduced below:

$$\log\left[\frac{\zeta(\phi)}{\zeta_g}\right] = -\frac{C_1^g\left(T - T_{g,eff}(\phi)\right)}{C_2^g + T - T_{g,eff}(\phi)} \tag{4.9}$$

where C_1^g, C_2^g, and ζ_g are the homopolymer WLF parameters. The ζ_g values for PEO–1 and PMMA–1.5 are 3.24 x 10^{-6} and 2.88 x 10^{-5} kg/s respectively.

The friction factor values when fitted to LMM using the literature values $\phi_{self,\ PEO}$ = 0.57[9] and $\phi_{self,\ PMMA}$ = 0.25[7] produced extremely poor fits. Several different values of ϕ_{self} were tried but the fits remained poor. The model fits improved as ϕ_{self} decreased and the best results were obtained for ϕ_{self} approaching zero. These fits are shown in Figure 4.9. The results indicate the PMMA dynamics are accelerated by addition of PEO more than expected based on the Fox relation. Similarly, PEO is slowed down by PMMA more than suggested by the Fox relation.

The LMM fits for PMMA tracer blends, even though not very good in describing the composition dependence of ζ_{PMMA}, describe the temperature dependence fairly well. However, for PEO tracer blends, the LMM fits completely fail to describe the composition as well as the temperature dependence of ζ_{PEO}, especially for PMMA–rich blends. For 20% and 50% PMMA blends, these fits are better but still not satisfactory. The quality of fits becoming worse for PEO tracer blends as PMMA content increases is consistent with our earlier hypothesis that PEO relaxes via conformation changes that do not depend on the surrounding matrix. The composition independent relaxation modes available to PEO become more pronounced as the matrix becomes stiffer.

(a)

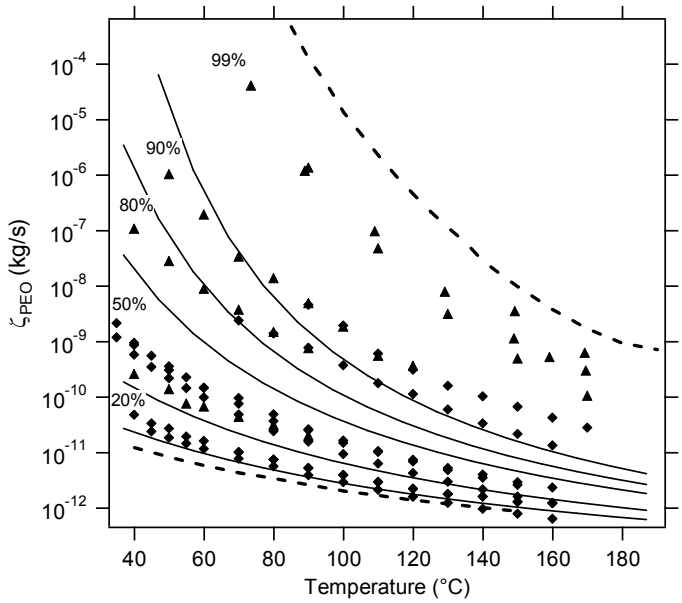

(b)

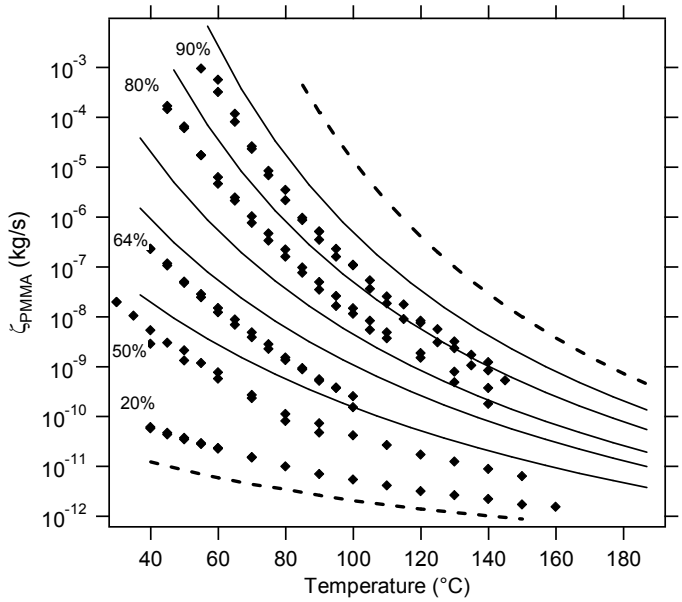

Figure 4.9. Lodge–McLeish predictions (solid lines) for (a) PEO and (b) PMMA with $\phi_{self,\ PEO} = \phi_{self,\ PMMA} = 0$. Thick dashed lines are homopolymer WLF fits and percentages indicate PMMA content in the blends. (▲) FRS data, and (♦) rheology data.

4.4 Summary

Terminal dynamics of PEO and PMMA were studied in PEO/PMMA blends using FRS and rheology. Monomeric friction factors were obtained for each component in the blend over a wide temperature and composition range. PEO friction factors were determined from FRS and rheology measurements while those of PMMA were only determined from rheology data. The FRS and rheology results agree remarkably well, lending support to the overall validity of the analysis. The PEO terminal dynamics exhibit a strong composition dependence, which is in contrast to the weak composition dependence of PEO segmental dynamics. Effects of PEO hydroxyl end groups on component chain dynamics were analyzed and found to be negligible. The influence of dye on polymer chain diffusion was also examined and it was concluded that the dye does not significantly affect chain diffusion. The Lodge–McLeish model was compared to the experimental data and it failed to predict component dynamics in PEO/PMMA blends even qualitatively.

4.5 References

[1] Lutz, T. R.; He, Y.; Ediger, M. D.; Cao, H.; Lin, G.; Jones, A. A. *Macromolecules* **2003**, *36*, 1724.
[2] Roland, C. M.; Ngai, K. L.; Santangelo, P. G.; Qiu, X. H.; Ediger, M. D.; Plazek, D. J. *Macromolecules* **2001**, *34*, 6159.
[3] Adachi, K.; Hirano, H. *Macromolecules* **1998**, *31*, 3958.
[4] Haley, J. C.; Lodge, T. P. *J. Chem. Phys.* **2005**, *122*, 234914.
[5] Haley, J. C.; Lodge, T. P.; He, Y.; Ediger, M. D.; Von Meerwall, E. D.; Mijovic, J. *Macromolecules* **2003**, *36*, 6142.
[6] He, Y.; Lutz, T. R.; Ediger, M. D. *Macromolecules* **2004**, *37*, 9889.
[7] Lodge, T. P.; McLeish, T. C. B. *Macromolecules* **2000**, *33*, 5278.
[8] Zeroni, I.; Ozair, S.; Lodge, T. P. *Macromolecules* **2008**, *41*, 5033.
[9] He, Y.; Lutz, T. R.; Ediger, M. D. *J. Chem. Phys.* **2003**, *119*, 9956.

[10] Colby, R. H. *Polymer* **1989**, *30*, 1275.
[11] Zawada, J. A.; Ylitalo, C. M.; Fuller, G. G.; Colby, R.H.; Long, T. E. *Macromolecules* **1992**, *25*, 2896.
[12] Zeroni, I. *Ph.D. Thesis*, University of Minnesota, **2008.**
[13] Lindsey, C. P.; Patterson, G. D. *J. Chem. Phys.* **1980**, *73*, 3348.
[14] Hamersky, M. W. *Ph.D. Thesis*, University of Minnesota **1997.**
[15] Milhaupt, J. M. *Ph. D. Thesis*, University of Minnesota **2000**.
[16] Wu, S. *J. Polym. Sci., Part B: Polym. Phys.* **1987**, *25*, 2511.
[17] Doi, M.; Edwards, S. F. *The Theory of Polymer Dynamics*; Oxford University Press: Oxford **1986**.
[18] Ferry, J. D. *Viscoelastic Properties of Polymers*, Third ed.; John Wiley & Sons: New York, **1980**.
[19] Johnson, C. E. *M. S. Thesis*, University of Minnesota, **2001.**
[20] Colby, R. H.; Rubinstein, M. *Macromolecules* **1990**, *23*, 2753.
[21] Fetters, L. J.; Lohse, D. J.; Milner, S. T.; Graessley, W. W. *Macromolecules* **1999**, *32*, 6847.
[22] Min, K. E.; Chiou, J. W.; Barlow, J. W.; Paul, D. R. *Polymer* **1986**, *28*, 1721.
[23] Fox, T. G. *Bul. Am. Phys. Soc.* **1956**, *1*, 123.

Chapter 5. Component Terminal Dynamics in Strongly Interacting Blends

5.1 Introduction

Miscible blends continue to attract considerable attention because they provide a low cost alternative route to new materials with tunable properties. For optimized material properties and processing conditions, a fundamental understanding of dynamic and viscoelastic properties of the blends is required. This is why we undertook the study of component terminal dynamics in PEO/PMMA blends described in the previous chapter and in reference 1. To this day, most studies of miscible blend component dynamics have focused on weakly interacting blends. There has been relatively little research done to understand component dynamics, either at the segmental or terminal level, in blends with strong specific interactions such as hydrogen bonding.[2–6]

It is well established that hydrogen bonding enhances miscibility in otherwise immiscible systems.[7–10] Intermolecular hydrogen bonding can potentially lead to a simplification of blend dynamics by coupling component dynamics, as indicated by the applicability of time–temperature superposition principle[11,12] in strongly interacting blends. Poly(4-vinyl phenol) (PVPh) is a common proton–donating polymer and forms hydrogen bonds with several classes of polymers. Since PVPh has a proton–donating hydroxyl group on each repeat unit, it forms *intramolecular* hydrogen bonds with itself besides forming *intermolecular* hydrogen bonds with other components in miscible blends.

We decided to investigate component dynamics in a strongly interacting binary blend that consists of PVPh as one of the components. The choice of a blend partner for PVPh was based on several considerations such as being miscible over the entire composition range, and preference for intermolecular interactions vs. intramolecular interactions over at least part of the composition range. Another important consideration was T_g of the blend partner. Since PVPh has a T_g of ~170 °C, it is a very glassy and stiff polymer at room temperature. It was desired that the other blend component have a significantly lower T_g to produce a large difference in polymer mobilities, hence making the blend *dynamically asymmetric*. A choice of polymer that fulfils all these criteria is PEO. The T_g of PEO is –60 °C, which means the difference of T_gs of PEO and PVPh is ~210 °C. Such a large T_g difference definitely creates dynamic asymmetry. Several studies of PEO/PVPh miscibility are present in the literature,[13–15] and both polymers are found to be miscible over the entire composition range.

The choice of PEO as the blend partner for PVPh is also motivated by a study of PEO/PMMA blend dynamics, the results of which were discussed in the previous chapter, as well as published elsewhere.[1] The Lodge–McLeish model[16] failed to predict the temperature dependence of component terminal dynamics in this dynamically asymmetric blend. There have been other studies on PEO/PMMA blends highlighting unusual PEO dynamics.[17,18] These results indicate relaxation mechanisms of PEO that are not fully understood.

To our knowledge, no comprehensive investigation of the temperature and composition dependence of component chain dynamics in a PEO/PVPh blend has yet been undertaken. Therefore, in this chapter we report component chain dynamics in

PEO/PVPh blends to address the effects of hydrogen bonding on blend dynamics. The fundamental questions we try to address are: Do terminal dynamics of a miscible polymer blend with intermolecular hydrogen bonding differ from those of a weakly interacting blend? Does intermolecular hydrogen bonding simplify blend dynamic behavior by coupling component dynamics?

To answer these questions, we carried out "tracer" rheology experiments in which a high molecular weight polymer tracer was blended with a low molecular weight matrix and its rheological response analyzed to extract terminal dynamics from viscoelastic measurements. The longest relaxation time of the tracer is readily obtained from the low frequency peaks of the elastic component of the dynamic viscosity, η''. The monomeric friction factor, ζ is extracted from these relaxation times via appropriate polymer dynamics models. The steady shear viscosity of the blends, with and without tracer, was also measured to understand effects of hydrogen bonding on blend viscosity. The composition dependence of the shape of η'' peaks was also investigated for both PEO and PVPh tracer blends. To understand the effects of hydrogen bonding on component blend dynamics, the results of all analyses are compared to those of PEO/PMMA blends reported in previous chapter as well as in reference 1, because while both PEO/PMMA and PEO/PVPh are blends with large T_g differences making them dynamically asymmetric, hydrogen bonding is absent in PEO/PMMA blends.

5.2 Results

5.2.1 Materials

A high molecular weight sample of PEO (M_n = 845 kg/mol; PEO–845) and another low molecular weight sample (M_n = 1 kg/mol; PEO–1) were purchased from Aldrich for use in rheology experiments. Two different PVPh samples, one high molecular weight (M_n = 290 kg/mol; PVPh–290) and the other low molecular weight (M_n = 5 kg/mol; PVPh–5) were synthesized via anionic polymerization in the lab as described in Chapter 3. The high molecular weight polymers were used as tracers in the rheology experiments. All polymers had polydispersity indices of less than 1.1. Table 5.1 summarizes the polymer molecular weights along with other properties.

Table 5.1. Properties of Polymers Used in this Work

Sample	M_n (kg/mol)	M_w/M_n	T_g (°C)	Use
PEO-1	1.1	1.04	–67	Matrix
PVPh-5	5	1.05	157	Matrix
PEO-845	845	1.08	–61	Tracer
PVPh-290	290	1.06	184	Tracer

Blends were prepared by co–dissolving the polymers with 0.5% by weight of the antioxidant 2,6–di–*tert*–butyl–4–methyl–phenol (BHT) in THF and stirring at room

temperature for 24–48 hours. For blends with high molecular weight tracers, the tracer dissolution was aided by gently heating the solution until the tracer dissolved. THF was removed by a nitrogen purge and the blends were dried to constant weight under vacuum at 80 °C. Tracer composition in the blends ranged from 1.0% – 1.8%. The blends were prepared to have the same component composition regardless of presence of tracer. For example, a 65% PVPh blend with PVPh tracer comprises 64 wt.% PVPh–5, 35% PEO–1, and 1% PVPh–290 tracer. Similarly a 65% PVPh blend with PEO tracer comprises 65 wt.% PVPh–5, 34% PEO–1 and 1% PEO–845 tracer.

5.2.2 Component Dynamics from Rheology

In the past, rheological measurements have been carried out to extract terminal component dynamics in miscible blends because of the relative ease and simplicity of these methods. For such measurements, it is of interest to choose components and molecular weights so that their contribution to some rheological material function is measurable and relatively easy to extract. One such feature is a peak in η'' that indicates the longest relaxation time of one of the components. The aim is to bring about a separation of longest relaxation times of both components such that the peak in η'' could be assigned to each component. However, it is usually not trivial to resolve the contribution of each component to η'' or G'. One such way of achieving this is to prepare blends in which a high molecular weight tracer is dispersed in a low molecular weight matrix, as previously shown for PEO/PMMA blends.[1,18] Another method that has been recently used for extraction of component dynamics is to mix low molecular weight chains in a high molecular weight, highly entangled matrix.[19]

5.2.3 Tracer Rheology

Tracer blends were used for all of the data presented in this work. Tracer blends comprise low molecular weight matrix components (PEO–1 and PVPh–5) and a high molecular weight tracer of either PEO or PVPh (PEO–845 or PVPh–290).

The underlying principle of using tracer blends is that the significantly large molecular weight of tracers will make them relax at a much longer time scale. This will result in easy separation of the longest relaxation times of the tracer and the matrix because chain relaxation gives rise to a peak in η'' and there will be two distinct peaks. The low frequency peak will correspond to relaxation of the tracer, while the high frequency peak will correspond to matrix relaxation.

5.2.4 Rheological Data Representation for Extraction of Dynamic Information

In this section we introduce the plots that were used to obtain almost all the dynamic information. Figure 5.1 shows plots of η', and η'' as a function of reduced angular frequency, ω. These plots exhibit the data for blends with PVPh–290 tracer as well as the matrix blends of the same composition but without the high molecular weight tracer. Similar plots are shown for blends with and without PEO–845 tracer in Figure 5.2. All figures show η' of the matrix, but only Figures 5.1 (a), and 5.2 (a) show matrix η'' data sets as well. For $\phi_{PVPh} \leq 0.5$, η'' data sets are not shown because their magnitude is relatively small and the signal to noise ratio is too small such that no useful information can be extracted.

The plots shown in Figures 5.1 and 5.2 are master curves created by horizontally and vertically shifting data sets to overlap η'' peaks. Depending on the blends, the rheological data sets were obtained over a temperature range of 40–140 °C. The horizontal shift factor, a_T was determined by superposing tan δ curves. Using a_T, both η' and η'' curves were shifted horizontally followed by shifting vertically by a factor $1/a_T$ which made the curves overlap simultaneously. In Figures 5.2 (c,d) the data sets for 50% PVPh and 65% PVPh blends show time–temperature superposition (tTS) failure as simultaneous overlapping of η', and η'' curves could not be achieved.

The plots shown in Figures 5.1 and 5.2 exhibit a peak in η'' data sets for blends with tracers. The η'' peaks are absent in the matrix data sets. This supports the assertion that η'' peaks arise because of the presence of tracer chains. The η'' peaks are associated with the longest relaxation time, τ_1, of tracer chains, which is determined from the reciprocal of the angular frequency at which tracer η'' peak is observed. Since the plots are master curves comprising multiple data sets, τ_1 for each data set was obtained by determining the terminal relaxation time at the reference temperature and then using the horizontal shift factors to calculate relaxation times at other temperatures.

(a)

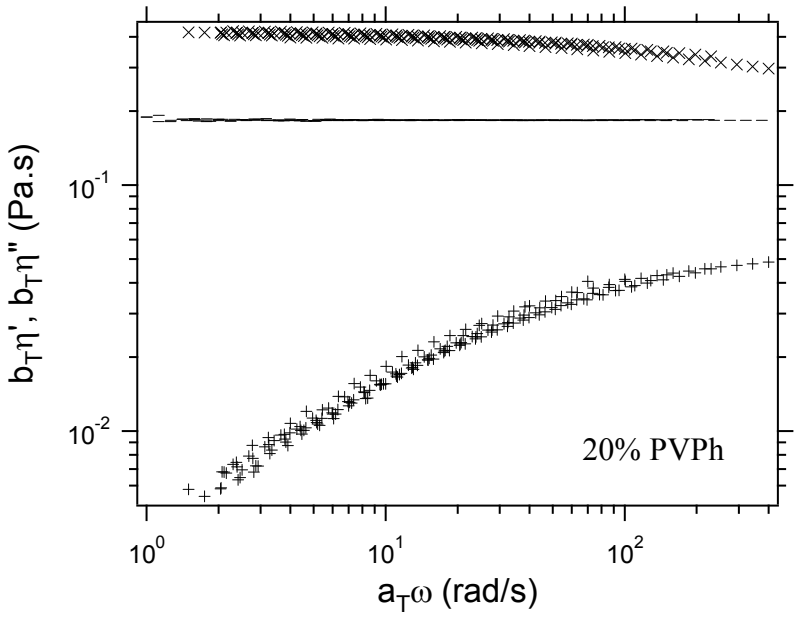

(b)

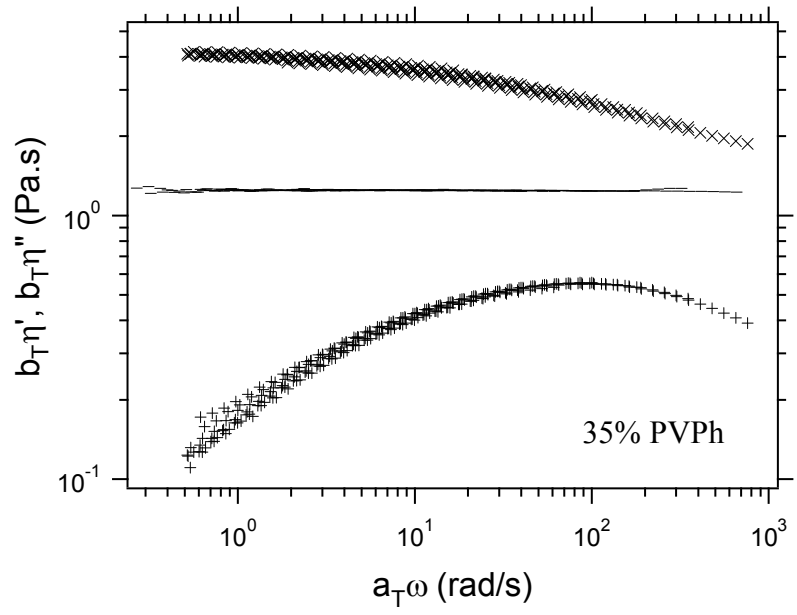

Figure 5.1. Plot of η', η'' vs. reduced frequency for PVPh–290 tracer in (a) 20% PVPh, and (b) 35% PVPh blends. Reference temperature for the master curves is 80 °C. (×) η' for tracer blend, (+) η'' for tracer blend, and solid line is for matrix η'.

(c)

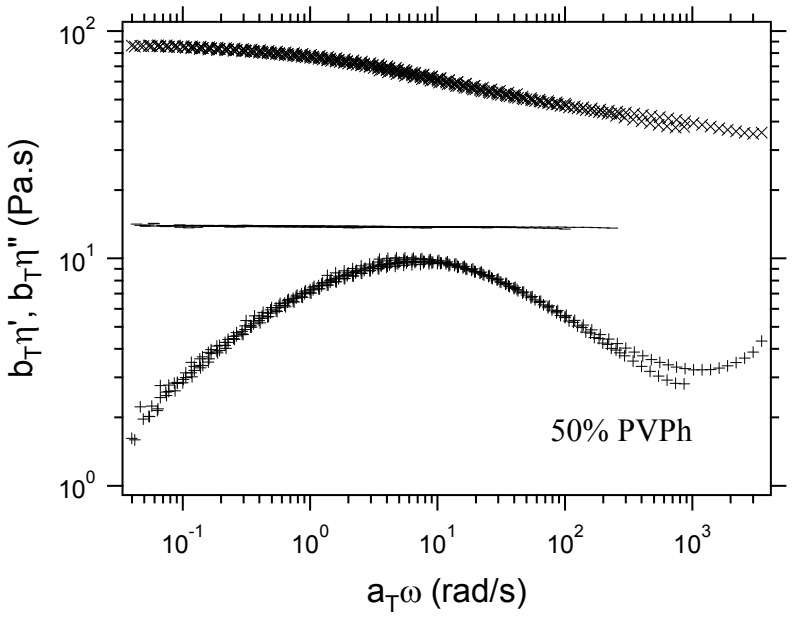

(d)

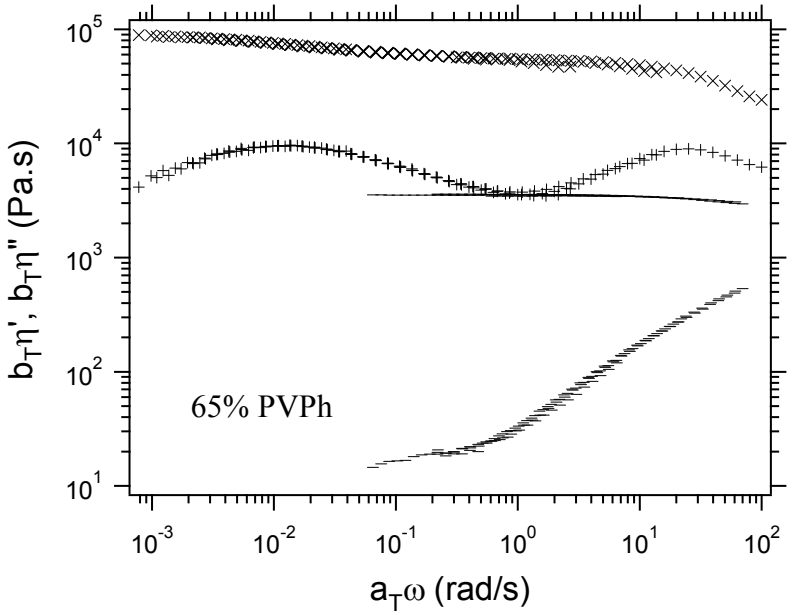

Figure 5.1. Plot of η', η'' vs. reduced frequency for PVPh–290 tracer in (c) 50% PVPh, and (d) 65% PVPh blends. Reference temperature for the master curves is 80 °C. (×) η' for tracer blend, (+) η'' for tracer blend, and solid line is for matrix η'.

(a)

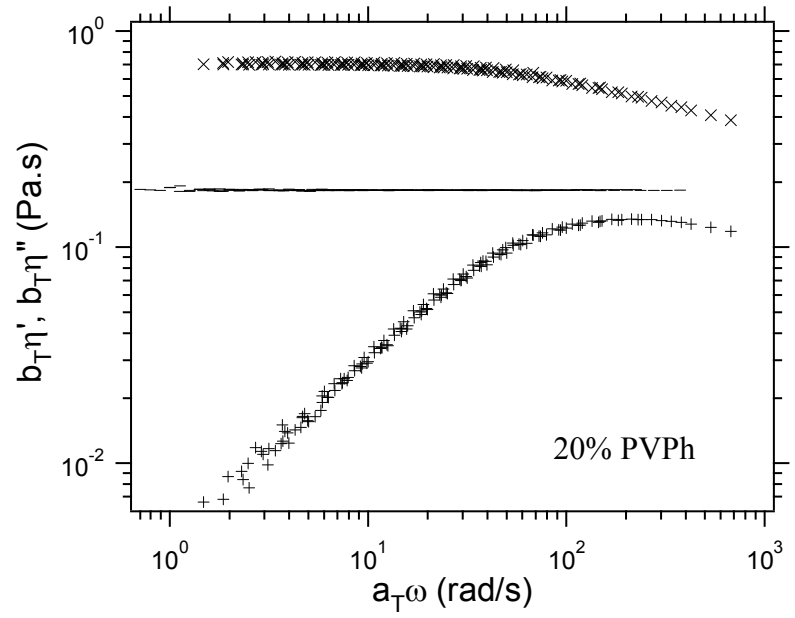

(b)

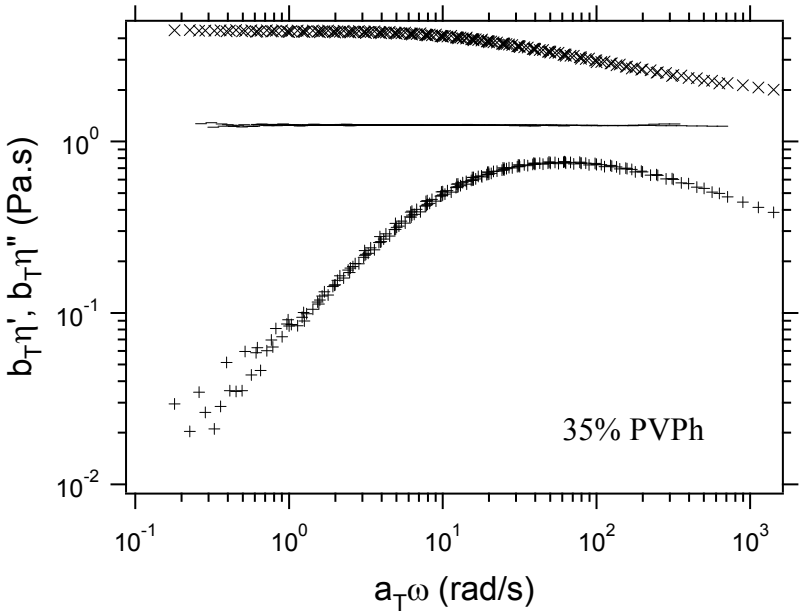

Figure 5.2. Plot of η', η'' vs. reduced frequency for PEO–845 tracer in (a) 20% PVPh, and (b) 35% PVPh blends. Reference temperature for the master curves is 80 °C. (×) η' for tracer blend, (+) η'' for tracer blend, and solid line is for matrix η'.

(c)

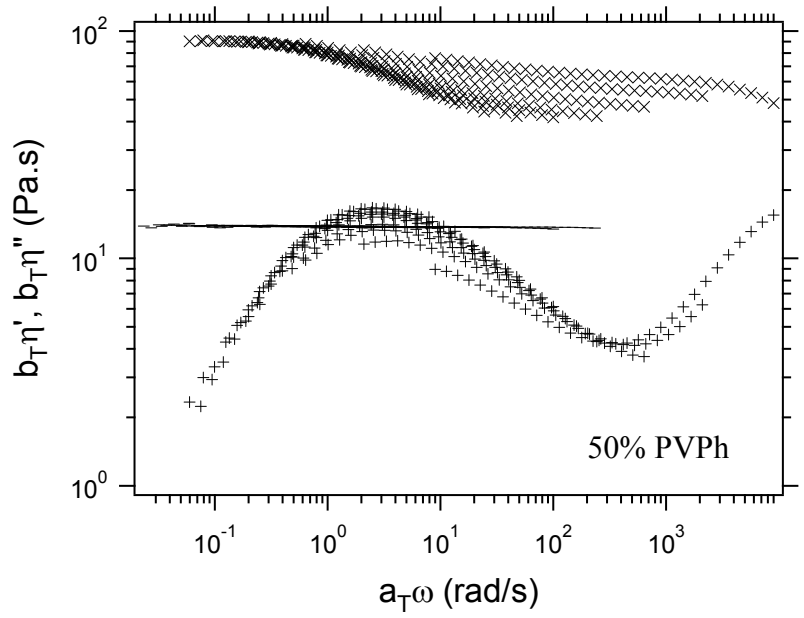

(d)

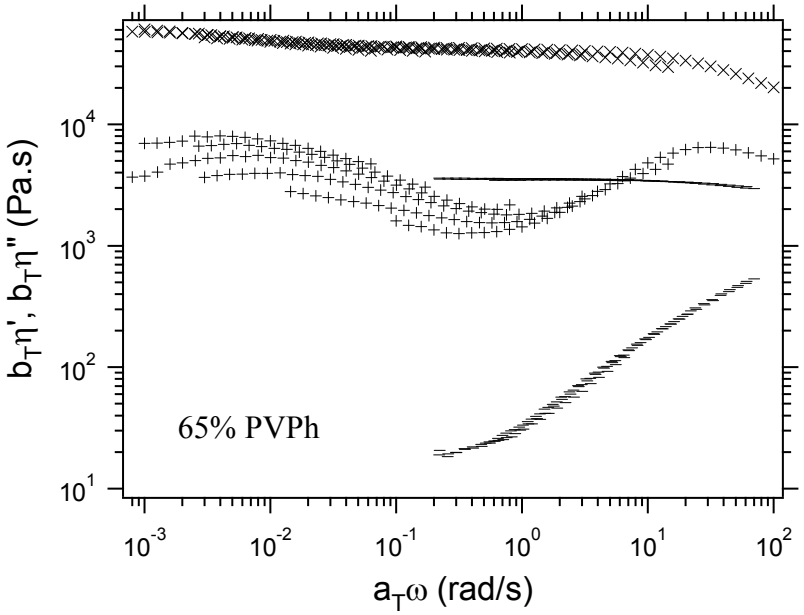

Figure 5.2. Plot of η', η'' vs. reduced frequency for PEO–845 tracer in (c) 50% PVPh, and (d) 65% PVPh blends. Reference temperature for the master curves is 80 °C. (×) η' for tracer blend, (+) η'' for tracer blend, and solid line is for matrix η'.

5.2.5 Determination of ζ from Rheology

The monomeric friction factor, ζ, can be extracted from rheological data based on the assumption of a particular polymer dynamics model. For entangled melts, reptation theory can be used to deduce ζ, while for low molecular weight, unentangled melts, such as PEO–1/PVPh–5, the Rouse model is used. For homopolymer melts of PEO–1 and PVPh–5, the steady shear viscosity is used to extract ζ.

5.2.6 Extraction of ζ from η and η''

For different blend compositions, the monomeric friction factor, ζ, is determined by analyzing relaxation peaks in η''. The difference in chain lengths of tracer and matrix polymers gives rise to two distinct η'' relaxation peaks, in which the lower frequency peak is attributed to tracer relaxation. From the tracer η'' relaxation peak, the longest relaxation time is determined as described in Section 5.2.4 and ζ is related to this longest relaxation time via the Rouse model relationship:[20]

$$\tau_1 = \frac{1}{3\pi^2}\frac{\zeta b^2}{kT}\left(\frac{M}{M_o}\right)^2 \tag{5.1}$$

This is how ζ_{PEO} and ζ_{PVPh} in the blend were determined.

PEO–1 homopolymer was subjected to steady rate sweeps to determine the steady shear viscosity. Since it is a low molecular weight, unentangled polymer, the Rouse model was used to relate η to ζ:[21,22]

$$\eta = \frac{1}{36}\rho N_{Av} b^2 \zeta \left(\frac{M}{M_o}\right)^2 \qquad (5.2)$$

where ρ is the homopolymer melt density (ρ_{PVPh} = 1.19 g/cm^3, ρ_{PEO} = 1.064 g/cm^3)[23,24] , N_{Av} is Avogadro's number, b is the statistical segment length, M is the polymer molecular weight and M_o is the monomer molecular weight.

To our knowledge, there are no reported values of b_{PVPh} in literature. Gestoso, *et al.*[25] reported a computer simulation study in which they calculated the radius of gyration, R_g, of PVPh to be 24 ± 8 Å. The simulated PVPh chain had a degree of polymerization, N, of 250. This corresponds to b_{PVPh} = 3.7 Å, which seems very unlikely because almost all flexible polymers have statistical segment lengths in the range of 5–7 Å. Moreover, computing the value of the characteristic ratio, C_∞, from this value of b results in C_∞ = 3.0. The characteristic ratio is a measure of chain flexibility; the larger C_∞ is, more stiff the polymer chains are because of local constraints. For polymers that primarily have C–C or C–O bonds along the backbone, C_∞ ranges from 4 to 12. Thus a C_∞ value of 3.0 suggests PVPh is one of the most flexible polymers known. This is not plausible because large phenyl groups in PVPh provide steric constraints which should make it quite a rigid polymer. Hence, we decided not to use this value of b_{PVPh}, and instead use the statistical segment length of 6.7 Å for poly(styrene) (PS)[24] because of structural similarity between PVPh and PS. The statistical segment length of PEO is 5.6 Å.[24]

ζ obtained via eq. 5.2 was divided by a factor of about 3 because we found in our analysis and also it has been reported that ζ obtained via this method is systematically

larger than that obtained via several other methods.[1] This is partly because of contribution of "glassy modes" to the viscosity of the short polymers.[26] Since the viscosity is the time integral of the stress relaxation modulus and as the terminal dynamics of the short chains are not much separated in time from the glassy modes, this contribution can be significant. Despite the small correction for ζ, none of our conclusions will be affected because ζ varies by many orders of magnitude over the temperature and composition range probed.

In order to perform steady rate sweeps on PVPh–5, it had to be loaded in the rheometer at temperatures much above its T_g of 157 °C for proper loading. So ideally, the loading temperatures would have to exceed 190–200 °C to ensure uniform loading and even edges. Heating to such high temperatures risks degradation of the sample. It has been reported in literature that PVPh may gradually cross–link at elevated temperatures,[27] which we confirmed by heating PVPh to different temperatures above its T_g and characterizing the heated sample via SEC. SEC traces showed a distinct broadening for PVPh samples heated to 200 °C and above, indicating the presence of larger structures which could result from intermolecular cross–linking with itself. Yang, *et al.* also reported possible degradation of PVPh after heating for prolonged periods at 200 °C.[28] Therefore, steady rate sweeps were not performed on PVPh–5. Instead, zero shear viscosities were calculated from the frequency dependence of G'' at various temperatures reported in the literature.[28] The authors of this study had used a different PVPh sample for each temperature above 190 °C that they made measurements at. It should be noted that these data were reported for a PVPh that had a molecular weight of 21.6 kg/mol. The steady shear viscosity was adjusted for the molecular weight difference using the scaling

relationship described by Rouse model. Using eq. 5.2, ζ of PVPh–5 was determined for different temperatures.

Monomeric friction factors of PVPh in the blends are plotted as a function of temperature in Figure 5.3, along with those for PEO and PVPh homopolymers. Those of PEO are plotted in Figure 5.4. To compare the temperature dependences of ζ_{PVPh} and ζ_{PEO} we have plotted ζ_{PVPh}/ζ_{PEO} as a function of temperature for different blend compositions in Figure 5.5. These results will be discussed in Section 5.3.

5.2.7 Extraction of ζ in the absence of η'' peaks

When the matrix is too rich in the fast component (blends with low PVPh concentration), as temperature increases, η'' peaks shift outside the experimental window because of a reduction in the longest relaxation time. For these data sets, the low frequency regions of the η'' curves (with peaks outside experimentally accessible frequency range) were overlapped with curves of the same blend where η'' peaks were observed. Longest relaxation times of these data sets were obtained by determining the relaxation time at the reference temperature and then using horizontal shift factors to calculate relaxation times at other temperatures.

For 10% PVPh blends with both PVPh–290 and PEO–845 tracers, no η'' peak was observed at any temperature within the experimentally accessible range of frequencies. This indicates relaxation of tracer chains more rapid than can be measured by the rheometer. Therefore, the method of extracting ζ described earlier cannot be used for this blend; instead, ζ was determined by utilizing a method described by Zeroni *et al.*[1]

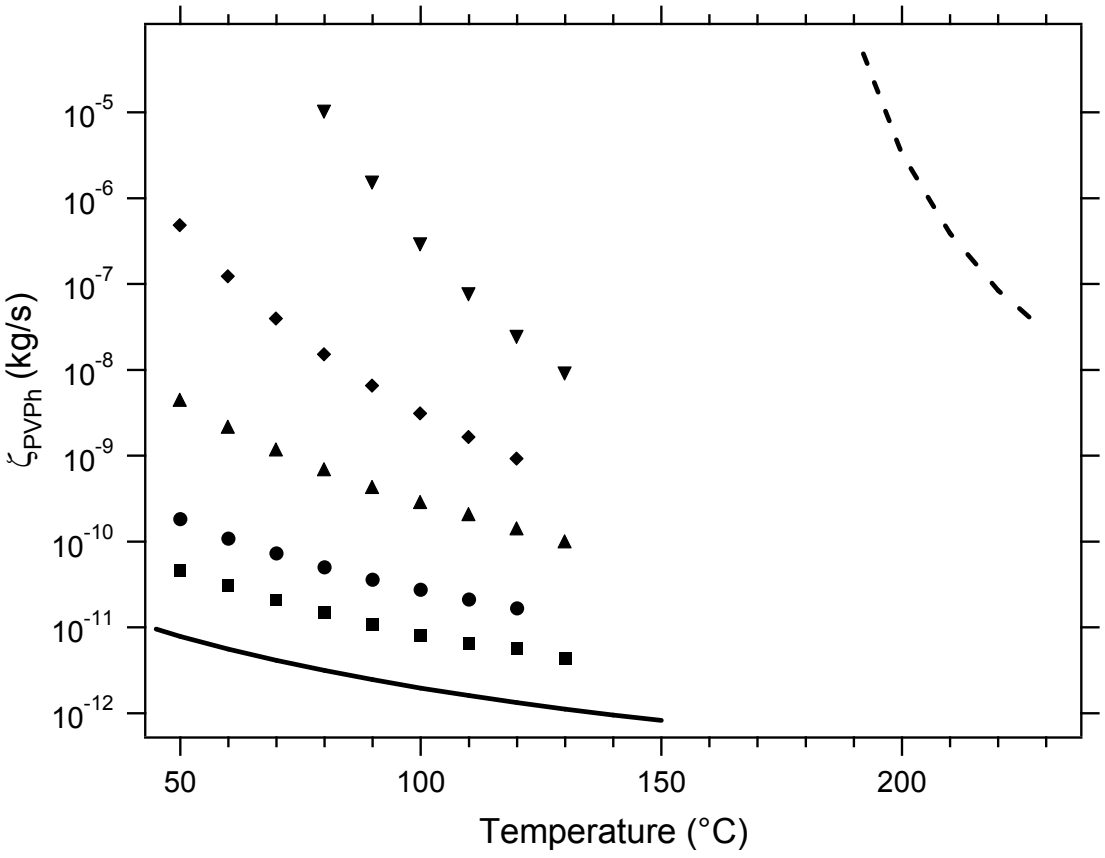

Figure 5.3. Monomeric friction factors of PVPh as a function of temperature for various PEO/PVPh blend compositions. (■) 10% PVPh, (●) 20% PVPh, (▲) 35% PVPh, (♦) 50% PVPh, (▼) 65% PVPh. Solid line represents homopolymer PEO–1, and dashed line represents homopolymer PVPh–5.

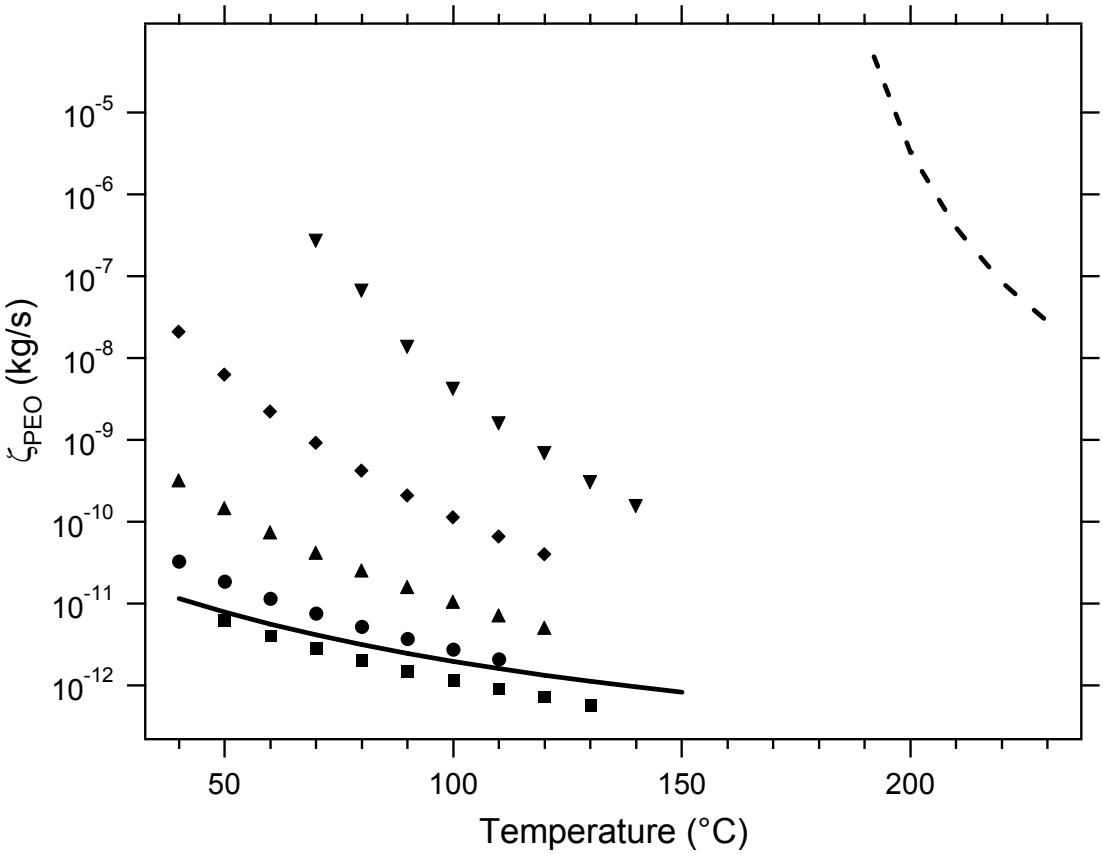

Figure 5.4. Monomeric friction factors of PEO as a function of temperature for various PEO/PVPh blend compositions. (■) 10% PVPh, (●) 20% PVPh, (▲) 35% PVPh, (♦) 50% PVPh, (▼) 65% PVPh. Solid line represents homopolymer PEO–1, and dashed line represents homopolymer PVPh–5.

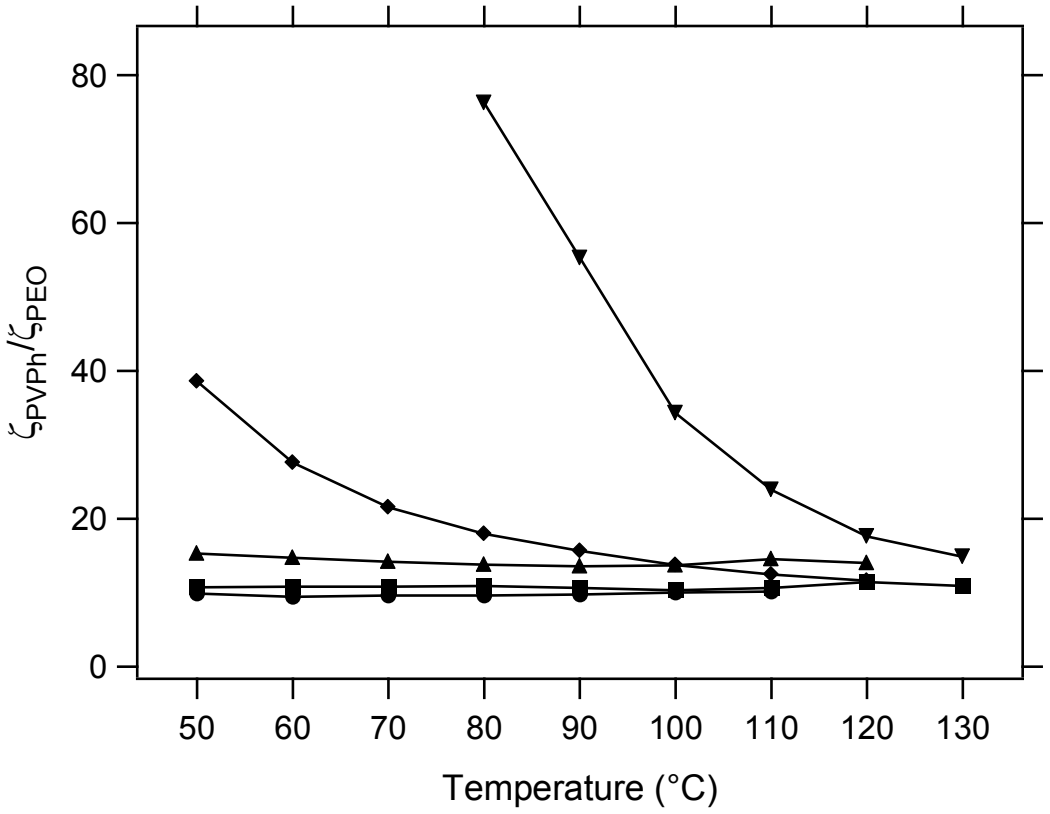

Figure 5.5. Ratios of PVPh and PEO friction factors as a function of temperature for various PEO/PVPh blend compositions. (■) 10% PVPh, (●) 20% PVPh, (▲) 35% PVPh, (♦) 50% PVPh, (▼) 65% PVPh.

in which it was assumed that polymer tracer contributes to the steady shear viscosity, η, of the blend, hence making it larger than that of the matrix.

The tracer contribution to blend viscosity can be quantitatively determined by equation 5.3:

$$\eta_{\text{blend}} = \phi_{\text{matrix}}\eta_{\text{matrix}} + \left(\phi_{\text{tracer}} + A\phi_{\text{tracer}}^2\right)\eta_{\text{tracer}} \tag{5.3}$$

where ϕ_i is volume fraction of component i and A is a fitting parameter which quantifies the extent of tracer–tracer contacts in the blend.[1,37] A major underlying assumption in using eq. 5.3. is that A is independent of composition. Each blend component has its own A value which could or could not be similar.

To determine the values of the dimensionless constant, A, for each component, ζ value of both homopolymers and different blend compositions are extracted at as many temperatures as possible using the methods described in Section 5.2.6, i.e., from η for homopolymers and from τ_1 for blends. All variables in eq. 5.3 are known except A and η_{tracer}. A value for A parameter is arbitrarily chosen and η_{tracer} is determined from eq. 5.3. for all blend compositions. The A parameter value is iteratively adjusted until η_{tracer} values for all blends yield corresponding ζ values (using eq. 5.2) that are in good agreement with the ζ values determined from methods described in Section 5.2.6. In determining ζ values from η_{tracer} using eq. 5.2, all parameters used were those of the tracer except the density, which was matrix density determined from interpolation of homopolymer densities. The matrix viscosities, η_{matrix}, as measured by steady shear

experiments were used in eq. 5.3 for extraction of η_{tracer} and are shown as a function of temperature in Figure 5.6.

Using this method, A_{PVPh} was determined to be –35 while A_{PEO} was determined to be –30. These A values for blends with both PVPh–290, and PEO–845 tracers resulted in good agreement of ζ values obtained via this method and those obtained from η'' peaks, for all but 20% PVPh blends in which ζ from this method was a little lower at all temperatures than that compared to ζ extracted from η'' peaks. We suspect the reason of this discrepancy to be relatively less precise determination of η'' peak position for the 20% PVPh blend because the peaks are positioned at or slightly beyond the maximum accessible frequency. It is quite possible that the actual peak position could reside outside the experimental window. The slight discrepancy in ζ values is not of concern as it does not change any conclusions. Comparison of these A values to those obtained in the study of PEO/PMMA blends[1] reveals that the value for PEO is the same, but that of PVPh is significantly more negative than that of PMMA ($A_{PMMA} = -20$).

The simplest method of extracting the dissipative contribution of a viscoelastic element is to use the additivity rule:[20]

$$\eta_{blend} = \phi_{matrix}\eta_{matrix} + \phi_{tracer}\eta_{tracer} . \qquad (5.4)$$

The additivity relationship does not work as well as eq. 5.3 for determining tracer monomeric friction factor. Since the A parameter in eq. 5.3 can be thought of as describing contribution of tracer – tracer contacts to blend viscosity, the negative A values indicate over–estimation of η_{blend} by the additivity rule.

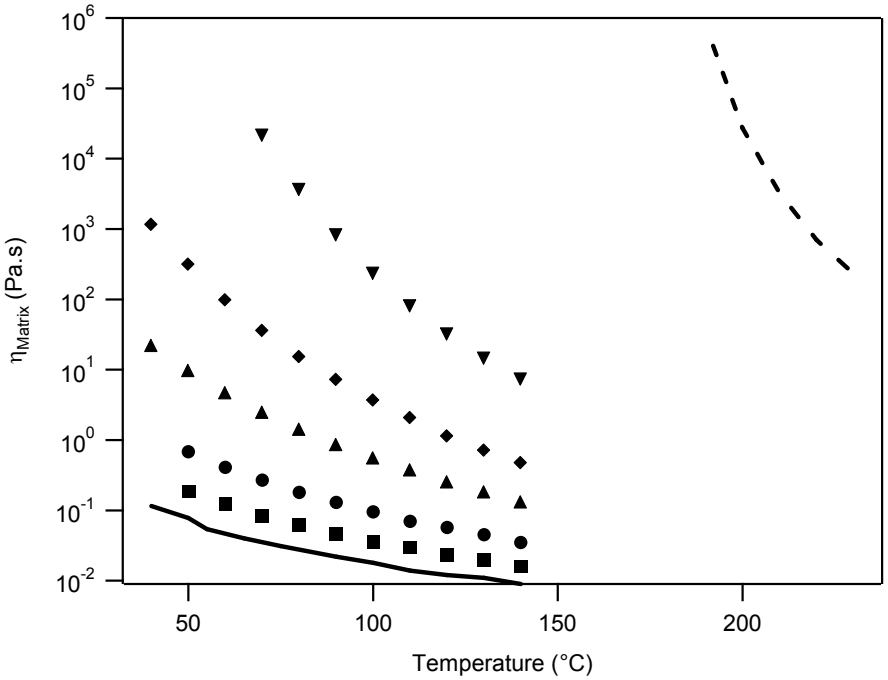

Figure 5.6. Matrix viscosity as a function of temperature for PEO–1/PVPh–5 blends. (■) 10% PVPh, (●) 20% PVPh, (▲) 35% PVPh, (♦) 50% PVPh, (▼) 65% PVPh. Solid line represents homopolymer PEO–1, and dashed line represents homopolymer PVPh–5.

5.2.8 DSC Thermograms

It is well established that for weakly interacting blends, the calorimetric glass transition is much broader than that for homopolymers because of dynamic heterogeneity as a result of self concentration effects and concentration fluctuations. We are interested in exploring how the glass transition will be affected by specific interactions such as hydrogen bonding in PEO/PVPh blends. There have been reports in the literature[28] that blends with hydrogen bonding do in fact exhibit narrower glass transitions, probably because of suppressed dynamic heterogeneity and composition fluctuations.

The glass transitions of PEO–1/PVPh–5 blends were studied using DSC. Figure 5.7 shows DSC thermograms for all of the blends studied. The corresponding derivative scans for the same blends are shown in Figure 5.8. T_g was determined by measuring the width of the glass transition from its onset to its finish and taking the mid–point of that transition in Figure 5.7. Blends with $\phi_{PVPh} \leq 0.35$ exhibit PEO crystallization peaks in these thermograms. PEO percent crystallinity in the blend was determined using equation 5.5:

$$\text{Percent crystallinity} = \frac{\left(\Delta H_f - \Delta H_c\right)}{\Delta H_f^{\circ}} \times 100 \qquad (5.5)$$

where ΔH_f and ΔH_c are the enthalpies of fusion and crystallization, respectively, and ΔH_f° is the enthalpy of fusion of perfectly crystallized PEO and is reported to be 205 J/g.[29]

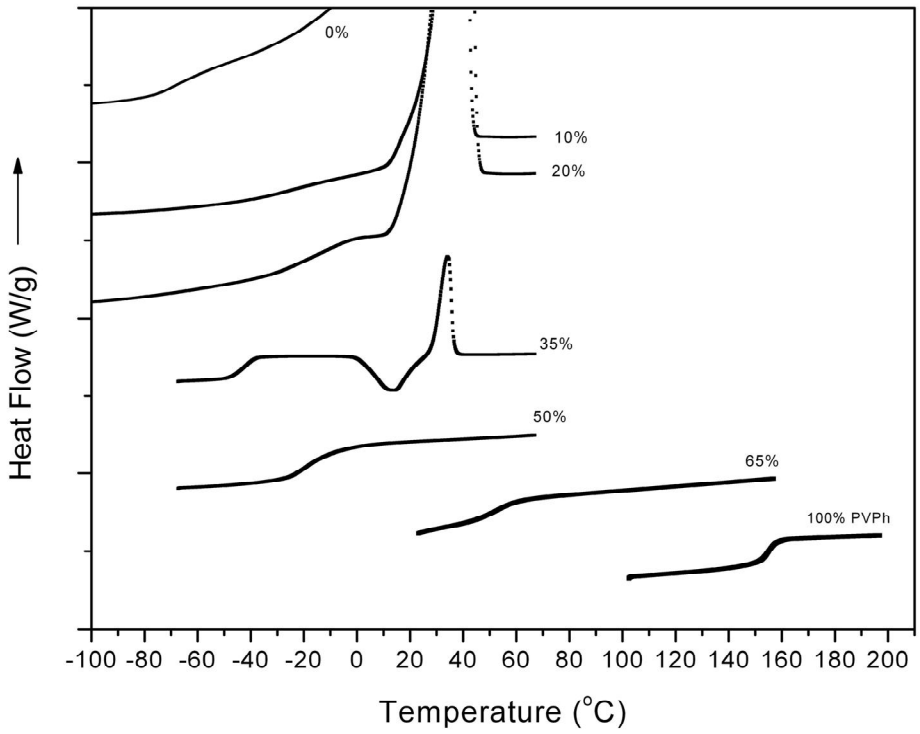

Figure 5.7. DSC scans for various compositions of PEO–1/PVPh–5 blends. The percent compositions listed for each scan in the figure are those of PVPh in the blend.

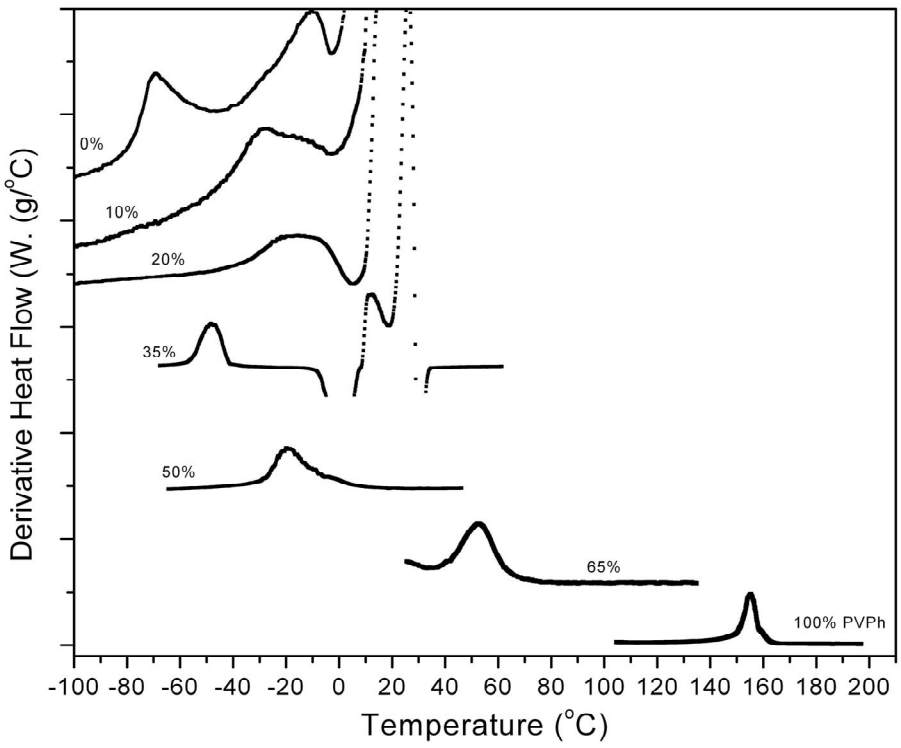

Figure 5.8. Differential DSC scans for various compositions of PEO–1/PVPh–5 blends. The percent compositions listed for each scan in the figure are those of PVPh in the blend.

Table 5.2 lists the blend compositions, T_gs, T_g widths, and percent crystallinity of PEO in the blend. These results will be discussed in Section 5.3.

Table 5.2. Thermal Properties of PEO/PVPh Blends Used in This Study

Blend composition (PEO/PVPh)	% PEO crystallinity in blend	T_g (°C)	T_g width (°C)
100/0	70	–68	16
90/10	62	–26	15
85/15	60	–22	23
80/20	56	–36	14
75/25	46	–42	11
71/29	3	–48	10
65/35	1	–42	9
50/50	–	–19	19
35/65	–	53	14
0/100	–	156	9

5.2.9 Quantification of Hydrogen Bonds

In order to understand the role of hydrogen bonding in component dynamics, it is important to have knowledge of the composition dependence of hydrogen bonding in PEO/PVPh blends. For a polymer blend like PEO/PVPh where one component can self associate as well as form intermolecular associations with the other component, Coleman, *et al*. have developed a theoretical model to predict thermodynamic properties. Only the key aspects of this theory are presented here; a detailed review can be found elsewhere.[30] This model will hereafter be referred to as the Coleman–Graf–Painter Association Model (CGPAM), and can be summarized by considering association equilibria between different blend components:

$$B_1 + B_1 \overset{K_2}{\rightleftharpoons} B_2 \tag{5.6}$$

$$B_h + B_1 \overset{K_B}{\rightleftharpoons} B_h{+}1 \ (h \geq 2) \tag{5.7}$$

$$B_h + A_1 \overset{K_A}{\rightleftharpoons} B_hA \tag{5.8}$$

where B represents vinylphenol (VPh) and A represents ethylene oxide (EO), B_1 is a VPh repeat unit, B_2 is a self associated VPh dimer, B_h is the hydrogen bonded VPh h–mer, A_1 is an EO monomer, and B_hA is the VPh h–mer hydrogen bonded to EO. K_2, K_B, and K_A

are equilibrium constants for equations 5.6–5.8, respectively, and can be expressed as functions of component volume fractions as follows:

$$\Phi_B = \Phi_{B_1}\Gamma_1\left[1+\frac{K_A\Phi_{A_1}}{r}\right] \tag{5.9}$$

$$\Phi_A = \Phi_{A_1}\left[1+K_A\Phi_{B_1}\Gamma_2\right] \tag{5.10}$$

where

$$\Gamma_1 = \left(1-\frac{K_2}{K_B}\right)+\frac{K_2}{K_B}\left(\frac{1}{\left(1-K_B\Phi_{B_1}\right)}\right) \tag{5.11}$$

$$\Gamma_2 = \left(1-\frac{K_2}{K_B}\right)+\frac{K_2}{K_B}\left(\frac{1}{\left(1-K_B\Phi_{B_1}\right)^2}\right) \tag{5.12}$$

and Φ_A and Φ_B are volume fractions of components A and B respectively, Φ_{A_1} and Φ_{B_1} are volume fractions of free A and B groups respectively, and $r = V_A/V_B$ is the ratio of segment molar volumes of components A and B. If values of the equilibrium constants (K_2, K_B, K_A), and segment molar volumes (V_B, V_A) are known, the fraction of hydrogen

bonded OH groups can be calculated from equations 5.9–5.12 for a given blend composition using eq. 5.13.[30]

$$f_{\mathrm{hb\_OH}} = 1 - \frac{\Phi_{\mathrm{B_i}}}{\Phi_{\mathrm{B}}} \tag{5.13}$$

The self–association equilibrium constants for PVPh (K_B = 66.8, K_2 = 21.0) and inter–association equilibrium constant for PEO–PVPh (K_A = 88.3) along with enthalpies of hydrogen bond formation, Δh were determined by Coleman *et al.*[31,32] Table 5.3 summarizes the parameters used to calculate the fraction of hydrogen bonding in PEO/PVPh blends that were investigated for this study.

Table 5.3. Parameters used for quantification of hydrogen bonds in PEO/PVPh blends

Polym.	Molar Vol.[33] (cm^3/mol)	Sol. Param.[33] $(cal/cm^3)^{1/2}$	Self-association				Inter-association	
			K_2	Δh_2 (kJ/mol)	K_B	Δh_B (kJ/mol)	K_A	Δh_A (kJ/mol)
PVPh	100.0	10.6	21.0	5.6	66.8	5.2		
PEO	38.1	9.4					88.3	5.4

Figure 5.9 shows CGPAM prediction of the *fraction* of hydrogen bonded OH and EO groups as a function of PVPh composition. Assuming 1g of blend, the *number* of hydrogen bonded EO and OH groups were calculated from the fraction of hydrogen bonded groups. The difference between total number of hydrogen bonded OH groups and bonded EO groups give the number of self associated OH groups. These results are displayed in Figure 5.10 as a function of PVPh composition. In both Figures 5.9 and 5.10, the CGPAM predictions are shown for two temperatures, 40 °C and 140 °C. These temperatures were chosen because in majority of the experiments, the temperature range probed was from 40–140 °C. Thus, the choice of temperatures for CGPAM predictions was made to depict temperature dependence over the experimentally studied temperature range.

(a)

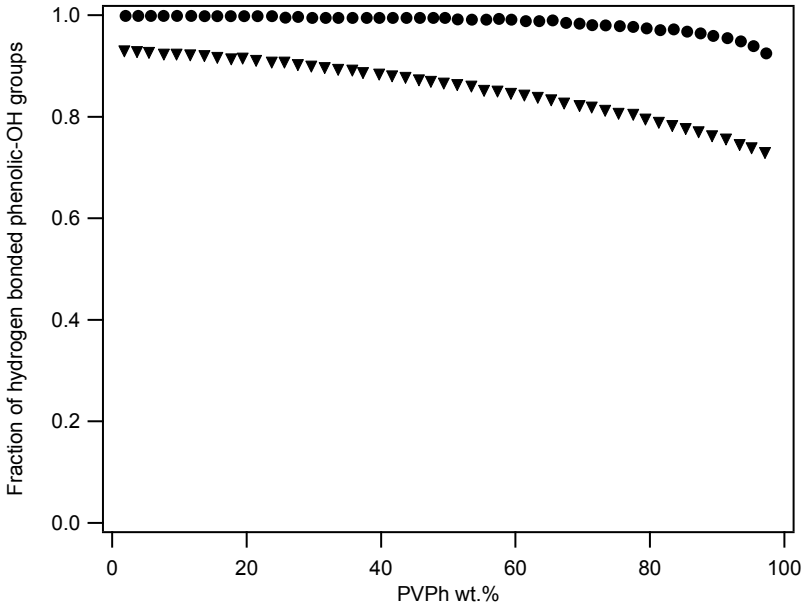

(b)

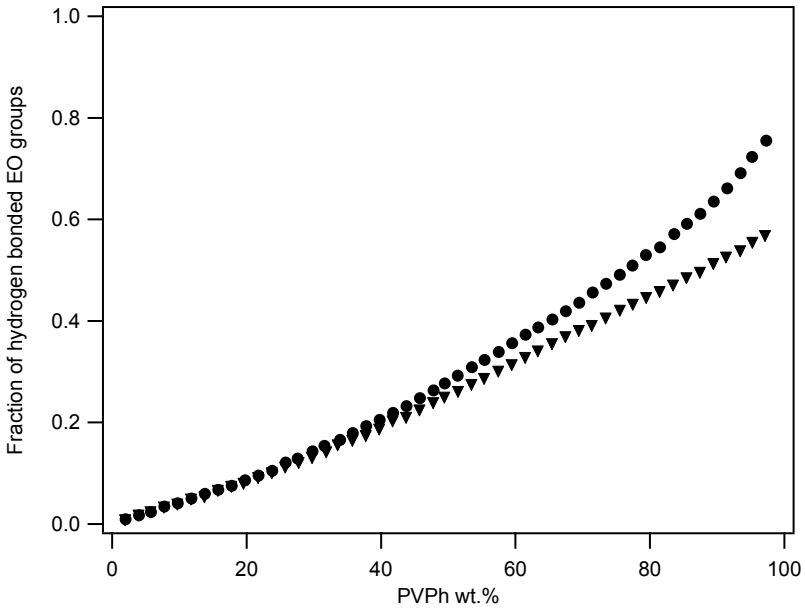

Figure 5.9. Fraction of hydrogen bonded (a) OH groups, and (b) EO groups as a function of PVPh composition at (●) 40 °C, (▼) 140 °C.

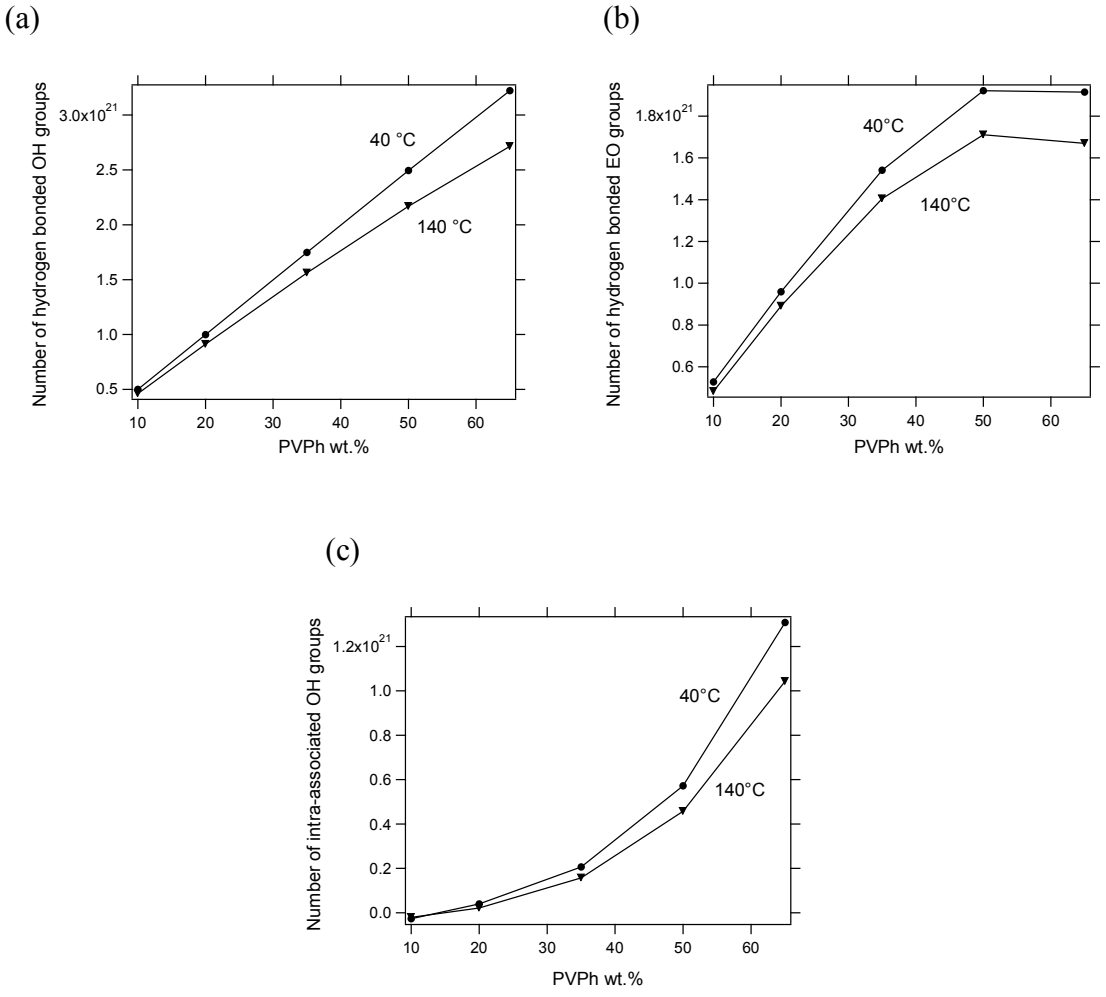

Figure 5.10. In 1g of PEO–1/PVPh–5 blend, number of (a) total hydrogen bonded OH groups, (b) hydrogen bonded EO groups, and (c) intra–associated OH groups as a function of PVPh composition at (●) 40 °C, (▾) 140 °C.

5.3 Discussion

5.3.1 Coleman–Graf–Painter Association Model Predictions

In Figure 5.9, CGPAM predictions of the fraction of hydrogen bonded OH groups show a relatively weak temperature dependence across the composition range. The temperature dependence becomes stronger as PVPh content is increased, especially at higher temperatures. The fraction of hydrogen bonded EO groups in blends up to 35% PVPh show almost no change with temperature. For 50% and 65% PVPh blends, the temperature dependence is stronger, but somewhat weaker compared to that of hydrogen bonded VPh groups.

When analyzing the *number* instead of the *fraction* of hydrogen bonded functional groups, the observations are different. In Figure 5.10 (c), the number of intra–associated OH groups exhibit a gradual increase with PVPh composition. The temperature dependence also becomes stronger as PVPh composition increases. There is no significant change in number of intra–associated VPh groups with temperature for $\phi_{PVPh} \leq 0.2$. In Fig. 5.10 (a) total number of hydrogen bonded VPh groups, i.e., those that have formed hydrogen bonds with other VPh as well as EO groups, increase almost linearly with PVPh composition. The temperature dependence also becomes stronger with increasing PVPh composition. The number of hydrogen bonded EO groups increases steadily with PVPh composition until the 50% PVPh blend, beyond which this number stays constant or even shows a slight decline with composition, indicating that it has reached a maximum.

These predictions will be crucial for understanding various dynamic and viscoelastic results for PEO/PVPh blends. We will use these CGPAM predictions to make general conclusions and will attempt to explain any behavioral trends.

5.3.2 Time–Temperature Superposition Breakdown

Figures 5.1 and 5.2 show master curves of η', η'' vs. ω for PEO–1/PVPh–5 blends ranging in composition from 20% - 65% PVPh. One of the common features of these plots is that η'' peaks shift to lower frequencies as PVPh composition increases, indicating an increase in tracer relaxation times. In Figure 5.1, we observe nicely overlapped master curves for η' and η'' for all four blend compositions (Figures a–d). Thus, the time–temperature superposition principle (tTS) is valid in blends with PVPh–290 tracer.

The case is not so straightforward for blends with the PEO–845 tracer. TTS is observed for 20% and 35% PVPh blends [Figure 5.2 (a,b)] but as seen is Figure 5.2 (c,d), tTS failed in 50% and 65% PVPh blends. This is a remarkable result because very similar behavior was observed in PEO/PMMA blends[1] which has no hydrogen bonding. TTS failure in PEO/PMMA was observed for PEO tracers in 80% and 90% PMMA blends. For convenience, the plots exhibiting tTS breakdown in PEO/PMMA are reproduced from reference 1 and shown in Figure 5.11. In both PEO/PVPh and PEO/PMMA, only the low frequency regions of tracer blend η' data sets overlap nicely, while the tracer blend η'' peaks do not overlap at all. The tTS failure in PEO/PVPh tracer blends, in spite of the presence of strong intermolecular interactions, is rather unexpected. This is because we would have expected coupling of component dynamics which would have

(a)

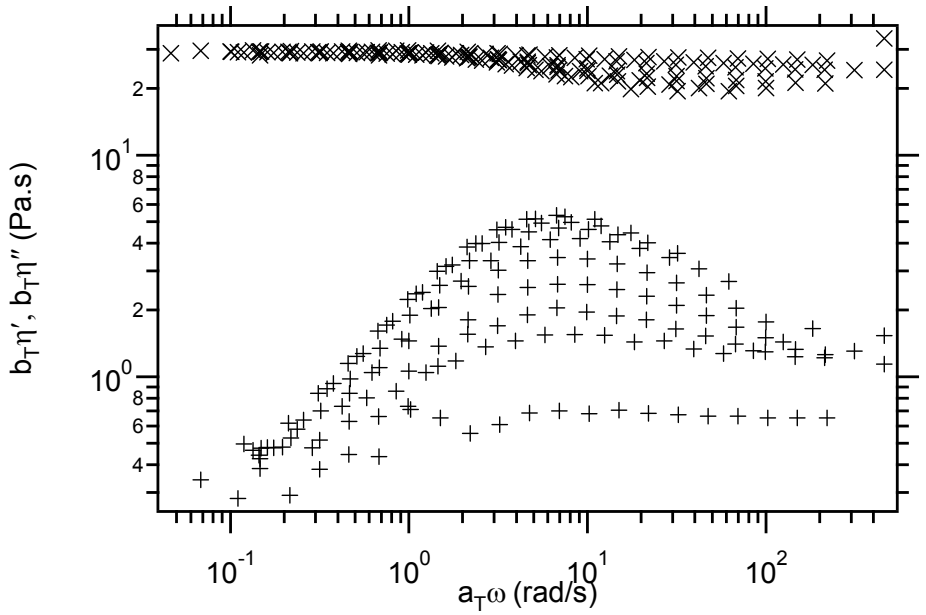

(b)

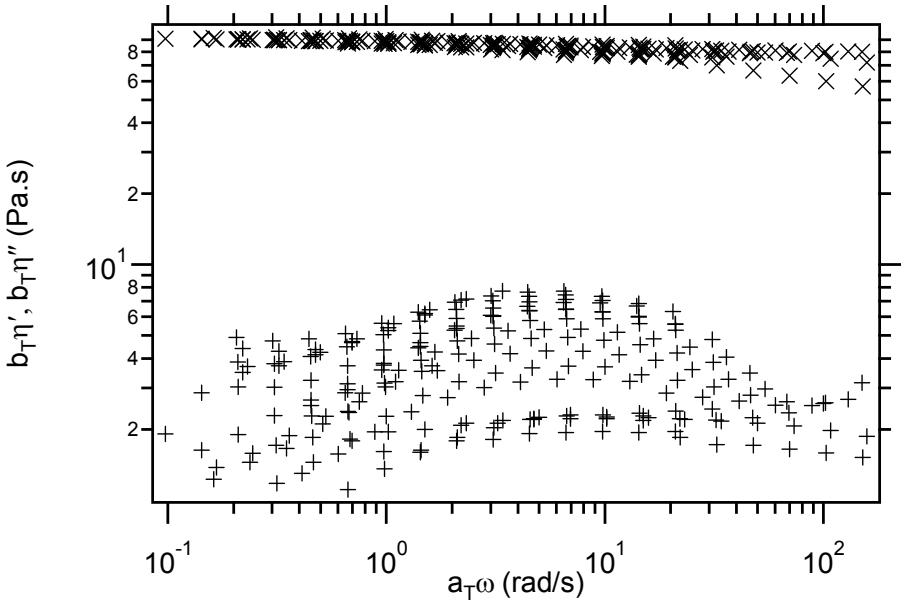

Figure 5.11. Plot of η', η'' vs. reduced frequency for PEO–900 tracer in PEO–1/PMMA–1.5 blends for (a) 80% PMMA, and (b) 90% PMMA compositions. (×) η' for tracer blend, (+) η'' for tracer blend.

resulted in similar temperature dependences of component relaxation times.

Since tTS breakdown is observed in both PEO/PMMA as well as PEO/PVPh blends with PEO tracers of similar molecular weights and in blends rich in the high T_g component, it is clear that hydrogen bonding does not play the major role in dictating temperature dependence of component dynamics. To explain tTS breakdown in PVPh and PMMA rich blends with PEO tracers, we have to consider differences in molecular weights of the matrix components and tracer chains. The scenario of such a large molecular weight tracer (PEO–845 in PEO/PVPh and PEO–900 in PEO/PMMA) in a much smaller matrix is comparable to that of bimodal blends where two significantly different molecular weights of the same polymer are blended together. Several studies[34–37] have shown theoretically that when a bimodal blend of long and short components is considered, the blend will exhibit *solution dynamics* if the degree of polymerization of the large component, N_L is greater than square of the degree of polymerization of the small component, N_S, i.e. $N_L >> N_S^2$. To check for this criterion, we compute the following N_L/N_S^2 ratios: $N_{PEO-845}/(N_{PEO-1})^2 \approx 37$; $N_{PEO-845}/(N_{PVPh-5})^2 \approx 11$; $N_{PEO-900}/(N_{PMMA-1.5})^2 \approx 91$. These results for PEO/PVPh and PEO/PMMA blends with PEO tracer meet the aforementioned criteria and hence, we can expect these blends to exhibit solution dynamics. However, it should be noted that a SANS study on PEO/PMMA blends with high molecular weight PEO and PMMA tracers[38] found no appreciable evidence of PMMA swelling while the findings for PEO swelling in the blend were inconclusive. However, the use of relatively smaller molecular weight polymer tracers as compared to the ones used in the dynamics study, could have acted to reduce the magnitude of any swelling.

One other reason to believe that PEO/PVPh blends assume solution dynamics will be discussed in detail later in this section, but will be briefly presented here. We compared the shape of the PEO tracer η'' relaxation to theoretical predictions of the Rouse and Zimm models, and found the Zimm predictions to more accurately describe the shape.

The tTS breakdown observed in PEO tracer blends in PEO/PVPh with $\phi_{PVPh} \geq 0.5$ and in PEO/PMMA with $\phi_{PMMA} \geq 0.8$ can probably be explained by considering that these blends are more like polymer solutions. We speculate that PEO tracer chain conformations are such that the chains tend to be "non–draining" in nature. If we assume matrix polymers moving past a PEO–845 coil, the inner regions of the tracer chain are somewhat shielded by the outer PEO repeat units. Thus, even though some matrix polymers penetrate inside the PEO tracer chain, the amount of matrix polymer in contact with PEO chains diminishes upon transitioning from the outer surface to inner regions of the coil. Thus, when a significant amount of PEO is present in the blend, the frictional environment encountered by PEO–845 chains is relatively uniform since matrix PEO chains have the same mobility as segments of PEO–845 tracer at the same length scale. The amount of stiff, slow moving PMMA or PVPh is not enough to provide considerable friction in the outer regions of PEO–845 chains.

As the blend is enriched in PVPh or PMMA, the frictional environment faced by PEO-845 becomes more heterogeneous. Outer regions of PEO–845 coils, even though more flexible and much more rapid than PVPh or PMMA, cannot relax as fast as the ones in the inner regions of the same coil because of differences in the frictional environment. This difference in mobility is affected by the temperature – the mobility difference

decreases with increasing temperature because of lesser friction experienced by outer PEO–845 segments. The different temperature dependence of relaxation rates in different parts of same PEO–845 chains cause breakdown of time–temperature superposition.

In PEO/PMMA, tTS fails for blends greater than 80% PMMA, while it breaks down for PEO/PVPh blends with 50% or greater PVPh. This is possibly because the matrix PVPh has a T_g of 157 °C while the matrix PMMA has a T_g of 56 °C. The matrix PEO in both cases has similar T_gs. The much higher T_g of PVPh relative to that of PMMA makes PEO/PVPh blends much stiffer at relatively lower PVPh concentrations compared to that in PEO/PMMA blends. The PEO tracers experience more dynamically heterogeneous environment at the same blend composition in PEO/PVPh as opposed to in PEO/PMMA blends, hence exhibiting tTS failure sooner (at relatively lower PVPh composition) in PEO/PVPh blends.

A scenario similar to what we have speculated above for tTS failure was suggested by Chen and co–workers.[39] They explained tTS failure in dynamically symmetric blends such as PEO/PVPh or PEO/PMMA by suggesting that the fast moving chains (PEO in our case) get split into two groups due to concentration fluctuations. A small fraction of the chains are surrounded in a transient region of excess stiffer chains while the remaining fraction experiences the mean blend composition. Hence this majority and minority component of these fast moving chains relax at different rates and the difference of these relaxation rates decreases with increasing temperature. The different temperature dependence of these relaxation rates causes tTS breakdown according to this postulate.

5.3.3 Composition and Temperature Dependence of ζ

As seen in Figures 5.3 and 5.4, ζ_{PVPh} and ζ_{PEO} increase upon reduction in temperature at fixed composition as well as upon increase of the high T_g component at fixed temperature. The PEO ζ shows no increase with the addition of 10% PVPh and is the same as that of pure PEO–1 homopolymer. Even with addition of 20% PVPh in the blend, the increase in ζ is not appreciable, especially at higher temperatures. On the other hand, PVPh ζ increases significantly upon addition of only 10% PVPh to the blend. To compare the temperature and composition dependence of PEO and PVPh more quantitatively, the ratio of PVPh and PEO friction factors, ζ_{PVPh}/ζ_{PEO} was analyzed. As seen in Figure 5.5, for 10% and 20% PVPh blends, ζ_{PVPh} is approximately 10 times larger than ζ_{PEO} indicating that even for a PEO rich environment, PVPh retains some of its significantly slower relaxation mechanism. This observation is contrary to what was observed in the PEO/PMMA blends[1] where ζ_{PMMA} and ζ_{PEO} have nearly the same values for $\phi_{PMMA} \leq 0.2$.

For the 10%, 20%, and 35% PVPh blends, PEO and PVPh exhibit the same temperature dependence, since ζ_{PVPh}/ζ_{PEO} stays constant with temperature. However for the 50% PVPh blend, this ratio increases as we lower the temperature. The increase with temperature is even more significant for the 65% PVPh blend.

Similar to the PEO/PVPh case, decoupling of friction factors was observed for 80% and 90% PMMA blends in PEO/PVPh upon reduction in temperature. These were the same blends in which tTS failure was observed upon addition of PEO tracer. The

same happened in 50% and 65% PVPh blends. i.e., decoupling of friction factors was observed and tTS failed for these two blends.

The strong temperature dependence of $\zeta_{PVPh}/\ \zeta_{PEO}$ for 50% and 65% blends can be explained by hydrogen bonding. CGPAM predictions in Figure 5.10 show that in 65% PVPh blend, the total number of hydrogen–bonded VPh groups [Figure 5.10 (a)] is larger than hydrogen bonded EO groups [Figure 5.10 (b)]. The increase in the number of hydrogen–bonded VPh groups with decrease in temperature relative to that of hydrogen bonded EO groups is also larger. Thus, PVPh experiences increasingly greater friction relative to PEO as temperature is lowered because more PVPh chains have limited mobility compared to PEO chains, since a larger number of VPh groups than EO groups are hydrogen bonded at lower temperatures. The same explanation applies to the 50% PVPh blend. The only difference is that the increase in the number of hydrogen bonded VPh groups upon reduction in temperature is lower relative to that of PEO. Hence, ζ_{PVPh} doesn't exhibit as strong a temperature dependence as in the 65% PVPh blend.

5.3.4 Composition and Temperature Dependence of Matrix Viscosities

Matrix viscositiy as a function of temperature and composition shown in Figure 5.6 exhibit trends similar to that of ζ_{PEO} and ζ_{PVPh}, i.e., as expected, viscosity monotonically increases with decreasing temperature at fixed composition, and increases with increasing composition of high T_g component (PVPh) at fixed temperature. Over a composition range from 0–65% PVPh, the matrix viscosity varies by as much as six orders of magnitude at a given temperature. Similar to contributions to η' and η'',

PEO–845 and PVPh–290 tracers would be expected to contribute to the steady shear viscosity of the blends. The contribution of PVPh–290 and PEO–845 tracers to the matrix viscosity is determined by taking ratios of tracer blend viscosity to matrix viscosity. This ratio is shown as a function of temperature in Figure 5.12.

5.3.5 PEO–845 tracer contribution to blend viscosity

In Figure 5.12 (a), $\eta_{\text{PEO tracer blend}}/\eta_{\text{matrix}}$ for all but the 65% PVPh blend is independent of temperature. The magnitude of this ratio varies from 4–6 for these blends, and that is primarily because of a small variation in amounts of PEO–845 tracer present in each blend. The ratio for the 65% blend shows a strong temperature dependence, and varies by almost an order of magnitude over the temperature range studied. At high temperatures, this ratio decreases to the same value as that of the 20% or 35% PVPh blends.

To explain why the 65% PVPh blend ratio has such strong temperature dependence while the same ratio for other blends do not, we have to consider the CGPAM (Figure 5.10), which predicts that the number of inter–associated EO groups stays relatively unaffected by temperature for 10% and 20% PVPh blends. Hence, we see no change with temperature of PEO tracer blend viscosity relative to that of the matrix for these blends. However, the number of inter–associated EO groups is almost the same for both 50% and 65% PVPh blends, as is the change in the number of inter–associated EO groups with temperature. Therefore, the much stronger temperature dependence for the 65% blend ratio compared to that of the 50% blend cannot be explained based on inter–molecular interactions alone.

(a)

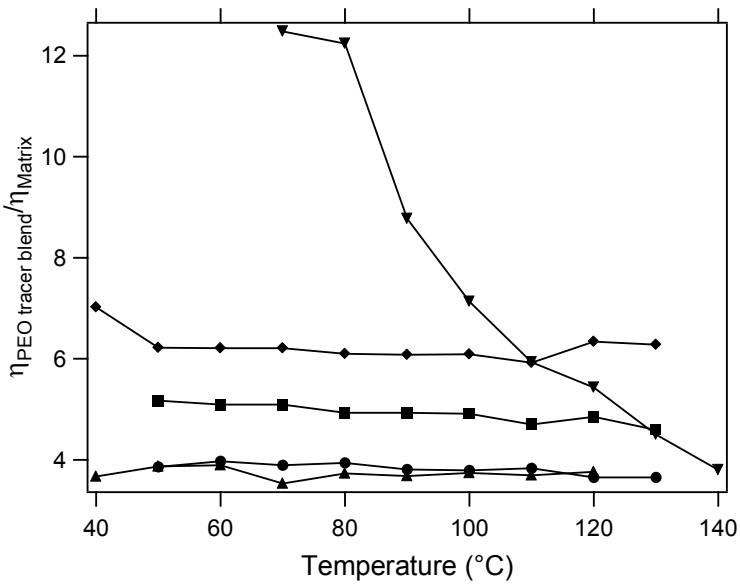

(b)

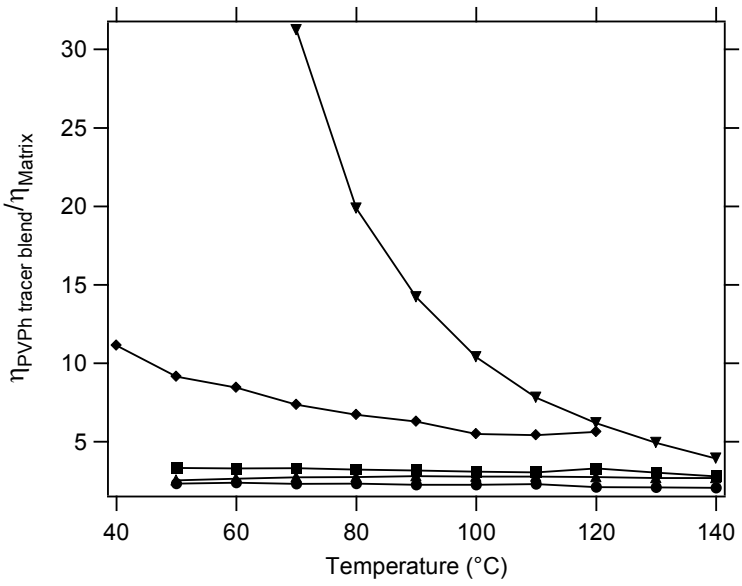

Figure 5.12. Ratio of (a) PEO–845 tracer blend viscosity to matrix viscosity, (b) PVPh–290 tracer blend viscosity to matrix viscosity as a function of temperature for PEO–1/PVPh–5 blends. (■) 10% PVPh, (●) 20% PVPh, (▲) 35% PVPh, (♦) 50% PVPh, (▼) 65% PVPh.

With an increase in PVPh concentration, the number of intra–associated OH groups also increases in a nonlinear fashion. The temperature dependence of the intra–associated VPh groups also becomes stronger with increasing PVPh composition. This is why an increase from 50% to 65% PVPh results in large PEO tracer chains encountering an increasingly rigid environment to move through (because of hydrogen bonded network) and this effect is enhanced with decreasing temperature.

Another explanation of why the ratio of viscosities for the 50% blend does not exhibit a strong temperature dependence like the 65% blend is that while the number of inter–associated EO groups is the same in both blends, the fraction of EO groups on tracer chains, relative to matrix, is higher in the 65% PVPh blend than in the 50% PVPh blend (since the tracer concentration stays constant while matrix PEO concentration decreases with increasing PVPh content). Therefore, in the 50% PVPh blend more matrix EO groups contribute to hydrogen bonding than in the 65% blend, in effect *diluting* tracer EO contributions and as a result, no appreciable change in temperature dependence is observed for the tracer blend viscosities.

Comparing the PEO–845 tracer contribution to blend viscosity in PEO–1/PVPh–5 blends to that of PEO–900 tracers to blend viscosity in PEO–1/PMMA–1.5 blends,[37] a significant difference in trends can be observed. In PEO/PMMA, as the blends become richer in PMMA, $\eta_{\text{PEO tracer blend}}/\eta_{\text{matrix}}$ decreases to a value of 1 meaning that contribution of the PEO–900 tracer to blend viscosity becomes negligible and the temperature dependence of blends with and without tracer remains qualitatively the same. This is because at high PMMA concentrations, the contribution of matrix PMMA dominates the blend dynamics despite its molecular weight being much smaller than that of tracer. In

the PEO/PVPh system, PVPh has an even higher T_g than PMMA but still the matrix PVPh does not dominate dynamics like PMMA does. This difference underscores the effect of hydrogen bonding on the contribution of the polymer tracer to blend viscosity.

5.3.6 PVPh–290 tracer contribution to blend viscosity

In Figure 5.12 (b), $\eta_{\text{PVPh tracer blend}}/\eta_{\text{matrix}}$ as a function of temperature is constant for 10%, 20%, and 35% PVPh blends. However for 50% and 65% PVPh blends, decoupling of blend and matrix viscosity is observed at lower temperatures. The viscosity ratio for 65% blend increases much more rapidly than for the 50% blend at lower temperatures. To understand this behavior, once again we consider CGPAM predictions which show that for 50% and 65% blends the total number of hydrogen bonded OH groups increase as temperature is lowered. Even though this increase occurs in both matrix as well as the tracer blend, only in the tracer blend do high molecular weight PVPh tracers self associate with VPh groups in low molecular weight matrix PVPh *and* with VPh groups in PVPh tracer chains. This tracer–tracer self association is absent in just the matrix blend without any tracers. Due to these tracer–tracer associations, larger hydrogen bonded networks are present in the blend at any given time, resulting in a larger increase in blend viscosity as compared to that of matrix at lower temperatures. The change with temperature in number of hydrogen bonded OH groups for 10%, 20%, and 35% blends is relatively small or even negligible, resulting in similar temperature dependence of tracer blend and matrix viscosities. The value of $\eta_{\text{PVPh tracer blend}}/\eta_{\text{matrix}}$ for 10% – 35% PVPh blends is roughly constant at 2.5 – 3 reflecting the contribution of PVPh–290 tracer to the blend viscosity.

Comparing the PVPh–290 tracer contribution to the blend viscosity in PEO–1/PVPh–5 blends to that of PMMA–100 to the blend viscosity in PEO–1/PMMA–1.5 blends reveals some similarities as well as contrasting behavior. Addition of PMMA–100 tracer produces a measurable increase in blend viscosity. As blends become richer in PMMA, and as the temperature is lowered, no decoupling of tracer blend and matrix viscosities is observed. This is in stark contrast to what is observed in PEO–1/PVPh–5 blends. It is evident from this comparison that hydrogen bonding is the reason of decoupling of tracer blend and matrix viscosities at lower temperatures for blends with high PVPh concentration.

5.3.7 Comparison of PVPh and PEO tracer blend viscosities

To compare the temperature and composition dependence of PEO and PVPh tracer blend viscosities, the ratio of blend viscosities was plotted as a function of temperature and is shown in Figure 5.13. $\eta_{\text{PVPh tracer blend}}/\eta_{\text{PEO tracer blend}}$ for the 65% PVPh blend increases more rapidly than for the 50% blend upon reduction in temperature. This ratio stays constant with temperature for 35%, 20%, and 10% blends at an approximate value of 0.5–0.6. These trends are very similar to those observed in comparison of PEO and PVPh friction factors ($\zeta_{\text{PVPh}}/\zeta_{\text{PEO}}$) shown in Figure 5.5.

To explain these trends, we again turn to CGPAM predictions. As previously described, according to CGPAM (Figure 5.10), in the 65% PVPh blend, the total number of hydrogen bonded VPh groups is greater than hydrogen bonded EO groups. Also, the increase in number of hydrogen bonded VPh groups upon reduction in temperature is larger than the increase in hydrogen bonded EO groups as temperature is reduced. This

leads to a more profound increase in viscosity at lower temperatures for PVPh tracer blends than for PEO tracer blends.

Another factor contributing to a stronger temperature dependence of PVPh tracer blend viscosity in the 65% blend is that the PVPh tracers self associate not only with matrix PVPh but also with other PVPh tracer chains, hence forming larger, hydrogen bonded aggregates at any given time. In the PEO tracer blend, the PEO tracers associate only with matrix PVPh, and do not have the ability to form tracer–tracer associations. Thus this does not result in as large an increase in viscosity at lower temperatures.

Similarly, in the 50% PVPh blend, the PEO concentration is still not high enough to significantly interfere with self association of VPh groups present in high molecular weight PVPh tracers. The larger composition of PEO in 50% blend relative to 65% PVPh blend does dilute the PVPh tracer–tracer contacts to some extent, resulting in relatively weaker decoupling of PEO and PVPh tracer blend viscosities at lower temperature.

For 10%, 20%, and 35% PVPh blends, the PEO concentration is high enough in the blends to significantly dilute tracer PVPh–tracer PVPh contacts, resulting in the same temperature dependence of PVPh tracer blend viscosities as that of PEO tracer blends. Also, for these three blends, $\eta_{\text{PVPh tracer blend}}$ is less than $\eta_{\text{PEO tracer blend}}$ because the degree of polymerization of PVPh tracer is approximately 1/3 that of a PEO tracer. At high PEO concentrations hydrogen bonding is not as significant a contributor to viscosity as the polymer molecular weight. Hence, higher molecular weight PEO tracer contributes more to blend viscosity relative to PVPh tracer.

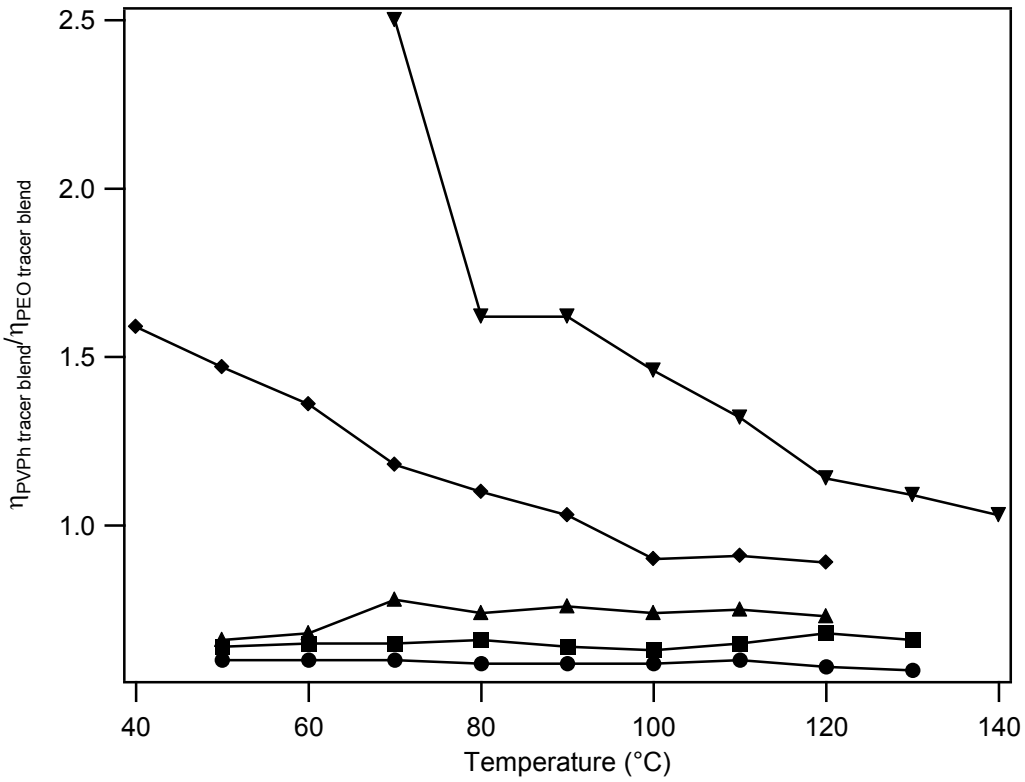

Figure 5.13. Ratio of PVPh tracer blend viscosity to that of PEO tracer blend viscosity as a function of temperature for various PEO–1/PVPh–5 blend compositions. (■) 10% PVPh, (●) 20% PVPh, (▲) 35% PVPh, (♦) 50% PVPh, (▼) 65% PVPh.

5.3.8 Shape of PEO and PVPh Tracer Blend Relaxation Spectra

The time–temperature superposition (tTS) failure in PVPh–rich blends containing the PEO–845 tracer prompted us to analyze the composition dependence of the *shape* of tracer relaxation spectra (η'' curves). For the 50% and 65% PVPh blends with PEO-845 tracer, the η'' curves were overlapped by horizontal shifting followed by a vertical shift. Since we did not try to overlap η' and η'' curves simultaneously, we obtained nicely overlapped η'' master curves for these blends. Tracer blend η'' values were divided by the maximum η'' value and these normalized data sets (η''/η''_{max}) were plotted against similarly normalized frequencies (ω/ω_{max}), where ω_{max} is the frequency corresponding to maximum η'' value. The plots of normalized relaxation spectra for all but 10% PVPh blends are shown in Figure 5.14. Also shown in the same figure are the plots of normalized relaxation spectra for blends with PVPh–290 tracer. To compare the shape of relaxation spectra with those predicted by theoretical models, η'' spectra were generated using the Rouse and Zimm models. Both these models predict the same form of equation for determining G', which is:

$$G' \sim \sum_{p=1}^{N} \frac{(\omega\tau_p)^2}{1+(\omega\tau_p)^2} \tag{5.14}$$

where τ_p is the average time for a section of chain containing N/p springs in the bead–spring model containing N+1 beads, to recover from a disturbance. The relationship between τ_p and the longest relaxation time, τ_1, is:

$$\tau_p = \frac{\tau_1}{p^y} \tag{5.15}$$

where $y = 2$ for the Rouse model and $y = 1.5$ for the Zimm model. To calculate G' at each ω, we used $N = 100$, so the summations for G' determination (as seen in eq. 5.14) were from $p = 1$ to $p = 100$. Once G' was calculated, η'' was calculated by using eq. 5.16:

$$\eta'' = \frac{G'}{\omega} \tag{5.16}$$

The Rouse and Zimm model predictions for η'' spectra are also displayed in Figure 5.14.

(a)

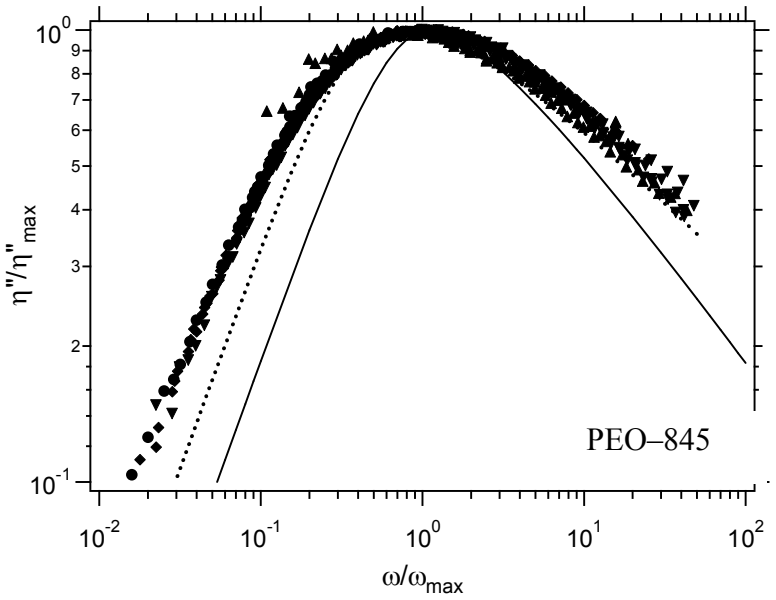

(b)

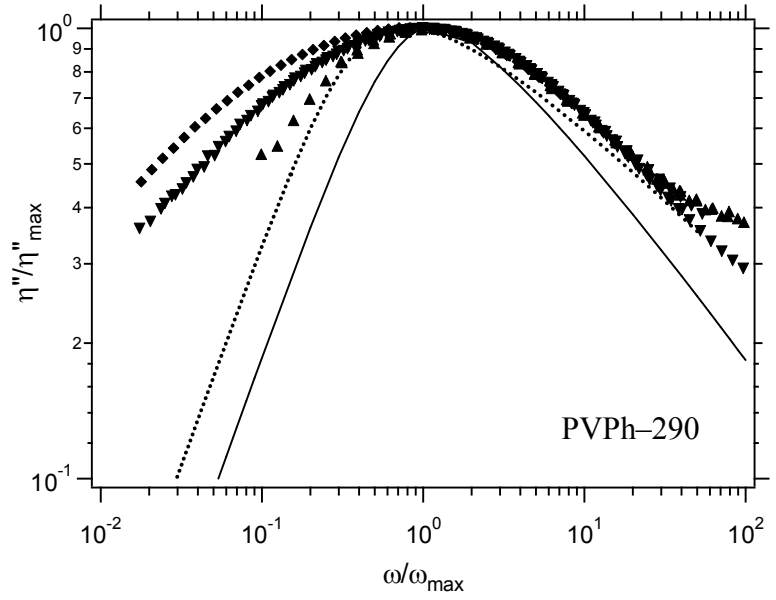

Figure 5.14. Ratio of η'' to η''_{max} as a function of normalized frequency for (a) PEO–845 tracer, (b) PVPh–290 tracer in PEO/PVPh blends. (●) 20% PVPh, (♦) 35% PVPh, (▼) 50% PVPh, (▲) 65% PVPh. Solid line is the Rouse prediction and the dotted line is the Zimm prediction.

For PVPh-290 tracer blends, a narrowing of the relaxation spectrum is observed as PVPh content in the blend is increased from 35% to 65%. For PEO–845 tracer blends, a negligible effect on relaxation spectra width is observed upon increase of PVPh content. Thus, the shape of PEO tracer relaxation spectra is composition independent (unlike that of PVPh tracers).

To gain more insight into why the shape of η'' peaks changes or does not change with composition, the Rouse and Zimm models were used to predict the shape of η'' peaks. The theoretically predicted data were normalized in the same manner as experimental data. As seen in Figure 5.14 (a), the shape of the PEO tracer relaxation spectra are better described by Zimm predictions rather than Rouse predictions. Despite doing a much better job than Rouse model in predicting shape of relaxation spectra, Zimm model predictions produce a curve that is still narrower in width than the experimental spectra. Zimm predictions fit experimental data well at high frequencies but fall a little short at low frequencies. One reason that Zimm prediction has narrower shape than actual PEO relaxation spectra is that PEO tracer, despite being relatively monodisperse, still has some polydispersity. Our calculations for the Zimm, or for that matter even the Rouse models do not take polydispersity into account.

PVPh–290 tracer relaxation spectra are also compared with the Rouse and Zimm predictions, as seen in Figure 5.14 (b). Both models fail to describe the experimental data at low frequencies. Overall the Zimm model does a much better job at predicting shape of relaxation spectra. PVPh relaxation spectra are much broader than that of PEO, as seen by comparing them to Zimm model predictions. The shape predicted by Zimm model is much narrower in comparison to that of PVPh tracer spectra and is almost the same as

that of PEO tracer spectra demonstrating the relative broadness of PVPh tracer spectra. The broader PVPh spectra relative to that of PEO indicate a larger distribution of tracer relaxation times.

To explain the composition dependence of the shape of the η'' curves in PVPh–290 tracer blends, we have to consider the different types of interactions present in the tracer blend *that are absent* in the matrix. These are tracerPVPh–matrixPEO, tracerPVPh–matrixPVPh, and tracerPVPh–tracerPVPh hydrogen bonds. In all the blends, the tracer composition is roughly constant (~1.5–1.8%). As the matrix PVPh content increases, tracerPVPh–tracerPVPh contacts are diluted as tracerPVPh–matrixPVPh contacts increase. At the same time tracerPVPh–matrixPEO contacts also decrease. The most significant contribution to the relaxation peak comes from tracerPVPh–tracerPVPh contacts because more these types of hydrogen bonds are present, more polydispersity is observed in relaxation times as a result of larger hydrogen bonded networks. So, as the matrix PVPh content increases from 35% to 65%, the tracerPVPh–tracerPVPh contacts decrease and the relaxation times become more narrowly distributed, resulting in a narrowing of the PVPh tracer relaxation spectra.

Also, focusing on the low frequency end of PVPh–290 tracer blend spectra, it can be seen that the relaxation profile has not reached the terminal regime indicating that relaxation processes are still in progress. This implies the presence of a large network–like structures that take longer to relax completely. As the matrix PVPh content increases, the relaxation times become smaller and relaxation peaks approach the terminal regime with a slope of 1 at the low frequency end. This indicates that as matrix PVPh content

increases, relaxing hydrogen bonded networks become smaller and, hence, relax more rapidly.

The η'' relaxation spectra for PEO–845 tracer blends, unlike PVPh relaxation spectra, exhibit a clear terminal regime. Since PEO cannot self associate the only interactions in PEO tracer blends that affect the shape of the relaxation spectra are tracerPEO–matrixPVPh. As PVPh composition changes in the blend, the amount of tracer EO and matrix EO groups bonded to PVPh vary, but that variation is not significant enough to make appreciable change in the width of relaxation spectra. If there were no interactions present, we would have expected the PEO relaxation spectra to broaden with increase in slower moving PVPh because of an increase in the dynamically heterogeneous environment. It is quite possible that PEO relaxation might broaden if PVPh composition in the blend were increased beyond 65 wt.%.

To check our expectation of relaxation spectra peak broadening upon addition of high T_g component to the blend, we compared the composition dependence of PEO/PVPh relaxation spectra shape to that of PEO/PMMA blends[1] where no specific interactions are present. The PEO/PMMA data analysis was performed in the same manner as described earlier. The spectra for PEO tracer blends, even though noisier than PEO/PVPh spectra, were conclusive enough. The normalized relaxation spectra for PEO–900 tracer in PEO–1/PMMA–1.5 blends are shown in Figure 5.15.

(a)

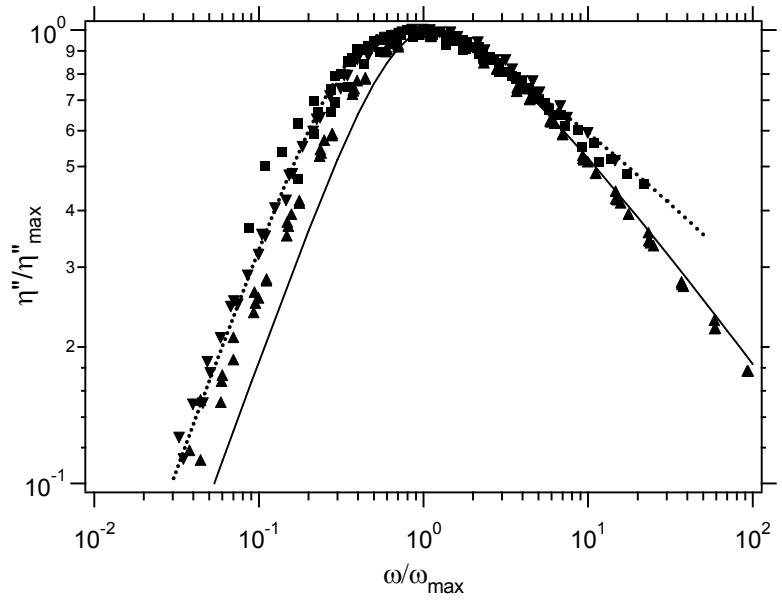

(b)

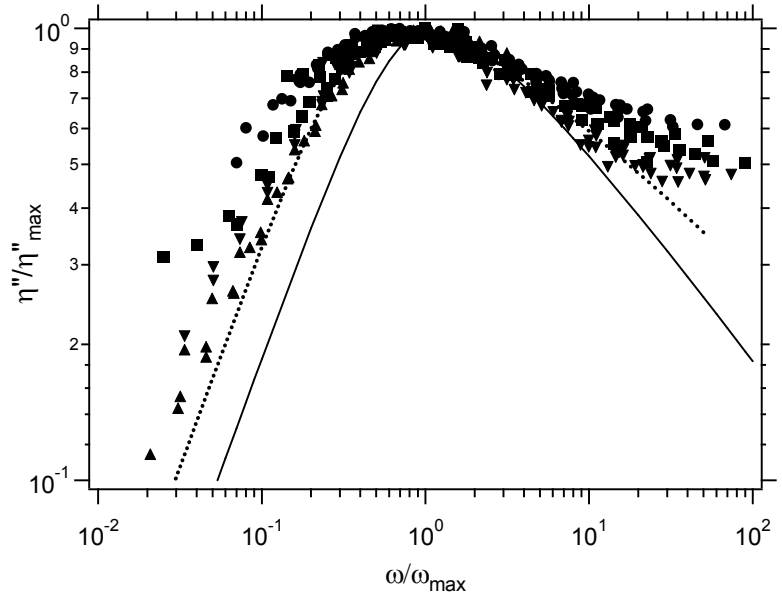

Figure 5.15. Ratio of η'' to η''_{max} as a function of normalized frequency for (a) PEO–900 tracer, and (b) PMMA–100 tracer in PEO–1/PMMA–1.5 blends. (▲) 50% PMMA, (▼) 80% PMMA, (■) 90% PMMA, (●) 100% PMMA. Solid line is the Rouse prediction and the dotted line is the Zimm prediction.

PEO–900 relaxation spectra show some moderate broadening with increasing PMMA composition, indicating more polydispersity in tracer relaxation times because of an increasingly heterogeneous dynamic environment. Even though this broadening of relaxation spectra is greater than that observed in PEO spectra in PEO/PVPh blends, it is still quite small compared to that in PMMA relaxation spectra in PEO/PMMA. At low PMMA concentrations, PEO spectra are quite nicely modeled by Rouse model but as PMMA increases beyond 80%, the Zimm model produces better predictions.

The PMMA–100 relaxation spectra, unlike those of PEO, show significant broadening upon addition of PMMA. This is in stark contrast to what was observed in PEO/PVPh blend where the high T_g, slow moving PVPh–290 relaxation spectra show significant *narrowing*, instead of broadening, upon addition of PVPh. The PMMA spectra narrow upon addition of PEO because as PEO composition increases, PMMA tracers experience progressively less friction, and hence can relax more homogeneously This is why relatively more monodisperse PMMA relaxation spectra are observed as blend composition changes from 100% PMMA to 50% PMMA. Comparing the experimental data to Rouse and Zimm predictions, it is seen that Rouse model describes the data poorly. Zimm model does a much better job in describing shape of PMMA relaxation spectra, especially for 50% PMMA.

Comparing tracer relaxation spectra in PEO/PVPh and PEO/PMMA blends, there is clear evidence of influence of hydrogen bonding on shape of η'' curves.

5.3.9 Calorimetric Glass Transition

The DSC scans for various compositions of PEO/PVPh blends in Figures 5.7, and 5.8 show single T_gs with relatively narrow transition widths. It is well established in athermal blends that glass transitions are broader than those of homopolymers. This is especially true for middle composition ranges where some blends exhibit glass transition widths as broad as 60 °C.[40] This broadening reflects dynamic heterogeneity as each component experiences a different effective environment because of self-concentration effects. Compared to athermal blends, the glass transition broadening in PEO–1/PVPh–5 blends is much narrower and is almost comparable to that in homopolymer PEO and PVPh even in the middle of the composition range. Similar observations have been reported for other PVPh blends.[28]

A single T_g for all PEO–1/PVPh–5 blends across the composition range is expected as it has been previously reported. In several such reports, PEO/PVPh miscibility is established based on presence of a single T_g in the blends. However, as reported by Lodge *et al.*[41] and Gaikwad *et al.*[42] miscible blends can exhibit two glass transitions if the difference in T_gs of blend components is large enough. They demonstrated two glass transitions in low molecular weight blends of PEO/PMMA, PEO/poly(vinyl acetate) (PEO/PVAc), and PEO/poly(lactide) (PEO/PLA). The component T_g differences in these blends ranged from 96–198 °C. The difference in T_gs of PEO and PVPh used in this study is 224 °C. The presence of a single T_g in this miscible blend despite such a large difference in component T_gs is quite remarkable, and is indicative of similar effective environments of each component as a result of coupling at the segmental level.

Figure 5.16 shows the composition dependence of PEO–1/PVPh–5 blend T_gs. The T_gs exhibit a negative deviation from linear dependence for PVPh compositions greater than 20%. Even though the deviation is negative for the composition range 20–35% PVPh, the trend is clearly a gradual increase in T_g as PVPh composition is lowered from 35% to 20%. Kuo, *et al.*[43] report negative deviation of composition dependence of PEO/PVPh blend T_gs except for blends very rich in PEO. They used composition intervals of 20 wt.% for studying the composition dependence of T_gs, which was larger than ours. We used composition interval of 5 wt.% for the PEO–rich blends. Because of their larger composition spacing, Kuo and co–workers recorded only one composition (20% PVPh) where they observed deviation of T_g from the general negative deviation trend. Due to probing of smaller composition intervals, we were able to more clearly see a change in shape of composition dependence of T_gs.

The experimental T_gs are higher at high PEO concentrations because PEO crystallizes in those blends at temperatures below 40 °C. This makes the amorphous part of the blend richer in PVPh, hence increasing the blend T_g. To account for effects of PEO crystallinity, which was calculated using eq. 5.4, the blend composition was recalculated after determining the amount of crystalline PEO in the blend. Experimental T_gs were assigned to the corresponding amorphous blend compositions and this composition dependence is shown in Figure 5.16 (b).

(a)

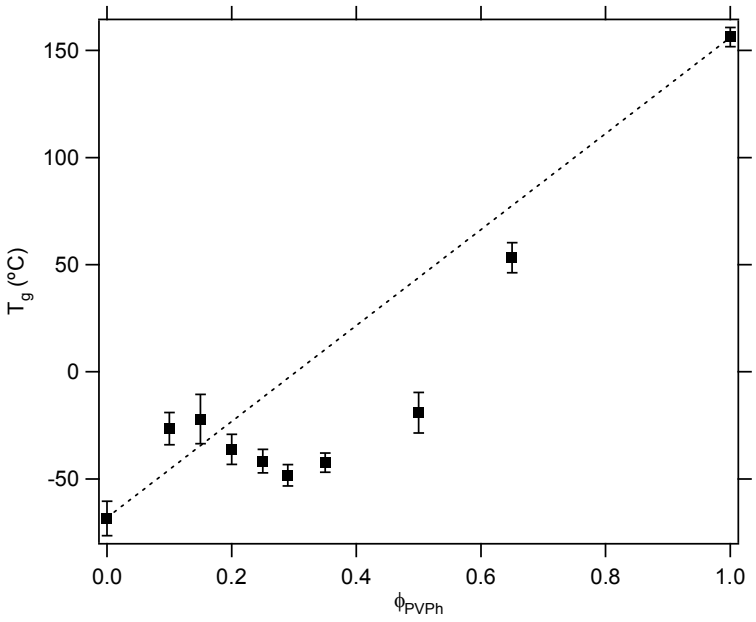

(b)

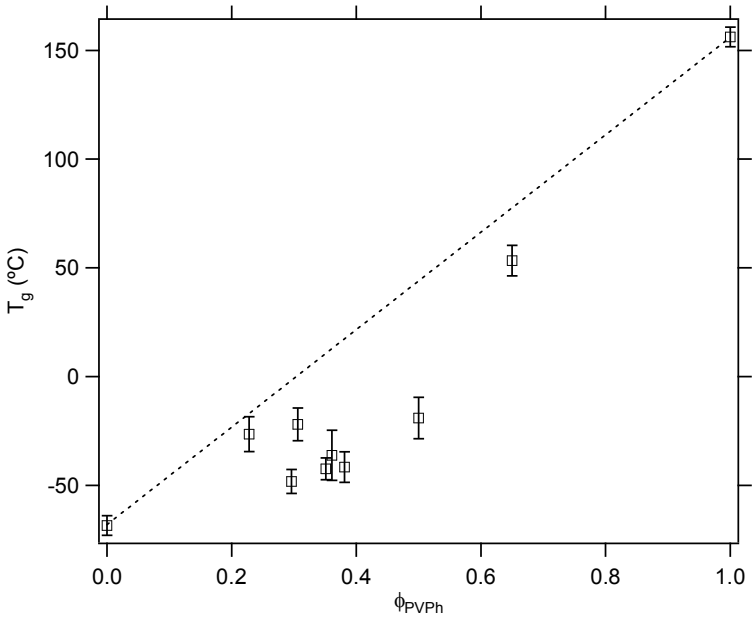

Figure 5.16. Composition dependence of PEO–1/PVPh–5 blend T_gs (a) before accounting for PEO crystallinity in blend, (b) after accounting for PEO crystallinity in blend. Dotted line represents linear composition dependence.

5.4 Summary and Conclusions

Rheological measurements were carried out using tracer blends of PEO/PVPh to extract dynamic information. Plots of η'' vs. frequency were prepared to extract longest relaxation times of tracer chains which were then used to extract monomeric friction factors. Time–temperature superposition failure was observed in PEO tracer blends with high PVPh composition. This phenomenon was previously observed in PEO/PMMA blends with PEO tracer and high PMMA composition. Composition dependence of the shape of η'' tracer relaxation spectra was investigated and a stark contrast was observed in shapes of blends with PVPh and PMMA tracers. For blends with PEO tracers, the composition dependence of the shape of η'' tracer relaxation spectra was quite similar for PEO/PMMA and PEO/PVPh blends. The shapes of relaxation spectra were also compared with Zimm and Rouse predictions and Zimm model described the experimental data better for all blends.

Tracer contribution to blend viscosities were also investigated and it was found that for high PVPh composition in the blends, temperature dependence of tracer blend viscosities was much stronger than that of just the matrix without any tracer. This behavior is also quite different than what PEO/PMMA blends exhibited.

Glass transition temperatures were measured for PEO/PVPh blends using DSC. Across the composition range, single and relatively narrow glass transitions were observed which is different than what has usually been observed in similar dynamically asymmetric blends without hydrogen bonding.

In light of all these observations, we can answer the two questions we posed at beginning of this chapter, one of them being how do component dynamics in blends with

hydrogen bonding compare with that in weakly interacting blends. Based on experimental results, there is reason to believe that hydrogen bonding does affect component chain dynamics to some extent but not nearly as much as had been anticipated. The most striking observation which reveals similar component dynamics in blends with and without hydrogen bonding is tTS failure in PEO tracer blends in PEO/PVPh as well as PEO/PMMA. Hydrogen bonding does seem to play a significant role in determining temperature dependence of viscoelastic properties such as blend viscosity and also in determining distribution of chain relaxation times as seen by strong composition dependence of shape of η'' relaxation spectra.

The second question posed was: Does intermolecular hydrogen bonding simplify blend dynamic behavior by coupling component dynamics? We can confidently say that it is not the case based on our experimental results and analysis.

5.5 References

[1] Zeroni, I.; Ozair, S.; Lodge, T. P. *Macromolecules* **2008***, 41*, 5033.
[2] Sanchis, A.; Prolongo, M. G.; Masegosa, R. M.; Rubio, R. G. *Macromolecules* **1995**, *28*, 2693.
[3] Prolongo, M. G.; Salom, C.; Masegosa, R. M.; Moreno, S.; Rubio, R. G. *Polymer*, **1997**, *38*, 5097.
[4] Li, D.; Brisson, J. *Macromolecules* **1996**, *29*, 868.
[5] Jin, X.; Zhang, S.; Runt, J. *Macromolecules* **2003**, *36*, 8033.
[6] Zhang, S.; Runt, J. *J. Polym. Sci., Part B. Polym. Phys.* **2004**, *42*, 3405.
[7] Coleman, M. M.; Lee, J. Y.; Serman, C. J.; Wang, Z.; Painter, P. C. *Polymer* **1989**, *30*, 1298.
[8] Kuo, S. W.; Chang, F. C. *Macromolecules* **2001**, *34*, 5224.
[9] Kuo, S. W.; Chang, F. C. *Macromolecules* **2001**, *34*, 4089.
[10] Serman, C. J.; Xu, Y.; Painter, P. C.; Coleman, M. M. *Polymer* **1991**, *32*, 516.
[11] Cai, H.; Ait-Kadi, A.; Brisson, J. *Polymer* **2003**, *44*, 1481.
[12] Yang, Z.; Han, C. D. *Macromolecules* **2008**, *41*, 2104.

[13] Qin, C.; Cheng, C.; Pires, A. T. N.; Belfiore, L. A. *Polym. Mater. Sci. Eng.*, **1989**, *61*, 945.
[14] Moskala, E. J.; Varnell, D. F.; Coleman, M. M. *Polymer* **1985**, *25*, 228.
[15] Zhang, X.; Takegoshi, K.; Hikichi, K. *Macromolecules* **1992**, *25*, 2336.
[16] Lodge, T. P.; McLeish, T. C. B. *Macromolecules* **2000**, *33*, 5278.
[17] Lutz, T. R.; He, Y.; Ediger, M. D.; Cao, H.; Lin, G.; Jones, A. A. *Macromolecules* **2003**, *36*, 1724.
[18] Haley, J. C.; Lodge, T. P. *J. Chem. Phys.* **2005**, *122*, 234914.
[19] Liu, C. Y.; Halasa, A. F.; Keunings, R.; Bailly, C. *Macromolecules* **2006**, *39*, 7415.
[20] Doi, M.; Edwards, S. F. *The Theory of Polymer Dynamics*; Clarendon Press: New York 1986.
[21] Ferry, J. D. *Viscoelastic Properties of Polymers*, Third ed.; John Wiley & Sons: New York, **1980**.
[22] Rouse, P. E. *J.Chem. Phys.* **1953**, *21*, 1272.
[23] Pelton, R.; Xiao, H.; Brook, M. A.; Hamielec, A. *Langmuir* **1996**, *12*, 5756.
[24] Fetters, L. J.; Lohse, D. J.; Richter, D.; Witten, T. A.; Zirkel A. *Macromolecules* **1994**, *27*, 4639.
[25] Gestoso, P.; Brisson, J. *J. Comput. Theor. Polym. Sci.* **2001**, *11*, 263.
[26] Inoue, T.; Okamoto, H.; Osaki, K. *Macromolecules* **1991**, *24*, 5670.
[27] Still, R. H.; Whitehead, A.; *J. Appl. Polym. Sci.* **1977**, *21*, 1199.
[28] Yang, Z.; Han, C. D. *Macromolecules* **2008**, *41*, 2104.
[29] Li, X.; Hsu, S. L. *J. Polym. Sci., Part B: Polym. Phys.* 22 (1984) 1331.
[30] Coleman, M. M.; Graf, J. F.; Painter, P. C. Specific Interactions and the Miscibility of Polymer Blends; Technomic Publishing: Lancaster, PA, 1991.
[31] Coleman, M. M.; Xu, Y.; Painter, P. C. *Macromolecules* **1994**, 27, 127.
[32] Serman, C. J.; Painter, P. C.; Coleman, M. M. *Polymer* **1991**, 32, 516.
[33] Le Menestrel, C.; Bhagwagar, D. E.; Painter, P. C.; Coleman, M. M.; Graf, J. F. *Macromolecules* **1992**, *25*, 7101.
[34] Brochard–Wyart, F.; Ajdarif, A.; Leibler, L.; Rubinstein, M.; Viovy, J. L. *Macromolecules* **1994**, *27*, 803.
[35] Daoud, M.; de Gennes, P. G.; *J. Polym. Sci., Polym. Phys. Ed.* **1979**, *17*, 1971.
[36] Wang, S.; Elkasabi, Y.; Wang, S. Q. *Macromolecules* **2005**, *38*, 125.
[37] Zeroni, I. *Ph.D.* Thesis, University of Minnesota, **2008.**
[38] Zeroni, I.; Lodge, T. P. *Macromolecules* **2008**, *41*, 1050.
[39] Chen, Q.; Matsumiya, Y.; Masubuchi, Y.; Watanabe, H.; Inoue, T. *Macromolecules* **2008**, *41*, 8694-8711
[40] Kim, J. K.; Lee, H. H.; Son, H. W.; Han, C. D. *Macromolecules* **1996**, *29*, 7155.
[41] Lodge, T. P.; Wood, E. R.; Haley, J. C. *J. Polym. Sci. Part B: Polym. Phys.* **2005**, *44*, 756.
[42] Gaikwad, A. N.; Wood, E. R.; Ngai, T.; Lodge, T. P. *Macromolecules* **2008**, *41*, 2502.
[43] Kuo, S.; Liu, W.; Chang, F. *Macromol. Chem. Phys.* **2005**, *206*, 2307.

Chapter 6. Determination of PVPh Chain Conformations and Dimensions Using Small Angle Neutron Scattering

6.1 Introduction

It is well established that PVPh forms miscible blends with several polymers, PEO being one of them. In this thesis, part of the work presented is a study of component chain dynamics in blends of PEO and PVPh. The hydroxyl groups in PVPh form *intermolecular* hydrogen bonds with ether groups in PEO, as well as *intramolecular* hydrogen bonds with other PVPh hydroxyl groups. Thus, hydrogen bonding plays an important role in miscibility and dynamic behavior of this blend.

To investigate the temperature and composition dependences of the monomeric friction factor, the longest relaxation time of PVPh (or PEO) tracer chains in the blend is determined and the friction factor, ζ, is extracted using eq. 2.3. However, to be able to precisely determine ζ, the value of the statistical segment length, b, is needed. To our knowledge, there is only one report in literature on chain dimensions of PVPh. Gestoso *et al.*[1] reported a computer simulation study which found a PVPh R_g of 24 ± 8 Å. The simulated PVPh chain had a degree of polymerization, N, of 250. The relationship between R_g and N for a Gaussian coil ($R_g^2 = Nb^2/6$) yields b = 3.7 ± 1.2 Å. This value is unrealistic because almost all flexible polymers have statistical segment lengths in the range of 5–7 Å. Moreover, computing the value of characteristic ratio, C_∞, from this

value of b results in C_∞ = 3.0. The characteristic ratio is a measure of chain flexibility; the larger C_∞ is, more stiff the polymer chains are because of local constraints. For polymers that primarily have C–C or C–O bonds along the backbone, C_∞ ranges from 4 to 12. Thus a C_∞ value of 3.0 suggests PVPh is one of the most flexible polymers. This is not plausible because large phenyl groups in PVPh provide steric constraints which should make it quite a stiff polymer. Hence, this reported value of R_g was not trustworthy and we did not use it in our computations. Since poly(styrene) (PS) is very similar in structure to PVPh, the only difference being absence of phenolic hydroxyl group in PS, we decided to use its statistical segment length value for PVPh.

Considering the lack of information in the literature on chain dimensions of PVPh, we decided to investigate chain conformations of PVPh in dilute solutions using small angle neutron scattering (SANS). Because of the need for contrast for measurable results, deuterated solvents were used to prepare PVPh solutions. SANS is a very useful technique to investigate polymer chain conformations in a melt or dilute solution. The wavelengths of neutrons are much smaller than a conventional He–Ne laser source (0.1–2 nm vs. 632.8 nm for He–Ne) and this is what allows access to a larger q range when compared to other radiation sources. The goal is to try to access as large a q range as possible by varying the sample to detector distance in order to obtain data in the Guinier regime (small q values). The Guinier regime is reached when product of q and radius of gyration, R_g, is less than 1, i.e., $qR_g \leq 1$. This allows for determination of R_g values without making prior assumptions about the structure of the coil, since no such information is required for Guinier analysis. If one cannot access the Guinier regime, i.e. if $1 \leq qR_g \leq 10$, then a structure factor specific to the shape of the molecule such as a

Gaussian coil, or hard sphere or rigid rod, has to be taken into account for determination of R_g.

6.2 Experimental

6.2.1 Materials

Dilute solutions of PVPh were prepared in deuterated tetrahydrofuran (d_8THF) and deuterated dimethyl sulfoxide (d_6DMSO). Fully deuterated THF and DMSO provide enough scattering length density contrast to obtain measurable scattered intensity. PVPh is soluble in both solvents. Both d_8THF and d_6DMSO were obtained from Cambridge Isotopes Laboratories and used as is. Two of the PVPh solutions contained d_8THF obtained from Sigma Aldrich.

Four different molecular weight samples of PVPh were used in preparing solutions. Table 6.1 lists the PVPh molecular weights used for these experiments. For each of the four molecular weights, multiple solution concentrations were prepared. All PVPh samples except one were synthesized in the lab using anionic polymerization. The 10,000 g/mol PVPh was obtained from Aldrich. Polydispersities of all four polymers were less than 1.2 based on SEC measurements. Table 6.1 also lists solution concentrations used for each solvent. All polymer samples from here onwards will be referred to by the name followed by their molecular weight in kg/mol. For example, 10,000 g/mol PVPh will be referred to as PVPh–10.

Table 6.1. PVPh molecular weights and solution concentrations used for each solvent

PVPh M_n (g/mol)	DMSO (wt.%)	THF (wt.%)
5,000	2.1	1.3
	3.0	2.2
	4.2	3.2
	6.1	
10,000	2.1	1.0
	2.9	1.9
	4.3	3.2
	6.2	
35,000	2.0	1.0
	3.1	2.0
	4.2	3.0
	5.9	
290,000	0.9	1.0
	2.2	2.1
	3.0	3.1

6.2.2 SANS Experiments

SANS experiments were performed at the National Institute of Standards and Technology (NIST) in the Center for Neutron Research (NCNR) in Gaithersburg, MD at the 30 m NIST/Exxon/University of Minnesota beamline (NG7). A wavelength of 6 ± 0.1 Å was used as the incident radiation. The sample to detector distance was adjusted between a range of 1 m – 13 m. The samples were dilute polymer solutions, so they were sealed in quartz banjo cells which were 1 – 1.5 mm thick. The samples were exposed for anywhere between 10–20 minutes. All scattering experiments were performed at room temperature. Data was corrected for solvent scattering, empty cell, and detector sensitivity and placed on an absolute scale using the direct beam method. The obtained 2–dimensional pattern was then azimuthally averaged to obtain a plot of intensity, I, (in units of cm^{-1}) vs. q (in units of Å).

6.3 Results and Discussion

The $I(q)$ vs. q curves for PVPh/DMSO solutions are presented in Figure 6.1. and those for PVPH/THF solutions are presented in Figure 6.2. In these plots, the incoherent scattering intensity, which was 0.036 cm^{-1} for DMSO and 0.062cm^{-1} for THF, has been subtracted. These background scattering values were obtained by averaging over the q range of 0.1 – 0.4 because solvent $I(q)$ values were approximately independent of q over this range.

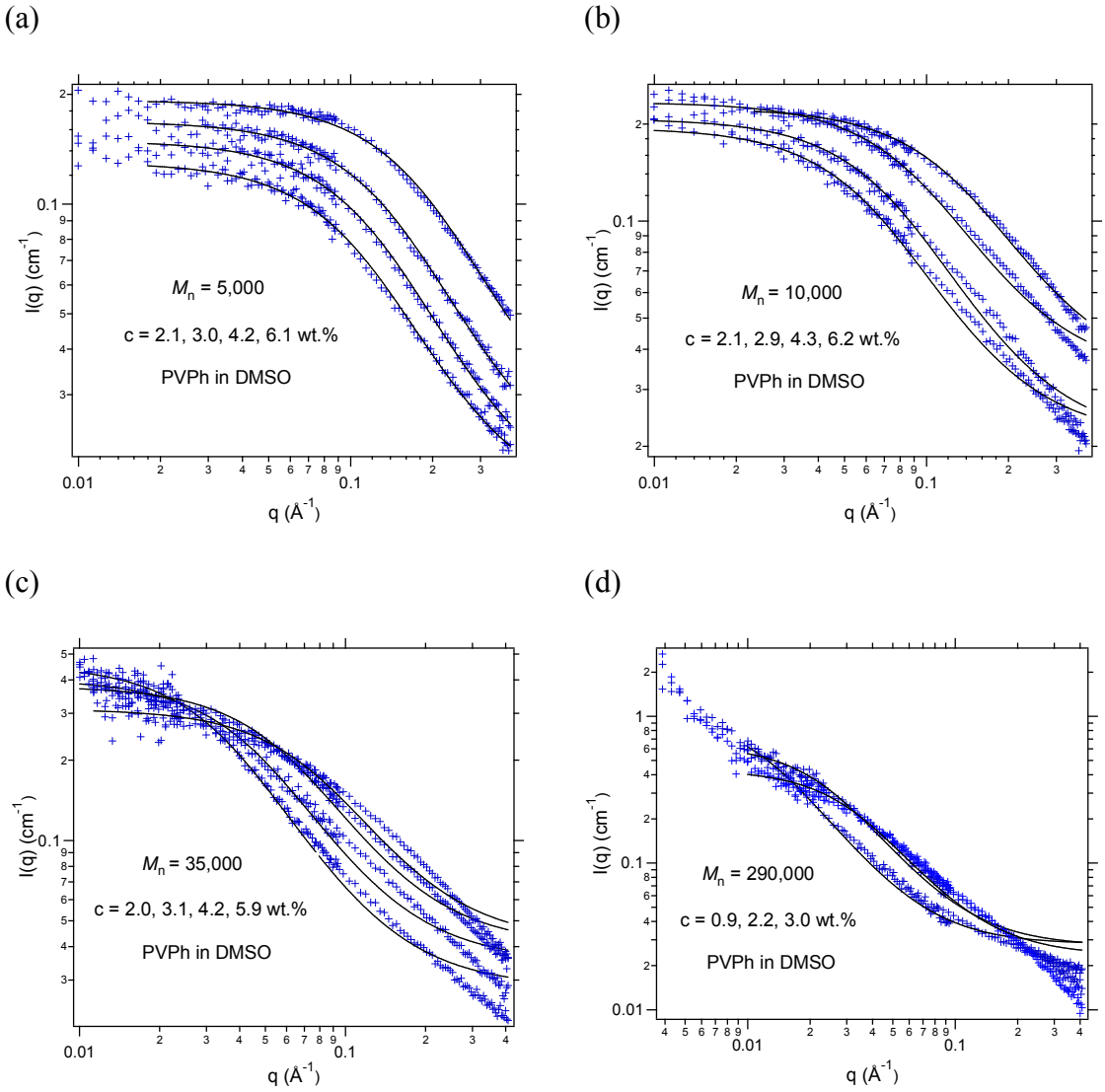

Figure 6.1. Coherent scattering profiles of PVPh in DMSO. Symbols are experimental data points while the solid lines are the best fits to Debye function as determined by linear regression.

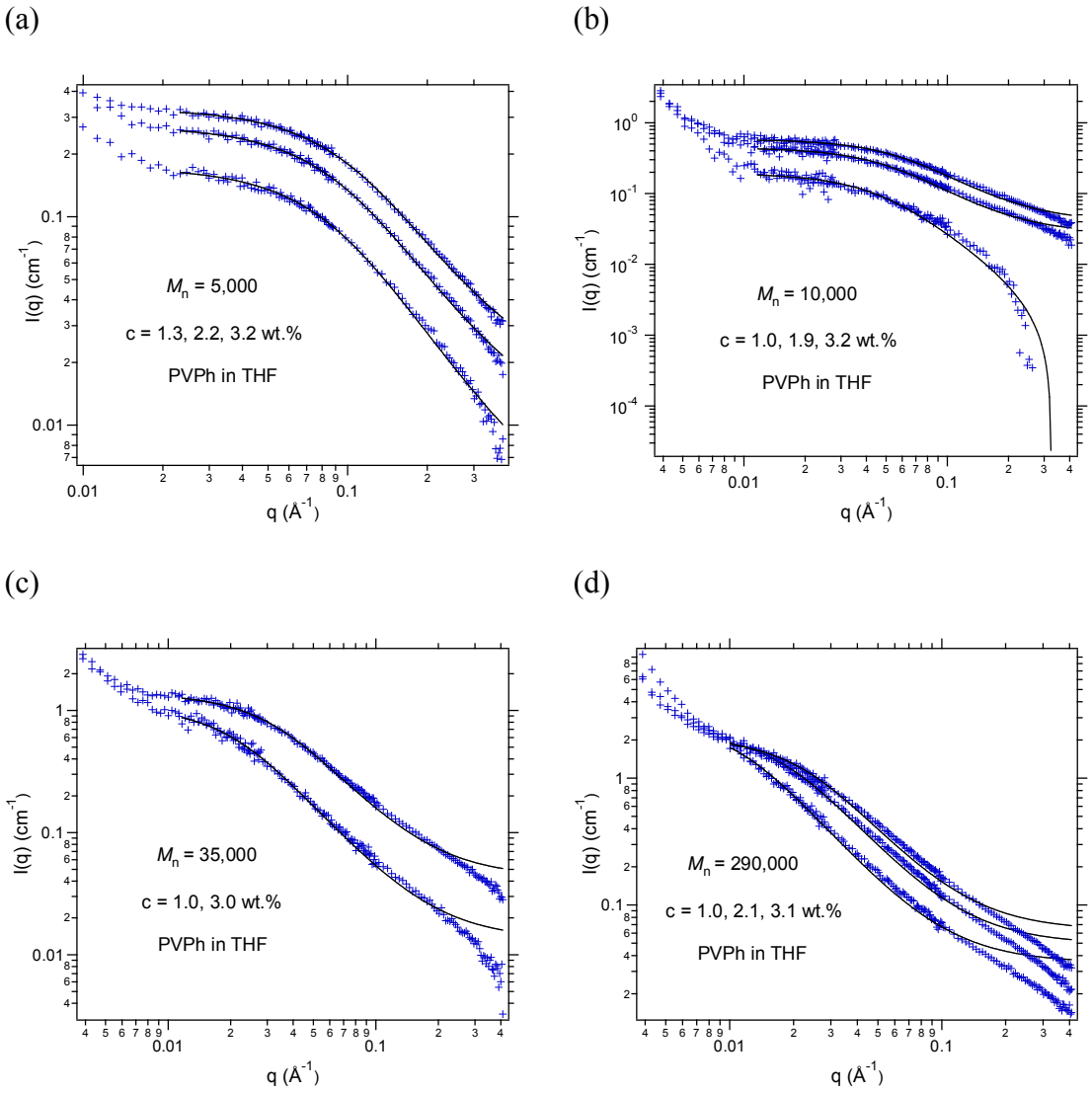

Figure 6.2. Coherent scattering profiles of PVPh in THF. Symbols are experimental data points while the solid lines are the best fits to Debye function as determined by linear regression.

The $I(q)$ vs. q curves shown in Figure 6.1 and 6.2 are for different concentrations of PVPh–5, PVPh–10, PVPh–35, and PVPh–290 solutions. In Figure 6.2 (c), the data for 2 wt.% are not shown because some of the THF had evaporated making the solution concentration uncertain. Each figure displays the effect of increasing concentration, showing an increase in scattered intensity as expected. In Figures 6.1 (c,d), and 6.2 (a–d), one other observation immediately stands out and that is that the coherent intensity starts rising instead of leveling off at low q values. Such a rise in intensity at low q is an artifact of the quartz banjo cells and is not representative of scattering from polymer chains in the solution. The very low q data, for which an unexpected increase in intensity is observed, was ignored in fitting to the Debye function. In Figure 6.3 four different intensity profiles are plotted for each of the four molecular weights of PVPh in THF for 3 wt.% concentrations. The different shapes of intensity profiles reveal the molecular weight dependence. As molecular weight increases, the scattered intensity increases at low q and the apparent radius of gyration also increases as seen by the shifting of curvature to lower values of q.

The radius of gyration for all solutions was determined by fitting the scattering data to the Debye function[2–4] using non-linear regression:

$$I(q) = \left[\frac{2A}{(qR_g)^4}\right]\left[e^{-(qR_g)^2} - 1 + (qR_g)^2\right] + B \qquad (6.1)$$

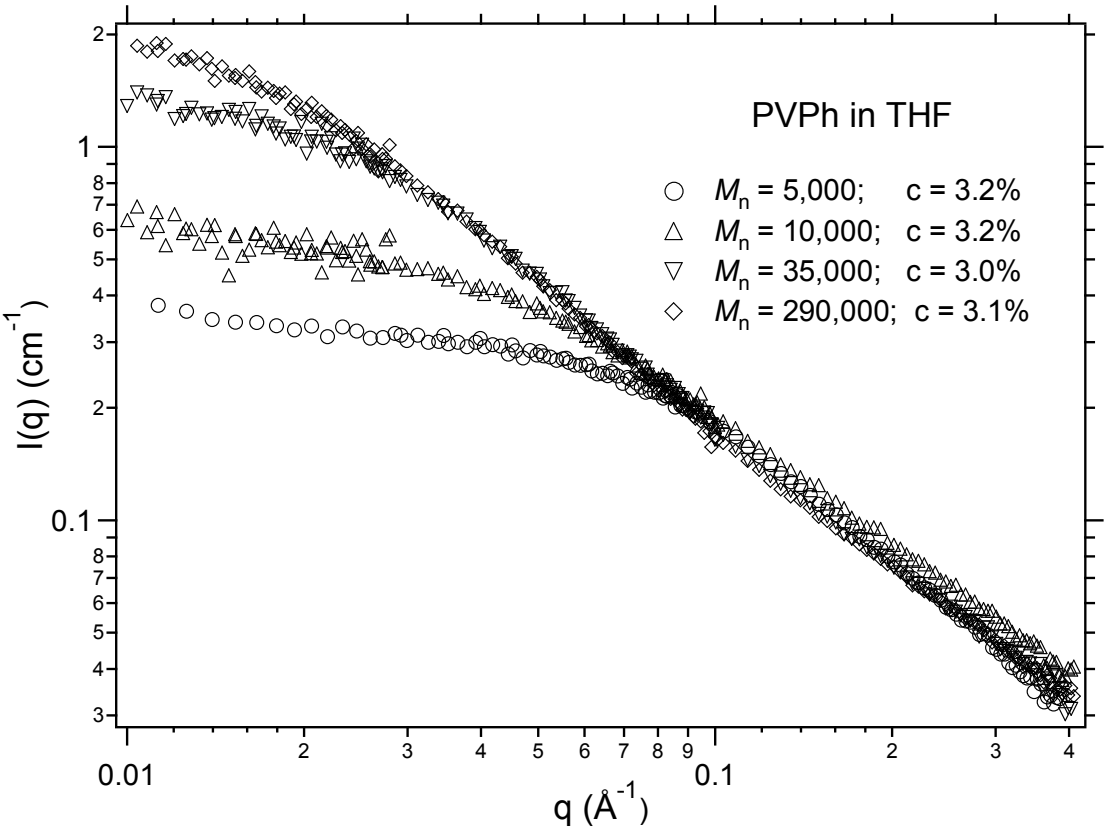

Figure 6.3. Coherent intensity profiles of different molecular weights of PVPh in THF.

where A is a prefactor, B is a baseline correction and R_g is the radius of gyration. Ideally, the Guinier plot could be used to extract R_g instead of using the Debye function, to avoid making prior assumptions about coil configurations. However, this approach was not initially used because for high molecular weight polymers, PVPh–35 and PVPh-290, the q range does not sufficiently extend into the Guinier regime in order to avoid curvature in $\ln[I(q)]$ vs. q^2 plots. One advantage of fitting the data to the Debye function instead of extracting R_g through a Guinier plot is that the data obtained over the entire q range can be utilized. Even though solvent scattering had been subtracted from solution intensity profiles, a baseline parameter was still used in the Debye fitting procedure. The Debye function seems to fit the data well especially for low molecular weights. For high molecular weight samples, PVPh–35 and PVPh–290, Debye fits were not as good. In addition, the extracted R_g values for PVPh–35 and PVPh–290 were very sensitive to the number of low q data points ignored for fitting purposes. Some of the low q data was not included in the fitting procedure because of the unexpected and unrealistic increase in low q intensity.

To estimate the accuracy of R_g values obtained from fitting the data to Debye function, we decided to extract R_g values using Guinier plots and compared with R_g values obtained from Debye fits. The Guinier plots are those of $\ln[I(q)]$ vs. q^2, and R_g is determined from the low q slope of the curve which equals $-R_g^2/3$. The Guinier analysis allows determination of R_g without any knowledge of particle shape or size. Hence, to determine the appropriate q range, we took the reciprocal of R_g obtained from Debye fitting as the upper limit of the q range. The R_g values obtained from Debye fits are plotted against solution concentration for different molecular weights in Figures 6.4 and

6.5. The R_g values were extrapolated to obtain infinite dilution R_g, shown by solid symbols. Similarly, the R_g values obtained from Guinier analysis were plotted against solution concentration and extrapolated to obtain infinite dilution R_g values. These R_g values are listed in Table 6.2 along with those obtained from Debye fitting.

Table 6.2. Comparison of infinite dilution R_g values from Debye and Guinier analysis

Solvent	M_n (g/mol)	Debye		Guinier	
		$R_{g,\ c\to 0}$ (Å)	Std. Deviation (Å)	$R_{g,\ c\to 0}$ (Å)	Std. Deviation (Å)
DMSO	5,000	17	0.2	15	0.3
	10,000	30	0.8	28	1.2
	35,000	58	5.1	57	4.2
	290,000	164	15.8	–	–
THF	5,000	19	0.1	20	0.2
	10,000	43	3.8	53	4.3
	35,000	87	–	–	–
	290,000	160	15.7		

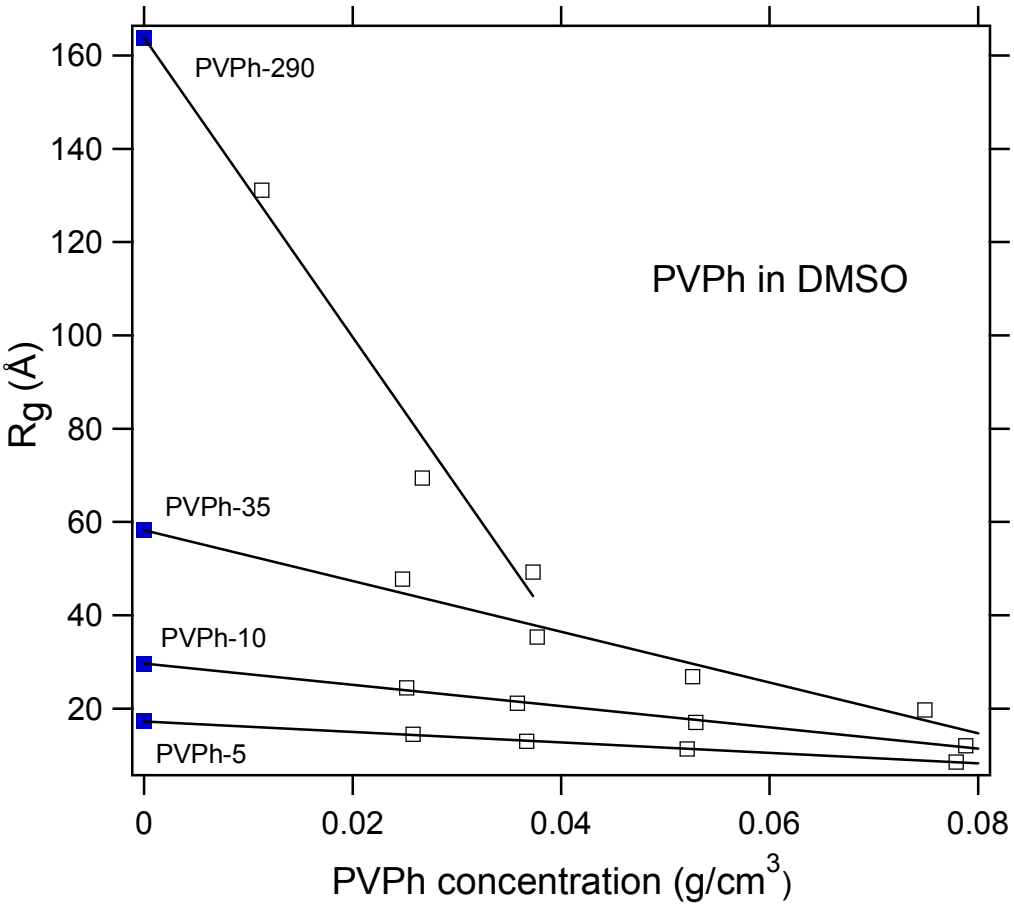

Figure 6.4. Concentration dependence of R_g values for PVPh in DMSO obtained by fitting the Debye function. Solid symbols are infinite dilution values of R_g.

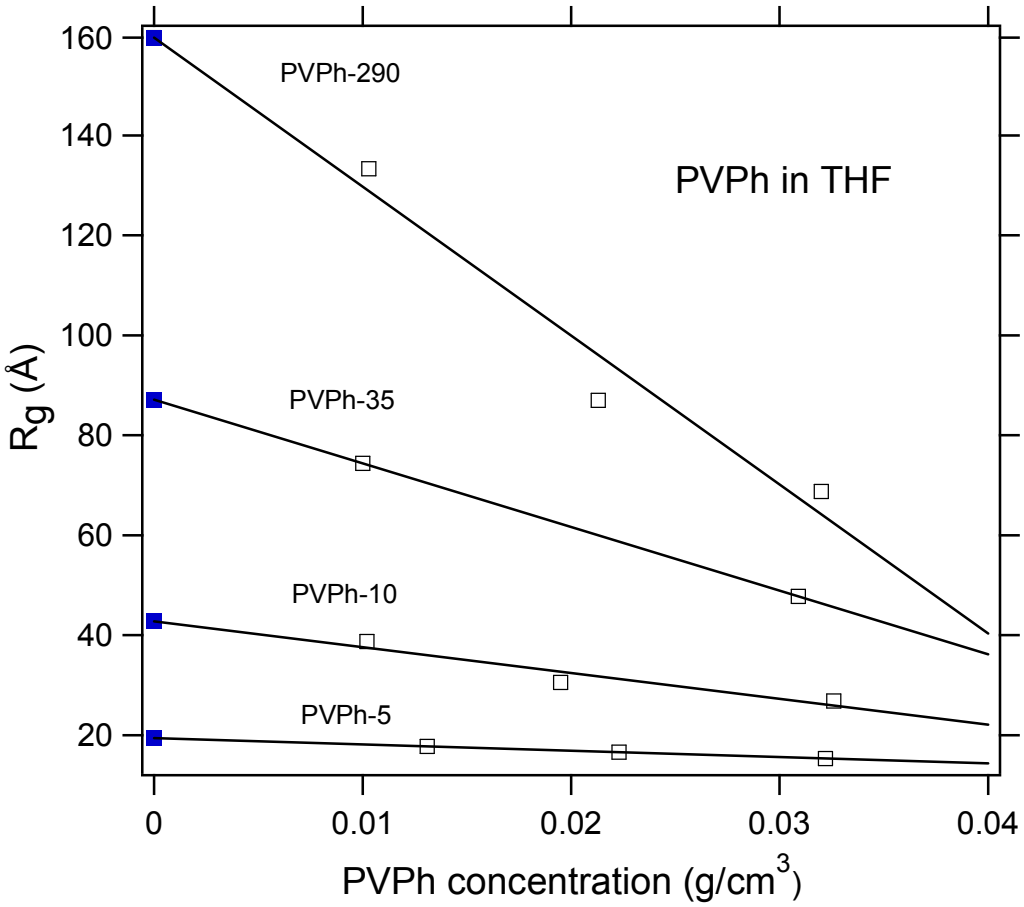

Figure 6.5. Concentration dependence of R_g values for PVPh in THF obtained by fitting the Debye function. Solid symbols are infinite dilution values of R_g.

As can be seen from Table 6.2, the Guinier and Debye R_g values for PVPh in DMSO are in reasonable agreement with each other. Overall, R_g values obtained from Debye fitting are slightly larger than those obtained from Guinier analysis. R_g for PVPh–290 in DMSO could not be obtained via Guinier analysis because the inability to access low enough q values as a result of large R_g. For PVPh in THF, the values for PVPh–5 are almost identical for both methods. The comparison reveals significant discrepancy, a difference of ~10 Å, in the R_g values obtained from these two methods for PVPh–10. No R_g could be determined by Guinier analysis for PVPh–35 and PVPh–290 due to inaccessibility of a low enough q. Considering these observations and the fact that Debye fits were not as good for high molecular PVPh samples as they were for lower molecular weights in both solvents, the R_g values obtained from Debye fitting still did not inspire full confidence in their accuracy and raised some questions about validity of assumption of PVPh chain conformations as flexible coils in both solvents.

To asses validity of assumption of Gaussian chains, plots of $q^2I(q)$ vs. q were prepared for PVPh in both DMSO and THF. Such a plot is known as a Kratky plot.[3,5,6] In a Kratky plot, at high q, the form factor of a Gaussian chain approaches a horizontal plateau and stays constant with increasing q. The magnitude of this plateau is $2/R_g^2$. So this is a good way of assessing the Gaussian nature of polymer chains. Any deviation from this horizontal asymptotic behavior at high q indicates non–Gaussian behavior of polymer chains. For rigid rods, for example, the plot of $q^2I(q)$ vs. q increases linearly even at high q and does not reach a horizontal plateau. In addition to Kratky plots, $\ln[I(q)]$ was plotted against $\ln[q]$. Such a plot is known as Porod plot,[5–7] and it provides information about the fractal dimension of the scattering objects. Such a plot produces a

slope of –2 at high q for Gaussian chains in a dilute solution, while for rigid rods a slope of –1 is produced.

For PVPh in DMSO, the Kratky plots for all concentrations of the four molecular weight samples showed a linear variation of $q^2I(q)$ as a function of q, suggesting the presence of rod–like structures instead of Gaussian chains. To confirm this, modified Kratky plots were prepared by plotting $qI(q)$ vs. q. For rods, a plot of $qI(q)$ vs. q will exhibit a horizontal asymptote at high q.[7] Indeed, for all samples of PVPh in DMSO, plots of $qI(q)$ vs. q showed a horizontal plateau at high q confirming presence of extended objects. The rod conformation was further confirmed by Porod plots which produced slopes at high q that ranged from –0.9 to –1.1 for all solutions of PVPh in DMSO. Representative Kratky and modified Kratky plots for 4.3 wt.% solution of PVPh–10 in DMSO are shown in Figure 6.6. The Kratky plots for all other blends are shown in Appendix A.

For the case of PVPh in THF, the Kratky plots for PVPh–5 solutions, even though not linear, do not exhibit a plateau at high q. The lowest solution concentration (1.3 wt.%) exhibits an approaching plateau at high q but as the concentration is increased, this approaching plateau diminishes and the plots become relatively more linear. The modified Kratky plots show no plateau at high q for the lowest concentration and progressively more horizontal $qI(q)$ profiles as concentration increases. The high q slopes in Porod plots were –2, –1.4, and –1.3 for solution concentrations of 1.3, 2.2 and 3.2 wt.% respectively, indicating increasing rigidity of coils as concentration increases.

(a)

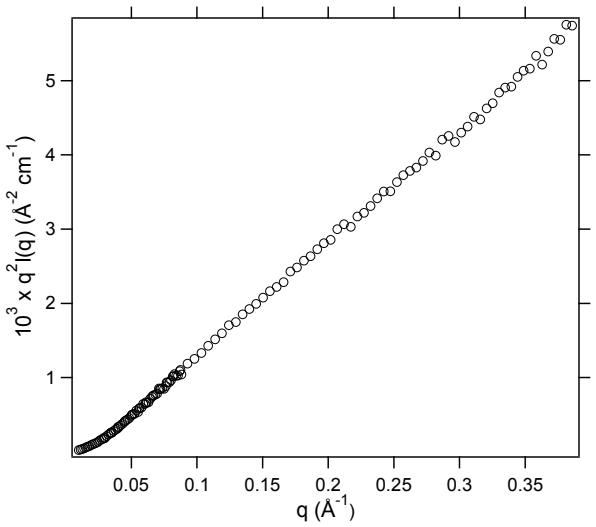

(b)

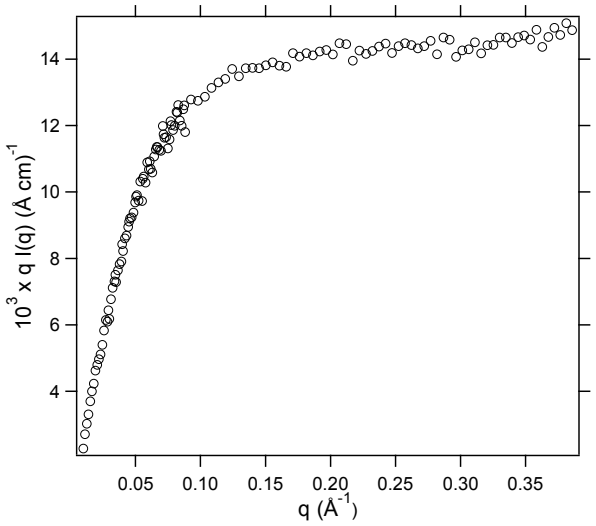

Figure 6.6. (a) Kratky plot for 4.3 wt.% solution of PVPh–10 in DMSO, and (b) modified Kratky plot for the same polymer solution. The linear dependence of $q^2I(q)$ on q in (a) indicates a rod–like configuration of polymer chains. The horizontal plateau at high q in (b) confirms the presence of rods.

For PVPh–10 in THF, a similar trend was observed, i.e., increasing apparent rigidity of polymer chains as solution concentration was increased. This was qualitatively deduced from Kratky and modified Kratky plots and quantitatively concluded from high q slopes in Porod plots which increased from –1.7 to –1.1 as concentration increased from 1.0 to 3.2 wt.%. For PVPh–35 in THF, data was obtained from only two solution concentrations and the high q Porod slopes were –1.5 and –1.2 for 1.0 and 3.0 wt.% solutions respectively. The Kratky plot for the 3 wt.% solution was qualitatively more linear than that for the 1% solution. Hence, the trend of increasing rigidity with increasing concentration is similar to that observed for PVPh–5 and PVPh–10 solutions. For PVPh–290 solutions, this trend was not observed and all three solution concentrations produced linear Kratky plots and high q Porod slopes of –1.1 to –1.2, again suggesting rod–like structures.

The aforementioned analysis presents a picture in which PVPh adapts to rod–like or extended chain conformations in DMSO. The conformations in THF solutions are not very obvious. For all but PVPh–290 solutions, there is an indication of PVPh conformational change from flexible coil to semi–flexible chain or rod as solution concentration increases. One way of further validating the conclusion of rod–like conformations of PVPh in DMSO and possibly THF (at least at higher concentrations) is to analyze the molecular weight dependence of R_g determined from fitting Debye function to the experimental data. R_g scales with molecular weight as $R_g \sim M^{\nu}$ where ν = 1/3 for a sphere, ν = 1/2 for Gaussian chains in a theta solvent or a melt, ν = 3/5 for chains in a good solvent, and ν = 1 for rigid rods. Figure 6.7 shows the molecular weight dependence of R_g for PVPh in DMSO and THF as determined by Debye fitting.

(a)

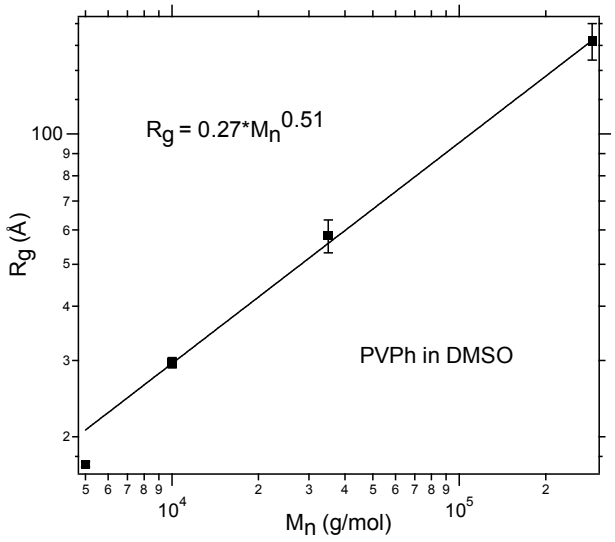

(b)

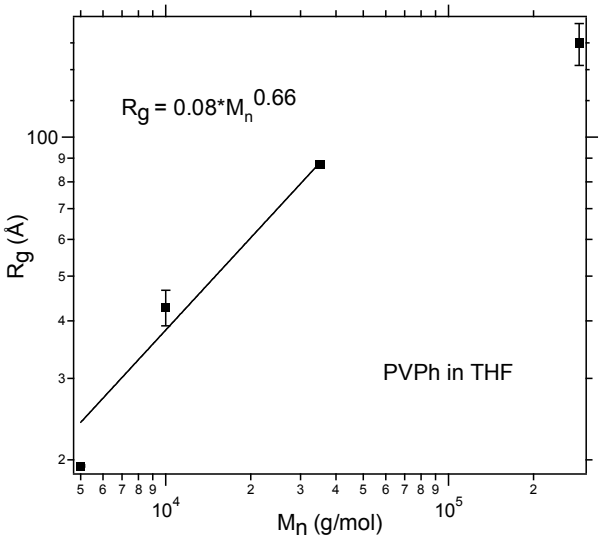

Figure 6.7 Molecular weight dependence of R_g in (a) DMSO, and (b) THF. The scaling exponent of 0.66 in (b) was obtained by fitting power law only to the first three data points.

The molecular weight scaling exponents were determined by fitting a power law to the data points.

For PVPh in THF, the PVPh–290 R_g value was not used in power law fitting because of the lack of confidence in its validity. This is because PVPh–290 R_g value was very sensitive to the number of data points used for fitting to the Debye function. If we take into account the largest R_g value, the molecular weight scaling exponent decreases to 0.38.

As seen from Figure 6.7, R_g scales as $M_n^{0.51}$ in DMSO, while in THF it scales as $M_n^{0.66}$. If we obtain the scaling relationship using R_g values obtained from Guinier analysis, R_g in DMSO scales as $M_n^{0.47}$. Thus the scaling exponent is not much different and does not change any conclusions. These scaling exponents suggest that DMSO is a theta solvent and THF is a good solvent for PVPh. This conclusion is completely at odds with that determined from Kratky and Porod plots for PVPh in these two solvents. That analysis had suggested presence of rod–like structures, and not Gaussian chains. If it were a rigid rod, R_g would have scaled with molecular weight as $R_g \sim M_n^1$.

In order to shed more light and attempt to understand this discrepancy, we compare R_g values obtained from Debye fitting with theoretical R_g predictions of Gaussian coils and rigid rods. For a rigid rod, $R_g = L/\sqrt{12}$ where L is the rod length. L was calculated by assuming a zig–zag conformation of carbon–carbon bonds along the polymer backbone, and then multiplying the number of repeat units by the length of one repeat unit, which was 0.25 nm. For a Gaussian coil, $R_g = b\sqrt{(N/6)}$ where b is the statistical segment length. PVPh statistical segment length is not known, so that of poly(styrene) (PS) was used because of similarity in their chemical structures. The

infinite dilution R_g values from Debye and Guinier analysis along with theoretically predicted rigid rod and Gaussian R_g values are tabulated in Table 6.3.

Table 6.3. Comparison of experimental and theoretical R_g values

M_n (g/mol)	Theoretical Predictions		$R_{g,\, c\to 0}$ in DMSO (Å)	$R_{g,\, c\to 0}$ in THF (Å)
	Rod R_g (Å)	Gaussian Coil R_g (Å)		
5,000	30	18	17	19
10,000	61	25	30	43
35,000	212	47	58	87
290,000	1758	135	164	160

As can be seen from Table 6.3, the theoretically predicted R_g values for rigid rods are significantly higher for all molecular weights, especially for the highest one. The theoretical R_g values for Gaussian coils are similar to experimentally determined ones in both solvents. This suggests that PVPh conformations in either solvent are Gaussian coils. Once again, this conclusion is completely at odds with that of conformations being rigid rods as concluded from Kratky and Porod plots. One possible reason for such contrasting conclusions could be that the PVPh chains, instead of adapting a stiff rod conformation adapt a helical conformation. It is possible that the neutron scattering data can be better explained by helical wormlike chain model proposed by Yamakawa.[8,9] This idea should be explored further.

If we assume PVPh chains as stretched out helices, we can compute the R_g of a helix and compare it to theoretical predictions of rods and Gaussian coils as well as the experimentally determined R_g values. The shape of a characteristic helix may be determined as a space curve that has a specific radius and a pitch. Yamakwa[8] determined the radius and pitch of an atatctic PS in cyclohexane at 34.5 °C and the values were 1.37 Å and 17.3 Å, respectively. Yamakawa[8] has shown an illustration of the characteristic helix of atactic PS, and based on that illustration we can estimate that each pitch of the helix contains 7 repeat units of PS. Knowing of the number of repeat units in a pitch enabled us to determine the number of pitches in the helix based on molecular weight of the polymer. The length, L, of the helix was determined by multiplying the length of a pitch by the number of pitches. The R_g of the stretched out helix was calculated using the relationship for a cylindrical structure: $R_g^2 = L^2/12 + r^2/2$, where r is the radius of the helix. The R_g values of different molecular weights of PS are tabulated in Table 6.4.

Table 6.4. R_g values for a stretched helix of atactic PS

M_n(g/mol)	a-PS Helix R_g (Å)
5,000	30
10,000	59
35,000	208
290,000	1724

If we compare these R_g values to those of rigid rods in Table 6.3, we can see they are very similar. However, it is critical to realize that the analysis for a helical structure is done for PS where no hydrogen bonding is present. Presence of hydrogen bonding would possibly increase the radius of the helix, increasing the number of repeat units in each pitch and considerably decreasing the length of the stretched helix. This will reduce the R_g and make it more comparable to the experimentally determined values. The only way to conclusively determine presence of PVPh helices is to fit the neutron scattering profiles with a helical form factor, and as mentioned earlier, this should be explored in the future.

6.4 Summary

SANS experiments were conducted to determine PVPh chain conformations and dimensions in dilute solutions of DMSO and THF. The experimentally determined intensity profiles were fitted to the Debye function and R_g values were extracted. Guinier law was also used to extract R_g values for some of the solutions where low enough q range could be accessed and comparison of results of these two methods showed reasonable agreement except for a PVPh–10 sample in THF.

Chain conformations were further explored by using Kratky and Porod plots which conclusively indicated presence of rigid rods. However, comparison of theoretically predicted R_g values of rigid rods revealed values that were significantly larger than those determined by Debye or Guinier analysis. Furthermore, theoretical R_g values for Gaussian coils were found to be similar to those obtained from Debye fitting suggesting that PVPh chains are Gaussian coils. In addition, the molecular weight

dependence of experimentally determined R_g suggested DMSO to be a theta solvent and THF to be a good solvent for PVPh chains. Hence, different analyses have led to contradictory, unambiguous conclusions. This is puzzling and at this point we cannot offer an explanation for reconciling these contradictory conclusions. It is possible that PVPh assumes a helical conformation in these solvents and the scattering data can be better modeled by a helical wormlike chain model. This idea should be explored further.

6.5 References

[1] Gestoso, P.; Brisson J. *Comp. Theor. Polym. Sci.* **2001**, *11*, 263.
[2] Debye, P. *J. Phys. Colloid Chem.* **1947**, *51*, 18.
[3] Roe, R. J. *Methods of X-Ray and Neutron Scattering in Polymer Science*, Oxford University Press, New York, **2000.**
[4] Higgins, J. S.; Benoit, H. *Polymers and Neutron Scattering*, Oxford: Clarendon Press, **1994**
[5] Kratky, O.; Porod, G. *Rec. Trav. Chim.* **1949**, *68*, 1106.
[6] Kratky, O.; Porod, G. *J. Colloid Interface Sci.* **1949**, *4*, 35.
[7] Hammouda, B. *Tutorial on Small-Angle Neutron Scattering from Polymers*, **1995**, National Institute of Standards and Technology.
[8] Yamakawa, H. *Helical Wormlike Chains in Polymer Solutions,* Springer, **1997**
[9] Yamakawa, H. *Ann. Rev. Phys. Chem.* **1984**, *35*, 23.

Chapter 7. Summary and Outlook

7.1 Introduction

This thesis focused on increasing fundamental understanding of component dynamics in miscible blends. A main goal of this work was to understand the role of hydrogen bonding in blend dynamics and to investigate how component dynamics in hydrogen bonding blends compare to that in blends where hydrogen bonding is not present. The weakly interacting blend studied in this work was PEO/PMMA while the strongly interacting system investigated was PEO/PVPh. As a result of the large difference in their T_gs, both PEO/PMMA and PEO/PVPh blends are dynamically asymmetric, meaning their component mobilities are very different in their homopolymer melts.

Terminal dynamics of PEO and PMMA were studied in the PEO/PMMA blends using FRS and rheology. Since low molecular weight, unentangled polymers were used for these measurements, the Rouse model was used to extract monomeric friction factors for each component over a wide range of temperature and composition. PEO chain dynamics exhibited a strong composition dependence which contrasted with the very weak composition dependence of PEO segmental dynamics. The friction factors obtained from FRS and rheology results agreed remarkably well.

The effects of PEO hydroxyl end groups on chain dynamics were explored by performing FRS and rheology measurements on PEO samples that did not have any hydroxyl end groups. The PEO friction factors of samples with and without hydroxyl end groups were not much different and had the same temperature dependence. Thus, it was

concluded that hydroxyl end groups do not significantly affect the dynamics of either component in the blend.

In FRS, a photochromic dye is attached to polymer chain to determine diffusion coefficients. The phtochromic dye can affect chain diffusion if the polymer chains are too small. However, the chain diffusion results were compared to a previous study of dye diffusion in a similar molecular weight matrix and it was concluded that the dye does not have any significant impact on diffusion of labeled PEO chains.

The Lodge–McLeish model was compared with the temperature and composition dependence of experimentally determined friction factors and it failed to describe the data even qualitatively. The quality of Lodge–McLeish fits improved upon decreasing self–concentration values but even for zero self–concentration (which produced the best fits), the model was unable to describe experimental results.

To understand the role of hydrogen bonding, component dynamics in PEO/PVPh blends were studied using rheological measurements. The longest relaxation times of high molecular weight tracer chains were obtained from plots of η'' vs. ω. The monomeric friction factors were determined from longest relaxation times using the Rouse model relationship. Time–temperature superposition failure was observed in PEO tracer blends with high PVPh composition. This phenomenon was also observed in PEO/PMMA blends with PEO tracer at high PMMA composition. This suggests that hydrogen bonding does not play a significant role in dictating the temperature dependence of component chain dynamics and that it does not completely couple the chain dynamics.

The composition dependence of the shape of η'' tracer relaxation spectra was investigated and a sharp contrast was observed in shapes of blends with PVPh and PMMA

tracers. The PVPh spectra significantly broadened with decreasing PVPh composition while the PMMA spectra narrowed upon decreasing PMMA composition. For PEO/PVPh and PEO/PMMA blends with PEO tracers, the composition dependence of shape of η'' tracer relaxation spectra was quite similar. The shapes of the relaxation spectra were also compared with Zimm and Rouse predictions and Zimm model described the experimental data better for all blends.

The tracer contribution to blend viscosities were also investigated and it was found that for high PVPh composition in the blends, the temperature dependence of the tracer blend viscosities was much stronger than that of just the matrix without any tracer. This behavior is also quite different than what PEO/PMMA blends exhibited.

Glass transition temperatures were measured for PEO/PVPh blends using DSC. Across the composition range, single and relatively narrow glass transitions were observed, which is different than what has usually been observed in similar dynamically asymmetric blends without hydrogen bonding. This suggests coupling of component dynamics at the segmental level.

In light of all these observations, we can answer the two important questions, one of them being how the component terminal dynamics in blends with hydrogen bonding compare with that in weakly interacting blends. Based on experimental results, there is reason to believe that hydrogen bonding does affect chain dynamics to some extent but not nearly as much as anticipated. The most striking observation which reveals a limited role of hydrogen bonding in dictating the temperature dependence of chain dynamics is tTS failure in PEO tracer blends in PEO/PVPh similar to that in PEO/PMMA. Hydrogen bonding does seem to play a significant role in determining temperature dependence of

viscoelastic properties such as blend viscosity, and also in determining distribution of chain relaxation times as seen by strong composition dependence of shape of η'' relaxation spectra. The other question we'd like to answer is: Does intermolecular hydrogen bonding simplify blend dynamic behavior by coupling component chain dynamics? We can confidently say that this is not the case based on our experimental results and analysis.

To determine friction factors of PVPh, knowledge of the statistical segment length of PVPh is needed. However, there are no reliable reported values for PVPh statistical segment length. We undertook a study to investigate chain conformations of PVPh in dilute solutions of THF and DMSO. One of the goals of this study was to determine PVPh chain dimensions. SANS experiments were performed and the experimental data was fitted to the Debye function and the R_g values were extracted. Guinier law was also used to extract R_g values for some of the solutions where insufficiently low q range could be accessed, and comparison of results of these two methods showed reasonable agreement for most samples.

Chain conformations were further explored by using Kratky and Porod plots which indicated presence of rod–like structures. However, comparison of theoretically predicted R_g values of rigid rods revealed values that were significantly larger than those determined by Debye or Guinier analysis. Furthermore, theoretical R_g values for Gaussian coils were found to be similar to those obtained from Debye fitting suggesting that PVPh chains are Gaussian coils. In addition, the molecular weight dependence of experimentally determined R_g suggested DMSO to be a theta solvent and THF to be a good solvent for PVPh chains. Based on these observations, it is clear that different analytical methods have led to contradictory, unambiguous conclusions. This is puzzling and at this point we

cannot offer an explanation for reconciling these contradictory conclusions. It is possible that PVPh assumes a helical conformation in these solvents and the scattering data can be better modeled by a helical wormlike chain model. This idea needs to be explored further.

7.2 Outlook

At the conclusion of this thesis, several questions regarding dynamics of miscible blends remain to be answered completely. In addition, there are opportunities for further exploration of ideas. Some of these are presented below.

1. To address contradictory conclusions regarding chain conformations of PVPh in dilute solutions, a helical conformation needs to be considered instead of a rigid rod. The helical wormlike chain model proposed by Yamakwa[1–3] should be tried to describe neutron scattering profiles of PVPh in DMSO and THF. In addition, dynamic light scattering studies should be conducted to determine the hydrodynamic radius of PVPh in these solutions.
2. TTS failure in PEO/PVPh similar to that in PEO/PMMA was explained in this thesis by a speculative hypothesis. This issue needs further exploration and a more robust explanation is needed to address this phenomenon.
3. For 65% PEO/PVPh blends in which tTS breakdown was observed, the master curves of matrix η' and η'' overlapped nicely and tTS was observed for those data sets. This means that addition of a high molecular weight tracer to the low molecular weight matrix causes tTS to break down. To address this issue in more detail, several blends with varying molecular weight PEO tracers should be prepared and oscillatory shear measurements performed using them to determine

molecular weights for which tTS failure is observed and for which it is not. This may assist in developing a robust explanation for the causes of tTS failure.

4. PEO/PVPh segmental dynamics should be investigated over a wide temperature and composition range. Then the direct correlation between segmental and terminal dynamics should be tested. This correlation failed in PEO/PMMA blends but has been shown to be successful in blends such as PI/PVE[4] and moderately successful in PB/PVE.[5]
5. In this work we investigated component chain dynamics in PEO/PVPh as well as PEO/PMMA blends. It will be very interesting to investigate component chain dynamics in PEO/PVPh/PMMA ternary blends. There are no known reports of segmental or chain dynamics study of this ternary blend. What makes this ternary blend intriguing is competing hydrogen bonding equilibria between PVPh–PVPh, PMMA–PVPh, and PEO–PVPh. It is reported in the literature[6] that at low temperatures, PVPh–PEO interactions are preferred while at high temperatures PVPh–PMMA interactions are preferred. It will be interesting to study composition dependence of tracer relaxation spectra since they exhibit different behaviors in weakly interacting and strongly interacting blends.

7.3 References

[1] Yamakawa, H. *Ann. Rev. Phys. Chem.* **1984**, *35*, 23.
[2] Yamakawa, H.; Fujii, M. *J. Chem. Phys.* **1976**, *64*, 5222.
[3] Yamakawa, H. *Macromolecules* **1977**, *10*, 692.
[4] Haley, J. C.; Lodge, T. P.; He, Y.; Ediger, M. D.; Von Meerwall, E. D.; Mijovic, J. *Macromolecules* **2003**, *36*, 6142.
[5] He, Y.; Lutz, T. R.; Ediger, M. D. *Macromolecules* **2004**, *37*, 9889.

[6] Lin, C-L.; Chen, W-C.; Kuo, S-W.;Chang, F-C. *Polymer* **2006**, *47*, 3436.

Bibliography

Adachi, K.; Hirano, H. *Macromolecules* **1998**, *31*, 3958.

Akiba, I.; Akiyama, S. *Polym. Networks Blends* **1997**, *7*, 147.

Aoki, Y.; Tanaka, T. *Macromolecules*, **1999**, *32*, 8560.

Arendt, B. H.; Krishnamoorti, R.; Kornfield, J. A.; Smith, S. D. *Macromolecules* **1997**, *30*, 1127.

Arrhenius, S. Z. *Physik. Chem.* **1887**, *1*, 285.

Berens, A. R.; Hopfenberg, H. B. *J. Membr. Sci.* **1982**, *10*, 283.

Brochard-Wyart, F. *C. R. Acad. Sci. Par.* **1987**, *305*, 657.

Brosseau, C.; Guillermo, A.; Cohen-Addad, J. P. *Macromolecules* **1992**, *25*, 4535.

Cai, H.; Ait-Kadi, A.; Brisson, J. *Polymer* **2003**, *44*, 1481.

Cao, H.; Lin, G.; Jones, A. A. *J. Polym. Sci., Part B: Polym. Phys.* **2004**, *42*, 1053.

Chuang, H. K.; Han, C. D. *J. App. Polym. Sci.* **1984**, *29*, 2205.

Chung, G. C.; Kornfield, J. A.; Smith, S. D. *Macromolecules* **1994**, *27*, 964.

Chung, G. C.; Kornfield, J. A.; Smith, S. D. *Macromolecules* **1994**, *27*, 5729.

Colby, R. H. *Polymer* **1989**, *30*, 1275.

Coleman, M. M.; Lichkus, M. A.; Painter, P. C. *Macromolecules* **1989**, *22*, 586.

Coleman, M. M.; Lee, J. Y.; Serman, C. J.; Wang, Z.; Painter, P. C. *Polymer* **1989**, *30*, 1298.

Coleman, M. M.; Graf, J.; Painter, P. C. *Specific Interactions and the Miscibility of Polymer Blends* **1991**, Technomic Publishing Co.: Lancaster, PA.

Coleman, M. M.; Painter, P. C. *Prog. Polym. Sci.* **1995**, *20*, 1.

Composto, R. J.; Kramer, E. J.; White, D. M. *Polymer* **1990**, *31*, 2320.

de Gennes, P. G. *J. Chem. Phys.* **1971**, *55*, 572.

de Gennes, P. G. *J. Phys.* **1975**, *36*, 1199.

de Gennes, P. G. *Macromolecules* **1976**, *9*, 587.

de Gennes, P. G. *Scaling Concepts in Polymer Physics* **1979**, Cornell University Press, Ithaca, NY.

de Gennes, P.G.; Leger, L. *Annu. Rev. Phys. Chem.* **1982**, *33*, 49.

Doi, M.; Edwards, S. F. *J. Chem. Soc. Farad. Trans.2: Mol. Chem. Phys.* **1979**, *75*, 38.

Doi, M.; Edwards, S. F. *J. Chem. Soc. Farad. Trans.2: Mol. Chem. Phys.* **1978**, *74*, 1789.

Doi, M.; Edwards, S. F. *J. Chem. Soc. Farad. Trans.2: Mol. Chem. Phys.* **1978**, *74*, 1802.

Doi, M.; Edwards, S. F. *J. Chem. Soc. Farad. Trans.2: Mol. Chem. Phys.***1978**, *74*, 1818.

Doi, M.; Edwards, S. F. *The Theory of Polymer Dynamics*; Oxford University Press: Oxford **1986**.

Doi, M. *Introduction to Polymer Physics* **1996**, Clarendon Press, Oxford.

Doolittle, A. K.; Doolittle, D. B. *J. App. Phys.* **1957**, *28*, 901.

Dionisio, M.; Fernandes, A. C.; Mano, J. F.; Correia, N. T.; Sousa, R. C. *Macromolecules* **2000**, *33*, 1002.

Fernandes, A. C.; Barlow, J. W.; Paul, D. R. *J. App. Polym. Sci.* **1986**, *32,* 5481.

Ferry, J. D. *Viscoelastic Properties of Polymers*, Third edition; John Wiley & Sons: New York, **1980**.

Fox, T. G. *Bull. Am. Phys. Soc.* **1956**, *1*, 123

Frischknecht, A. L.; Milner, S. T. *Macromolecules* **2000**, *33*, 5273.

Gaikwad, A. N.; Wood, E. R.; Ngai, T.; Lodge, T. P. *Macromolecules* **2008**, *41*, 2502.

Gisser, D. J.; Ediger, M. D. *J. Phys. Chem.* **1993**, *97*, 10818.

Green, P. F.; Adolf, D. B.; Gilliom, L. R. *Macromolecules* **1991**, *24*, 3377.

Han, C. D.; Yang, H. H. *J. Appl. Polym. Sci.* **1987**, *33*, 1199.

Haley, J. C.; Lodge, T. P.; He, Y.; Ediger, M. D.; Von Meerwall. E. D.; Mijovic, J. *Macromolecules* **2003**, *36*, 6142.

Haley, J. C.; Lodge, T. P. *J. Chem. Phys.* **2005**, *122*, 234914.

He, Y.; Lutz, T. R.; Ediger, M. D.; Lodge, T. P. *Macromolecules* **2003**, *36*, 9170.

He, Y.; Lutz, T. R.; Ediger, M. D. *J. Chem. Phys.* **2003**, *119*, 9956.

He, Y.; Lutz, T. R.; Ediger, M. D.; Ayyagari, C.; Bedrov, D.; Smith, G. D. *Macromolecules* **2004**, *37*, 5032.

He, Y.; Lutz, T. R.; Ediger, M. D. *Macromolecules* **2004**, *37*, 9889.

He, Y.; Zhu, B.; Inoue, Y. *Prog. Polym. Sci.* **2004**, *29*, 1021.

Hiemenz, P. C.; Lodge, T. P. *Polymer Chemistry*, Second Ed.; CRC Press: Boca Raton, **2007**.

Hirose, Y.; Urakawa, O.; Adachi, K. *Macromolecules* **2003**, *36*, 3699.

Hokinson, I.; Kiff, F. T.; Richards, R. W.; King, S. M.; Farren, T. *Polymer* **1995**, *36*, 3523.

Huyskens, P. L.; Luck, W. A. P.; Zeegers-Huyskens, T. *Intermolecular Forces*; Springer-Verlag: New York, **1991**.

Israelachvili, J. N. *Intermolecular and Surface Forces*, 2nd ed.; Academic Press: New York, **1991**.

Ito, H.; Russell, T. P.; Wignall, G. D. *Macromolecules* **1987**, *20*, 2213.

Jack, K. S.; Whittaker, A. K. *Macromolecules* **1997**, *30*, 3560.

Jeffery, G. A. *An Introduction to Hydrogen Bonding* **1997**, Oxford University Press, New York.

Jin, X.; Zhang, S.; Runt, J. *Macromolecules* **2003**, *36*, 8033.

Jin, X.; Zhang, S.; Runt, J. *Macromolecules* **2004**, *37*, 2817.

Jin, X.; Zhang, S.; Runt, J. *Macromolecules* **2004**, *37*, 4808.

Kamath, S.; Colby, R. H.; Kumar, S. K.; Karatasos, K.; Floudas, G.; Fytas, G.; Roovers, J. E. L. *J. Chem. Phys.* **1999**, *111*, 6121.

Kant, R.; Kumar, S. K.; Colby, R. H. *Macromolecules* **2003**, *36*, 10087.

Kendall, J.; Monroe, K. P. *J. Am. Chem. Soc.* **1917**, *39*, 1787.

Kim, E.; Kramer, E. J.; Wu, W. C.; Garrett, P. D. *Polymer* **1994**, *35*, 5706.

Kim, E.; Kramer, E. J.; Osby, J. O. *Macromolecules* **1995**, *28*, 1979.

Kumar, S. K.; Colby, R. H.; Anastasiadis, S. H.; Fytas, G. *J. Chem. Phys.* **1996**, *105*, 3777.

Kuo, S. W.; Chang, F. C. *Macromolecules* **2001**, *34*, 4089.

Kuo, S. W.; Chang, F. C. *Macromolecules* **2001**, *34*, 5224.

Kuo, S. W.; Huang, C. F.; Chang, F. C. *J. Poym. Sci., Part B: Polym. Phys.* **2001**, *39*, 1348.

Kuo, S. W.; Lin, C. L.; Chang, F. C. *Polymer* **2002**, *43*, 3943.

Lartigue, C.; Guillermo, A.; Cohen-Addad, J. P. *J. Polym. Sci., Part B:Polym. Phys.* **1997**, *35*, 1095.

Landau, L. D.; Lifshitz, E. M. *Statistical Physics (Part 1)* **1980**, Pergamon Press, New York, NY, 3rd ed.

Landry, C. J. T., Teegarden, D. M. *Macromolecules* **1991**, *24*, 4310.

Le Menestrel, C.; Kenwright, A. M.; Sergot, P.; Lauprêtre, F.; Monnerie, L. *Macromolecules* **1992**, *25*, 3020.

Leroy, E.; Alegria, A.; Colmenero, J. *Macromolecules* **2002**, *35*, 5587.

Lezcano, E. G.; De Arellano, D. R.; Prolongo, M. G.; Coll, C. S. *Polymer* **1998**, *39*, 1583.

Liu, C.; Wang, J.; He, J. *Polymer* **2002***, 43*, 3811.

Lodge, T. P.; Rotstein, N. A.; Prager, S. *Advances in Chemical Physics* **1990**, *LXXIX*, 1.

Lodge, T. P. *Phys. Rev. Lett.* **1999**, *83*, 3218.

Lodge, T. P.; McLeish, T. C. B. *Macromolecules* **2000**, *33*, 5278.

Lodge, T. P.; Wood, E. R.; Haley, J. C. *J. Polym. Sci., Part B: Polym. Phys.* **2005**, *44*, 756.

Lumma, D.; Borthwick, M. A.; Falus, P.; Lurio, L. B.; Mochrie, S. G. J. *Phys. Rev. Lett.* **2001**, *86*, 2042.

Lutz, T. R.; He, Y.; Ediger, M. D.; Cao, H.; Lin, G.; Jones, A. A. *Macromolecules* **2003**, *36*, 1724.

Lutz, T. R.; He, Y.; Ediger, M. D.; Pitsikalis, M.; Hadjichristidis, N. *Macromolecules* **2004***, 37*, 6440.

Milner, S. T.; McLeish, T. C. B. *Phys. Rev. Lett.* **1998**, *81*, 725.

Min, K. E.; Chiou, J. S.; Barlow, J. W.; Paul, D. R. *Polymer* **1987**, *28*, 1721.

Min, B.; Qiu, X.; Ediger, M. D.; Pitsikalis, M.; Hadjichristidis, N. *Macromolecules* **2001***, 34*, 4466.

Minnick, M. G.; Schrag, J. L. *Macromolecules* **1980**, *13*, 1960.

Miwa, Y.; Tanabe, T.; Yamamoto, K.; Sugino, Y.; Sakaguchi, M.; Sakai, M.; Shimada, S. *Macromolecules* **2004**, *37*, 8612.

Miwa, Y.; Usami, K.; Yamamoto, K.; Sakaguchi, M.; Sakai, M.; Shimada, S. *Macromolecules* **2005**, *38*, 2355.

Moskala, E. J.; Howe, S. E.; Painter, P.C.; Coleman, M. M. *Macromolecules* **1984**, *17*, 1671.

Moskala, E. J.; Varnell, D. F.; Coleman, M. M. *Polymer* **1985**, *25*, 228.

Ngai, K. L.; Roland, C. M. *Macromolecules* **2004**, *37*, 2817.

Painter, P. C.; Park, Y.; Coleman, M. M. *Macromolecules* **1988**, *21*, 66.

Painter, P. C.; Park, Y.; Coleman, M. M. *Macromolecules* **1989**, *22*, 570.

Painter, P. C.; Park, Y.; Coleman, M. M. *Macromolecules* **1989**, *22*, 580.

Pathak, J. A.; Colby, R. H.; Kamath, S. Y.; Kumar, S. K.; Stadler, R. *Macromolecules* **1998**, *31*, 8988.

Pathak, J. A.; Colby, R. H.; Floudas, G.; Jerome, R. *Macromolecules* **1999**, *32*, 2553.

Pedrosa, P.; Pomposo, J. A.; Calahorra, E.; Cortazar, M. *Macromolecules* **1994**, *27*, 102.

Qin, C.; Cheng, C.; Pires, A. T. N.; Belfiore, L. A. *Polym. Mater. Sci. Eng.*, **1989**, *61*, 945.

Roland, C. M.; Ngai, K. L.; Santangelo, P. G.; Qiu, X. H.; Ediger, M. D.; Plazek, D. J. *Macromolecules* **2001**, *34*, 6159.

Roovers, J.; Toporowski, P. M. *Macromolecules* **1992**, *25*, 1096.

Roovers, J.; Toporowski, P. M. *Macromolecules* **1992**, *25*, 3454.

Rouse, P. E. *J. Chem. Phys.* **1953**, *21*, 1272.

Salaniwal, S.; Kant, R.; Colby, R. H.; Kumar, S. K. *Macromolecules* **2002**, *35*, 9211.

Sakaguchi, T.; Taniguchi, N.; Urakawa, O.; Zadachi, K. *Macromolecules* **2005**, *38*, 422.

Sakai, V. G.; Chen, C.; Maranas, J. K.; Chowdhuri, Z. *Macromolecules* **2004**, *37*, 9975.

Sakai, V. G.; Maranas, J. K.; Peral, I.; Copley, J. R. D. *Macromolecules* **2008**, *41*, 3701.

Schantz, S. *Macromolecules* **1997**, *30*, 1419.

Serman, C. J.; Xu, Y.; Painter, P. C.; Coleman, M. M. *Polymer* **1991**, *32*, 516.

Serman, C. J.; Painter, P. C.; Coleman, M. M. *Polymer* **1991**, *32*, 1049.

Silva, G. G.; Machado, J. C.; Song, M.; Hourston, D. J. *J. App. Polym. Sci.* **2000**, *77*, 2034.

Trask, C. A.; Roland, C. M. *Macromolecules* **1989**, *22*, 256.

Vivas de Meftahi, M.; Fréchet, J. M. J. *Polymer* **1988**, *19*, 477

Waestlund, C.; Maurer, F. H. J. *Macromolecules* **1997**, *30*, 5870.

Wang, C. H.; Zhang, X. Q.; Fytas, G.; Kanetakis, J. *J. Chem. Phys.* **1989**, *91*, 3160.

Wang, J.; Cheung, M. K.; Mi, Y. *Polymer* **2001**, *42*, 3087.

Williams, M. L.; Landel, R. F.; Ferry, J. D. *J. Am. Chem. Soc.* **1955**, *77*, 3701.

Wisnewsky, C.; Marin, G.; Monge, P. *Eur. Polym. J.* **1984**, *20*, 691.

Wu, S. *Polymer* **1987**, *28*, 1144.

Wu, S. *J. Polym. Sci., Part B: Polym. Phys.* **1987**, *25*, 2511.

Xia, J. L.; Wang, C. H. *J. Chem. Phys.* **1991**, *94*, 3229.

Xu, Y., Painter, P. C.; Coleman, M. M. *Macromolecules* **1992**, *25*, 7076.

Yang, H. H.; Han, C. D.; Kim, J. K. *Polymer* **1994**, *35*, 1503.

Yang, Z.; Han, C. D. *Macromolecules* **2008**, *41*, 2104.

Zawada, J. A.; Ylitalo, C. M.; Fuller, G. G.; Colby, R.H.; Long, T. E. *Macromolecules* **1992**, *25*, 2896.

Zawada, J. A.; Fuller, G. G.; Colby, R. H.; Fetters, L. J.; Roovers, J. *Macromolecules* **1994**, *27*, 6861.

Zeroni, I.; Ozair, S.; Lodge, T. P. *Macromolecules* **2008***, 41*, 5033.

Zetsche, A.; Fischer, E. W. *Act. Polym.* **1994**, *45*, 168.

Zhang, X.; Takegoshi, K.; Hikichi, K. *Macromolecules* **1992**, *25*, 2336.

Zhang, S.; Painter, P. C.; Runt, J. *Macromolecules* **2002**, *35*, 8478.

Zhang, S.; Painter, P. C.; Runt, J. *Macromolecules* **2002**, *35*, 9403.

Zhang, S. H.; Casalini, R.; Runt, J.; Roland, C. M. *Macromolecules* **2003**, *36*, 9917.

Zhang, S. H.; Jin, X.; Painter, P. C.; Runt, J. *Polymer* **2004**, *45*, 3933.

Zhang, S.; Painter, P. C.; Runt, J. *Macromolecules* **2004**, *37*, 2636.

Zhang, S.; Runt, J. *J. Polym. Sci., Part B. Polym. Phys.* **2004**, *42*, 3405.

Zhu, K. J.; Chen, S. F.; Ho, T.; Pearce, E. M.; Kwei, T. K. *Macromolecules* **1990**, *23*, 150.

Appendix A

In this appendix, Kratky plots are shown for PVPh solutions in DMSO and THF.

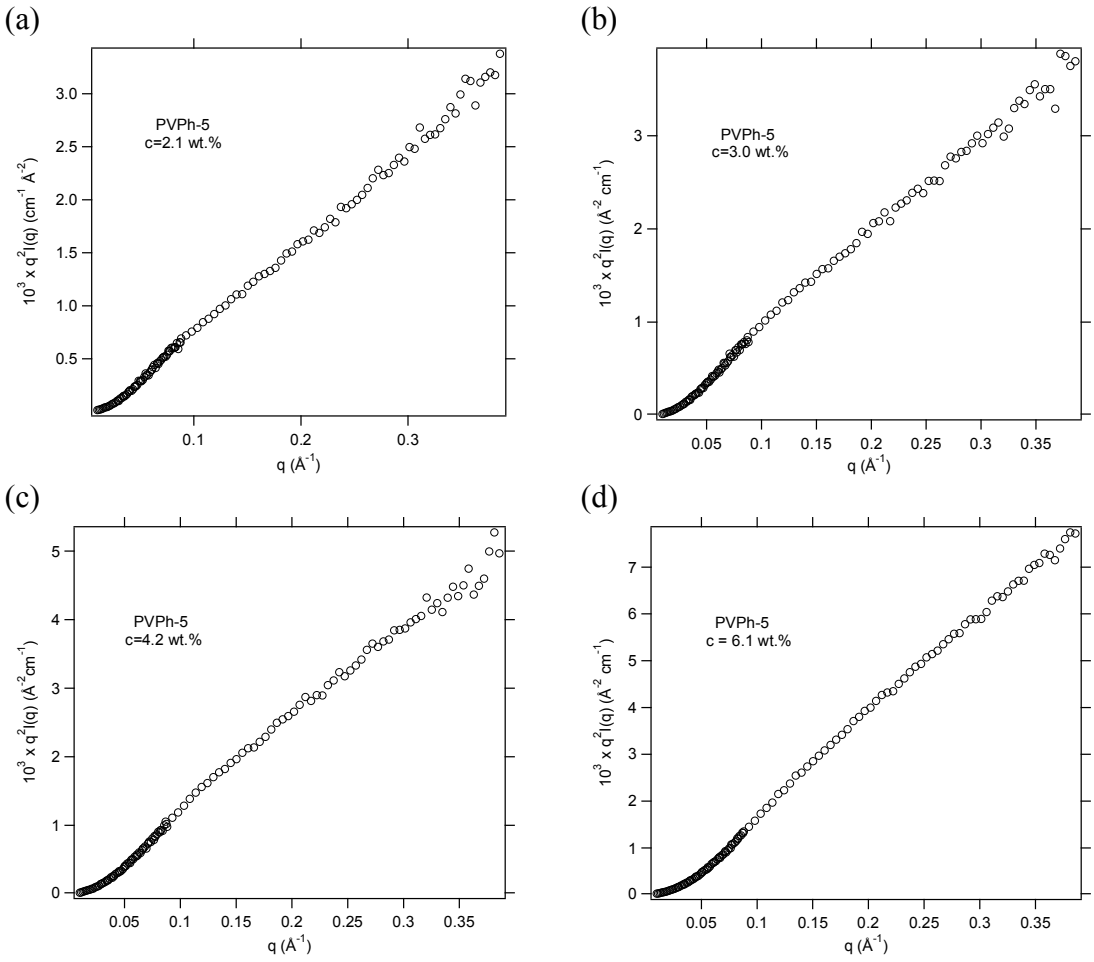

Figure A.1. Kratky plots for PVPh–5 in DMSO.

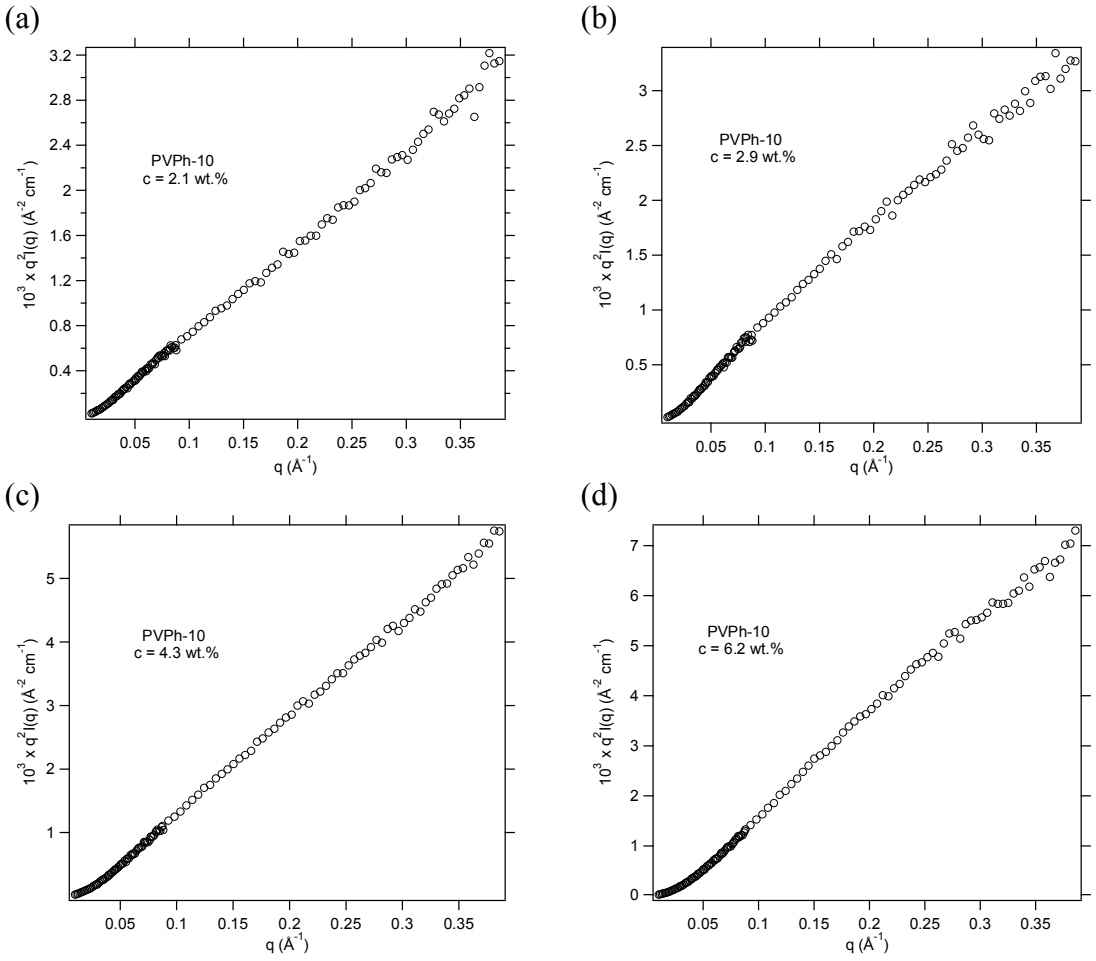

Figure A.2. Kratky plots for PVPh–10 in DMSO.

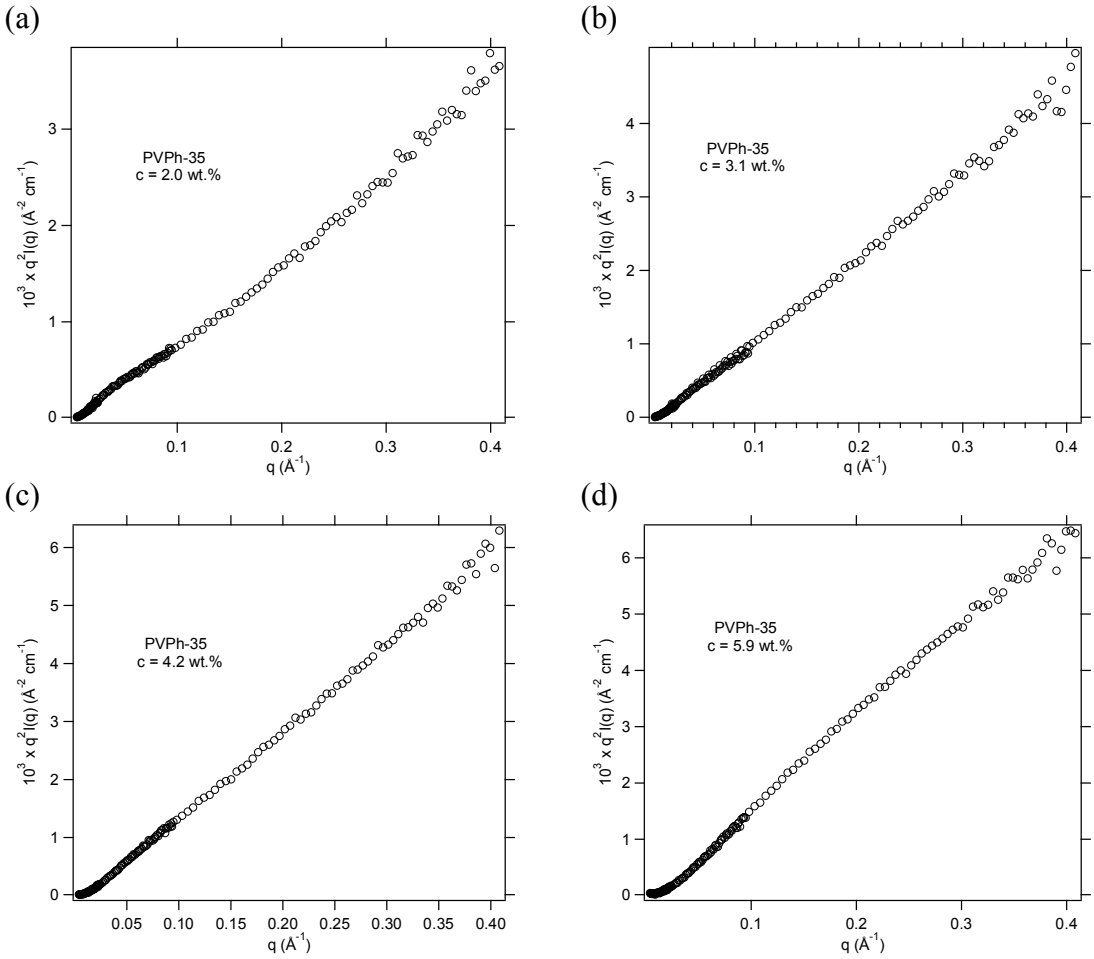

Figure A.3. Kratky plots for PVPh–35 in DMSO.

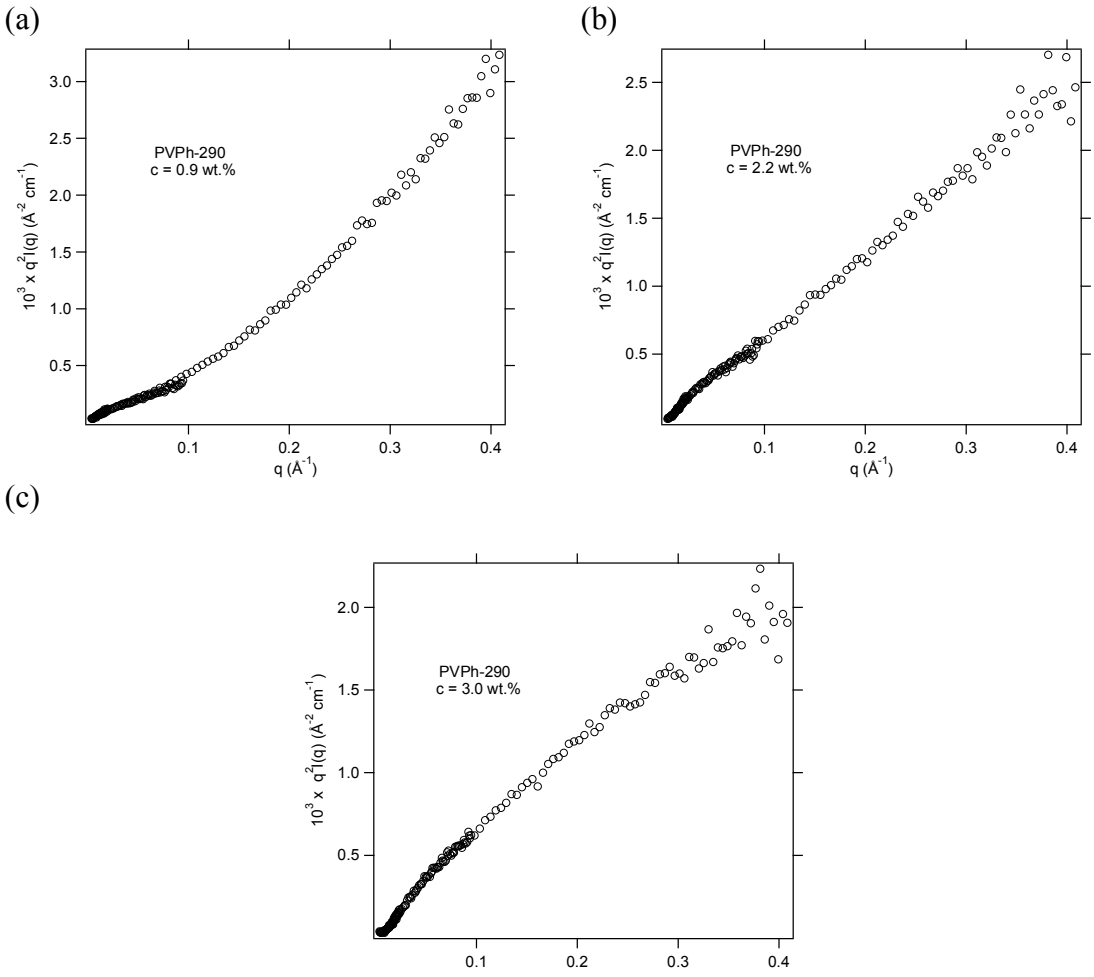

Figure A.4. Kratky plots for PVPh–290 in DMSO.

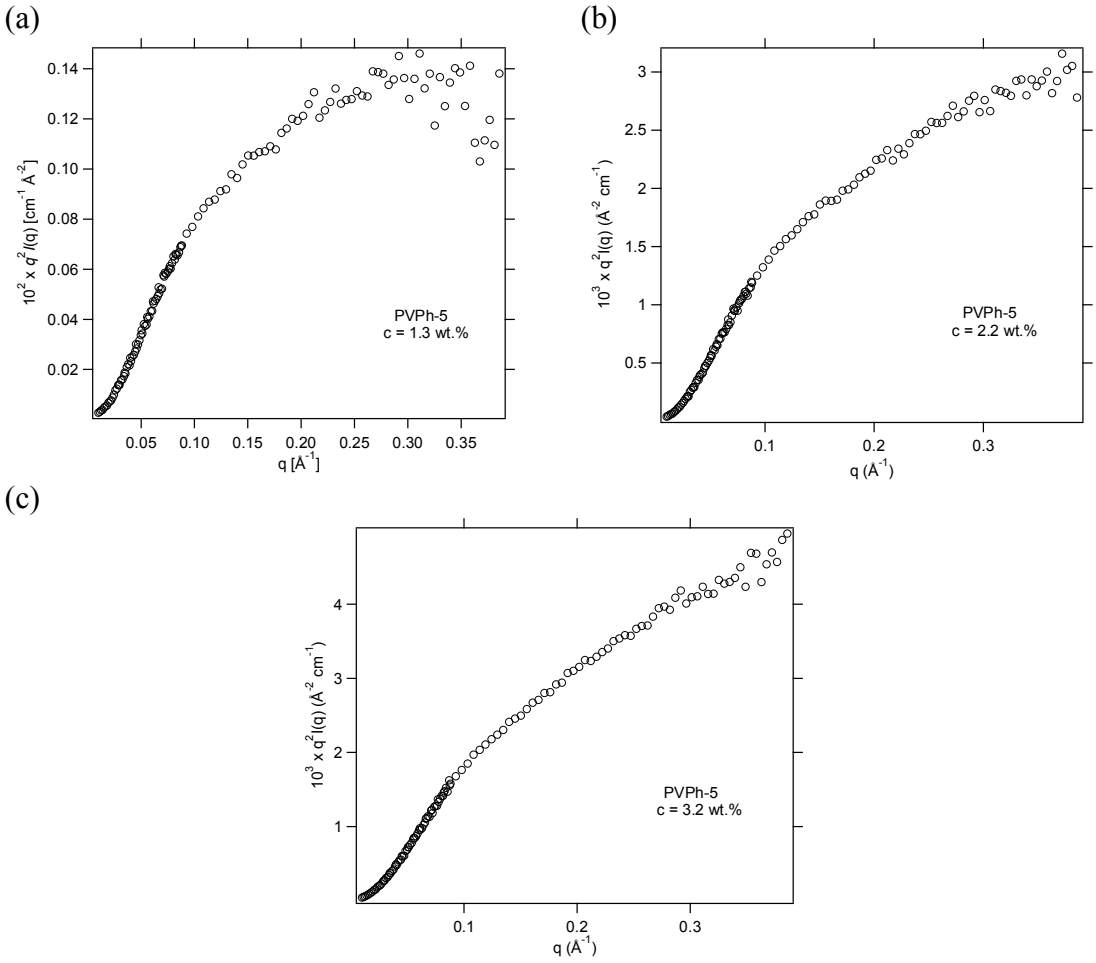

Figure A.5. Kratky plots for PVPh–5 in THF.

(a)

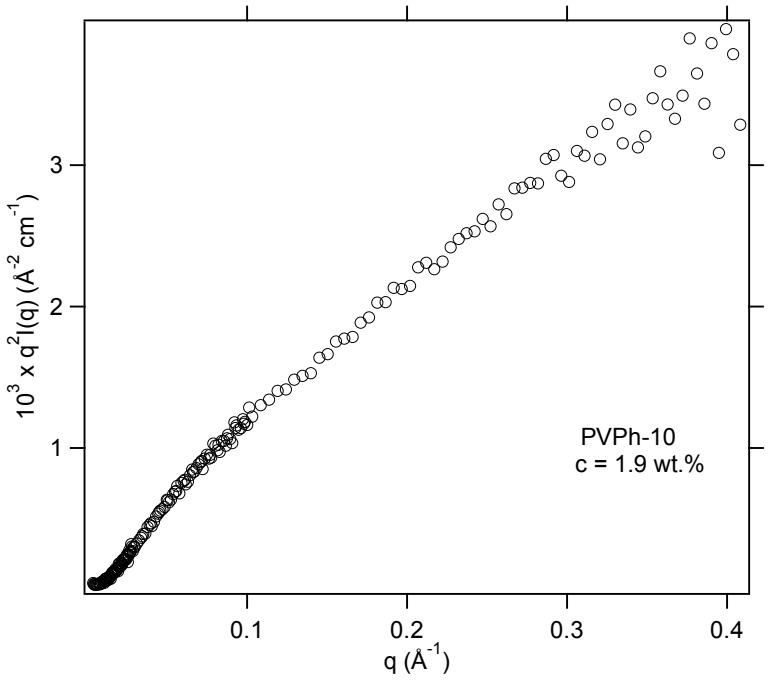

(b)

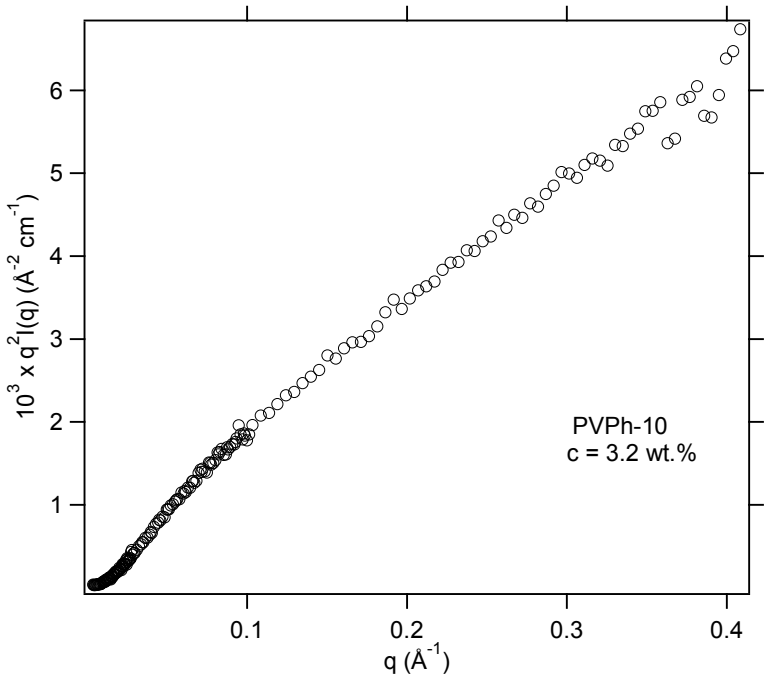

Figure A.6. Kratky plots for PVPh–10 in THF.

(a)

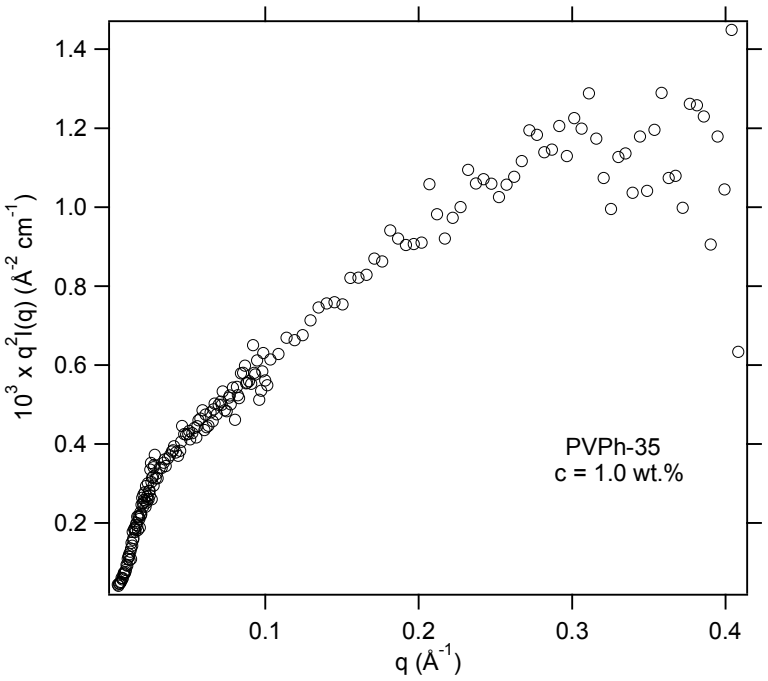

(b)

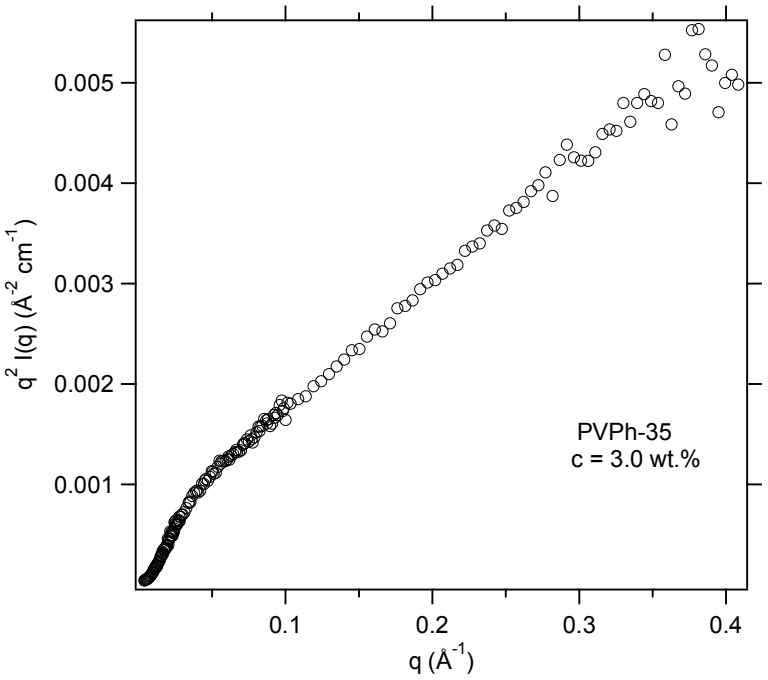

Figure A.7. Kratky plots for PVPh–35 in THF.

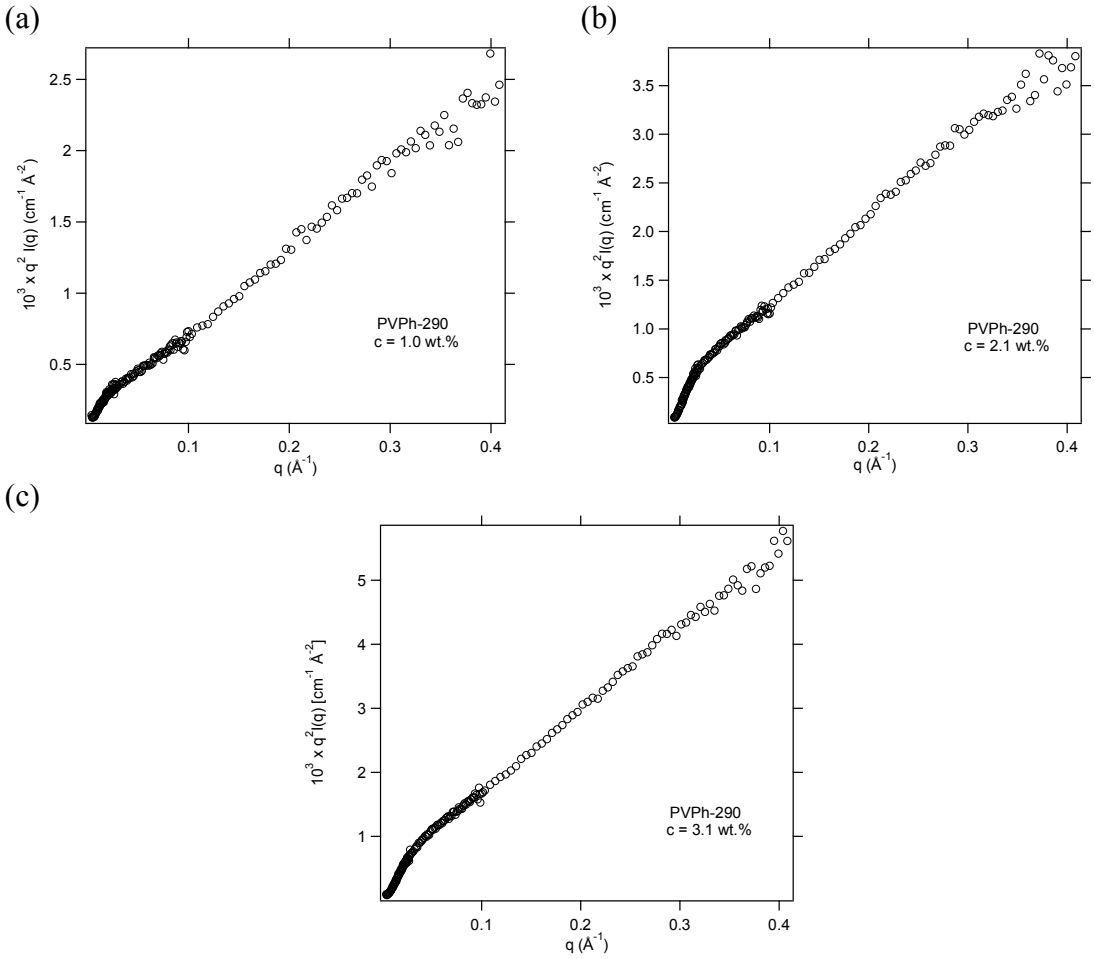

Figure A.8. Kratky plots for PVPh–290 in THF.